Instituto Universitario Mixto de Tecnología Química (Universitat Politècnica de València - Consejo Superior de Investigaciones Científicas)

PhD in Sustainable Chemistry

Porous solids for adsorption and separation of gas and vapor mixtures

Author:

Eduardo Pérez Botella

Supervisors:

Fernando Rey Susana

Valencia

October 2021

UNIVERSITAT POLITÈCNICA DE VALÈNCIA

INSTITUTO DE TECNOLOGÍA QUÍMICA

CSIC
Consejo Superior de Investigaciones Científicas

Acknowlegdements /
Agradecimientos (ES)

First of all, the official acknowledgements. I would like to thank the Spanish Ministry of Science, Innovation and Universities (MCIU) for my grant FPU15/01602, which has allowed me to carry out this thesis. I thank again the MCIU for paying my short stay in Brussels and for the funding provided through many different projects (RTI2018-101784-B-I00, Program Severo Ochoa SEV-2016-0683; and previous ones), which covered the costs of my research activities and allowed for my assistance to numerous international conferences which completed my training as a scientist. I thank the *Instituto de Tecnología Química*, the *Universitat Politècnica de València* (UPV) and the *Consejo Superior de Investigaciones Científicas* for providing the infrastructure needed for carrying out successful research. I thank the UPV and the *Departamento de Ingeniería Química y Nuclear* for allowing me to take part in teaching activities. I thank the *Universitat de València*, where I got my BSc degree in Chemistry, for the solid base in chemistry it provided me with.

As you will see, I am going to repeat myself a lot, which, luckily, is due to having beautiful people around me. Allow me to switch to Spanish.

Gracias a mis amigas y amigos y (ex-)compañeras y (ex-)compañeros del ITQ por darme un poquito de luz cada día en esta época tan oscura, los gestos bonitos dejan mella. Gracias, Nuria, por ser tan bonita, por haberme apoyado en los momentos dolorosos y por transmitirme tu ilusión y tu alegría en cada conversación. Gracias, Andrés, por haber estado tan cerca el último año y por ayudarme a mantenerme a flote

1

Gracias a Miguel, por ser mi otro hermano, el no biológico, y por acompañarme en tantos momentos buenos y malos y darme tanto amor. Gracias por todas las conversaciones maldiciendo sobre la tesis y la frustración y tus sabios consejos.

Gracias a mi familia, por ser la mejor familia del mundo y darme un apoyo incondicional y totalmente necesario en esta época tan dura. Gracias mamá y papá, por TODO. Por haber sido los pilares de nuestra casa mientras viví en ella y después; por haber cuidado tanto de Rodri y de mí, y por querernos tanto. Gracias Rodri por tu amor, tu admirable fuerza de voluntad y por haber querido pasar tanto tiempo conmigo en tu preciada vida. Gracias por animarme a seguir. Gracias a mi tía Maria Elena, por ser mi segunda madre, y a mis ~~primas~~ hermanas Ana y Elena. Gracias a Felo y Sesé, por ser los tíos guays. Danke, meine liebe Oma, für deine bedingungslose Liebe, ich hab dich sehr sehr lieb. Gracias tío Fernando por darnos tanto amor. Gracias María por tu ánimo, tus sarcasmos nutritivos y tu cariño. Os quiero muchísimo.

Gracias a Ari por existir y por seguir tu camino junto al mío, por ser el ser de luz más bonito del mundo, por quererme tanto y tan bien y ayudarme a tener la estabilidad emocional necesaria para seguir adelante día a día.

Abstract / *Resumen (ES)/*
Resumen (VAL)

Abstract

In this thesis, the properties of different zeolitic adsorbents and their use in separations of fluid mixtures of industrial interest have been studied. The selection of the materials has been carried out putting a special emphasis on low polarity small pore zeolitic adsorbents, more specifically, pure silica zeolites, aluminophosphates and silicoaluminophosphates. The separations that have been considered are related mostly to energy production, natural and biogas upgrading, purification of hydrogen, gasoline octane number improvement and purification of biobutanol.

The adsorption properties of the zeolitic materials have been studied by single component adsorption isotherm measurements, single component adsorption kinetics measurements and multicomponent dynamic adsorption experiments, i.e. breakthrough experiments. The adsorption isotherms were analysed in terms of their shape, the maximum adsorption capacity and used to calculate isosteric heats of adsorption, ideal thermodynamic selectivities and ideal working capacities in hypothetical swing adsorption processes. The adsorption kinetics measurements have allowed to compare the diffusional behavior of different adsorbates in different materials and to calculate diffusional time constants, which were, in turn, used for calculating ideal kinetic selectivities/separation factors. The breakthrough experiments were used to ultimately see how materials perform at conditions close to the industrial

case and to calculate for each material mixture selectivities and relevant swing adsorption process operation parameters, i.e. productivity, recovery and purity.

The physical properties of the studied materials, such as structure, crystalline order, atom connectivity, particle size and shape and textural properties have been critically evaluated and used to explain the results obtained in the adsorption studies.

In chapter 1, a general introduction on zeolites, their synthesis, properties and applications is provided, together with an introduction on adsorption phenomena and on the industrial separations of interest to this thesis. In chapter 2 the objectives of this thesis work are presented. In chapter 3 the synthesis of the adsorbents used is presented, together with the characterization and adsorption equipment and the adsorption data analysis procedures. In chapter 4, the adsorption of light gases on pure silica RWR zeolite is studied with special focus on the separation of hydrogen isotopes and the purification of hydrogen from steam methane reformery off-gas. In chapter 5 I study the adsorption properties of CO_2 on aluminophosphates, silicoaluminophosphates and zeolites of LTA, CHA and AFI structures, and more specifically their isosteric heats of adsorption. In chapter 6, I study the effect of pore size and pore topology on the separation of CO_2 from CH_4 by means of pure component isotherms and breakthrough experiments of the mixture. In chapter 7, the adsorption properties of C5-C7 hydrocarbons on pure silica STW zeolite are studied with special focus on the separation of dibranched from monobranched and linear hydrocarbons. A comparison with pure silica MFI zeolite (silicalite-1) is established. In chapter 8 a set of pure silica zeolites is studied as adsorbents for the vapor phase separation of 1-butanol from acetone, ethanol and water, typical components of the ABE fermentation broth. Pure component isotherms were measured and breakthrough experiments were carried out using multicomponent mixtures. Special focus is put on the recovery of 1-butanol from the desorption curve, and the dependence of purity with recovery is studied.

Resumen (ES)

En esta tesis se han estudiado las propiedades de diferentes adsorbentes zeolíticos y su uso en separaciones de mezclas fluidas de interés industrial. La selección de los materiales se ha realizado poniendo especial énfasis en los adsorbentes zeolíticos de poro pequeño de baja polaridad, más concretamente, zeolitas pura sílice, aluminofosfatos y silicoaluminofosfatos. Las separaciones que se han considerado están relacionadas principalmente con la producción de energía, procesado del gas natural y del biogás, purificación de hidrógeno, mejora del índice de octano de la gasolina y purificación de biobutanol.

   Las propiedades de adsorción se han estudiado mediante medidas de isotermas de adsorción de un solo componente, medidas de cinéticas de adsorción de un solo componente y experimentos de adsorción dinámica multicomponente, es decir, experimentos de curvas de ruptura. Las isotermas de adsorción se analizaron en cuanto a forma y capacidad máxima de adsorción y se utilizaron para calcular los calores isostéricos de adsorción, las selectividades termodinámicas y las capacidades de trabajo ideales en procesos hipotéticos de adsorción por oscilación. Las medidas de cinéticas de adsorción han permitido comparar el comportamiento difusional de diferentes adsorbatos en diferentes materiales y calcular las constantes de difusión temporales, que a su vez fueron utilizadas para calcular selectividades cinéticas ideales / factores de separación. Los experimentos de curvas de ruptura se utilizaron para ver cómo se comportan los materiales en condiciones cercanas al caso industrial, para calcular las selectividades reales de mezcla y los parámetros de operación relevantes de procesos de adsorción, es decir, productividad, recuperación y pureza.

   Las propiedades físicas de los materiales estudiados, como la estructura, el orden cristalino, la conectividad atómica, el tamaño y la forma de las partículas y las propiedades texturales, han sido evaluadas y empleadas para explicar los resultados obtenidos en los experimentos de adsorción.

En el capítulo 1, se presenta una introducción general sobre las zeolitas, su síntesis, propiedades y aplicaciones, junto con una introducción acerca de los fenómenos de adsorción y las separaciones industriales de interés para esta tesis. En el capítulo 2 se presentan los objetivos de este trabajo de tesis. En el capítulo 3 se presenta la síntesis de los adsorbentes utilizados, junto con los equipos de caracterización y adsorción y los procedimientos de análisis de datos de adsorción. En el capítulo 4, se estudia la adsorción de gases ligeros en Si-RWR con especial énfasis en la separación de isótopos de hidrógeno y la purificación del hidrógeno presente en la corriente de salida de un proceso de reformado de metano con vapor. En el capítulo 5 estudio las propiedades de adsorción de CO_2 en aluminofosfatos, silicoaluminofosfatos y zeolitas de estructuras LTA, CHA y AFI, y más específicamente los calores isostéricos de adsorción. En el capítulo 6, estudio el efecto del tamaño de poro y la topología de poro en la separación de CO_2 de CH_4 mediante isotermas de compuestos puros y experimentos de ruptura de la mezcla. En el capítulo 7, se estudian las propiedades de adsorción de hidrocarburos de las fracciones C5-C7 en Si-STW con la atención puesta en la separación de hidrocarburos dirramificados de monorramificados y lineales. Se establece una comparación con Si-MFI. En el capítulo 8 se estudia una serie de zeolitas puramente silíceas para la separación de una mezcla de vapores de 1-butanol, acetona, etanol y agua proveniente de un proceso de fermentación. Se han realizado experimentos de adsorción de los compuestos puros, así como de mezclas de ellos mediante curvas de ruptura. Se presta atención a la recuperación de 1-butanol durante el proceso de adsorción, estudiándose la recuperación del producto deseado frente a la pureza del mismo.

Resum (VAL)

En aquesta tesi, s'han estudiat les propietats de diferents adsorbents zeolítics i el seu ús en separacions de mescles de fluids d'interès industrial. La selecció dels materials s'ha dut a terme posant un èmfasi especial en els adsorbents zeolítics de porus petit de baixa polaritat, més concretament, les zeolites pura sílice, aluminofosfats i silicoaluminofosfats. Les separacions que s'han considerat estan relacionades principalment amb la producció d'energia, el processament de gas natural i de biogàs, la purificació d'hidrogen, la millora del nombre d'octans de la gasolina i la purificació de biobutanol.

Les propietats d'adsorció s'han estudiat mitjançant isotermes d'adsorció d'un component, cinètiques d'adsorció d'un component i experiments d'adsorció dinàmica multicomponent, és a dir, experiments de corbes de ruptura. Les isotermes d'adsorció es van analitzar en funció de la seva forma i capacitat màxima d'adsorció i es van utilitzar per calcular les calors isostèriques d'adsorció, les selectivitats termodinàmiques i les capacitats de treball ideals en els hipotètics processos d'adsorció per oscil·lació . Les mesures de cinètiques d'adsorció han permès comparar el comportament difusional de diferents adsorbats en diferents materials i calcular constants temporals de difusió, que, al seu torn, s'han utilitzat per al càlcul de selectivitats cinètiques ideals/factors de separació. Els experiments de corbes de ruptura es van utilitzar per, veure com funcionen els materials en condicions properes al cas industrial i per calcular per a cada mescla les selectivitats i els paràmetres d'operació rellevants per a processos d'adsorció, és a dir, la productivitat, la recuperació i la puresa.

Les propietats físiques dels materials estudiats, com ara l'estructura, l'ordre cristal·lí, la connectivitat dels àtoms, la mida i la forma de les partícules i les propietats texturals s'han avaluat i s'han utilitzat per explicar els resultats obtinguts en els experiments d'adsorció.

En el capítol 1, es proporciona una introducció general sobre les zeolites, la seva síntesi, propietats i aplicacions, juntament amb una

introducció referent a fenòmens d'adsorció i separacions industrials d'interès en aquesta tesi. En el capítol 2 es presenten els objectius d'aquest treball de tesi. En el capítol 3 es presenta la síntesi dels adsorbents utilitzats, juntament amb els equips de caracterització i adsorció i els procediments d'anàlisi de dades d'adsorció. En el capítol 4, s'estudia l'adsorció de gasos lleugers a Si-RWR amb especial atenció a la separació d'isòtops d'hidrogen i la purificació de l'hidrogen present en el corrent de sortida d'un procés de reformat de metà amb vapor. En el capítol 5 estudio les propietats d'adsorció de CO_2 en aluminofosfats, silicoaluminofosfats i zeolites d'estructures LTA, CHA i AFI i, més concretament, les seus calors d'adsorció isostèriques. En el capítol 6, estudio l'efecte de la mida i la topologia de porus sobre la separació de CO_2 de CH_4 mitjançant isotermes de components purs i experiments de ruptura de la mescla. En el capítol 7, s'estudien les propietats d'adsorció d'hidrocarburs de les fraccions C5-C7 en Si-STW amb especial atenció a la separació d'hidrocarburs lineals i monorramificats de dirramificats. S'estableix una comparació amb Si-MFI. En el capítol 8 s'estudia una sèrie de zeolites purament silícies per a la separació d'una mescla de vapors de 1-butanol, acetona, etanol i aigua provinent d'un procés de fermentació. S'han realitzat experiments d'adsorció dels compostos purs, així com de mescles d'ells mitjançant corbes de ruptura. Es para atenció a la recuperació de 1-butanol durant el procés d'adsorció, estudiant-se la recuperació del producte desitjat enfront de la puresa d'aquest.

List of symbols and abbreviations

Symbols, variables and parameters

a: arbitrary length variable or number. Also a parameter in Wagner's equation.

$\alpha_{a,b}^{eq}$: ideal equilibrium selectivity.

$\alpha_{a,b}^{kin}$: ideal kinetic selectivity.

$\alpha_{a,b}^{mix,eq}$: mixture equilibrium selectivity

b: arbitrary length variable or number. Also a parameter in Wagner's equation.

C: concentration, usually in mol/m^3.

c: parameter in Wagner's equation.

d: diameter, may be used in different contexts, units of length, i.e. m, cm, mm, μm or Å. May also be a parameter in Wagner's equation.

D: diffusion coefficient, usually given in m^2/s.

D/r^2: diffusional time constant , usually given in s^{-1}.

δ: chemical shift, usually given in ppm relative units

ϵ: voidage/void fraction of an adsorption column.

i: arbitrary number.

k**:** kinetic constant, , units depending on the type of kinetic equation.

K**:** equilibrium constant, units depending on the type of equilibrium equation.

l**:** length, may be used in different contexts, units of length, i.e. m, cm, mm, μm or Å.

m**:** mass, usually given in g. May also be the number of n-rings of a structural building unit in zeolite structure description.

n**:** number of moles, in other cases it may be the number of terms of a summation and in zeolite structure description it refers to the amount of Si atoms in a ring.

$\dot{n}$**:** molar flow, usually given in mol/s.

ν**:** frequency, given in MHz.

P**:** pressure, usually given in kPa = 0.01 bar = 10 mbar.

$\overline{Prod}$**:** productivity, given in mol/kg/h.

$\overline{Pur}$**:** purity, expressed as a percentage.

π**:** number pi

q_{st}**:** isosteric heat of adsorption, kJ/mol.

$q_{st,0}$**:** isosteric heat of adsorption at zero (low) coverage, kJ/mol.

Q**:** adsorbed amount, also referred to as loading, usually given in mmol/g.

r**:** radius, may be used in different contexts, usually in units of length, i.e. m, cm, mm, μm or Å.

$\overline{R}$**:** recovery, expressed as a percentage.

σ**:** kinetic diameter of a molecule, usually in Å.

t**:** time, usually given in s, min, h or d.

T: temperature, usually given in °C or K.

τ: retention time of a compound in a breakthrough experiment, given in min or s.

v: rate, usually given in s^{-1} or mol/s.

V: volume, usually given in m^3.

WC: working capacity usually given in mmol/g.

x: molar fraction in the adsorbed/liquid/solid phase. Also an arbitrary number in chemical formulae of inorganic solids or an exponent in Wagner's equation.

y: molar fraction in the gas phase. Also an arbitrary number in chemical formulae of inorganic solids or an exponent in Wagner's equation.

z: an exponent in Wagner's equation

ω: fractional loading.

2ω: angle in diffractometry.

Units

SI units and units derived therefrom by multiplication times a power of 10 (such as g, kJ, mmol, μm, etc.) are not included in this list.

Å: Ångstrom; length unit; equals 10^{-10} m

cm^3 STP: standard cubic centimeter, i.e. measured at Standard Temperature (0 °C) and Pressure (1 bar = 100 kPa); mol amount units, equals $4.403 \cdot 10^{-5}$ mol.

esu: electrostatic unit, also represented by Fr (Franklin) or statC (Statcoulomb), equals 1 $cm^{\frac{3}{2}}g^{\frac{1}{2}}s^{-1}$.

ppm: parts per million, unit of chemical shift relative to a reference species.

Abbreviations

This list does not include zeolite structure codes and is not comprehensive regarding names of specific porous materials. Abbreviations of organic compounds' names are listed.

22DMB: 2,2-dimethylbutane

23DMB: 2,3-dimethylbutane

23DMPe: 2,3-dimethylpentane

24DMPe: 2,4-dimethylpentane

22DMPr: 2,2-dimethylpropane

2MB: 2-methylbutane

2MPe: 2-methylpentane

3MH: 3-methylhexane

ABE: acetone, butanol, ethanol

AIPO: aluminophosphate

atrz: 3-amino-1,2,4-triazole

BET: Brunauer-Emmett-Teller

BP: backpressure regulator

BTX: benzene, toluene, xylenes

BuOH: 1-butanol

C#: when speaking of hydrocarbons, number of C atoms of a certain group of compounds / fraction, e.g. C5 refers to hydrocarbons containing 5 C atoms.

CBU: composite building unit

CCS: carbon (dioxide) capture and storage

COF: covalent organic frameworks

CV: checkvalve

DA: Dubinin-Astakhov

DAC: direct air capture

DDBQ: 2,2-dimethyl-2,3-dihydro-1H-benzo[de]isoquinoline-2-ium

DEDMAOH: diethyldimethylammonium hydroxide

EA: elemental analysis

ES: Spanish

ESA: electric swing adsorption

EV: electrovalve

FCC: fluid catalytic cracking

FESEM: field emission scanning electron microscopy

FID: flame ionization detector

GC: gas chromatograph

HMI: hexamethyleneimine

ICP-AES: ion-coupled plasma atomic emission spectroscopy

ICP-OES: ion-coupled plasma optical emission spectroscopy

ITQ: Instituto de Tecnología Química

IUPAC: International Union of Pure and Applied Chemistry

K222: Kryptofix222, hexacosa-4,7,13,16,21,24-diaza-1,10-bicyclo[8,8,8]hexacosane

LiLSX: Li-exchanged low silica X zeolite

LPG: liquefied petroleum gas

M: tetrahydro-1,4-oxazine, also known as morpholine.

m-dobdc: 2,5-dioxido-1,4-benzenedicarboxylate

MAS-NMR: magical angle spinning nuclear magnetic resonance

MFC: mass flow controller

MFM: mass flow meter

MOF: metal-organic framework

MON: motor octane number

MPV: multiposition valve

MS: mass spectrometer

MTO: methanol to olefins

MTPQ: 4-methyl-2,3,6,7-tetrahydro-1H,5H-pyrido[3.2.1-ij]quinolinium

nC5: n-pentane

nC6: n-hexane

nC7: n-heptane

NMR: nuclear magnetic resonance

ON: octane number

OSDA: organic structure directing agent

ox: oxalate

PFG NMR: pulsed field gradient nuclear magnetic resonance

PSA: pressure swing adsorption

PTFE: polytetrafluoroethylene, also known as Teflon

QENS: quasi-elastic neutron scattering

R: (in zeolite structure description) ring, goes after a number (example: 4R, 4-ring)

REY: rare-earth exchanged Y zeolite

ROG: refinery off-gas

RON: research octane number

RPSA: rapid pressure swing adsorption

SAPO: silicoaluminophosphate

SBU: secondary building unit

SDA: structure directing agent

SEM: scanning electron microscopy

SMROG: steam methane reforming off-gas

TCD: thermal conductivity detector

TEA: triethylamine

TEAOH: tetraethylammonium hydroxide

TEOS: tetraethylorthosilicate

TGA: thermogravimetric analysis

TMAdAI: N,N,N-trimethyl-1-adamantammonium iodide

TMAdAOH: N,N,N-trimethyl-1-adamantammonium hydroxide

TMAOH: tetramethylammonium hydroxide

TPABr: tetrapropylammnonium bromide

Tri2PMP: tri-(2-propyl)-methylphosphonium

trz: 1,2,4-triazole

UPV: Universitat Politècnica de València

17

USY: ultra stabilized Y zeolite

VAL: Valencian

VPSA: vacuum pressure swing adsorption

VSA: vacuum swing adsorption

VUB: Vrije Universiteit Brussel

WGS: water-gas shift

XRD: X-Ray Diffraction

ZIF: zeolite imidazolate framework

ZLC: zero length column

Contents

Chapter 1

Introduction

This chapter has as its aim to define all the concepts and convey the basic knowledge needed for understanding the methods, results and conclusions of this thesis' research. For the sake of clarity I have divided it into three sections, i.e. *zeolites*, *adsorption* and *chemical separations*. In the first section, zeolites, a type of microporous materials that I have used in this thesis work, are thoroughly explained in terms of their structure, composition and properties and a brief review on their applications is given. In the second section, the fundamentals of adsorption science are presented, with special attention to its industrial application and our case of interest (adsorption on microporous materials). Finally, the concept of chemical separation and the state of the art of separations I have addressed in this research are presented. These separations are of industrial importance and are related to chemical and energy production. The replacement of the current separation methods by optimized adsorption processes could mean an improvement in terms of sustainability and economical savings. Special emphasis is put on the use of zeolites as adsorbents for these separations, as it is the starting point for this thesis.

1.1 Zeolites

Zeolites are crystalline microporous aluminosilicates widely used as catalysts, adsorbents and ion exchangers. They belong to the tectosilicate type minerals and some of them can occur naturally. Their well-defined pore size, compositional tunability, thermal stability and commercial availability since the 1950s [1–4] have boosted their use in industrial and domestic applications, which take advantage of their unique properties. In the following sections I will first present a short historic review of zeolites and their use (section 1.1.1), then I will explain these materials in terms of their structure and composition (section 1.1.2), from which their properties derive. Later, I will present the general synthetic procedures to obtain these materials (section 1.1.3) and finally I will briefly review their properties and wide field of application (section 1.1.4).

1.1.1 A short history of zeolites

The term zeolite was coined by the Swedish mineralogist Axel F. Cronstedt in 1756 [5] when he observed froth forming on the surface of the mineral stellerite upon heating [6]. The mineral was apparently "boiling" and thus, he named it "zeolite", from the Greek *zein* "to boil" and *lithos* "stone". Later, this phenomenon was ascribed to the presence of hydration water inside of the pores of the mineral, which is liberated upon heating.

For the next years no noticeable discovery was made by chemists in what refers to zeolites and it was not until 1840 that Damour demonstrated the reversible hydration and dehydration of these materials [7]. The first demonstration of the cation-exchange properties of natural zeolites (chabazite and natrolite) was in 1858 [8] and the first report on zeolite synthesis was in 1862, with the synthesis of levyne [9]. The first industrial success of these materials was as water softeners for laundry compositions [10–12], basing on their ion-exchange properties. This still remains one of their major applications.

The adsorption of species other than water was first reported by

Friedel in 1896 [13] and further studied by Grandjean in 1909 [14]. Selective adsorption and exclusion of molecules, i.e. the molecular sieve effect, was first described in 1924 by Weigel and Steinhoff, which observed how water, methanol, ethanol and formic acid were adsorbed on chabazite, whilst acetone, diethyl ether and benzene were excluded [15]. This effect could not be explained until the structural porosity of zeolites was described following the first structural elucidations of these materials [16–18]. In 1932, McBain coined the term "molecular sieve" referring to zeolites and their very high selectivity when applied to adsorption processes [19]. McBain's work was a turning point in zeolite science, as it encouraged a young researcher, Richard M. Barrer, currently considered the father of zeolite science, to dive into these materials' field of research [20].

Barrer studied the separation of mixtures of many different molecules on zeolites and realized the great potential of these materials as adsorbents for separation processes. Over the next 20 years he successfully attempted the synthesis of zeolites by mimicking the crystallization conditions of natural zeolites (hydrothermal, i.e. alkaline media and temperature above 200 °C), thus obtaining some synthetic analogues of natural zeolites, such as chabazite and mordenite [21–23], and others with no natural counterpart, which he named as zeolites P and Q [24–26].

In 1949 he described the alkaline-ammonium cation exchange in zeolites followed by calcination as a strategy to obtain them in their proton-exchanged form [27]. During his time at the Imperial College (1954-1976), Prof. R. M. Barrer achieved the first zeolite syntheses using tetraalkylammonium cations [28–30], which, in retrospect, has turned out to be the most fruitful strategy for obtaining new zeolitic materials to the present time, and still remains state-of-the-art (see section 1.1.3) [31–34].

Barrer's discoveries attracted the interest of the industry on zeolites and resulted in the development of commercial zeolite production and their application. The most relevant of these contributions were by Union

Carbide in the USA within a research programme which started in 1949, with Barrer as an academic consultant. Robert M. Milton enrolled in this research programme with the objective to develop an adsorption method to separate N_2 from O_2 instead of traditional cryogenic distillation. Inspired by the works on molecular sieving by McBain and Barrer, he attempted this separation using chabazite as the adsorbent. While trying to obtain this zeolite (which he managed by 1950 [35]), he varied the synthesis conditions by means of lowering the temperature to 25-150 °C and using more reactive silica sources and more alkaline media. This lead to the rapid obtention of zeolites A and X, along with other 14 new zeolite materials [1, 20]. Donald W. Breck joined Milton's group in 1951 and he discovered zeolite Y in 1954. This zeolite is isostructural to zeolite X, but presented lower Al content. In the following years, the zeolite research group at Union Carbide developed the scaling up of these syntheses and in 1954 zeolites A and X were commercialized for adsorption applications [1, 3, 4, 35]. Meanwhile close to 24 new zeolitic materials were discovered by this group [1, 36–38].

The breakthrough in zeolite science in the 1950s mostly led by Union Carbide boosted other companies' interest in these materials, as well. In the next years, many new and modified zeolites were discovered and used in adsorption, ion exchange and catalysis applications. More information on the use of zeolites will be given in section 1.1.4.

1.1.2 Structure and composition

Zeolites are crystalline microporous aluminosilicates, the framework of which consists of corner-sharing TO_4 tetrahedra (see fig. 1.1), where T are tipically Si or Al atoms. The empirical formula of an aluminosilicate zeolite can be represented by $M_y^{z+}[Si_{1-x}Al_xO_2]^{x-}$, where $x = y \cdot z$ and is most frequently limited to $0 \leq x \leq 0.5$, a phenomenon known as Löwenstein's rule [39]. The presence of tetrahedrally coordinated Al atoms leads to negative charges in the framework that are compensated by extraframework cationic species, represented in the formula above as

M^{z+} [40]. These cations are located inside the pores and cavities of the zeolite framework and can be of an organic (typically alkylammonium) or inorganic nature (alkaline, alkaline earth and other metals), depending on the synthesis conditions and on whether the material has been subjected to post-synthesis treatments (calcination, ion-exchange). Natural zeolites and many synthetic zeolites contain metallic cations, which are usually hydrated and account for Cronstedt's discovery.
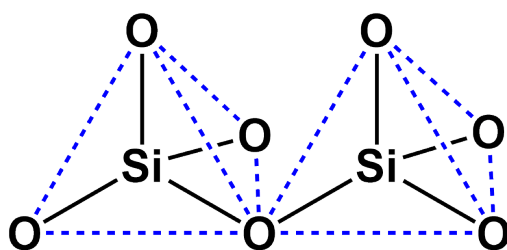
Figure 1.1: *Two corner-sharing TO$_4$ tetrahedra.*

There is as well the special case of zeolites with no aluminium at all, known as zeosils or pure-silica zeolites. Logically, they contain no extra framework cations. Pure-silica and high-silica (Si/Al > 5) zeolites are under intense research, as they present a hydrophobic surface and even larger thermal and chemical stabilities than traditional zeolites, which makes them very appealing for adsorption applications [2, 41–43].

On the other hand, the T atoms can be different from Si and Al. For instance, there are many compositional variants of zeolites which present structures analogous or different from aluminosilicate zeolites. An advanced "chemistry search" in the Database of Zeolite Structures [44] is a straightforward way to obtaining a quick overview on the rich compositional variability of zeolites. Apart from Si and Al, which are not necessarily present in all zeolite-like materials (zeotypes), other atoms can be found in tetrahedral coordination in the framework, such as B, Be, Co, Fe, Ga, Ge, Mg, P, Ti and Zn. It must be noted that the presence of some of these "heteroatoms" can facilitate the crystallization of specific structures which are otherwise not achievable. This is the case of the structure-directing effect of Ge, which favors the formation of small T-O-T angles and thus, the crystallization of low density structures [45, 46].

Aluminophosphate (AlPO) materials are isoelectronic with pure-silica zeolites and present a perfectly alternating sequence of AlO_4 and PO_4 tetrahedra. They have proven interesting for adsorption and heat exchange applications, even though frequently they present more limited thermal and chemical stabilities if compared to zeolites [46, 47]. There is a series of AlPO-related materials, which are in concept, heteroatom-substituted AlPOs [48, 49]. The possible "heteroatoms" include Si, Fe, Mg, Mn, Co, Zn, Ti, V and/or Cr among others. In silicoaluminophosphate (SAPO) materials, part of the T positions of the framework are occupied by Si atoms. Silicon substitution in SAPOs follows conceptually more complicated patterns than Al substitution in aluminosilicate zeolites, as Si can "replace" a single P atom (isolated Si), but also larger framework fragments, yielding what is known as Si-islands or Si-rich domains (see fig. 1.2). SAPOs have found use in adsorption and catalysis. Metal aluminophosphate and metal silicoaluminophosphate materials have been widely studied as catalysts [49–53].

Depending on the T atoms present in a framework, the chemical and physical properties of the material will vary. The presence of atoms with redox properties, such as Ti, Co, Fe or V, will have a great influence on the redox chemistry of the material [54, 55]. The acidity/basicity of specific adsorption sites depends as well on the composition of the framework. The ratio of tetravalent (Si, Ge, etc.) to trivalent (Al, B, etc.) atoms, usually the Si/Al ratio, largely defines the polarity of the material. For instance, zeolites with a higher Al content (also known as low-silica zeolites) adsorb larger amounts of polar compounds, such as water, than high- or pure-silica zeolites [56]. Additionally, the charge-balancing extraframework cations can contribute with their specific chemical properties to the chemistry of the material [57].

However, the most important feature of zeolites and the one that has made them interesting for any application, since they were first studied in detail by Barrer, is their structure-derived porosity. The flexibility of the T-O-T angle allows for different spatial dispositions of the tetrahedra [31],
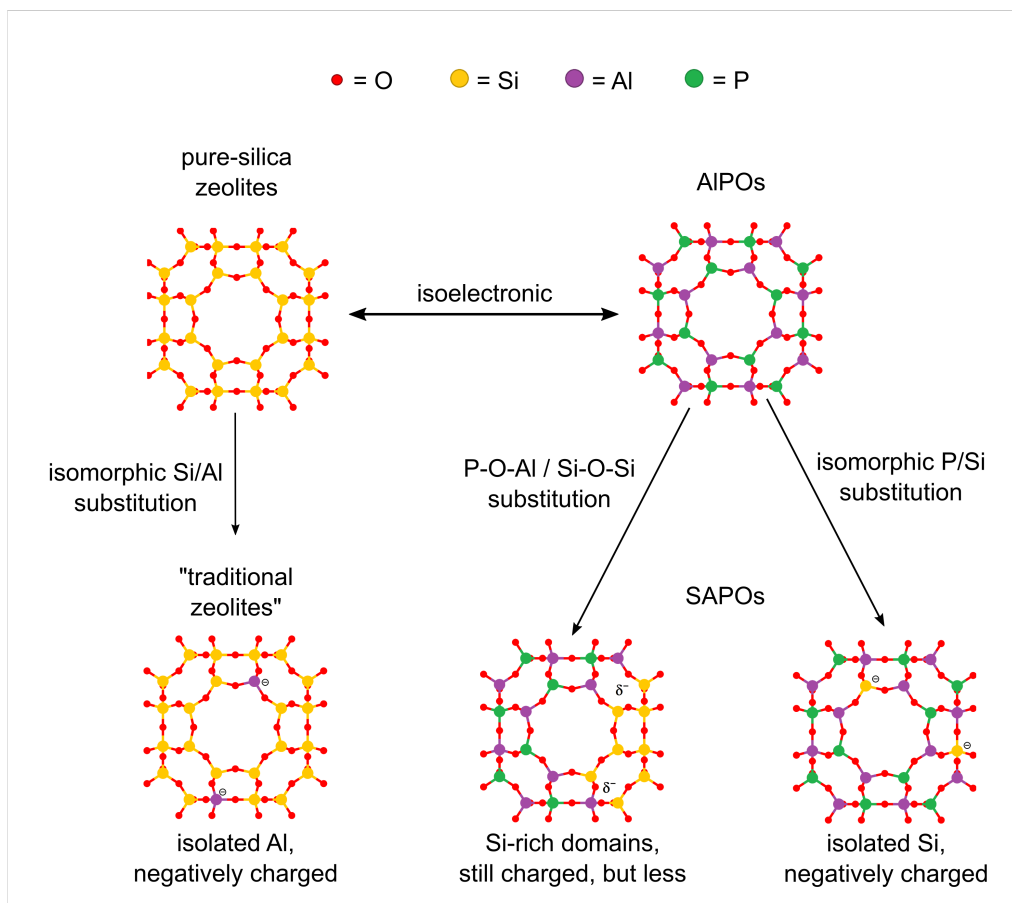
Figure 1.2: *Isomorphic substitution scheme of SAPOs, exemplified in an LTA-cavity.*

thus resulting in a large number (millions) of different hypothetical porous structures [58]. More than 250 different zeolitic structures are known to exist at the present time, of which some can be found in nature and others are synthetic. Each structure is given a three-letter code and registered in the Database of Zeolite Structures [44], where a thorough structural and crystallographic description is provided.

Structural description of zeolites is usually performed in terms of their building units. The TO_4 tetrahedra, i.e. the primary building units of zeolites, can be linked following different arrangements, which result in secondary building units (SBUs), composite building units (CBUs) or the so called "tiles". SBUs contain a maximum number of 16 T atoms and were initially intended to be the sole descriptor of zeolite structures, i.e. a single SBU type (of which a total number of 23 are listed in the Database of Zeolite Structures [44]) should suffice for the description

of each framework. At the same time, different SBUs could be used to describe a single framework and different frameworks could be described using the same SBU. However, in 2007 it was realized that the SBUs were insufficient for the universal description of zeolite structures and the listing of new SBUs ceased. Instead, the broader concepts of CBU and/or tiles were introduced and recommended. It must be noted that there is an overlap between these descriptors, and some arrangements of tetrahedra can belong to two or all three of these kinds of descriptors. For instance the double 4-ring belongs to all three of them and is named differently in each case ("4-4" according to the SBU nomenclature, "d4r" according to the CBU nomenclature and "t-cub" according to the tiles nomenclature). Examples of typical building units are given in fig. 1.3:
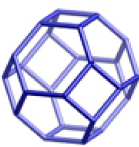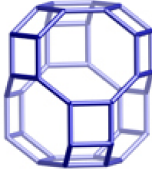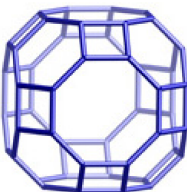
Nomenclature				
SBU	4	4-4	6*1	-
CBU	-	d4r	mei	mor
tile	-	t-cub	-	t-tes
Nomenclature				
SBU	6-6	-	-	-
CBU	d6r	sod	cha	lta
tile	t-hpr	t-toc	t-cha	t-grc

Figure 1.3: *Examples of building units and their possible names, according to the IZA Structure Commission [44]. Vertices represent T atoms, oxygen atoms are not depicted.*

A more general notation of the CBUs, also applicable for new structures and building units, follows the scheme $[n_i^{m_i}]$, where m is the number of n-rings defining the polyhedron and $\sum m_i$ the total number of faces. Thus, the *d6r* building unit could be expressed more generally as $[4^6 6^2]$ and the *sod* building unit, as $[4^6 6^8]$ [59]. In some cases, instead of polyhedral building units, chain building units may be useful for structural description.

Another approach for structural description of zeolites is based on the

size, connectivity, topology and geometry of their pore systems. The pores are the void spaces inside the framework that are not occupied by framework atoms. These pores can be accessible, or inaccessible to molecules of various sizes, depending on how they are connected and the size of the pores. Polyhedral pores with windows (the n-rings are called windows) smaller or equal to 6R are named cages, and only a few very small molecules, e.g. water, can penetrate these. The *sod* building unit shown in fig. 1.3 is an example of a cage, and receives the name of sodalite cage or β-cage. Finite polyhedral pores with at least one of its faces consisting of a window larger than 6R are called cavities, an example of which is the *lta* building unit shown in fig. 1.3, also called the α-cavity. Pores that extend indefinitely in one direction and whose size allows for diffusion of guest molecules along its length are called channels. Zeolites with pore systems which present channels in only one direction, or non-intersecting channels in different directions are called unidirectional. When channels in different directions intersect, they can form bidirectional or tridirectional channel systems.

According to the minimum window size of the largest pores present in their structure, zeolites can be classified as follows [40, 56, 59, 60]:

• **Small pore zeolites** have a minimum pore diameter between 3 and 5 Å, which corresponds to rings consisting of 8-9 TO_4 tetrahedra (8 - 9R).

• **Medium pore zeolites** have a minimum pore diameter between 5 and 6 Å, which corresponds to 10-rings (10R).

• **Large pore zeolites** have a minimum pore diameter between 6 and 7.5 Å, which corresponds to 12R.

• **Extra large pore zeolites** have a minimum pore diameter above 7.5 Å, which corresponds to rings of more than 12 tetrahedra.

Within these groups, there are many structures with different pore sizes and shapes. If a zeolite presents more than one kind of pores, it will be classified according to the largest pore present. For example, the

STW framework presents intersecting channels with different minimum window sizes, i.e. 8R and 10R, and is considered a medium pore zeolite.

The topology of the pore system can be of high importance as well, as it has a large impact on the interaction and diffusion of molecules inside the pores. In this thesis I have decided to give a name to two common kinds of channel system topologies, depending on how the cross section of a channel varies along its length. Channels that consist of interconnected cavities, i.e. their cross section varies considerably, will be referred to as "cavity-like". Channels with a more constant cross section will be referred to as "channel-like".

1.1.3 Synthesis of zeolites

1.1.3.1 Direct synthesis

The synthesis of zeolites is usually performed following the hydrothermal method, which mimics the natural conditions that lead to the crystallization of zeolites. This includes a source of the T atoms (in nature, it is volcanic ash and volcanoclastic materials), a structure directing agent (SDA; in nature, usually alkaline or alkaline-earth cations), a mineralizing agent (usually alkaline aqueous solutions), temperatures below 600 °C and autogenous pressures [61, 62]. Through imitation of the natural process some zeolites were obtained, mostly analogues of minerals existing in nature. However, it was by modifying it that the structural and compositional richness of these materials started to become apparent.

The synthetic processes that have lead to the discovery of new zeolitic structures and compositional variants follow these guidelines in general terms, but present many singularities. The T-atom source is usually an oxidized form of the T-atom. For instance, typical Si sources are amorphous, fumed or colloidal silica, silicates, alkyl silicates and other zeolites/materials. This kind of Si sources with enhanced surface area and solubility were a key for success when Milton and coworkers [35] started the search for new zeolites in 1949. Typical Al sources include

different kinds of alumina, aluminum hydroxides, aluminum alkoxides and aluminates. In the case of AlPOs and SAPOs, P is most frequently added as phosphoric acid [63].

The role of the SDAs is of large importance, as they not only promote the crystallization of specific structures, but also may remain inside the pores of the final material to some extent and act as charge-balancing ions. The first SDAs that were used in zeolite syntheses were cations of inorganic nature, such as Na^+, Ca^{2+} or K^+. Nonetheless, the most remarkable type of SDAs and the ones that meant a breakthrough in zeolite science are organic SDAs (OSDAs), which are in most cases amines and alkylammonium cations [31–34]. These OSDAs were initially referred to as "templates" [64, 65], a term which is still frequently (and inaccurately) used to address OSDAs in general. It has its origin in the so-called "template effect" that some OSDAs possess, in which their presence in the synthesis gel leads to the crystallization of a specific structure with matching topological features [64]. Other molecule types, such as alkylphosphonium cations, alkylsulphonium cations, phosphazenes, crown macrocycles, metal complexes, and self-assembled molecules have been used as OSDAs, but with a quantitatively more modest degree of success than nitrogen OSDAs [66]. The way in which these OSDAs favor the crystallization of a specific structure is not yet fully understood, despite of the large research effort put into it [32, 33, 67, 68]. However, the rational design of OSDAs in the search for particular zeolites has given good results in some cases [42, 69–71]. In general terms, linear OSDAs favor the crystallization of 1D structures, branched OSDAs favor the crystallization of interconnected 2D and 3D structures and bulky OSDAs favor the crystallization of structures possessing cavities. The lower charge density of the OSDAs in comparison with the alkaline and alkaline-earth cations allows for less charged frameworks, thus facilitating the obtention of final materials with a higher Si/Al ratio [33, 56]. More than one kind of inorganic or organic SDA may be present in the synthesis gel and both may act as SDAs,

but they also may have been added to increase basicity, as explained below. Furthermore, the T atoms present in the synthesis gel can have a structure directing effect, too, as they may favor the crystallization of structures bearing specific CBUs. This is the case for Ge, or Be, which favor D4R and 3R, respectively [34].

The mineralizing agent intervenes directly in the breaking and formation of T-O-T bonds, and helps establishing a dynamic equilibrium that ends in the formation of the zeolite [68]. Possible mineralizing agents are the hydroxide and fluoride anions [72]. Hydroxide anions are the most widely used mineralizing agent and they are frequently added along with the SDA. If an extra amount of hydroxide anions is needed it is usual that inorganic (NaOH, KOH, NH_4OH) bases are used for low silica zeolites and organic (amines, alkylammonium) bases are used for high and pure silica zeolites. The source of fluoride anions can be hydrofluoric acid, which in turn decreases the pH of the gel (this may be desirable for preventing OSDA decomposition), or ammonium fluoride. Some zeolites have been synthesized both from gels containing hydroxide and fluoride and there are interesting consequences to the use of one or the other. The fluoride anion has in some way a structure directing effect, too, in which it favors the formation of certain CBUs and phases with lower densities [73, 74]. On the other hand, zeolites synthesized from fluoride containing gels tend to present an extremely low amount of defects [75]. The H_2O/SiO_2 is important as well, especially in high silica gels in fluoride media, as it affects which kind of frameworks will be obtainable basing on the density of the final material and the size of the crystals [72, 76, 77].

Another way of directly influencing the synthesis outcome is to introduce crystal seeds of the desired zeolite structure in the synthesis gel. This strongly promotes the crystallization of the desired phase, as the nucleation step is skipped and the crystals can start to grow immediately [68].

Crystallization temperature and time have a decisive effect in the synthesis of zeolites [35, 63, 68]. Higher temperatures and longer

crystallization times will favor the obtention of more dense, usually more stable phases instead of more open phases. On the contrary, the pressure in the gas phase does not seem to have any effect on the synthesis [35]. Other synthesis parameters that have a remarkable influence on the product obtained are ageing of the gel at lower temperature prior to the hydrothermal process and stirring/rotation speed during the crystallization [68].

As can be seen, there are many different variables that affect the result of hydrothermal synthesis of zeolites. The complexity of these heterogeneous systems has not allowed for a full rationalization of the crystallization mechanisms, or of the specific conditions that lead to the crystallization of a specific phase with a well defined crystal size and composition. However, general trends on how each and every of these parameters affect the synthesis outcome are understood and applied to new synthetic processes in order to reduce the range of possible results.

1.1.3.2 Post-synthetic modification of zeolites

Even though many zeolites can be obtained by direct synthesis with tailored composition and structure, it is common that further processing, i.e. post-synthetic treatment, is needed to achieve the desired properties in the final material. Ion exchange, calcination, hydrogenation, steaming, metal supporting, insertion of aluminium and grafting of functional groups are some of the most frequently used methods [78]. Here, I will present briefly the methods relevant to this thesis, i.e. ion exchange, calcination, hydrogenation and steaming, and their main purpose. Examples of their use for obtaining tailored materials for specific applications will be given in section 1.1.4.

Ion exchange of aluminosilicate materials allows us to modify their acid-base, redox and textural properties (pore sizes and interaction with adsorbates). It is usually performed in an aqueous solution with a high concentration of the species to be exchanged. After reaching equilibrium, the zeolite is filtered, washed and dried and can be subject to further

exchange or modifications. Exchange of small cations, such as metals or ammonium is the usual case. If the zeolite pores are too narrow for the extraframework species to diffuse, ion exchange may not be possible, which is usually the case for OSDAs.

Activation of zeolites, upon which extraframework species are modified or removed, is crucial prior to their use as catalysts or adsorbents [79]. Calcination at high temperatures in oxidizing (air, dry air) or inert (vacuum, nitrogen, argon) atmospheres are frequent methods to activate zeolites. If the zeolite has been synthesized in the presence of an inorganic SDA, or has been subject to ion exchange, these inorganic cations lose their hydration sphere upon calcination, thus allowing for their interaction with other species. In the case of OSDA-zeolites, calcination in air leads to the combustion of these organic species, thus freeing the pores. Calcination of ammonium-exchanged zeolites leads to the obtention of their acidic H-form [27]. A specific method that allows for P-removal in zeolites which have been synthesized using a P-containing OSDA is hydrogenation at high temperature followed by calcination in air [66].

Steaming processes involve high temperatures and an atmosphere rich in water. These promote the hydrolization of the T-O-T bonds and can have diverse effects in the final material. Partial or complete loss of crystallinity and the dealuminization of the framework with the consequent formation of silanol groups and mesopores are the most common outcomes [80].

1.1.4 Properties and applications

Zeolites and related materials present high thermal and moderate to high chemical stabilities [2, 56]. In general terms, traditional aluminosilicate zeolites are thermally stable up to 700 °C, can be dissolved in acids and strong bases and partially retain their crystallinity upon steaming at high temperature [78]. Specifically, steaming at high temperatures has been used as a post-synthetic treatment to remove aluminum from the framework, increase its stability and modify defect distribution, the

most known and illustrative case of this being the development of fluid catalytic cracking (FCC) catalyst USY (Ultra Stabilized Y zeolite) [80]. It is common, that high- and pure silica materials present even larger thermal (up to 1300 °C, relatively close to the melting point of quartz, i.e. 1713 °C [61]) and chemical stabilities (only soluble in hydrofluoric acid and strong bases). AlPOs are somewhat less thermally stable than zeolites, retaining their crystallinity at temperatures up to 1000 °C and up to 600 °C in a moist atmosphere [56]. SAPOs tend to be moisture-sensitive and slowly collapse if exposed to ambient moisture after long periods of time. In the absence of water, however, their stabilities resemble those of AlPOs. It is frequent that AlPOs and SAPOs undergo changes of structure upon hydration [81–83]. The effect of mechanical stress on zeolites, e.g. by excessive grinding, can lead to a partial or even total loss of crystallinity [84, 85].

The most important property of zeolites, and the one on which their applicability as catalysts, adsorbents and ion exchangers depends, is their structural porosity. Closely related to this feature, their narrow pore size distribution, i.e. very regular pore sizes, makes them useful for applications, in which size or shape selectivity is involved [86, 87]. Furthermore, their chemical properties can be tailored by synthetic or post-synthetic procedures for specific applications. When extraframework species present in their pores possess acid-base or redox properties, these are transferred to the containing zeolite to a greater or lesser extent. Below, a brief review of interesting applications and the underlying properties of zeolites is provided. Probably due to their early commercial availability, zeolites of type LTA (Linde Type A, includes zeolites 3A, 4A and 5A) and FAU (faujasite, includes zeolites X and Y) are the most frequently addressed ones in all types of applications.

1.1.4.1 Ion exchangers

As mentioned in section 1.1.1, the first industrial application of zeolites was as ion exchangers for water softening in laundry compositions

[10–12], which still remains one of their major uses. In the 1950s zeolites A, X, chabazite, mordenite and others were tested for their ion exchange properties [88–90]. Depending on their pore size, these materials can act as ion exchangers for diverse cations. Logically, if the cation's size (may also include its hydration shell) is larger than the pore opening, the exchange will not be possible to a great extent. This size exclusion together with the different affinities of ions when using zeolites as exchangers can allow for ion separation, and more specifically, ion sieving [57, 91]. For instance, zeolite 4A (sodium form of zeolite A) proved useful for the separation of Ni^{2+} and Co^{2+} cations from an aqueous solution, in which the cobalt is preferably exchanged [90].

Since then, a great number of ion exchange isotherms and selectivities of natural and synthetic zeolites with ANA, CHA, HEU, EDI, ERI, FAU, FER, GIS, KFI, LAU, LTA, MER, MFI, MOR, PHI, SCO, STI structures have been determined, and were reviewed by Dyer in 2007 [91]. The general conclusions on ion exchange affinities are as follows:

- High silica zeolites tend to prefer cations with low charge density (large and monovalent), whilst low silica zeolites prefer cations with high charge density (small and multivalent).

- Cations that have high heats of hydration, such as Li^+ or Mg^{2+}, tend to present slow exchange kinetics.

- Other cations are usually preferred over transition metal cations (depends on the material).

It must be noted that ion exchange isotherm measurements face an important problem when dealing with dilute ion solutions and low silica zeolites. Introducing sodium-exchanged A, X or Y zeolites into pure water will cause an almost immediate alkalinization of the aqueous phase due to the slow exchange of sodium cations with hydronium cations (see reaction 1.1) [92, 93].

$$Na^+ \, (zeo) + 2\,H_2O \rightleftharpoons Na^+ \, (soln) + H_3O^+ \, (zeo) + OH^- \, (soln) \qquad (1.1)$$
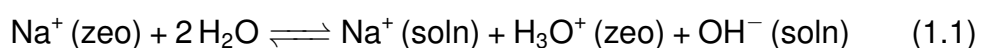
The initial increase in the pH is followed by a slow decrease, as the framework undergoes hydrolysis and part of the hydronium ions are released. At low electrolyte concentrations, and especially at low pH values, this effect will be important and the ion exchange properties of the material may be difficult to determine.

The use of zeolites as ion exchangers for industrial applications has been reviewed by several authors [57, 91, 94–96]. Zeolite 4A has been used since the late 70s as a component in laundry detergents, replacing phosphates in their function as water softeners and thus avoiding the environmental hazard of these, i.e. eutrophication [97]. A synthetic zeolite with GIS structure showing better performance than zeolite 4A was commercialized in 1994 for the same application [98, 99]. Natural zeolites, more specifically clinoptilolite, has been widely used for ammonium removal from water. Heavy metal cations removal from water and wastewater using zeolites has been reported as well, with clinoptilolite being again the most frequently addressed material. Furthermore, the use of zeolites in radioactive ion removal from waste streams has been known since the 1960s, when zeolite 4A was demonstrated to be highly selective towards radioactive strontium exchange [90, 100]. Natural zeolites chabazite and clinoptilolite and synthethic zeolites with CHA, FAU and LTA structures have been used for the mitigation of the effects of nuclear accidents or the presence of radioactive waste, and more specifically, for removal of radioactive caesium [91, 101, 102].

It must be noted that the use of zeolites for water treatment purposes may involve processes other than ion-exchange, such as filtration, surface precipitation, or adsorption [103]. This allows for the removal of other contaminants different than cations, such as particulate matter, anions (F^-) [104], or organic contaminants.

1.1.4.2 Catalysts

Industrial application of zeolites in catalysis was first envisaged by the Union Carbide zeolite research group in the 1950s. In 1954, Milton

and Breck studied the use of partially H$^+$-exchanged X zeolite for the cracking of hydrocarbons, and discovered it was much more active than the existing silica-alumina catalysts [35]. That same year, they developed methods for metal dispersion in A, X and Y zeolites and performed catalytic tests on the resulting materials [105–109]. Short thereafter, and persuaded by Milton and coworkers, researchers in other companies started studying zeolites for their potential use as catalysts. In 1959, zeolite Y (FAU structure, Si/Al $\geq$ 3) was commercialized as an acid catalyst for isomerization and cracking processes by the Union Carbide [1, 110–112]. In the coming years, other companies stepped on this research field, such as Socony Mobil Oil Company, USA, and started producing their own zeolite-containing catalysts [113, 114]. Soon zeolite cracking catalysts were implemented instead of the old amorphous silica-alumina catalysts in every refinery.

Since then, zeolites have been used as catalysts in a wide variety of industrial processes, especially in oil refining and petrochemistry and processes at their interface. Zeolites with MFI, FAU and MOR structures are the ones that have found more application niches [115]. A description of some of the most important examples is provided below [87, 116–120].

- **Oil refining**

  - **Fluid catalytic cracking (FCC)** is a process used for the production of gasoline from heavy oil fractions [121]. Zeolites with FAU structure, more specifically Y-type rare-earth exchanged (REY) and ultra-stabilized Y zeolites (USY) have been used in this application and the latter remains the preferred catalyst for this process. Furthermore, zeolite ZSM-5 has been used as an additive in FCC catalyst compositions, as it increases the yield to light olefines and the octane number of the gasoline.

  - **Hydrocracking** is a process in which heavy unsaturated and aromatic fractions are converted into lighter saturated

compounds in the gasoline, diesel or kerosene fractions by hydrogenation, cracking and isomerization [122]. Zeolite USY is used as an acid catalyst in the hydrocracking unit, along with a hydrogenation-dehydrogenation catalyst, which can be a noble metal, such as Pt or Pd, or a transition metal, such as W or Ni, depending on the sulfur content of the feed.

– **Dewaxing** of lubricants and fuels is a process that started using zeolites as its catalyst in the late 1960s. Acidity and shape selectivity are crucial to this process in which long chain linear alkanes undergo cracking and/or isomerization to form branched species. In order to selectively transform the linear alkanes, medium pore zeolites have been preferably used. Industrial dewaxing processes have used catalysts based on mordenite (British Petroleum Co.) [123], ZSM-5 (Mobil Oil Corp.) [124], and other proprietary catalysts presumably containing SAPO-11 (Chevron) [125–127], Beta, ZSM-22 or ZSM-23 (Mobil Oil Corp.) [128, 129].

– **Catalytic reforming of naphta** (mainly linear paraffins in the C_6-C_{10} fraction) produces branched alkanes and aromatics (benzene, toluene, xylenes; BTX). Reforming itself happens in the presence of hydrogen and an alumina supported Pt-Re or Pt-Re-Sn catalyst, however post-reforming shape-selective reactions are necessary to improve the quality of the product. The first zeolitic catalyst used for this process was erionite, which allowed for selective cracking of the remaining short chain n-paraffins to produce liquefied petroleum gas (LPG; mainly propane and butane) [130]. Later, ZSM-5 was introduced as the shape-selective catalyst [131], which also allows the entry of monobranched paraffins and benzene and toluene. The monobranched paraffins undergo cracking in the pores of ZSM-5 and the resulting olefins alkylate the aromatic species [119, 132].

– **Isomerization of light straight run naphta** (C_5 - C_6 fraction) produces branched paraffins. The catalyst system needed for this reaction presents an acidic function and a hydrogenation function. Apart from super acidic chlorinated alumina and sulphated zirconia, noble metal supported zeolites have been used for this process, such as Pt-loaded modified mordenite [119] and other Pt-promoted proprietary zeolitic catalysts [116].

– **Isomerization of light olefins**, especially linear butenes and pentenes, produces isoamylenes (2-methyl-2-butene and 2-methyl-1-butene) and isobutene (2-methylpropene). It can be carried out in the presence of a zeolitic catalyst, more specifically modified and non-modified ferrierites [133–136].

– **Alkylation of olefins with paraffins**, mainly n-butene and isobutane, yielding iso-octanes is industrially carried out using liquid sulphuric or hydrofluoric acids. Several processes for alkylation wielding a zeolitic catalyst have been developed but are not operational at a large scale [137]. Pt-supported Y zeolite [138] and other FAU structured materials have been reported.

– **Olefin oligomerization** needs propene and butenes as a starting material and yields C_6+ iso-olefins. Phosphoric acid supported on silica was the first catalyst used for this purpose and remains the most widespread one [139]. Some processes have been developed that use zeolitic adsorbents, such as Ni-mordenite [119, 140] and modified ZSM-5 [141–143].

• **Oil refining and petrochemistry interface**

– **Methanol to olefins (MTO)** is a process that converts methanol into light olefins (ethene and propene). SAPO-34 [144] and ZSM-5 [145, 146] catalysts have been commercialized for this application.

- **Catalytic cracking for propene production** uses primarily ZSM-5 catalysts, which favor the formation of light C_2 - C_4 olefins upon cracking of heavier hydrocarbons [116, 119].

- **Aromatization of light paraffins and olefins** in the C_2 - C_8 range produces H_2 and BTX and is carried out in the presence of a bifunctiponal (acidic, dehydrogenation) catalyst. Light paraffins in the C_2 - C_4 range can be aromatized using a zeolitic catalyst [147], such as Ga/HZSM-5 [148]. Hydrocarbons in the C_6 - C_8 range can be converted into benzene, toluene and H_2 using an L-type zeolite [149].

• **Petrochemistry**

- **p-Xylene** (para-xylene, see fig. 1.4) is an important chemical feedstock for polyethylene terelphthalate production. It can be produced by a variety of processes, most of which use ZSM-5 zeolite based catalysts due to its shape selectivity [150].

  * **Xylene isomerization** processes convert m-xylene and o-xylene to p-xylene by using shape-selective catalysts, such as ZSM-5. Zeolites Y and Pt-loaded mordenite were used first, but the superior shape selectivity of ZSM-5 made this the catalyst of choice [151].

  * **Toluene disproportionation-transalkylation** processes are designed to produce benzene and xylenes (especially p-xylene) from toluene (along with higher aromatics). ZSM-
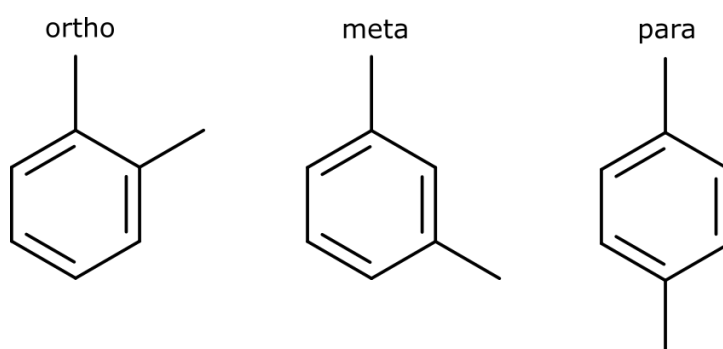
Figure 1.4: Xylene isomers. From left to right: o-xylene, m-xylene and p-xylene.

5 and other proprietary (ATA-11, ATA-12 and ATA-21 [152, 153]) catalysts are used.

* **Alkylation of toluene** with methanol is another process for p-xylene production that uses modified ZSM-5 zeolites [87, 116, 150].

– **Alkylbenzenes** (e.g. cumene, ethylbenzene) can be produced by alkylation-transalkylation of benzene and/or toluene using medium and large pore zeolitic catalysts, such as ZSM-5, modified mordenites, MCM-22, Beta and Y, depending on the desired outcome [87, 116, 154].

– ε-**Caprolactam** is the precursor to Nylon-6 and may be produced from cyclohexanone by ammoximation and Beckmann rearrangement. MFI-structured materials are employed as catalysts for these two steps (see fig. 1.5), more specifically, the ammoximation is carried out in the liquid phase with H_2O_2 and NH_3 in the presence of titanium silicalite-1 (TS-1) and the Beckmann rearrangement happens in the vapour phase in the presence of silicalite-1 (S-1) [155].
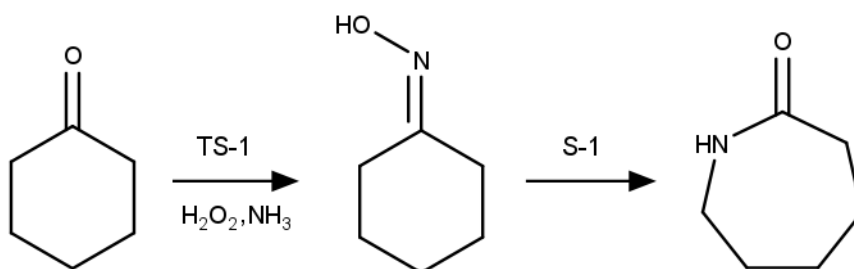
Figure 1.5: *Reaction scheme for the production of ε-caprolactam using MFI-structured catalysts.*

1.1.4.3 Adsorbents

The use of zeolites as adsorbents stems ultimately from their microporosity and regular pore size. The studies of Damour in 1840 and Friedel in 1896 on the reversible adsorption of molecules by zeolites

46

were the first light that was shed on the adsorption properties of these materials [7, 13]. However, it was not until McBain identified the possibility of carrying out extremely selective adsorption processes using these materials and coined the term "molecular sieves" that the way to a practical application of these was cleared [19]. As said in section 1.1.1, short thereafter Barrer systematically studied the adsorption of molecules of practical and theoretical interest in zeolites [21, 156]. Since then, various applications of zeolites as adsorbents for the separation of mixtures have been developed and commercialized. Zeolites 3A, 4A and 5A, along with 13X are the ones on which most adsorption studies have been carried out and the ones most used in industrial separations, probably due to their early commercial availability. Zeolite A is produced hydrothermally in its Na-form and is commonly referred to as zeolite 4A, due to its pore size of 4 Å. Upon $50 - 70\%$ exchange of Na^+ per Ca^{2+}, zeolite 5A (5 Å pore size) is obtained, and, analogously, K^+-exchange of 4A yields 3A (3 Å pore size) [157]. Zeolite 13X is the Na-form of zeolite X.

Due to this thesis' focus being on the use of zeolites as adsorbents, a thorough review of the application of zeolites in industrial adsorption and separation processes will be provided in section 1.3 and not here.

1.2 Adsorption on nanoporous materials

Adsorption is defined as the enrichment in the concentration of molecules, atoms or ions present in a fluid phase in the vicinity of an interface [158]. In the case of a solid-gas or solid-liquid system, this interface is the surface of the solid. Adsorbable molecules in the fluid phase are the *adsorptive* or *sorptive*, adsorbed molecules are called the *adsorbate* or *sorbate* and the solid material receives the name of *adsorbent* or *sorbent*[*]. The opposite process, in which molecules leave that surface and go back to the fluid phase is called desorption.

Adsorbents need to possess a high specific surface area, as the

---

[*]When the prefix *ad-* is not present, it may be used for absorption phenomena, as well (see section 1.3).

maximum adsorption capacity will depend on it. Porosity increases the surface area per volume of material, thus porous materials are a common choice as adsorbents. Porous materials with pores with diameters below 100 nm are known as nanoporous materials and can be classified into different groups according to their pore size [158]:

- **Microporous**, with $d_p < 20$Å.

- **Mesoporous** , with 20Å $< d_p < 500$Å.

- **Macroporous**, with 500Å $< d_p$.

There is a large number of examples of nanoporous materials, such as activated carbons, carbon molecular sieves, carbon nanomaterials, zeolites, metallosilicates, mesoporous silicas, metal-organic frameworks (MOFs) or covalent organic frameworks (COFs). Throughout this work I have used zeolites, AlPOs and SAPOs as adsorbents, which belong to the microporous materials group.

1.2.1   Basics of adsorption

1.2.1.1   Thermodynamics of adsorption processes

Adsorption phenomena are most frequently studied by measuring adsorption isotherms. In a typical experiment, the temperature is set constant and a clean (previously treated) sample of adsorbent is exposed to certain values of pressure of the desired adsorptive/s. At each pressure P, equilibrium is reached and the amount adsorbed Q may be calculated by the pressure drop (volumetric method) or the gain in mass (gravimetric method). Generally speaking the amount adsorbed will increase with pressure, although the shape of the isotherm may vary greatly depending on the adsorbate-adsorbent pair and the specific conditions of the experiment.

Years of accumulated adsorption isotherm data have allowed to establish a classification of typical isotherm shapes (see fig. 1.6), which

gives information on the textural properties of the solid that is being dealt with [158].
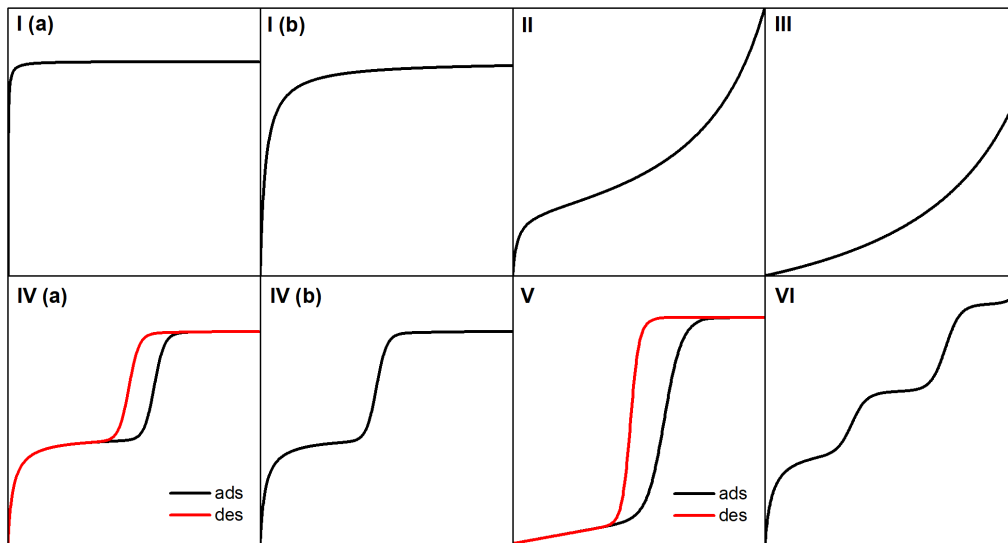
Figure 1.6: *Isotherm types, according to the new IUPAC classification. The x-axis is relative pressure and the y-axis is the adsorbed amount. In cases where a single line is depicted, adsorption and desorption are equal. Where two lines are depicted, i.e. there is a hysteresis phenomenon, red is for desorption and black for adsorption*

Type I(a) and I(b) isotherms belong to microporous solids, such as zeolites, and practically all the experimental isotherm presented in this thesis belong to this type. The steep low-pressure regime is due to the strong interactions that take place in the close-fitting pores of these materials. The steeper this region, the stronger are the interactions. Above a certain pressure, saturation is reached and the limited micropore space of the solid cannot take in more molecules, thus the horizontal asymptote.*

Type II isotherms are given by relatively weak adsorption on nonporous or macroporous adsorbents, where multilayer adsorption and capillary condensation take place. Some microporous materials present mixed features of type I and II isotherms to some extent, as the interparticle space allows for multilayer adsorption and capillary condensation. Type III isotherms belong to nonpororus or macroporous adsorbents, as well,

---

*At very high relative pressures another steep increase may be seen, which is due to capillary condensation of the adsorptive, i.e. condensation outside the micropores, possibly in the space between adsorbent particles (interparticle space).

but in this case the interaction with the adsorbate is very weak. Type IV isotherms are typical of mesoporous solids. Type IV(a) isotherms present a hysteresis loop related to capillary condensation in the pores and are given by solids in which the opening of the pore exceeds a certain value, which depends on the nature of the adsorbate. Hysteresis is a concept that refers to the case in which adsorption and desorption follow a different path in the isotherm plot. Type IV(b) isotherms belong to solids having smaller mesopores and cylindrical or conical pores with closed ends, in which capillary condensation does not result in a hysteresis phenomenon. A final plateau or inflexion point is typical in this type of isotherms. Type V isotherms are seen in micro- and mesoporous adsorbents in cases where the sorbent-sorbate interaction is weak. In this sense, their low pressure regime is similar to that of type III isotherms. At higher pressures, pore filling occurs and the adsorbate-adsorbate interactions prevail, thus leading to a steep increase in the adsorbed amount. Hysteresis is typical in these isotherms. Type VI isotherms are given by highly uniform nonporous surfaces, in which layer by layer adsorption is distinguishable.

Adsorption phenomena are always exothermic, as the entropy decreases. This means that, at a constant pressure, the adsorbed amount will decrease with increasing temperature. They can be physical (physisorption) or chemical (chemisorption), depending on the strength of the interaction between the adsorbate and the adsorbent surface. The intermolecular forces that are involved in physisorption include interaction between induced or permanent dipoles and/or quadrupoles, whilst in chemisorption there is a change in the electronic structure of the adsorbent and the adsorbate and the formation of a chemical bond [159]. Therefore, the absolute value of enthalpy of physisorption is generally lower ($\leq$ 50 kJ/mol) than that of chemisorption ($\geq$ 50 kJ/mol). It is common that an industrial adsorptive separation process using zeolites preferably involves physisorption instead of chemisorption, whereas a catalytic process involves chemisorption and further reaction. Note that adsorption is one of the necessary steps in any heterogeneous catalytic

process.

The adsorption enthalpy is defined as the energy that is released due to a specific amount of a molecule becoming adsorbed on a surface and thus has a negative value. The isosteric heat of adsorption q_{st} is the negative adsorption enthalpy and is positive. There are several ways to determine the experimental q_{st}, which may be direct (calorimetry) or indirect, based on isotherms measurement at different temperatures (Clausius-Clapeyron's equation, see section 3.3.2.2). The isosteric heat of adsorption varies with the adsorbed amount, and its trend gives information on the nature and relative strength of the interactions taking place (see fig. 1.7) [159, 160]. Trends like a in fig. 1.7 are typical of surfaces with a finite number of relatively strong adsorption sites in which electrostatic interactions or even chemisorption takes place. When these sites are fully occupied, adsorption in other sites that present weaker interactions with the adsorbate happens and thus, the drop in q_{st}. Trends like b, where the q_{st} decreases slowly with Q, indicate an energetically heterogeneous surface. Trends like c are typical of systems where adsorbate-adsorbent interactions are weaker than adsorbate-adsorbate interactions. At larger loadings, there is an increase in the q_{st} due to lateral interactions of the sorbate.

Desorption, which is the opposite process of adsorption, is a necessary step in the application of solids as adsorbents or heterogeneous catalysts, as the separated or reacted species, respectively, need to be recovered. A large isosteric heat of adsorption will mean a strong sorbate-sorbent interaction, and probably selective adsorption over other species, which is desirable. However, it will also involve a larger energy input (in form of increase in temperature or decrease in pressure, see section 1.2.2) in order to desorb the adsorbed molecules, thus leading to higher energetic costs in a hypothetical separation process. Therefore, a certain compromise needs to be sought in most cases.
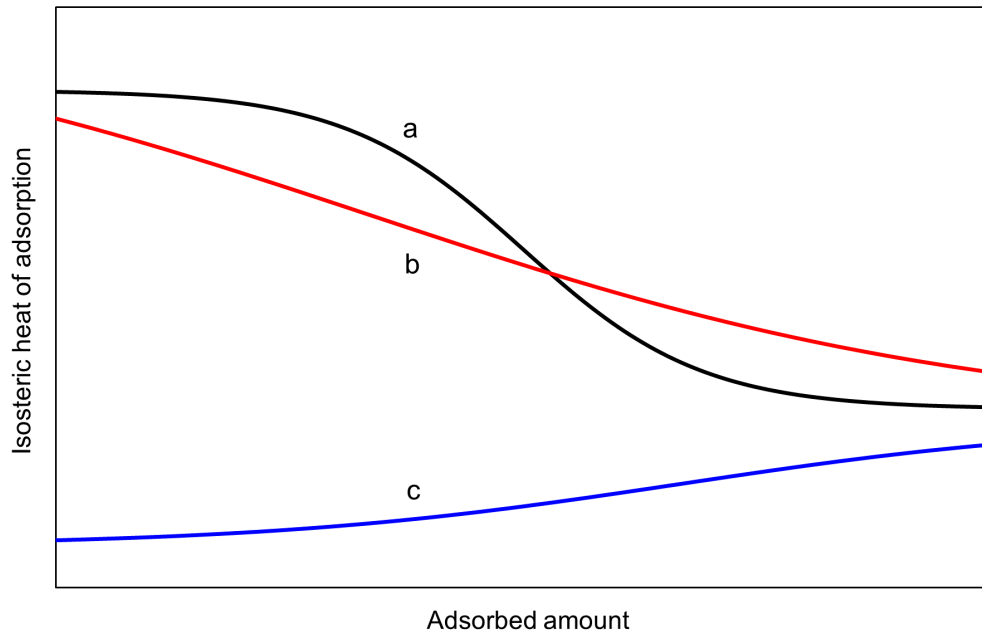
Figure 1.7: Possible trends of isosteric heat of adsorption. Trend a *is typical of a solid with a finite number of strong adsorption sites and otherwise weak adsorption sites. Trend* b *belongs to a solid with an energetically heterogeneous surface. Trend* c *is typical of systems with weak adsorbent-adsorbate interactions.*

1.2.1.2 Diffusion in adsorption processes

Diffusion of adsorptives to the surface of the adsorbent and diffusion of adsorbates between adsorption sites are processes inherent to adsorption phenomena. Especially when dealing with microporous adsorbents, where the adsorption sites are usually found inside the pores, (intracrystalline) diffusion may be a decisive factor as to whether adsorption occurs at an acceptable rate or does not. In adsorption processes that take advantage of a thermodynamic selectivity to carry out a separation, fast adsorption kinetics, i.e. large diffusivities, are necessary. However, in the case that one of the components of the mixture that is to be separated diffuses much faster than others, a kinetically controlled separation may be feasible. The extreme case, where some components of the mixture enter the pores and others are too big for entering the pores and being adsorbed, receives the name of molecular sieving. This phenomenon is very representative of zeolites, to the point that they have been referred to as molecular sieves for a long

time [2, 35, 161].

The kinetics of adsorption can be characterized at three different levels, i.e. elementary adsorption steps and microscopic and macroscopic diffusion processes [162].

- **Elementary adsorption steps** may follow many different mechanisms, depending on the specific characteristics of the sorbate-sorbent system, i.e. molecular structure, adsorbent structure, sorbate-sorbent interactions, sorbate-sorbate interactions. They are not strictly diffusive processes, as the distances (from several Å to nm) involved are short compared to the length scales needed for the study of the overall diffusion process. In other words, a large number of elementary steps results in diffusion. Elementary adsorption steps may be assessed by molecular dynamics simulations and experimental techniques like quasi-elastic neutron scattering (QENS) and pulsed field gradient nuclear magnetic resonance (PFG NMR), also considered microscopic techniques.

- **Microscopic** diffusion processes are studied at a scale where the adsorbate-adsorbent system is homogeneous, i.e. inside a single particle of the adsorbent, typically of the order of μm. The techniques that allow the study of microscopic diffusion processes are referred to as microscopic and are mainly based on neutron scattering, more specifically QENS, nuclear magnetic resonance (NMR), more specifically PFG NMR and light diffraction.

- **Macroscopic** diffusion processes are studied at a scale that encompasses a large number of adsorbent particles, and the space between them. They are also referred to as mass-transfer processes. In the case of porous adsorbents, two diffusion regimes can be differentiated, i.e. intracrystalline and intercrystalline. Intercrystalline diffusion, which is diffusion in the space between adsorbent particles, is usually much faster than intracrystalline

diffusion, which is diffusion inside the pores of the material. Macroscopic diffusion processes are studied by techniques such as uptake/desorption rate measurements, zero length column (ZLC) chromatography or frequency response.

1.2.2 Swing adsorption processes

Industrial adsorption processes use a technology named swing adsorption, in which the adsorbent bed is subjected to cycling conditions of pressure or temperature, thus giving rise to pressure swing adsorption (PSA) or temperature (thermal) swing adsorption (TSA). PSA is mostly used in bulk separations, where the component to be separated represents $>$ 10% of the stream to be processed, whereas TSA is preferably used in purification applications, i.e. where the component to be removed is present at concentrations $<$ 10% (usually $<$ 2%) [163–165]. PSA technology was developed in the 1960s [166, 167] and meant a great breakthrough, as it promoted research on adsorption processes and new adsorbents [163, 168, 169]. Other variants of swing adsorption processes, including inert purge, vacuum swing adsorption (VSA), vacuum pressure swing adsorption (VPSA), electric swing adsorption (ESA) and rapid PSA (RPSA) have been developed or used in combination with typical TSA and PSA [163, 170, 171].

The conceptual scheme of a swing adsorption process is relatively simple (see fig. 1.8). A minimum of two adsorbent beds in parallel are necessary. Taking the case of just two parallel beds, the stream to be purified or fractionated is flown through bed no. 1, that has just been regenerated and is thus activated and ready to adsorb. Meanwhile, bed no. 2 is being subject to regeneration by either decreasing pressure (PSA, VSA or PVSA), increasing temperature (TSA) or flowing an inert gas[*]. When bed no. 1 is saturated and bed no. 2 fully regenerated, bed no. 1 enters the regeneration step and bed no. 2 the adsorption step, thus allowing the overall process to operate continuously [172]. The

---

[*]A combination of desorption methods is not excluded.
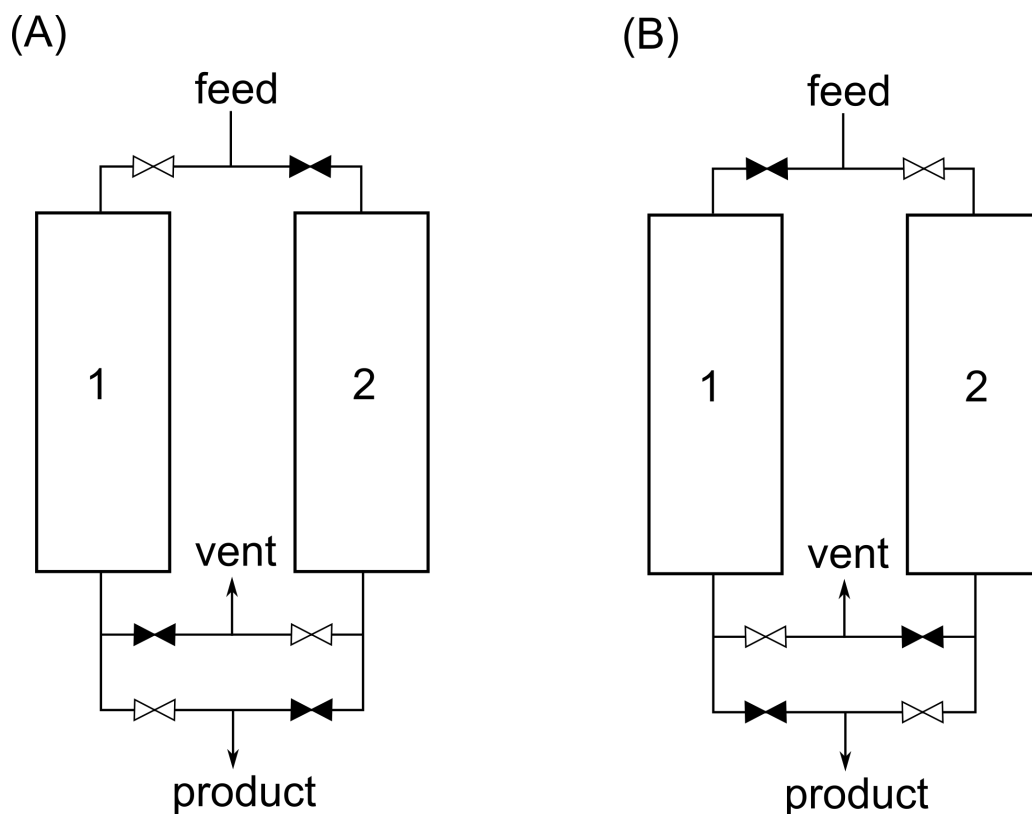
Figure 1.8: *Simplified scheme of a swing adsorption process. Two adsorbent beds (rectangles 1 and 2) are connected in parallel, the pairs of opposed triangles represent valves, white when open and black when closed. In (A) the adsorption step takes place in bed 1 while bed 2 is being regenerated. In (B) the opposite situation takes place.*

process efficiency is highly dependant on the interplay between adsorbent properties and process design, which allows for the use of different adsorbents for the same separation [160].

Important parameters which help describe the performance of a swing adsorption process are the product purity, product recovery and adsorbent productivity [168]. The adsorbent productivity is the amount of feed processed per unit time and amount of adsorbent and may be referred to a specific component of the mixture. The product purity refers to a certain component and equals its molar fraction (usually expressed as a percentage) in the volume-averaged product obtained throughout a certain step in the process. The product recovery also refers to a specific component and equals the amount of that component present in the product divided by the amount of that component present in the feed that has been processed.

Another important parameter in the selection of the adsorbent for a swing adsorption process is its working capacity, which is defined as the difference between the adsorbed amount at the end of the adsorption step and the adsorbed amount at the end of the desorption step, and can be estimated from its adsorption isotherms. For TSA and PSA processes, a simplified graphical explanation of the working capacity is provided in fig. 1.9.
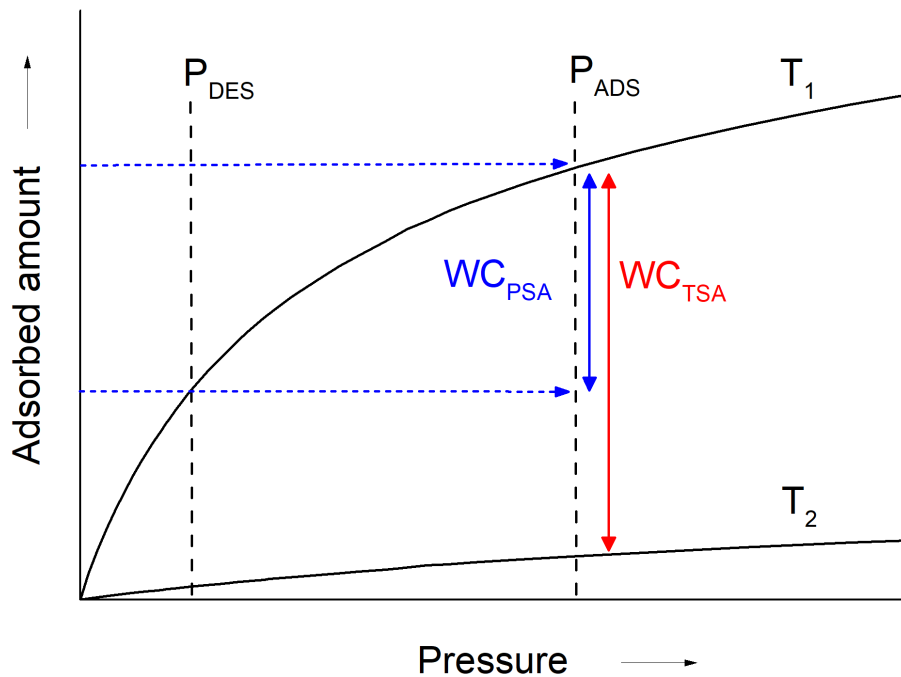
Figure 1.9: *Working capacity in PSA (WC_{PSA}) and TSA (WC_{TSA}) processes exemplified on two hypothetical isotherms at two different temperatures on the same adsorbent. P_{ADS} is the pressure in the adsorption step and P_{DES} is the pressure in the desorption step of a hypothetical PSA process, with $P_{ADS} > P_{DES}$. T_1 is the temperature in the adsorption step and T_2 is the temperature in the desorption step of a hypothetical TSA process, with $T_1 < T_2$. WC_{PSA} is calculated as the difference in the adsorbed amounts between P_{ADS} and P_{DES} and WC_{TSA} is calculated as the difference in the adsorbed amounts between T_1 and T_2.*

As can be seen, the working capacity not only depends on the equilibrium adsorption capacity of the adsorbent, but also on the isotherm shape. High adsorption capacities are desired, as they will decrease the required quantity of adsorbent. Isotherms with a moderate affinity towards the adsorbate (neither too steep nor too flat) will also favor a large working capacity.

1.3 Industrial separations

Separation processes are essential in the chemical industry, as many valuable compounds need to be extracted or purified from mixtures [172, 173]. In order to separate the components of a mixture, differences in their physical and/or chemical properties are exploited, and depending on which property the separation bases on, various types of processes/techniques are distinguished, a few of which are listed below:

- **Distillation** techniques are used to separate the components of a liquid mixture basing on differences in their boiling points and are the most widely implemented separation processes in the chemical industry. However, due to the very close boiling points and the extreme conditions needed for performing some relevant separations (oxygen from air, olefin-paraffin), some of these processes are energetically very expensive [173, 174].

- **Extraction** processes are used to separate dissolved substances by contacting two liquid phases, which are inmiscible or partially miscible with each other. The relative solubilities of the compounds to be separated in the two different liquid phases are the driving force of this separation technique [175].

- **Crystallization** processes are used to separate dissolved solids from the liquid phase (and from other dissolved substances). It involves the formation of a crystalline solid from a solution, generally by the lowering of the temperature or by evaporation of a solvent [175].

- **Absorption** is a bulk phenomenon in which a material (absorbate, usually in a fluid phase) is retained by another (absorbent, usually liquid or solid) [175]. The driving force in absorptive separation processes is the difference in the interaction strength of the different components of the mixture with the absorbent.These interactions can be of either physical or chemical nature.

- **Adsorption** (see section 1.2) is defined, according to the International Union of Pure and Applied Chemistry (IUPAC) [175] as an increase in the concentration of a dissolved substance (adsorbate) at the interface between a condensed (adsorbent) and a fluid phase due to the operation of surface forces. There are different mechanisms according to which an adsorptive separation can be performed:

  - **Thermodynamic** separations are performed at equilibrium and their effectiveness relies on differences in the interaction strength of the adsorbates.

  - **Kinetic** separations are performed away from equilibrium and their effectiveness relies on differences in the adsorption rate of the adsorbates.

  - **Molecular sieving** separations are exclusive to nanoporous adsorbents and imply size and/or shape exclusion of some components of the mixture from the pores. It can be understood as an extreme case of kinetic separation.

- **Membranes** are defined as continuous layers, usually consisting of a semi-permeable material [175]. Closely related to adsorption phenomena in nanoporous adsorbents, the separation mechanisms in membranes rely on an interplay of kinetic and thermodynamic control, which can be successfully described by the solution-diffusion model [176]. The substances permeate from the concentrated side to the diluted side of the membrane and the larger their permeability, the more rapidly do they cross from one side to the other.

The separations relevant to this thesis are directed towards separating fluid mixtures. The compounds involved in these separations and relevant properties thereof are listed in table 1.1.

In the following sections, the state of the art of these separations will be presented and briefly reviewed with special focus on the role of zeolites as adsorbents, in order to make our starting point clear. Not all of these separations use zeolites at an industrial level and thus, the last section

includes a review of other industrial/commercial applications of zeolites as adsorbents.

1.3.1 Purification of hydrogen

Hydrogen is primarily ($>$ 95%) produced in refineries, as a major component in steam methane reforming off-gas and refinery off-gas (SMROG and ROG, respectively) [184, 185]. The compositions of these streams is as follows:

- **SMROG** per se consists of a mixture of CO and H_2, i.e. syngas (see reaction 1.2), and can be subjected to a water-gas shift reaction process (WGS, see reaction 1.3) to maximize the yield to H_2 and to decrease CO concentration for its further use in other processes.

$$CH_4 + H_2O \rightleftharpoons 3\,H_2 + CO \tag{1.2}$$

$$CO + H_2O \rightleftharpoons H_2 + CO_2 \tag{1.3}$$
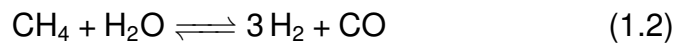
  The resulting product, and the one on which the separation is performed typically contains $70 - 80\%$ H_2, $15 - 25\%$ CO_2, $3 - 6\%$ CH_4, $1 - 3\%$ CO, trace N_2 and is saturated with H_2O. Note that it is equivalent to the pre-combustion stream mentioned in section 1.3.3.

- **ROG** typically contains $65 - 90\%$ H_2, $3 - 20\%$ CH_4, $4 - 8\%$ C_2H_6, $1 - 3\%$ C_3H_8, lesser amounts ($> 0.5\%$) of C_{4+} hydrocarbons and is saturated with H_2O.

The separation of the components of these mixtures is mainly directed towards producing a highly pure ($> 98\%$) H_2 product, however it may also be optimized to produce ammonia synthesis gas (3:1 mixture of H_2 and N_2) [186, 187]. Additionally, the process can be designed to produce a secondary product stream containing $> 99\%$ CO_2 for its sequestration or use (CCS, see section 1.3.3.2). The waste stream is frequently used as fuel for its calorific value.

Table 1.1: *Relevant properties of frequently used adsorbates in this work [40, 177–183]*

Molecule	T_b (K)	d_{kin} (Å)	Polarizability (10^{-25} cm³)	Dipole moment (10^{-18} esu cm)	Quadrupole moment (10^{-26} esu cm²)
H_2	20.3	2.83 - 2.89	8.04	0	0.662
D_2	23.6	2.83 - 2.89	7.95	0	—
H_2O	373.2	2.64	14.5	1.85	—
N_2	77.4	3.64 - 3.80	17.4	0	1.52
O_2	90.2	3.47	15.81	0	0.39
CO	81.7	3.69	19.5	0.110	2.50
CO_2	216.6	3.30	29.11	0	4.3
CH_4	111.2	3.76	25.93	0	0
C_2H_4	169.4	4.16	42.52	0	1.50
C_2H_6	184.6	4.44	44.3 - 44.7	0	0.65
Ethanol	351.8	4.53	51.1 - 54.1	1.69	—
C_3H_6	225.46	4.67	62.6	0.366	—
C_3H_8	231.02	4.30 - 5.12	62.9 - 63.7	0.084	—
Acetone	329.22	4.60 - 4.79[a]	63.3 - 64.0	2.88	—
1-Butanol	390.6	4.63[a]	—	1.65	—
n-Pentane	309.22	4.50	99.9	0	—
2-Methylbutane	300.99	5.0	—	0.13	—
2,2–Dimethylpropane	282.65	6.2 - 6.46	102.0	0	—
n-Hexane	341.88	4.3	119	0	—
2-methylpentane	334.0	5.5	—	0.1	—
2,3–Dimethylbutane	331.2	6.2[b]	—	—	—
2,2–Dimethylbutane	322.9	6.3	—	—	—
n-Heptane	371.57	4.3	136.1	0	—
3-Methylhexane	365.0	5.9[b]	—	—	—
2,3–Dimethylpentane	362.9	6.2[b]	—	—	—
2,4–Dimethylpentane	353.7	5.8[b]	—	—	—

[a]Critical diameter from [181]. [b]Critical molecular w-h parameter from [183].

The purification of hydrogen from SMROG or ROG is carried out by different means, depending on the desired product composition and purity and the intended use of the waste stream. The two types of technology that have been implemented industrially are PSA and membranes.

- **PSA** technology is used in 85% of the hydrogen production facilities globally [188]. PSA units use multiple columns (4 to 12) to achieve high product purities ($>$ 99.999%) [189] and base on the selective adsorption of the other components of the mixture, as H_2 tends to interact poorly with the adsorbents used[*]. Processes directed to producing only H_2 frequently use various adsorbents in different layers in the same bed, in order to optimize the adsorption-desorption cycle. Examples of layered beds include combinations of activated carbon and zeolite 5A [194] activated carbon and zeolites X and Y [195] or activated carbon and silica gel [196]. Processes directed to the obtention of both H_2 and CO_2 use combinations of adsorbents in different beds, such as activated carbon and zeolites [197], or add systems for CO_2 capture prior or after the primary H_2 PSA [198]. The order in which the adsorbents are placed, the interplay between the adsorbents, and the interplay between adsorbents and process design are crucial for these process to operate properly.

  Currently, research in H_2 purification by PSA is directed towards [188]:

  - Developing **RPSA** (rapid PSA) processes that allow cost reduction.

  - Improving the **mass transfer** coefficients in current and potential adsorbents by shaping them into monoliths and sheets.

  - **Sorption-enhanced SMR** processes, in which CO_2 is

---

[*]H_2 tends to interact relatively strongly with noble and transition metals, less so with other inorganic moieties [190–193].

separated from the reaction medium simultaneously to its production, thus displacing equilibrium.

- **Membrane technology:** There are two types of membranes that have been commercialized for hydrogen separation [191], which are:

  - **Polymeric membranes** (polyimide, cellulose acetate) have been implemented in small and large scale applications where the required product purity is not extremely high. Their selectivity to H_2 is moderate and for achieving the desired purity, several sequential stages may be necessary. Their permeability to H_2 is high and they are relatively cheap.

  - **Dense metal membranes** have been implemented in small scale niche applications, where the required product purity is extremely high, e.g. H_2 for fuel cells. They present very high H_2 selectivities and moderate permeabilities. They consist mainly of palladium alloys, which makes them selective towards H_2, and are more expensive than polymeric membranes. Implementation of these membranes in SMR reactors for in-situ separation of the product H_2 is being researched as a promising option to improve the overall efficiency of the process.

1.3.2 Separation of hydrogen isotopes

The separation of the isotopes of hydrogen, i.e. H_2, D_2, T_2, is of current interest to the industry and represents an especially challenging case of separation [199]. Deuterium (in the form of heavy water) is used as a neutron moderator in chemical reactors, as an isotopic tracer and for the production of deuterated chemicals and drugs [199–201]. Both deuterium and tritium are raw materials for fusion energy technologies, which are under intense research [202–204]. The production of deuterium and tritium and the removal of tritium from nuclear waste [205] are processes that require the separation of these isotopes from mixtures or compounds containing them.

Hydrogen isotopes present very similar physical and chemical properties, which makes their separation technically difficult and/or energy intensive [206]. Mature technologies for the separation of hydrogen isotopes, especially deuterium from hydrogen include cryogenic distillation and electrolysis of heavy water coupled to the Girdler-Sulfide process [200, 201, 205, 207, 208], both of which are highly energy demanding. Other methods that have been studied are thermal diffusion, membrane technology, adsorption, chromatography [206, 209], combinations of chromatography and cryogenic distillation [210], combined electrolysis catalytic exchange [211–213] and quantum sieving [201, 214].

Separation-oriented adsorption studies of hydrogen isotopes on activated carbons, silicas and zeolites have been reported since the 1930s by several authors [215–221]. According to these studies, the heavier isotopes were more strongly adsorbed than the lighter isotopes mainly due to their larger heats of adsorption, and no remarkable influence of the pore size was observed, not even in microporous adsorbents [216, 219, 220]. This thermodynamic preference towards the heavier isotope is still of interest to researchers and new materials with improved separation prospects are being discovered, especially MOFs [222, 223] and zeolites [224–228]. Zeolites of types A, X and Y have been extensively studied for this purpose. Trapdoor phenomena in zeolites have been described as well, in which a D_2-sensitive Cs-exchanged chabazite can separate D_2 at low concentrations [229].

In the mid 1990s the term "quantum sieving" was proposed by Beenakker et al. to denote the quantum effect that arises when the difference between pore size and adsorbate size is close to the de Broglie wavelength of the adsorbate[*] [201, 214]. Since then, numerous studies featuring different kinds of adsorbents, i.e. carbon nanomaterials and carbon molecular sieves [206, 224, 230–234], boron nitride nanomaterials [206, 235], MOFs and COFs [236–239], POCs [200] and zeolites [199,

---

[*]It must be noted that it is conceived mainly as a kinetic effect, but may also affect equilibrium adsorption.

230, 240, 241], have been carried out. In the case of zeolites and zeotypes, all of the proposed materials present small pores, i.e. 8-rings and minimum pore openings below 4.1 Å.

1.3.3 Separation of carbon dioxide

Carbon dioxide (CO_2) is an ubiquitous compound, found mainly in gaseous state in the Earth. Its separation from mixtures with methane, nitrogen, water, hydrogen, etc, are very active research topics [43, 242–244]. Mixtures of industrial interest, where CO_2 is sought to be removed are classified according to the reason of interest and listed below:

- Methane containing mixtures with intended use as fuel:

  - **Natural gas**, a fossil fuel where the main component is usually CH_4 ($30 - 98\%$), and the other components (CO_2, light hydrocarbons, H_2O and H_2S) are present in variable amounts [245–248]. It can appear associated to an oil deposit, or non associated.

  - **Coalbed methane**, which is fossil methane found along with coal, with a methane content of 50-99 %, tipically above 80 % and variable amounts of CO_2, N_2 , light hydrocarbons, H_2S and SO_2 [249–252].

  - **Landfill gas and biogas**, renewable fuels derived from fermentation of residues and biomass, which contain CH_4 and CO_2 as the major components and a considerable amount of N_2 and H_2O [253, 254].

- Hydrogen containing mixtures

  - **Pre-combustion streams** from steam reforming of methane or other hydrocarbons for hydrogen production, where the off-gas consists mainly of H_2 ($70 - 80\%$) and CO_2 ($15 - 25\%$), with

lesser amounts of CH_4 $(3 - 6\%)$, CO $(1 - 3\%)$, trace N_2 and is saturated with H_2O [185].

- Mixtures where the main objective is to capture the CO_2

  - **Post-combustion streams**, also called flue gases, which are the byproduct of combustion processes for energy production in general and also importantly in cement and metallurgy industries. The composition of this stream is mainly N_2, CO_2 and H_2O [255]. Oxyfuel technology is a special case, in which the fuel is burnt in the presence of oxygen instead of air, and thus, nitrogen is not present in the flue gases.

  - **Ambient air**, where CO_2 is only a lesser component.

The separation of CO_2 from these mixtures generally uses similar principles, as, independently from the aim, they focus on retaining the CO_2 and leaving the other components in the mixture [256]. They even overlap in what refers to carbon dioxide capture in natural gas processing or hydrogen production [244]. The state of the art of the mentioned separations is summarized below, except for the case of hydrogen production, that can be found in section 1.3.1.

1.3.3.1 Removal of carbon dioxide from methane-rich mixtures

Methane (CH_4) can be obtained from fossil (natural gas, coalbed methane) or renewable (biogas and landfill gas) sources, and its major use is as a fuel, its global electric power generation share being 23% in 2018 and with expectations of growth in the coming decades [257, 258]. It also serves as a starting material in some petrochemical processes, such as methane reforming for syngas and/or hydrogen production [259–261].

Natural gas is found in underground deposits, frequently along with oil (associated natural gas) or coal (coalbed methane). Biogas and landfill gas are produced in anaerobic digestion processes of anthropogenic waste, which take place in sewage plants (waste water) or landfills (solid

waste), respectively [253, 254]. These methane containing gas mixtures need to be upgraded to meet specifications prior to use and/or transport. Components with no calorific value, such as CO_2, H_2O and N_2 have to be kept below specific levels in order to allow for the use of the mixture as a fuel. Furthermore, H_2O, CO_2 and other minor components, such as H_2S need to be removed to prevent corrosion and plugging problems in the processing and transportation operations [242, 253, 262]. Hydrocarbons in the C2 and C3 fractions contribute to the heating value of the mixture positively and do not need to be removed generally. However, hydrocarbons longer than propane need to be separated despite of their potential contribution to the calorific value of the mixture, as they can condense during the processing and cause plugging problems [247, 263].

As suggested above, the removal of carbon dioxide is central to the upgrading process, as it is frequently a major component of these mixtures (see section 1.3.3) and, apart from being a diluent and decreasing the heating value of the mixture, it is also a sour gas, which can cause plugging problems and corrosion [247, 256]. The state-of-the-art techniques for CO_2 removal from natural gas include absorption in chemical, physical or hydrid solvents, adsorption, membranes, cryogenic distillation and methanation [247, 264]. Absorption in aqueous alkanolamines involves the formation of a carbamate upon flowing the gas through the amine solution and it is the traditionally preferred method for large scale facilities [247, 256]. After this process, the treated gas is saturated with water and will require drying. The amine solution needs to be regenerated to release the acid gases (CO_2 and H_2S), a step which is highly energy intensive. The high capital and operation costs inherent to this technology make it impracticable for small scale facilities and remote deposits. In the search for more optimal and environmentallly friendly processes, also applicable to medium and small scale facilities, other separation techniques are under consideration and research. Adsorption (more specifically PSA, pressure swing adsorption) and membrane technologies have the potential to be much less energy

intensive and to reduce the operation costs significantly [242, 246, 247, 256, 265, 266].

PSA processes for carbon dioxide separation from methane have been studied on a wide range of materials, such as zeolites, metal organic frameworks (MOFs), carbon molecular sieves, activated carbons, porous polymers or amine impregnated mesoporous silica [242, 246, 256]. Out of these, zeolites, titanosilicates, carbon molecular sieves and metal-based adsorbents have found commercial application [256]. However, the search for better adsorbents that can further improve the efficiency and economy of the process is still a very active research field.

Traditional A, X and Y-type zeolites have been commercialized or patented for this separation [246, 267, 268], as well as silicalite, mordenite [269], natural clinoptilolite [270] and titanosilicate ETS-4 [242, 271]. Selectivity on most of these materials, more specifically on low silica traditional zeolites, is achieved by exploiting differences in the interaction strength, i.e. the heat of adsorption (see section 1.2.1.1), between the adsorbates and the adsorbent. CO_2 adsorbs more strongly than methane on these materials, due to the electrostatic interaction of its quadrupolar moment with the charged framework and their extraframework cations [265]. In some cases even chemisorption takes place and strongly bound carbonate-like species can be formed [272, 273]. In consequence, these materials present large thermodynamic CO_2/CH_4 selectivities. However, this is disadvantageous for the regeneration step, as a higher energy input will be needed for desorbing the strongly adsorbed (or even chemically bonded) CO_2. Furthermore, natural gas and the other addressed gas mixtures frequently contain a certain amount of water, which will also strongly adsorb on these highly polar (and thus hydrophilic) zeolites. It may be the case that this simultaneous removal of water and CO_2 is intended, but this depends greatly on the specific process conditions [274, 275]. In most cases, this competitive adsorption is undesired, and it is also noteworthy that water will not only compete with CO_2 in the adsorption process, but may also favor its chemisorption and the

formation of bicarbonate-like species [272, 273, 276, 277].

Due to the reasons mentioned above, current research on this separation is mostly directed towards finding materials with a lower surface polarity, and thus a lower heat of adsorption of CO_2, that maintain a high CO_2/CH_4 selectivity as well as a large working capacity. These parameters can be tuned by proper selection of the structure and composition [265, 278–280]. Promising values of CO_2/CH_4 selectivity and heat of adsorption of CO_2 have been obtained using medium-, high- and pure silica zeolites with LTA [279], RHO [280], MWF, PWN [281, 282], FAU [265], CHA [283], AEI, STT and RRO [284] structures and other aluminophosphates (AlPOs) and silicoaluminophosphates (SAPOs) with analogous and different structures [285–289]. Some recent patents aim in this direction, as well [290–292]. Out of these new generation zeolitic adsorbents, structures featuring small pores (see section 1.1.2) stand out, as they maximize the intrinsic structural selectivity. This seems reasonable, as they present similar pore diameters (ca. $3-4$) to the kinetic diameters of CO_2 (3.3) and CH_4 (3.8). The main drawback of these tailored materials is their production cost, which is by far larger than that of commercial zeolites and hinders their industrial deployment.

1.3.3.2 Carbon dioxide capture

Carbon dioxide (CO_2) occurs from both natural and anthropogenic sources, with anthropogenic contributions (transport, industry, energy production) being by far larger than natural ones (respiration of living beings, tectonic activity). The anthropogenic CO_2 emissions have been rapidly increasing for the last 50 years and they surpass largely the amount of CO_2 that the biosphere can reabsorb [293]. Furthermore, there is a clear correlation between these greenhouse gas emissions (of which CO_2 is the main contributor [294], followed by CH_4 and N_2O) and climate change and therefore, there is an urging need to mitigate their effect.

Anthropogenic carbon dioxide emissions can be prevented and countered following different strategies, such as optimizing the use of

energy, reducing carbon intensity by switching to renewable energy sources or enhancing its sequestration [295]. Despite the great effort that is being put into the first two options, it is widely accepted that the world's energy supply will continue to depend on fossil fuels to some degree for at least this century [293], and this intrinsically will lead to CO_2 production. Thus, CO_2 capture and sequestration (CCS) is a necessary strategy to reduce CO_2 emissions and its concentration in the atmosphere and to mitigate climate change [244].

CCS technologies have been implemented in different industries, and deal with mixtures of diverse nature, such as natural gas, steam methane reforming off-gas (pre-combustion stream), flue gases (post-combustion stream), and ambient air (see section 1.3.3). A total of 19 large scale CCS facilities were in operation in 2019, out of which 10 have been implemented in natural gas upgrading, 3 in hydrogen production (pre-combustion), 2 in fertiliser production and 2 in power generation (post-combustion). It is noteworthy that most CCS operating facilities have been implemented in industries where CO_2 removal needs to be performed anyway. Still, a large effort needs to be put in the development and deployment of more CCS facilities [244].

At the present time, and similarly to the case of natural gas processing, the most mature CO_2 removal technique for post-combustion streams is chemical absorption with aqueous amines [244, 296]. The flue gas of processes that use oxy-fuel technology consists mostly only of H_2O and CO_2, which allows for an easy separation of the former by condensation [297]. In the case of pre-combustion, swing adsorption processes are state-of-the-art (see section 1.3.1), having displaced the previously used chemical absorption-based technology [184, 298, 299]. Direct air capture (DAC) is still under development, due to the difficulty of separating CO_2 from an ultradilute source [244, 300]. Promising technologies for CCS from pre- and post-combustion streams include adsorption and membrane processes, but these need to be improved in order to allow for wider deployment of CCS facilities [296, 301]. In DAC, the development of

improved and less costly amine-supported adsorbents is key for its future large scale deployment [244].

As said above, swing adsorption processes for CO_2 removal are only state-of-the art in the hydrogen production industry. In the case of carbon capture from natural gas using adsorption technology, the same as for natural gas upgrading applies (see section 1.3.3.1). Therefore, I will dedicate the last paragraph of this section to comment on the removal of CO_2 from post-combustion streams using swing adsorption methods.

Similarly to the CO_2/CH_4 separation, the CO_2/N_2 separation has been studied on different adsorbents, including activated and microporous carbons, graphene-based materials, MOFs, amine-functionalized adsorbents, metal oxides and carbonates, zeolites, AlPOs and SAPOs [302–306], but none of these adsorbents has been applied to a CO_2 removal swing adsorption process that is competitive with current amine-scrubbing state-of-the-art techniques. In what refers to zeolites and zeolite-type adsorbents (AlPOs, SAPOs and titanosilicates), most research has focused on type A, X and Y zeolites, out of which zeolite 13X is considered the best option for post-combustion CO_2 removal by PSA [243, 302–304, 307, 308]. It is noteworthy that hydrophilicity and energy intensive regeneration are frequently mentioned as problems inherent to zeolites. This is true if one considers only low silica zeolites, but may be minimized if other types of zeolitic adsorbents are taken into account. Similarly as in the case presented in section 1.3.3.1, materials with lower polarity, such as high and pure-silica zeolites, AlPOs and SAPOs are promising as well [304, 309–312]. The CO_2 isotherm shape in these materials favors a large PSA working capacity at moderate pressures (1-10 bar), whilst requiring much less energy for regeneration and keeping high selectivities if an adequate (small pore) structure is chosen. The selectivity in these cases stems from structural factors mainly, especially for pure-silica zeolites and AlPOs. Materials with CHA, DDR, LTA, MFI and RHO structures have been described [279, 280, 285, 287–289, 310–317]. Again, the main drawback of most of these materials is their

expensiveness and the difficulty to produce them at a large scale.

1.3.4 Separation of olefins from paraffins

Light olefins (ethene, propene, butenes) are important raw materials for the production of polymers (e.g. polyethylene, polypropylene) and chemicals (e.g. ethylbenzene, cumene) [318]. They are produced mainly in catalytic cracking, steam cracking, thermal cracking, MTO and catalytic dehydrogenation processes [118, 120, 319, 320], along with other hydrocarbons. The separation of light olefins from the other products is performed by cryogenic distillation. Due to their close boiling points (see table 1.1), the separation of these olefins, also called alkenes, from their analogous paraffins, also called alkanes (ethane, propane, butanes), is one of the most energy-consuming processes in the chemical industry [173, 321]. Therefore, finding alternative and complementary less energy-intensive methods for separating light olefins is of high interest.

Membrane-, absorption- and adsorption-based technology are promising candidates to replace the distillative separation of olefins from their analogous paraffins [322]. These ways of separating olefins from paraffins may rely on differences in the physical and/or chemical properties of said molecules (see table 1.1). Olefins present slightly smaller kinetic diameters and larger dipolar or quadrupolar moments, and can establish chemical bonds (π-interactions) with some metallic species [321]. In the case of adsorptive separation, this allows for different separation mechanisms, i.e. thermodynamic, kinetic and molecular sieving, depending on the properties of the chosen adsorbent.

Studies on the adsorptive separation of C2-C4 alkenes from alkanes have been carried out on different adsorbents, out of which zeolites and MOFs are the most promising [322]. Adsorbents that contain Ag and Cu, such as supported silicas and aluminas, exchanged zeolites (AgY, and several MOFs, may be thermodynamically selective towards the olefin thanks to a π-complexation mechanism [323–325]. However, the high heat of adsorption in these cases also makes regeneration

71

more energy-demanding. Furthermore, the strongly adsorbed olefin can oligomerize inside of such adsorbents giving rise to pore obstruction. Thermodynamic selectivity may, as well, stem from physical interactions with the adsorbent. Adsorbents with a polar surface are selective towards the olefin, which is the most frequent situation [321]. Aluminosilicate zeolites with FAU and LTA structures, more specifically, 13X, 4A and 5A, along with some exchanged titanosilicates of types ETS-10 and ETS-4 have achieved moderately high selectivities ($>$ 3) towards ethene and propene. MOFs such as M-MOF-74*, M_2(m-dobdc)† and NOTT-300 are promising for ethene and propene-selective separations [322]. Several nonpolar MOFs have been reported to be thermodynamically selective towards ethane over ethene. It is of high interest to achieve high working capacities and selectivities using paraffin-selective adsorbents, as these represent the lesser amount of the steam cracker product stream, and thus, their separation would require smaller adsorbent inventory and enable the direct production of a highly pure olefin stream [322, 326–328]. At the same time, by selectively adsorbing the alkane, the risk of olefin oligomerization is avoided. Whereas thermodynamically selective adsorbents have received most attention, it is kinetically selective and molecular sieving adsorbents that present the largest selectivities [322]. Various pure- and high silica zeolites with LTA, DDR, IHW, CHA, ITE and ITW structures present extraordinary high ($7 \times 10^2 - 4.6 \times 10^4$) propene/propane kinetic selectivities [329–334]. Similarly, zeolite ITQ-55 presents a very high ethene/ethane kinetic selectivity [335], which derives from an ethene adsorption-driven change in the framework structure. Further advantages of these pure-silica materials is that no reactions of the olefins will take place inside their nonpolar surface and their hydrophobicity will prevent competitive adsorption of water and other relatively polar molecules. MOF [$Ca(C_4O_4)(H_2O)$] presents an unprecedented molecular sieving effect, in which it adsorbs selectively only ethene and completely excludes ethane [336]. Other MOFs, such

---

*M = Mg, Co, Fe, Ni, Zn or Mn
†M = Co, Fe, Ni or Mn; m-dobdc = 2,5-dioxido-1,4-benzenedicarboxylate

as ZIF-8, ZIF-67[*], Zn(ox)0.5(trz) and Zn(ox)0.5(atrz)[†] present kinetic selectivities of the order of $10^2 - 10^3$ of propene over propane. These are probably not as high as for zeolites due to the higher flexibility of MOFs in general. Pure silica and aluminophosphate zeolites with CHA, IHW and RRO have been reported to be kinetically selective towards the linear olefins of the C4 fraction [331, 333, 337].

1.3.5 Separation of linear, branched and dibranched paraffins

Gasoline is a liquid hydrocarbon mixture which consists mainly of hydrocarbons in the C4 - C12 fractions and is one of the most widely used fuels. The octane number (ON) is a measure of the performance of the gasoline upon combustion in an internal combustion engine (ON of ca. 100 is desired) and it is regulated by official institutions. The ON of gasoline depends on its composition, in which some of its components, such as branched paraffins, aromatics or olefins increase the ON of the mixture [338]. Nonetheless, some of these components, such as benzene, aromatics and olefins, are restricted due to their environmental and/or health hazard [339]. This leaves branched paraffins as the component of choice to meet ON specifications. Hydroisomerization of straight run naphta (mostly linear C4 - C10 paraffins) is an effective method of obtaining higher ON components for the gasoline blend. These are reacted with hydrogen in the presence of a highly active supported metal hydrogenation catalyst to yield the desired multibranched products. Due to equilibrium limitations, low temperatures are needed in order to minimize hydrocracking [87, 339, 340]. A strategy which prevents hydrocracking from taking place and thus increases the yield and productivity of the unit includes separation of the branched products from the effluent and recycling of the linear and monobranched hydrocarbons to the head of the unit [341, 342]. The separation of linear from branched

---

[*]ZIF = zeolitic imidazolate framework
[†]ox = oxalate, trz = 1,2,4-triazole, atrz = 3-amino-1,2,4-triazole

isomers is done by adsorption using zeolite 5A as the adsorbent. This zeolite has been implemented in hydrocarbon separation processes since the 1960s [174, 343–347]. In fact, molecular sieving separations of linear and branched paraffins were one of the first major industrial successes of zeolites [86, 156, 346, 348]. Other zeolites, such as X, Y and ZSM-5 have been commercialized for this purpose, as well [349–352].

However, if applied at the exit of the hydroisomerization unit, the ideal target is the separation of linear and monobranched hydrocarbons from multibranched ones, as it would increase the efficiency of the whole process by recycling both low-octane linear and monobranched hydrocarbons to the head of the unit and yielding a multibranched product enriched raffinate with a high ON. Several materials have been studied and patented for this purpose, out of which silicalite-1 (Si-MFI) and other materials with MFI structure have been most frequently considered [353–362]. Other zeolites with diverse structures, such as AFI [363], AEL, ATO, BEA, FAU, FER [351, 353], ATS, CFI [364, 365], EUO, MWW, NES [360, 366–368], MEL, MRE and MTT [361], have been patented for this separation as well, but none of them clearly surpasses Si-MFI [368].

1.3.6   Separation of acetone, butanol and ethanol

Environmental concern and the future shortage of petroleum-derived products have boosted the research and production of renewable fuels and chemicals [369]. Biobutanol, chemically speaking, 1-butanol, is an excellent biofuel with analogous properties to gasoline and it serves as a platform molecule for the production of important chemicals. 1-Butanol can be produced from fermentation of starch and sugars, in what is known as the ABE (acetone, butanol, ethanol) fermentation, first patented by Chaim Weizmann* in the 1910s [370–373]. This process has been intermittently used throughout the years to obtain 1-butanol and/or acetone and is currently of great practical interest [369, 374,

---

*Known under the name Charles Weizmann in Britain, where he carried out his research activities.

375]. Different strains of bacteria of the class clostridia, e.g. *clostridium acetobutylicum* and *clostridium beijerinckii* can perform this fermentation. The process is carried out in anaerobic conditions and the product consists of a diluted aqueous solution (< 3 wt%) of acetone, butanol and ethanol in a 3:6:1 molar ratio, respectively [376]. Along with the liquid products, some CO_2 and H_2 are produced in the fermentation.

The recovery of 1-butanol from the fermentation broth was originally carried out by distillation. However, mainly due to its low concentration in the product, this turns out to be a highly energy intensive method and requires a high energy integration and capital cost [375, 377]. Alternatively, it can be carried out following different methods, such as extraction, gas stripping, pervaporation (membrane) or adsorption, out of which the last two seem the most promising [377, 378]. Many studies on liquid-phase adsorptive separation of butanol from the ABE product have been carried out using a variety of adsorbents [376], such as activated carbons [379–384], polymeric resins [381, 383, 385–388], zeolites [379, 383, 384, 387, 389–394] or MOFs [382, 384]. In 2014 Abdehagh et al. proposed the combination of gas stripping and adsorption (i.e. vapor phase adsorption) as an effective recovery method [378].

The isolation of butanol from the fermentation broth using vapor phase adsorption on microporous materials has since been studied by different groups on activated carbons [395–397], zeolites [395, 398–401] and MOFs [401–403]. The effect of CO_2 as a carrier gas has been considered in some of these works [401, 403].

As can be seen, zeolites have been used as adsorbents for liquid and vapor phase separations, with silicalite-1 being the most frequently studied material, probably due to it being the first pure silica zeolite available [404, 405]. Cavity-like zeolites, such as pure silica LTA (Si-LTA) and SAPO-34, i.e. CHA-structured SAPO, were used in combination by Van der Perre et al. to achieve an unprecedentedly high recovery and purity of 1-butanol [398].

75

1.3.7 Zeolites as adsorbents in other industrial and commercial separations

Drying of gaseous and liquid mixtures, the separation of oxygen from air and the separation of nitrogen from methane are three relevant industrial separations in which zeolitic adsorbents are used. Even though they are not specifically related to my research, they represent interesting examples of how the unique adsorption properties of these adsorbents can be exploited to achieve the desired separations.

1.3.7.1 Drying applications

Zeolites are widely used in drying applications at industrial and laboratory scale [406]. This is not surprising, as their name ultimately stems from their ability to reversibly adsorb water [5]. Natural and synthetic low silica zeolites are significantly hydrophilic due to their charge dispersion, i.e. negatively charged framework and extraframework cations [2]. Water molecules interact strongly with the zeolites' highly polar surface thanks to their dipole and quadrupole moments [406]. Zeolites of type A (with commercial names 3A, 4A and 5A) and X (13X) have been widely used for the drying of gas and liquid streams, mainly in TSA processes, but in the case of 13X, also in PSA processes [43, 406]. Their ability to selectively adsorb low concentrations of water from mixtures at temperatures above ambient has helped them replace the previously used active alumina and silica adsorbents [4, 407]. Indeed, drying is one of the earliest applications where zeolites were successfully used as adsorbents [2, 274, 346, 407–410]. Milton patented the use of zeolite 4A in a TSA process for drying natural gas [408], and the use of both 5A and 13X for simultaneous drying and sweetening of natural gas [274]. He also proposed the use of type X and A zeolites for drying vapor streams [407, 410]. Zeolite 3A, which can act as a molecular sieve towards water, has been implemented in the drying of olefins [40, 406], thus avoiding possible oligomerization inside the pores of the adsorbent. This molecular sieving

effect has proven practical, as well, for drying mixtures which contain other polar compounds, such as alcohols or even the ethanol/water azeotrope [411–413]. An RPSA drying process for natural gas that uses 3A zeolite as the adsorbent has been recently patented by ExxonMobil [414, 415]. Drying of streams containing highly acidic gases has been achieved by using high-silica mordenite and chabazite, which present sufficient chemical stability towards acids [160]. Furthermore, at a laboratory scale, beads of zeolites 3A and 4A are non-regeneratively used for drying of organic solvents [416].

1.3.7.2 Air: oxygen and nitrogen

The separation of oxygen from air at a large scale is carried out by cryogenic distillation. However, at smaller scales, the use of zeolite LiLSX in VPSA processes therefor is state of the art [2, 157, 163, 417, 418]. In 1959, Milton patented different type A exchanged zeolites [3] and observed the size exclusion of N_2 at low temperatures in these. He showed interest in further exploring this approach. Nonetheless, a thermodynamically controlled separation based on selective adsorption of N_2 at close to ambient temperatures became the method of choice [2]. Since the 1960s, different exchanged type X zeolites have been tested for carrying out this separation in PSA processes, with the focus on the obtention of pure oxygen. Three patents assigned to Union Carbide Corporation were issued in 1964 on this topic, in which the separation is achieved using zeolites of types X, Y and L (materials with a pore size of at least 4.6 Å) at low temperatures [419], Sr^{2+}-, Ba^{2+}- and Ni^{2+}-exchanged X zeolites at ambient temperature [420] or Li^+-exchanged X at ambient temperatures [417]. In the three patents, a pore size above 4 Å is pointed at as an important factor to enhance mass transfer of N_2. The interactions of the quadrupole of N_2 with the cations are considered the basis of the selectivity of these adsorbents. A notable effort was put in developing better adsorbents for air separation in the following years, in most cases still pulling the thread of alkali- or earth-alkali-exchanged type X zeolites

[421–423]. In 1989, Chao from UOP patented LiLSX (Lithium Low Silica X) zeolite, which presented extraordinary N_2/O_2 selectivity and N_2 working capacity [418]. Chao carried a systematic study on the Si/Al ratio and the extent of Li-exchange, which allowed for his discovery. He concluded that low Si/Al ratios and Li-exchange percentages above 80% yielded materials with the best selectivities (see fig. 1.10). Further improvements were achieved by Kirner, who reduced the Si/Al ratio from 1.25 to 1 and the threshold of Li-exchange from 80% to 70% [424]. This material still remains the material of choice for current processes [425, 426] and its development is a beautiful example of how the properties of zeolites can be tailored for a specific application.
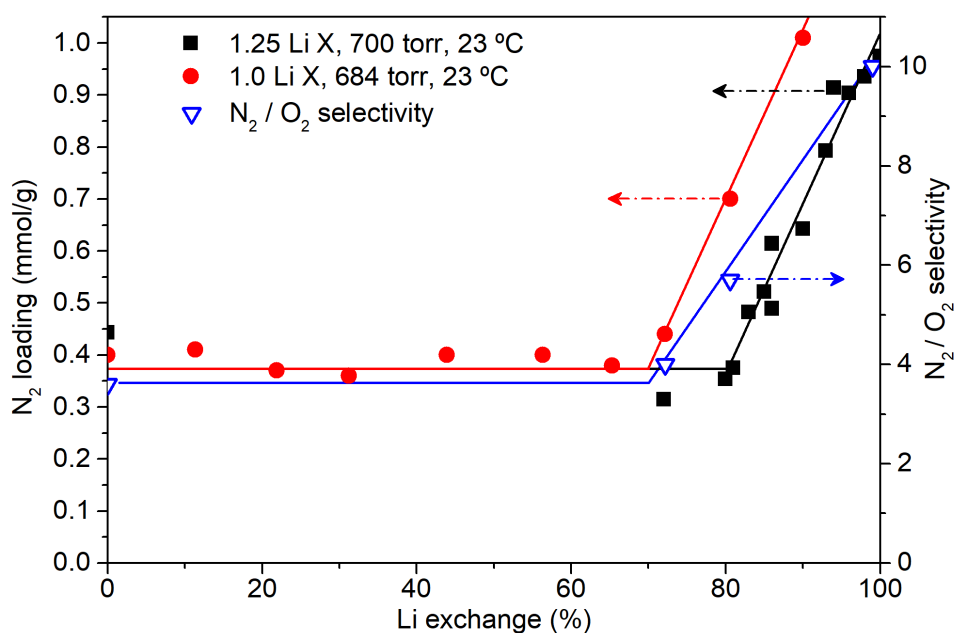
Figure 1.10: *Nitrogen loading of zeolites Li(1.25)X and Li(1.0)X and selectivity of Li(1.0)X vs lithium ion exchange. Li(1.25)X stands for LiLSX with an Si/Al ratio of 1.25 and Li(1.0)X stands for LiLSX with an Si/Al ratio of 1.0.*

Some years later, another zeolite-related material, i.e. contracted Engelhard titanosilicate CTS-1 (Na,Sr-ETS-4 treated at 300-340 °C), was patented to carry out the separation of oxygen from air basing on the molecular sieving of oxygen at room temperature [427, 428], thus recovering Milton's original idea [3].

1.3.7.3 Nitrogen removal from natural gas

The separation of nitrogen from methane is important in landfill gas, natural gas and biogas processing, as nitrogen needs to be removed for increasing the heating value of the mixture and meet specifications for transport through pipelines ($< 3\%$) and as liquefied natural gas ($< 1\%$) [247, 256]. Currently the most widely employed method for nitrogen removal from natural gas is cryogenic distillation, which is highly energy demanding. Alternative methods that are being researched are based on adsorption and membranes, and can be selective towards either N_2 or CH_4.

Most known adsorbents preferentially adsorb methane over nitrogen due to the larger polarizability of the former (see table 1.1) [160, 242, 429]. However, methane-selective pressure swing adsorption processes present the disadvantage that methane is present in these mixtures at a much higher concentration than nitrogen and thus, the required bed size would be much larger. On the other hand, the fact that N_2 is smaller (3.64 Å) than CH_4 (3.76 Å), allows for a nitrogen-selective separation under kinetic control and even by molecular sieving.

Zeolite 4A was patented for this purpose by Habgood [430], but the hydrophilicity of this material and the high temperatures needed for its activation rendered it impractical [431]. Natural clinoptilolites in their original and calcium-exchanged forms have been studied as adsorbents that kinetically distinguish between nitrogen and methane [432]. Clinoptilolite in its magnesium-exchanged form were patented by Chao for their use in a PSA unit to separate N_2 from CH_4 [433]. Titanosilicate materials developed by Engelhard Corporation (now BASF), such as ETS-4, CTS-1, Ba-ETS-4 and Sr-ETS-4, have been demonstrated to be excellent adsorbents for this application [242, 428, 434]. They have been commercialized under the name Molecular Gate™ and consist of a mixed octahedral-tetrahedrally coordinated framework with 8-ring openings, the size of which can be tailored by ion-exchange and thermal treatment [427, 429, 435].

Chapter 2

Objectives

The objectives of this thesis are all related to the study of the adsorption properties and potential applications in industrial separations of zeolites and related materials, such as AlPOs and SAPOs. The specific objectives of this thesis are:

- To study the adsorption and separation properties of ordered microporous materials, keeping a focus on pure silica zeolites, AlPOs and SAPOs, and especially on those presenting small pores. A list of the materials used for this thesis' research is given in section 3.2.

- To gain expertise in the measurement and analysis of adsorption isotherms and kinetics, and the obtention of isosteric heats, selectivities and kinetic parameters and to relate the aforementioned parameters with the structure and chemical composition of the materials under study.

- To deal with separations of current industrial interest, such as the purification of hydrogen, the separation of hydrogen isotopes, the separation of carbon dioxide from gas mixtures, the separation of light olefins from paraffins, the separation of butanol from vapor mixtures with acetone and ethanol or the separation of multibranched from monobranched and linear hydrocarbons.

- To test the materials in dynamic mixture adsorption experiments, i.e. breakthrough curves, which are the closest I can get with the resources available at our institute to the case of an industrial separation.

Chapter 3

Materials and Methods

In this section, I will provide details on the equipment used for characterization, synthesis and adsorption experiments, materials, adsorptives and experimental procedures.

3.1   Characterization techiques and equipment

3.1.1   X-Ray Diffraction

X-Ray Diffraction (XRD) has been used for identifying the structure of the adsorbents and gaining insight into their crystallinity, purity and reversible hydration processes (especially in AlPOs and SAPOs). For routine structural characterization, a Cubix PANalytical diffractometer with CuKα radiation (λ_1 = 1.5406 Å) at 45 kV and 40 mA in the 2θ range from 4 to 40° was used. Some samples hydrated readily when exposed to atmospheric air and thus were measured after dehydration by heating under dry air flow in an in situ reaction chamber Anton-Paar XRK-900 coupled to a PANalytical Empyrean diffractometer with CuKα radiation (λ_1 = 1.5406 Å) at 45 kV and 40 mA in the 2θ range from 3 to 75°.

3.1.2   Nuclear Magnetic Resonance

Nuclear Magnetic Resonance (NMR) techniques can be used to study the close-range chemical environment in molecules and crystals.

3.1.2.1 Liquid NMR

Liquid Nuclear Magnetic Resonance spectra of ^{1}H and ^{13}C were recorded on a Bruker DRX-300 spectrometer. These were used to follow the steps in the synthesis of OSDAs and to confirm the identity of OSDAs before the crystallization of the inorganic material.

3.1.2.2 Solid State NMR

Solid-state NMR spectra were obtained on a Bruker Avance III HD 400 MHz spectrometer using magic-angle spinning (MAS NMR) techniques at room temperature. Spectra of ^{29}Si, ^{27}Al and ^{31}P were recorded and analysed to assess the chemical environment of framework atoms. Chemical shifts of said nuclei are expressed in ppm relative units throughout this thesis (see eq. (3.1)). ^{27}Al MAS NMR spectra were recorded at $\nu_0(^{27}\text{Al})$ = 104.21 MHz, with a spinning rate of 20 kHz and a $\pi/12$ pulse length of 1.3 µs with a 1 s repetition time. Al(NO$_3$)$_3$·9 H$_2$O was used as reference for the ^{27}Al chemical shift. ^{31}P MAS NMR spectra were recorded at $\nu_0(^{31}\text{P})$ = 161.9 MHz using a spinning rate of 10 kHz, a $\pi/2$ pulse length of 3.7 µs with spinal proton decoupling and a repetition time of 20 s. Phosphoric acid was used as chemical shift reference. ^{29}Si MAS NMR spectra were recorded at $\nu_0(^{29}\text{Si})$ = 79.5 MHz using a spinning rate of 5 kHz with a $\pi/3$ pulse length of 3.5 µs, spinal proton decoupling and 180 s (for as-made samples) or 60 s (for calcined samples) as repetition time. The ^{29}Si chemical shift was referred to tetramethylsilane. ^{1}H/^{13}C CP MAS NMR spectra were recorded at $\nu_0(^{13}\text{C})$ = 100.6 MHz and $\nu_0(^1\text{H})$ = 400.1 MHz using a spinning rate of 10 kHz, a $\pi/2$ pulse length of 2.5 μs with spinal proton decoupling, a contact time of 2 ms and a repetition time of 3 s.

$$\delta_{\text{nucleus}} = \frac{\nu_{\text{nucleus}} - \nu_{\text{ref}}}{\nu_{\text{ref}}} \qquad (3.1)$$

Chemical environment and defects: The chemical environment of the framework atoms, especially Si and Al, was studied following the directions given in [436]. The possible environments of Si are Q^4, i.e. Si united by oxygen bridges to other 4 Si atoms, Q^3, i.e. Si united by oxygen bridges to other 3 Si atoms, and, analogously defined, Q^2, Q^1 and Q^0.

In the case of aluminosilicate zeolites, Q^n environments (with $n \leq 4$) are interpreted as Si atoms with (4-n) Al atoms in their second coordination sphere and these give signals in known ranges, as shown in fig. 3.1.
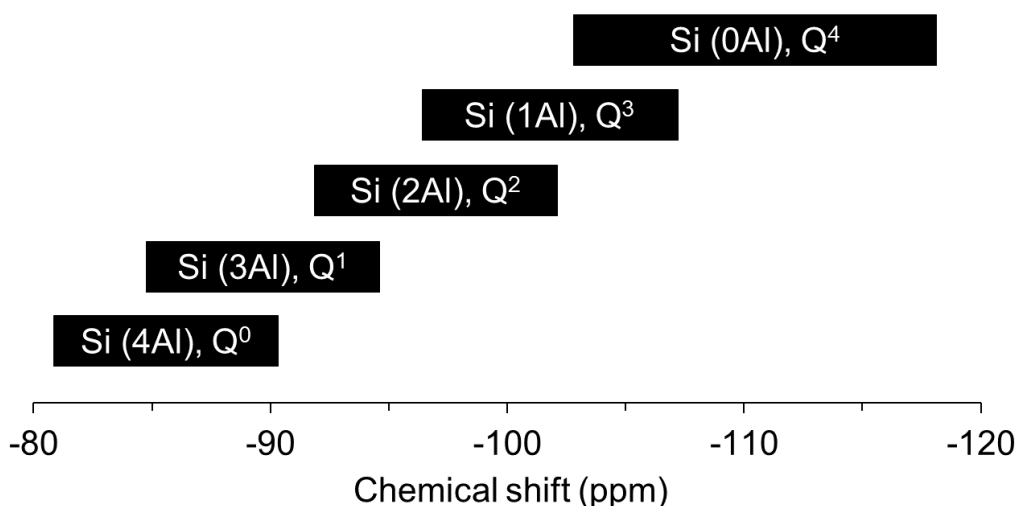
Figure 3.1: ^{29}Si *MAS NMR chemical shifts ranges of Si species. Adapted from* [436].

However, in the case of pure silica zeolites, signals in the range of -105 to -120 ppm belong to $Si(OSi)_4$, i.e. Q^4, and signals above -105 ppm are interpreted as connectivity defects, i.e. Q^3 or silanols, the presence of which can be confirmed in ^{1}H - ^{29}Si cross-polarization MAS NMR experiments.

In the cases of Al and P in AlPOs and SAPOs, it is frequent to identify signals revealing a certain amount of penta- and hexacoordinated species, which are normally a result of hydration [437, 438]. Another possibility in what refers to Al is that extraframework Al may be present. The ^{1}H/^{13}C CP MAS NMR spectra were used to confirm the integrity of

the OSDA in the as-made material. The analysis of ^{27}Al, ^{31}P and ^{1}H/^{13}C CP MAS NMR spectra lays beyond the scope of this thesis.

Estimated negative framework charge: The estimated framework negative charge is a parameter which enables the comparison of isosteric heats of adsorption between materials with different chemical composition and connectivities*. In the case of zeolites, it is equal to the Al/(Si + Al) molar ratio calculated from the ICP-OES results (see section 3.1.3). In SAPOs, the estimated framework negative charge is calculated by combining the ICP-OES with the ^{29}Si MAS NMR analyses results. The Si/(Si + Al + P) ratio is obtained from the ICP-OES data. However, this value does not give a proper estimate of the framework charge, in contrast to the case of isomorphic Al substitution in aluminosilicate materials. This is due to the different possible substitution patterns of Si in SAPOs (as single or isolated Si atoms or as Si-rich domains or SiO_2-islands), in which not all the Si atoms contribute equally to the framework charge [52, 53, 439, 440]. More specifically, isolated Si atoms contribute with 1 negative charge per substituted P atom, whereas the contribution of a Si-rich domain is proportionally smaller and depends on its size. With the purpose to differentiate between both types of Si in SAPOs, the ^{29}Si spectra were fitted using two different Gaussian functions, one centered at values between -100 and -120 ppm for SiO_2-islands and at the other at ca. -90 ppm for isolated Si species. After proper integration of the functions, the fraction of isolated Si is calculated. This fraction is multiplied times the Si/(Si + Al + P) ratio thus giving the estimated framework negative charge. The minor contribution of the Si-islands has been disregarded. The estimated framework negative charge of AlPOs and pure-silica zeolites is zero.

---

*This parameter is especially useful in chapter 5.

3.1.3 Inductively Coupled Plasma Optical Emission Spectroscopy

Inductively Coupled Plasma Optical Emission Spectroscopy (ICP-OES), also known as Inductively Coupled Plasma Atomic Emission Spectroscopy (ICP-AES) was used to analize the chemical composition of the materials, more specifically, the content of Si, Al, P, Na, Ca, B and Ge after dissolution of the samples in a 5 wt% 1:1 HF/HNO_3 solution in MilliQ water. The device used is a Varian 715-ES ICP-Optical Emission Spectrometer.

3.1.4 Scanning electron microscopy

Crystal shape and size were characterized by Scanning Electron Microscopy (SEM) and Field Emission Scanning Electron Microscopy (FESEM) techniques. SEM images were obtained using a JEOL JSM6300 microscope and FESEM images were obtained using a Zeiss Ultra 55 microscope with an accelerating voltage of 1 kV.

3.1.5 Elemental Analysis

Elemental analysis (EA) was used to determine the chemical composition of organic products or the organic fraction of materials, i.e. it gave the C, H and N content in the analyzed samples. A Fisons EA1108 Elemental Analyzer was used and sulfanilamide was taken as reference standard.

3.1.6 Thermogravimetric analysis

Thermogravimetric analysis (TGA) in air was used to calculate the organic mass fraction in as-made zeolites and the temperature above which the OSDA is eliminated under air atmosphere. A Netzsch TGA Jupiter STA 449 F3 was employed, with a heating ramp of 10 °C/min, and 800 °C maximum temperature for routine analysis. Nitrogen was flown (20

ml/min) as a protective gas for the balance and dry air was flown (50 ml/min) for providing the oxidizing atmosphere.

3.1.7   Adsorption for textural analysis

Textural analysis, i.e. assessment of surface area, pore volume and pore size distribution, was carried out by standard adsorption techniques using volumetric devices (see section 1.2.1.1).

3.1.7.1   Nitrogen adsorption at -196 °C

A Micromeritics ASAP2420 was used to measure N_2 adsorption at -196 °C on the samples and determine their surface areas and micropore volumes. Activation was carried out at at 400 °C under vacuum. The Brunauer-Emmet-Teller (BET) and t-plot methods were used in order to obtain estimations of the surface area and the micropore volume, respectively [158, 441, 442].

3.1.7.2   Argon adsorption at -186 °C

A Micromeritics ASAP2020 was used to measure Ar adsorption at -186 °C on the samples and determine their pore size distribution following Horvath-Kawazoe's method [443]. Activation was carried out at at 400 °C under vacuum.

3.1.7.3   Carbon dioxide adsorption at 0 °C

In the cases where the adsorption of N_2 or Ar was very slow at their respective analysis temperatures or even did not take place, adsorption of CO_2 at 0 °C was measured using a Micromeritics ASAP2010 device. The analysis of the isotherms using Dubinin-Astakhov's (DA) method [444] allowed us to obtain estimated surface areas and micropore volumes.

3.2 Materials and their synthesis

3.2.1 Nomenclature of zeolitic materials

The names of many materials are chosen by the researchers who develop/discover them. This results in a priori cryptic names, the meaning and origin of which can be found at the Database of Zeolite Structures [44]. Usually, the first material that is discovered that presents a new structure is taken as the reference material for this structure, and the official structure code it is assigned with takes as inspiration the name of this reference material. A list of the structures of interest in this thesis including some examples of materials bearing said structures, along with the explanation of their names is provided below:

- **AFI** (code derived from AlPO-5, aluminophosphate 5)

    - SSZ-24, acronym of Standard Oil Synthetic Zeolite 24, pure silica zeolite.

    - AlPO-5, reference material for this structure.

    - SAPO-5, silicoaluminophosphate 5

- **CHA** (code derived from chabazite)

    - SSZ-13, acronym of Standard Oil Synthetic Zeolite 13, high or pure silica zeolite.

    - AlPO-34, aluminophosphate 34

    - SAPO-34, silicoaluminophosphate 34

- **IHW** (code derived from ITQ-32, Instituto de Tecnología Química 32)

    - ITQ-32, high or pure silica zeolite

- **ITW** (code derived from ITQ-12, Instituto de Tecnología Química 12)

    - ITQ-12, pure silica zeolite

- **LTA** (code derived from Linde Type A)

- ITQ-29, acronym of Instituto de Tecnología Química 29, high or pure silica zeolite. May contain Ge.

- 4A, common name for LTA aluminosilicate zeolite with Si/Al ratio of 1 in its Na form

- 5A, common name for LTA aluminosilicate zeolite with Si/Al ratio of 1 in its Ca/Na form

- UZM-9, aluminosilicate zeolite with Si/Al ratio of 5, also known as LTA-5

- AlPO-42, aluminophosphate 42

- SAPO-42, silicoaluminophosphate 42

- **MFI** (code derived from ZSM-5, Zeolite Socony Mobile 5)

  - ZSM-5, reference material for this structure.

  - Silicalite-1, pure silica MFI zeolite

- **MTF** (code derived from MCM-35, Mobil Composition of Matter 35)

  - MCM-35, pure silica zeolite

- **RTH** (code derived from RUB-13, Ruhr University Bochum 13)

  - RUB-13, pure silica zeolite

- **RWR** (code derived from RUB-24, Ruhr University Bochum 24)

  - RUB-24, pure silica zeolite

- **STT** (code derived from SSZ-23, Standard Oil Synthetic Zeolite 23)

  - SSZ-23, pure silica zeolite

- **STW** (code derived from SU-32, Stockholm University 32)

  - HPM-1, pure silica zeolite

For the sake of clarity, I have chosen to normalize the nomenclature of materials in a way that simplifies their identification and comparison. The general nomenclature used in this thesis is explained below:

- **Aluminosilicate zeolites**: framework code + "-" + inverse of the estimated framework negative charge (see section 3.1.2.2). This means that an aluminosilicate zeolite with LTA structure and Si/Al ratio of 5, usually referred to as LTA-5, will be renamed as LTA-6.

- **Pure silica zeolites**: "Si-" + framework code. ITQ-29 is thus renamed as Si-LTA.

- **AlPOs**: "AlPO-" + framework code. This way, AlPO-42 becomes AlPO-LTA.

- **SAPOs**: "SAPO-" + framework code + "-" + inverse of the estimated framework negative charge. A SAPO material with LTA structure and an estimated framework negative charge of 0.08 is renamed as SAPO-LTA-13.

In cases, where two samples of the same kind have been studied, they are differentiated by adding a letter suffix, e.g. Si-RTH-a, Si-RTH-b.

3.2.2 Synthesis of zeolitic materials

Similarly to what is described in section 1.1.3, most of the materials of this thesis have been synthesized hydrothermally. In this section, the detailed synthesis procedures of zeolitic materials are described and ordered alphabetically according to their structure code. After the obtention of the as-made material, unless otherwise stated, the materials were submitted to calcination in air in order to remove the occluded OSDA molecules. In some cases a tube furnace was used with a controlled flow of dry air and in other cases, a muffle furnace was used. The maximum temperature reached in the calcination is indicated for all samples, along with the time. Usually, before reaching the maximum temperature of the calcination procedure, an intermediate plateau at 300 or 350 °C was maintained for at least 1 h in order to desorb all the moisture that might be present in the sample. The detailed calcination procedures are only specified in cases that differ from this general method.

I carried out the synthesis of Si-AFI, Si-MTF and Si-STT, and collaborated in the synthesis of AlPO-LTA, AlPO-AFI and SAPO-AFI materials, with Jose Valero. Si-RTH samples were synthesized by Jorge Simancas and I carried out their hydrogenation and calcination. The synthesis of CHA, LTA, IHW, ITW, MFI zeolites, SAPO-CHA-7 and Si-RWR-b was carried out by Amparo Moraleda. The synthesis of SAPO-LTA materials was carried out by Raquel Martínez-Franco, and the synthesis of SAPO-CHA-10 was carried out by Isabel Millet. Andrés Sala synthesized zeolite Si-STW. Nuria González-Camuñas synthesized AlPO-CHA. Gabriel de Biasi Báfero synthesized the Si-RWR-a sample.

The OSDAs were either bought or synthesized. The syntheses of the non-commercial OSDAs lay beyond the scope of this thesis. OSDAs other than simple amines/ammonium salts are depicted for the sake of clarity.

3.2.2.1 AFI

Si-AFI was synthesized according to a procedure reported in the Verified Syntheses of Zeolitic Materials webpage of the International Zeolite Association [63, 445]. A solution of N,N,N-trimethyl-1-adamantammonium hydroxide (TMAdAOH, 0.329 mmol OH/g, see fig. 3.2) was mixed with water and potassium hydroxide (Sigma-Aldrich) until homogeneity was reached. Fumed silica (Sigma-Aldrich) was added and the resulting gel stirred manually. The resulting gel had the composition:

$$1 \text{ SiO}_2 : 0.06 \text{ K}_2\text{O} : 0.15 \text{ TMAdAOH} : 40 \text{ H}_2\text{O}$$
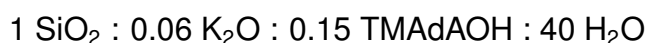
The gel was transferred to PTFE-lined stainless steel autoclaves and crystallization was carried out at 150 °C for 10 d in static conditions. The crystalline solids were recovered by filtration and washed thoroughly with water until neutral pH was reached. The material was dried at 100 °C and finally, calcined at 580 °C in a muffle furnace for 3 h.

AlPO-AFI was synthesized following a procedure reported on the Verified Syntheses of Zeolitic Materials webpage of the International Zeolite
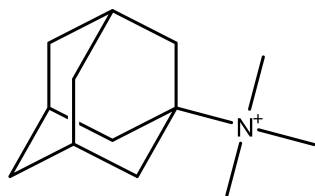
Figure 3.2: *N,N,N-trimethyl-1-adamantammonium.*

Association [63, 446]. Phosphoric acid (85 wt%, Sigma-Aldrich) was dissolved in water under stirring. Triethylamine (TEA, 99 wt%, Sigma-Aldrich) was added dropwise under continuous stirring. Aluminium isopropoxide (99 wt%, Sigma-Aldrich) was then slowly added while cooling at 0 °C and stirring. The mixture was stirred at room temperature for another 2 h, or until complete evaporation of the 2-propanol. Finally, aqueous HF (50 wt%, Sigma-Aldrich) was added and the mixture was stirred for further 2 h. The final gel composition was:
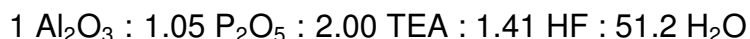
$$1 \ Al_2O_3 : 1.05 \ P_2O_5 : 2.00 \ TEA : 1.41 \ HF : 51.2 \ H_2O$$

The resulting gel was transferred to PTFE-lined stainless steel autoclaves and crystallization was carried out at 200 °C for 3 to 24 h under static conditions. The product was then filtered off, washed with deionized water until the filtrate was pH-neutral and dried at 100 °C. Calcination was carried out at 600 °C in a muffle furnace for 3 h.

SAPO-AFI-46 and SAPO-AFI-34 were synthesized following a procedure reported on the Verified Syntheses of Zeolitic Materials webpage of the International Zeolite Association [63, 447] using cyclohexylamine as the OSDA and varying the Si content of the gel. Aluminium isopropoxide (99 wt%, Sigma-Aldrich) was suspended in water to form a slurry. An aqueous solution of phosphoric acid (85 wt%, Sigma-Aldrich) was then added dropwise to the slurry under stirring. The resulting mixture was further stirred for 1 h to ensure homogeneity and evaporation of the 2-propanol resulting from hydrolysis of the Al source. Cyclohexylamine (99.9 wt%, Sigma-Aldrich) was then added dropwise under stirring. The

resulting mixture was further stirred for 1.5 h to ensure homogeneity. Finally, colloidal silica (Ludox AS40, 40 wt%, Sigma-Aldrich) was added and the mixture was stirred for another 10 min. The final gel compositions of SAPO-5-46 and SAPO-5-34 were, respectively:
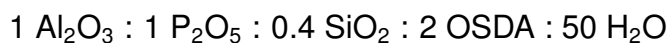
$$1\ Al_2O_3 : 1\ P_2O_5 : 0.4\ SiO_2 : 2\ OSDA : 50\ H_2O$$
$$1\ Al_2O_3 : 1\ P_2O_5 : 0.8\ SiO_2 : 2\ OSDA : 50\ H_2O$$

The resulting gel was transferred to PTFE-lined stainless steel autoclaves and crystallization was carried out at 200 °C for 3 h under static conditions. The product was then filtered off, washed with deionized water until neutral pH was measured in the filtrate and dried at 100 °C. Calcination was carried out at 600 °C in a muffle furnace for 3 h.

3.2.2.2 CHA

Si-CHA was synthesized from a gel containing fluoride following a reported procedure [448]. In particular, tetraethylorthosilicate (TEOS, 98 wt%, Merck) was added to an aqueous solution of TMAdAOH. The mixture was stirred during the time required to evaporate the ethanol formed during the hydrolysis of TEOS and the excess of water. Finally, an aqueous solution of HF (50 wt%, Sigma-Aldrich) was added and the mixture was homogenized. The molar composition of the gel was the following:

$$1\ SiO_2 : 0.50\ TMAdAOH : 0.50\ HF : 3\ H_2O$$

The gel was introduced in PTFE-lined stainless steel autoclaves and heated at 150 °C during 2 d with rotation. The autoclaves were cooled down and the zeolite was recovered by filtration, washing with deionized water and drying at 100 °C. The zeolite was submitted to calcination at 580 °C in a muffle furnace for 3 h.

CHA-19 was synthesized in fluoride medium following a procedure based in the one reported for the pure silica zeolite [448]. TEOS (98 wt%, Merck)

and aluminium isopropoxide (99 wt%, Sigma-Aldrich) were added to an aqueous solution of TMAdAOH. The mixture was stirred during the time required to evaporate the ethanol formed during the hydrolysis of TEOS, the 2-propanol resulting from hydrolysis of the Al source and the excess of water and, finally, an aqueous solution of HF (50 wt%, Sigma-Aldrich) was added. The mixture was homogenized and the molar composition of the gel was the following:

$$1 \; SiO_2 : 0.005 \; Al_2O_3 : 0.50 \; TMAdAOH : 0.50 \; HF : 3 \; H_2O$$

The gel was introduced in PTFE-lined stainless steel autoclaves and heated at 150 °C during 4 d with rotation. The autoclaves were cooled down and the zeolite was recovered by filtration, washing with deionized water and drying at 100 °C. The zeolite was submitted to calcination at 580 °C in a muffle furnace for 3 h.

CHA-18 was synthesized following a procedure reported on the Verified Syntheses of Zeolitic Materials webpage of the International Zeolite Association for preparing zeolite SSZ-13 [63, 449]. For this preparation, an aqueous solution containing NaOH (Sigma-Aldrich) and TMAdAOH was prepared. Then, aluminium hydroxide (57 wt% Al_2O_3, Sigma-Aldrich) followed by fumed silica (Aerosil 200, Degussa) were incorporated and the mixture was homogenized by stirring in order to form a gel of the following molar composition:

$$1 \; SiO_2 : 0.025 \; Al_2O_3 : 0.20 \; TMAdAOH : 0.10 \; Na_2O : 44 \; H_2O$$

The gel was introduced in PTFE-lined stainless steel autoclaves and heated at 160 °C during 4 d with rotation. The autoclaves were cooled down and the zeolite was recovered by filtration, washing with deionized water until a pH-neutral filtrate was obtained and drying at 100 °C. The zeolite was submitted to calcination at 580 °C in a muffle furnace for 3 h.

CHA-6 was prepared according to a previously reported procedure

[450]. The required amount of N,N,N-trimethyl-1-adamantammonium iodide (TMAdAI) was added to an aqueous solution of NaOH together with sodium silicate solution (26.7 wt% SiO_2, 7.9 wt% Na_2O, Supelco) and, finally, zeolite Y (CBV500, Zeolyst) was incorporated to the mixture. After homogenization of the ingredients by stirring for 2 h, a gel of the following molar composition was obtained:

$$1 \ SiO_2 : 0.027 \ Al_2O_3 : 0.09 \ TMAdAI : 0.34 \ Na_2O : 25 \ H_2O$$

The mixture was introduced in PTFE-lined stainless steel autoclaves and heated at 135 °C during 4 d in static conditions. The autoclaves were cooled down and the zeolite was recovered by filtration, washing with deionized water until the filtrate had pH = 7 and drying at 100 °C. The zeolite was submitted to calcination at 580 °C in a muffle furnace for 3 h.

CHA-3 was synthesized following a procedure reported on the Verified Syntheses of Zeolitic Materials webpage of the International Zeolite Association [63, 451]. Commercial zeolite Y (CBV500, Zeolyst) was added to an aqueous solution of KOH in a polypropylene bottle in order to form a gel of the following molar composition:

$$1 \ SiO_2 : 0.19 \ Al_2O_3 : 0.03 \ Na_2O : 0.39 \ K_2O : 43 \ H_2O$$

The mixture was stirred for 10 min at room temperature and then heated at 100 °C for 5 d in static conditions. The zeolite was then recovered by filtration, washing with deionized water until neutral pH of the filtrate and drying at 100 °C. There was no need to calcine this sample, as no OSDA was used.

AIPO-CHA was synthesized according to a previously reported procedure [289]. The OSDA ((S)-1-methyl-2-(pyrrolidin-1-ylmethyl)pyrrolidine, see fig. 3.3) was dispersed in a solution of phosphoric acid (85 wt%, Sigma-Aldrich) in water. Aluminium isopropoxide (99 wt%, Sigma-Aldrich) was then added and the resulting mixture stirred for 2 h at room temperature

for homogenization and evaporation of the 2-propanol resulting from hydrolysis of the Al source. HF (50 wt%, Sigma-Aldrich) was then added, reaching pH = 7 and the resulting mixture was stirred for 1 h at room temperature. The gel composition was:

$$1\ Al_2O_3 : 1.3\ P_2O_5 : 1.6\ OSDA : 1.3\ HF : 425\ H_2O$$

The gel was introduced in a PTFE-lined autoclave and kept at 175 °C for 18 h under static conditions. The solid was recovered by filtration and, after thorough washing with water, dried in an oven at 100 °C. The material was submitted to calcination at 650 °C in a muffle furnace for 3 h.
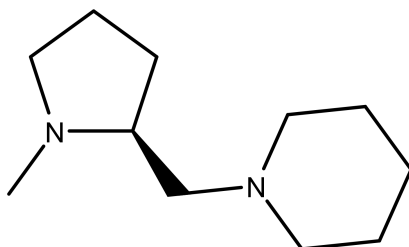
Figure 3.3: *(S)-1-methyl-2-(pyrrolidin-1-ylmethyl)pyrrolidine.*

SAPO-CHA-10 was prepared by a previously reported method [51]. Colloidal silica (Ludox AS40, 40 wt%, Sigma-Aldrich) was used as the silica source and partially hydrated alumina (75 wt%, Condea Pural) as the aluminium source. Phosphoric acid (85 wt%, Sigma-Aldrich) was dissolved in water and tetraethylammonium hydroxide (TEAOH, 35 wt%, Sigma-Aldrich) was added. The alumina was then added and the mixture stirred for 5 min. Finally the silica source was added and the mixture was stirred at room temperature until complete homogenization (ca. 20 min). The resulting gel composition was:

$$1\ Al_2O_3 : 0.8\ P_2O_5 : 0.27\ SiO_2 : 1.8\ TEAOH : 36\ H_2O$$

The crystallization was carried out at 175 °C for 2 d. The solids were filtered off and washed until neutral pH was reached in the washing

waters. The solid was dried at 100 °C overnight and finally calcined at 550 °C in a muffle furnace for 3 h.

SAPO-CHA-7 was obtained following a procedure reported on the Verified Syntheses of Zeolitic Materials webpage of the International Zeolite Association [63, 452]. Partially hydrated alumina (75 wt%, Condea Pural) was slowly added to an aqueous solution of phosphoric acid and stirred during 4 h. Then, a mixture containing fumed silica (Aerosil 200, Degussa), morpholine (M, 99 wt%, Sigma-Aldrich, see fig. 3.4) and water was prepared and added dropwise to the former one. The gel was homogenized by stirring for 3 h. The molar composition of the gel was the following:

$$1 \; Al_2O_3 : 1.06 \; P_2O_5 : 1.08 \; SiO_2 : 2.09 \; M : 66 \; H_2O$$
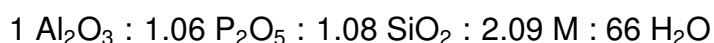
The gel was aged at 38 °C during 24 h and later introduced in PTFE-lined stainless steel autoclaves and heated at 200 °C for 24 h in static conditions. The autoclaves were cooled down and the sample was recovered by filtration, washing with abundant deionized water and drying at 100 °C. It was submitted to calcination at 580 °C in a muffle furnace for 3 h.
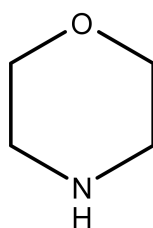
Figure 3.4: *Tetrahydro-1,4-oxazine, also known as morpholine.*

3.2.2.3   IHW

Si-IHW was prepared following a previously described procedure [453]. TEOS (98 wt%, Merck) was hydrolyzed in an aqueous solution of 4-cyclohexyl-1,1-dimethylpiperazinium hydroxide (1 mmol/g), used as the

OSDA (see fig. 3.5). The mixture was stirred until all the ethanol resulting from the hydrolization of TEOS and the excess amount of water were evaporated. HF (50 wt%, Sigma-Aldrich) was added and the mixture was stirred for homogenization. A suspension of previously synthesized aluminosilicate ITQ-32 (Si/Al = 32) in water was added and the mixture stirred, resulting in a gel of the following composition:[*]

$$1 \ SiO_2 : 0.54 \ OSDA : 0.54 \ HF : 7 \ H_2O$$

The gel was introduced in PTFE-lined stainless steel autoclaves and heated at 175 °C for 2 d with rotation. The autoclaves were cooled down and the sample was recovered by filtration, washing with abundant deionized water and drying at 100 °C. It was calcined at 580 °C in a muffle furnace for 3 h.

Figure 3.5: *4-cyclohexyl-1,1-dimethylpiperazinium.*

3.2.2.4   ITW

Si-ITW was prepared following a previously reported procedure [454, 455]. TEOS (98 wt%, Merck) was hydrolyzed in an aqueous solution of the OSDA, i.e. 1,3,4-trimethylimidazolium hydroxide (0.7 mmol/g, see fig. 3.6). The mixture was stirred until all the ethanol resulting from the hydrolization of TEOS and the excess amount of water were evaporated. HF (50 wt%, Sigma-Aldrich) was added and the mixture was stirred for homogenization. The gel had the following composition:

$$1 \ SiO_2 : 0.56 \ OSDA : 0.56 \ HF : 7 \ H_2O$$

---

[*]The final material is esentially pure silica, presenting Si/Al > 300.

The gel was introduced in PTFE-lined stainless steel autoclaves and heated at 175 °C for 13 d with rotation. The autoclaves were cooled down and the sample was recovered by filtration, washing with abundant deionized water and drying at 100 °C. It was calcined at 650 °C in a muffle furnace for 10 h.

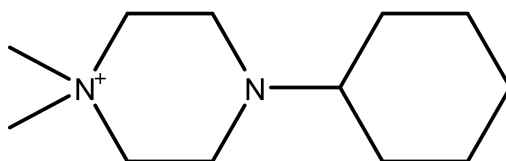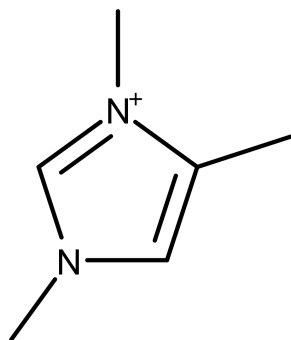**Figure 3.6:** *1,3,4-trimethylimidazolium.*

3.2.2.5 LTA

Si-LTA was prepared following a previously described procedure [456]. The gel was prepared by hydrolyzing TEOS (98 wt%, Merck) in an aqueous solution of 4-methyl-2,3,6,7-tetrahydro-1H,5H-pyrido[3.2.1-ij]quinolinium (MTPQ, see fig. 3.7a) and tetramethylammonium hydroxides (TMAOH, 25 wt% aqueous solution from Sigma-Aldrich). The mixture was stirred until the ethanol formed upon hydrolysis of TEOS and the appropriate excess of water were evaporated to reach the gel composition given below. Finally, a 5 wt% of previously synthesized Si-LTA seeds and an aqueous solution of HF (50 wt%, Sigma-Aldrich) were added to yield the gel of composition:

$$1 \ SiO_2 : 0.25 \ MTPQ : 0.25 \ TMAOH : 0.5 \ HF : 3 \ H_2O$$
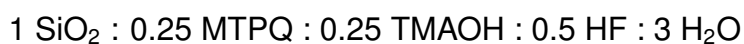
The mixture was introduced in PTFE-lined stainless autoclaves and heated at 135 °C for 7 days under rotation. After this time the solids were filtered, washed with abundant deionized water, dried at 100 °C and finally calcined in a muffle furnace at 700 °C for 3 h.

a)   b)
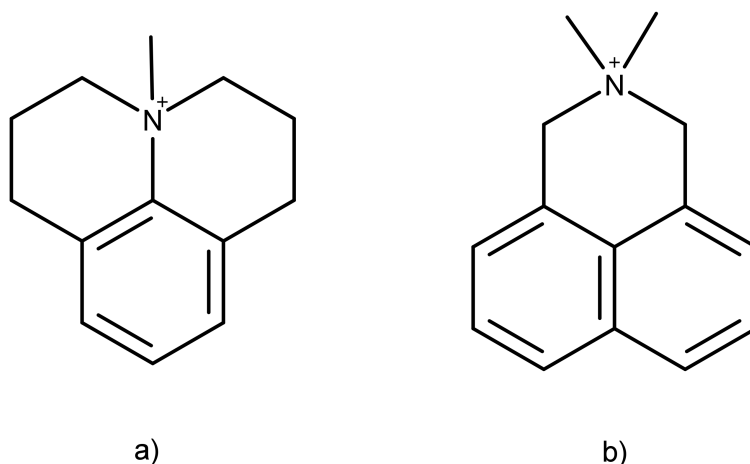
Figure 3.7: *a) 4-methyl-2,3,6,7-tetrahydro-1H,5H-pyrido[3.2.1-ij]quinolinium (MTPQ) and b) 2,2-Dimethyl-2,3-dihydro-1H-benzo[de]isoquinoline-2-ium (DDBQ).*

LTA-31 was synthesized following a similar method to the one described for Si-LTA [456, 457]. The gel was prepared by hydrolyzing TEOS (98 wt%, Merck) in an aqueous solution of MTPQ and TMAOH. Then the appropriate amount of aluminum isopropoxide (99 wt%, Sigma-Aldrich) was added and the mixture was kept under stirring until ethanol and 2-propanol and the appropriate excess of water were evaporated to reach the gel composition given above. After that, an aqueous solution of HF (50 wt%, Sigma-Aldrich) was added and, finally, pure silica ITQ-29 seeds were incorporated as a suspension in water to reach 15 mol% of the total silica.

$$1 \ SiO_2 : 0.01 \ Al_2O_3 : 0.25 \ MTPQ : 0.25 \ TMAOH : 0.5 \ HF : 3 \ H_2O$$

The mixture was introduced in PTFE-lined stainless autoclaves and heated at 125 °C for 3 days under rotation. After this time the mixture was filtered, washed with abundant deionized water, dried at 100 °C and finally calcined in a muffle furnace at 700 °C for 3 h.

LTA-6 was synthesized basing on the method appearing on Example 1 in [458]. Aluminium sec-butoxide (97 wt%, Sigma-Aldrich) was added to an aqueous solution of tetraethylammonium (TEAOH, 35 wt% aqueous

solution, Sigma-Aldrich) and diethyldimethylammonium (DEDMAOH, 20 wt% aqueous solution, Sigma-Aldrich) hydroxides under stirring. Colloidal silica (Ludox AS40, 40 wt%, Sigma-Aldrich) was then added and the mixture stirred for 1 h and aged at 95 °C overnight. An aqueous solution of TMACl (98 wt%, Sigma-Aldrich) and NaCl (Sigma-Aldrich) was then added and the mixture homogenized for 30 min. The gel composition was:

$$1 \ SiO_2 : 0.05 \ Al_2O_3 : 0.3 \ TEAOH : 0.2 \ DEDMAOH : 0.05 \ TMACl : 0.05 \ NaCl : 17 \ H_2O$$

The mixture was introduced in PTFE-lined stainless steel autoclaves and crystallization was carried out at 100 °C for 13 d under static conditions. After this time the mixture was filtered, washed with deionized water until neutral pH was reached, dried at 100 °C and finally calcined in a muffle furnace at 500 °C for 3 h.

LTA-4.5 was synthesized basing on the method appearing on Example 10 in [458]. Aluminium sec-butoxide (97 wt%, Sigma-Aldrich) was added to an aqueous solution of DEDMAOH (20 wt%, Sigma-Aldrich) under stirring. Colloidal silica (Ludox AS40, 40 wt%, Sigma-Aldrich) was then added and the mixture stirred for 20 h and aged at 95 °C overnight. An aqueous solution of TMACl (98 wt%, Sigma-Aldrich) and NaCl (Sigma-Aldrich) was then added and the mixture homogenized for 30 min. The gel composition was:

$$1 \ SiO_2 : 0.06 \ Al_2O_3 : 0.85 \ DEDMAOH : 0.12 \ TMACl : 0.05 \ NaCl : 30 \ H_2O$$

The resulting gel was introduced in PTFE-lined stainless steel autoclaves and crystallization was carried out at 125 °C for 10 d under static conditions. After this time the mixture was filtered, washed with water, dried at 100 °C and finally calcined in a muffle furnace at 500 °C for 3 h.

LTA-3 was synthesized following a modified recipe based on that reported for zeolite Alpha in the Verified Syntheses of Zeolitic Materials webpage of the IZA Synthesis Commission [63, 459]. Sodium aluminate (54 wt% Al_2O_3, 39 wt% Na_2O, Carlo Erba), TMAOH (25 wt% aqueous solution, Sigma-Aldrich), colloidal silica (Ludox AS40, 40 wt%, Sigma-Aldrich) and water were used for the preparation of a gel of the following molar composition:

$$1 \ SiO_2 : 0.17 \ Al_2O_3 : 0.78 \ TMAOH : 0.2 \ Na_2O : 33 \ H_2O$$

The synthesis mixture was aged at 35 - 40 °C during 24 h prior to the crystallization at 100 °C for 28 h. The zeolite was recovered by filtration and washing with deionized water until the filtrate was pH-neutral, followed by drying at 100 °C. The zeolite was then calcined at 500 °C in a muffle furnace for 3 h.

AIPO-LTA was synthesized following a previously described procedure [460]. Pseudoboehmite (Catapal A SASOL, 75 wt% Al_2O_3), phosphoric acid (85 wt%, Sigma-Aldrich) and water were mixed and the mixture was stirred for 30 min at room temperature. Hydrofluoric acid (50 wt%, Sigma-Aldrich) and hexacosa-4,7,13,16,21,24-diaza-1,10-bicyclo[8,8,8]hexacosane (Kryptofix222, K222, see fig. 3.8) (99 wt%, Sigma-Aldrich) were then successively added. The gel was stirred for 14 h at room temperature. The final gel composition was:
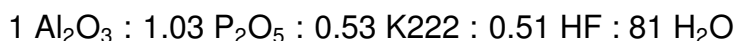
$$1 \ Al_2O_3 : 1.03 \ P_2O_5 : 0.53 \ K222 : 0.51 \ HF : 81 \ H_2O$$

The mixture was transferred to PTFE-lined stainless steel autoclaves and crystallization was carried out at 200 °C for 1 d under static conditions. The product was then filtered off, washed with deionized water until the pH of the filtered liquid was neutral and dried at 100 °C. Calcination was carried out at 600 °C in a tube furnace under dry air flow for 5 h, with a heating ramp of 1 °C/min.
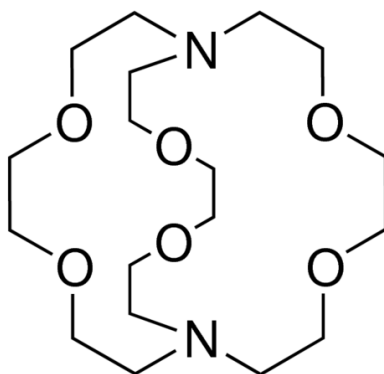
Figure 3.8: *Hexacosa-4,7,13,16,21,24-diaza-1,10-bicyclo[8,8,8]hexacosane, also known as Kryptofix222.*

SAPO-LTA-104, SAPO-LTA-24 and SAPO-LTA-13 were obtained as reported in [52]. Two OSDAs were used separately for synthesizing different materials, i.e. 2,2-Dimethyl-2,3-dihydro-1H-benzo[de]isoquinoline-2-ium (DDBQ, see fig. 3.7b) was used for the synthesis of SAPO-LTA-13 and 4-methyl-2,3,6,7-tetrahydro-1H,5H-pyrido[3.2.1-ij]quinolinium (MTPQ, see fig. 3.7a) was used for synthesizing SAPO-LTA-104 and SAPO-LTA-24. Phosphoric acid (85 wt%, Sigma-Aldrich) was added to the aqueous solution of the respective OSDA hydroxide. Then alumina (75 wt%, Condea Pural) was added and the gel stirred for 5 min at room temperature. Colloidal silica (Ludox AS40, 40 wt%, Sigma-Aldrich) was added, and the mixture was stirred for 20 min. If required, hydrofluoric acid (50 wt%, Sigma-Aldrich) was finally added to the gel, and the resultant mixture was stirred for another 20 min.

For the synthesis of SAPO-LTA-13, DDBQ was used as the OSDA, 5 wt% of previously prepared SAPO-LTA crystals were added as seeds and no HF was used. The final gel composition was:

$$1 \ Al_2O_3 : 0.85 \ P_2O_5 : 0.30 \ SiO_2 : 1.85 \ OSDA : 111 \ H_2O$$

For the synthesis of SAPO-LTA-104 and SAPO-LTA-24, MTPQ was used as the OSDA, and the syntheses gels contained HF, with the respective gel compositions being:

$$1 \ Al_2O_3 : 0.9 \ P_2O_5 : 0.19 \ SiO_2 : 1.9 \ OSDA : 1.9 \ HF : 38 \ H_2O$$

104

$$1 \text{ Al}_2\text{O}_3 : 0.9 \text{ P}_2\text{O}_5 : 0.19 \text{ SiO}_2 : 1.9 \text{ OSDA} : 0.19 \text{ HF} : 38 \text{ H}_2\text{O}$$
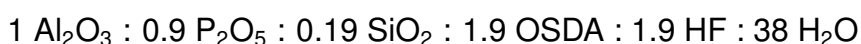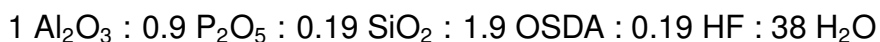
The gels were transferred to PTFE-lined stainless steel autoclaves and heated at 175 °C and under static conditions for 5 d. Crystalline products were filtered off, washed with deionized water until the filtrate had neutral pH and dried at 100 °C. Calcination of the samples was carried out in a tube furnace using a 1 °C/min ramp up to 580 °C under N_2 flow. The temperature was held for 8 h under dry air flow, and finally, the samples were cooled to room temperature under N_2 flow.

3.2.2.6 MFI

Si-MFI-a was synthesized following a recipe reported in the Verified Syntheses of Zeolitic Materials webpage of the IZA Synthesis Commission [63, 461].   Fumed silica (Aerosil 200, Degussa), tetrapropylammnonium bromide (TPABr, 98 wt%, Aldrich), ammonium fluoride (98 wt%, Aldrich) and water were mixed and homogenized in order to form a gel of the following molar composition:

$$1 \text{ SiO}_2 : 0.08 \text{ TPABr} : 1 \text{ NH}_4\text{F} : 20 \text{ H}_2\text{O}$$

The mixture was transferred to PTFE-lined stainless steel autoclaves and heated at 175 °C for 3 d in static conditions. After this time, the zeolite was recovered by filtration, washing with deionized water and drying at 100 °C. The zeolite was then submitted to calcination in a muffle furnace at 550 °C for 3 h.

Si-MFI-b was synthesized following a previously described procedure [462].   TEOS (98 wt%, Merck) was hydrolized in the presence of an aqueous solution of tetrapropylammonium hydroxide (TPAOH, 1M, Aldrich), ethanol (99.5 wt%, Aldrich) and water.   The mixture was homogenized and stirred until a gel of the following composition was obtained:

$$1 \text{ SiO}_2 : 9.7 \text{ EtOH} : 0.25 \text{ TPAOH} : 24 \text{ H}_2\text{O}$$
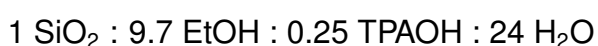
The mixture was transferred to PTFE-lined stainless steel autoclaves and heated at 150 °C for 3 d in static conditions. After this time, the zeolite was recovered by filtration, washing with deionized water and drying at 100 °C. The zeolite was then submitted to calcination in a muffle furnace at 550 °C for 3 h.

3.2.2.7 MTF

Si-MTF was synthesized following a previously described procedure [463]. Hexamethyleneimine (HMI, 99 wt%, Sigma-Aldrich), colloidal silica (Ludox AS-40, 40 wt% SiO_2, Sigma-Aldrich) and water were mixed and the mixture was stirred for 1 h at room temperature. A solution of NH_4F (Sigma-Aldrich) in water was added to the previous mixture. Crystal seeds of previously synthesized Si-MTF were added, comprising a 2.5 mol% of total Si. After homogenization, the final gel composition was:

$$1 \ SiO_2 : 0.5 \ HMI : 0.55 \ NH_4F : 195 \ H_2O$$

The mixture was transferred to PTFE-lined stainless steel autoclaves and crystallization was carried out at 175 °C for 7 d under static conditions. The product was then filtered off, washed with deionized water until the pH of the filtrate was neutral and dried at 100 °C. Calcination was carried out at 900 °C in a muffle furnace for 5 h, with two intermediate steps, one at 350 °C and another at 600 °C lasting 1 h each.
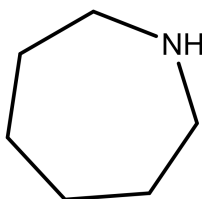
Figure 3.9: *Hexamethyleneimine, also known as 1-azacycloheptane.*

3.2.2.8 RTH

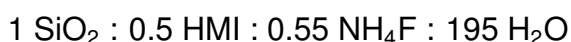**Si-RTH** materials were synthesized following a previously described procedure [464]. TEOS (99 wt%, Aldrich) was hydrolyzed in an aqueous

solution of tri-(2-propyl)-methylphosphonium (Tri2PMP, see fig. 3.10). The mixture was stirred until the ethanol formed upon hydrolysis of TEOS and the appropriate excess of water were evaporated and, finally, an aqueous solution of HF (50 wt%, Sigma-Aldrich) was added to yield a gel of the following composition:

$$1 \; SiO_2 : 0.4 \; Tri2PMP : 0.4 \; HF : 5 \; H_2O$$

The mixture was transferred to PTFE-lined stainless steel autoclaves and crystallization was carried out at 150 °C for 16 d in the case of Si-RTH-a and at 175 °C for 19 d in the case of Si-RTH-b with rotation in both cases. The products were then filtered off, washed with abundant hot deionized water and dried at 100 °C.
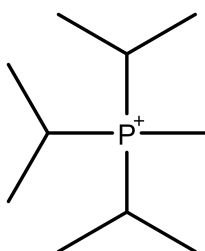
Figure 3.10: *Tri-(2-propyl)-methylphosphonium.*

In order to remove the P-containing OSDA and free the porosity of the materials, these were submitted to subsequent steps of hydrogenation at high temperature and calcination. As-made materials were pelletized and sieved to select particle sizes between 0.1 and 0.8 mm. Hydrogenation was carried out in a tube furnace with the ramp depicted in fig. 3.11 and under a flow of 72 cm^3 STP/min of H_2 and 48 cm^3 STP/min of N_2. After the treatment, the flow was switched to 100 cm^3 STP/min of N_2 and the system was left to cool. Throughout the procedure, the gas flow going out of the tube furnace was stripped through a solution of $Cu(NO_3)_2$ (100 ml, ca. 1 mol/l) in order to prevent harmful phosphines of being released into the atmosphere. The samples Si-RTH-a and Si-RTH-b were recovered as grey solids and the complete removal of the P was verified by means of ICP-OES analysis. The treated samples were further submitted to

calcination in a muffle furnace reaching a 4 h plateau at 700 °C with intermediate steps at 350 °C and 550 °C, each lasting 1 h. The final materials were white.
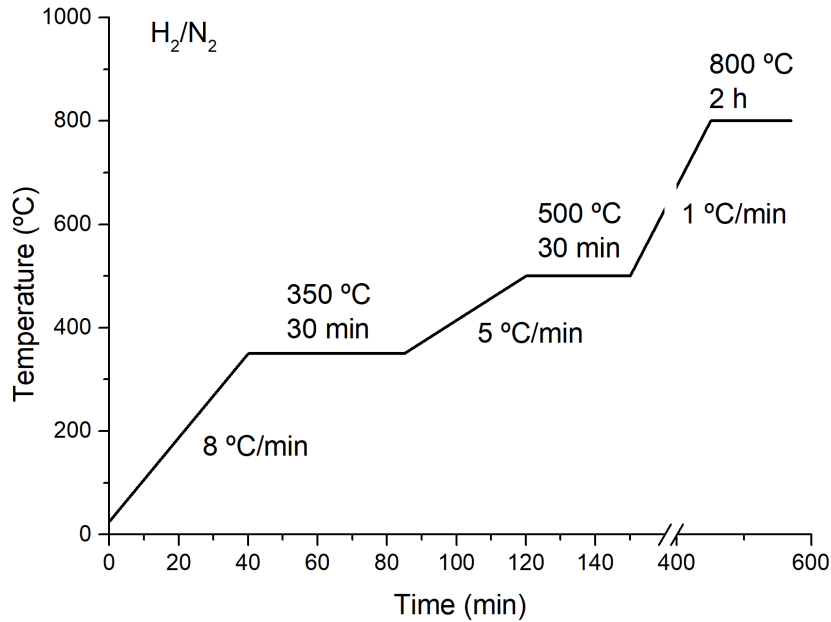
Figure 3.11: *Temperature program used for the hydrogenation of RTH samples.*

3.2.2.9 RWR

Si-RWR samples were synthesized via a previously described procedure, which involves methods apart from hydrothermal synthesis [465–467].

Si-RWR-a was prepared via a two-step procedure. First, the layered silicate Na-RUB-18 was prepared. NaOH (EMSURE), distilled water and fumed silica (Aerosil 200, Sigma-Aldrich) were mixed in the following proportions:

$$1 \; SiO_2 : 2 \; NaOH : 27.2 \; H_2O$$

The mixture was heated at 100 °C for 24 h, yielding a solution of sodium metasilicate (Na_2SiO_3). An extra amount of silica was then added, giving a gel of composition:

$$1 \ SiO_2 : 0.3 \ Na_2SiO_3 : 8.8 \ H_2O$$

The mixture was stirred manually until homogeneity was reached and the resulting gel was transferred to a PTFE-lined stainless steel autoclave and heated at 100 °C during 14 d under static conditions. The obtained solid was filtered, washed with distilled water until neutral pH of the filtrate and dried at room temperature. The obtained Na-RUB-18 sample was then submitted to direct ion exchange with H^+ by suspending it in an aqueous solution (0.06 mol/L) of HCl (Sigma-Aldrich) and stirring for 4 h at room temperature*. The solid was filtered and washed with distilled water until no Cl^- was detected and dried at room temperature. The material was then refluxed in N-methylformamide (Sigma-Aldrich) for 1 h at 180 °C, in a proportion of 2 g in 30 mL of solvent. The resulting suspension was centrifuged, the deposited solids dried at 120 °C. The solid was then calcined at 550 °C in a tube furnace, with a ramp of 2 °C/min under Ar flow (20 cm^3 STP/min), switching to O_2 flow (20 cm^3 STP/min) once the maximum temperature was reached and maintaining these conditions for 6 h.

Si-RWR-b was prepared, too, via a two-step procedure. The layered silicate Na-RUB-18 was prepared through a different method. Colloidal silica (Ludox AS-40, 40 wt% SiO_2, Sigma-Aldrich) was mixed with an aqueous solution of NaOH (Sigma-Aldrich) in the following proportions:

$$1 \ SiO_2 : 0.5 \ NaOH : 7.5 \ H_2O$$

The resulting gel was transferred to a PTFE-lined stainless steel autoclave and heated at 100 °C during 25 - 28 d under static conditions. The obtained solid was filtered, washed with distilled water until neutral pH of the filtrate and dried at room temperature. The obtained Na-RUB-18 sample was then submitted to direct ion exchange with H^+ by suspending it in an aqueous solution (0.1 mol/L) of HCl (Sigma-Aldrich) and stirring for 2 d at room temperature†. The solid was filtered and washed with distilled

---

*The proportions were: 1 g of solid each 100 mL of solution
†The proportions were: 2 g of solid each 100 mL of solution

water until no Cl⁻ was detected and dried at 100 °C. The material was then refluxed in N-methylformamide (Sigma-Aldrich) for 1 h at 180 °C, in a proportion of 2 g in 50 mL of solvent. The solid was filtered, washed with deionized water and dried at 100 °C. Calcination was carried out at 550 °C in a muffle furnace for 6 h.

3.2.2.10 STT

Si-STT was synthesized following a previously described procedure [468]. TEOS (98 wt%, Merck) was added to an aqueous solution of TMAdAOH and the mixture was stirred during the time required to evaporate the ethanol formed during the hydrolysis of TEOS and the excess amount of water. HF (50 wt%, Sigma-Aldrich) was added and the mixture was homogenized. The molar composition of the gel was the following:

$$1 \text{ SiO}_2 : 0.52 \text{ TMAdAOH} : 0.52 \text{ HF} : 10 \text{ H}_2\text{O}$$

The gel was introduced in PTFE-lined stainless steel autoclaves and heated at 150 °C during 13 d with rotation. After this time, the autoclaves were cooled down and the zeolite was recovered by filtration, washing with deionized water and drying at 100 °C. The zeolite was submitted to calcination at 580 °C in a muffle furnace for 3 h.

3.2.2.11 STW

Si-STW was synthesized following a previously described method [469]. TEOS (98 wt%, Aldrich), a hydroxide solution of the dicationic OSDA (see fig. 3.12) and hydrofluoric acid (50 wt%, Sigma-Aldrich) were mixed and homogenized in order to form a gel of the following molar composition:

$$1 \text{ SiO}_2 : 0.25 \text{ OSDA} : 0.5 \text{ HF} : 4 \text{ H}_2\text{O}$$

The mixture was transferred to PTFE-lined stainless steel autoclaves and heated at 175 °C for 7 d with rotation. After this time, the autoclaves were cooled down and the zeolite was recovered by filtration, washed with deionized water and dried at 100 °C. The zeolite was calcined in a muffle furnace at 550 °C for 5 h.
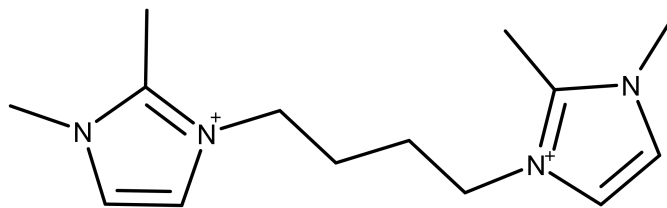
Figure 3.12: *Dicationic imidazolium-based OSDA for the synthesis of Si-STW.*

3.2.3 Characterization results

The characterization of the materials was done partly before (XRD, NMR, TG, SEM) and partly after (XRD, NMR, ICP-OES, SEM, textural analysis) the removal of the OSDAs. The first step after the crystallization of a solid phase is to check if the desired structure has been obtained, if there are impurities and if a highly crystalline materials have been obtained. For this purpose, the as-made material is analyzed by X-Ray-Diffraction prior to calcination. MAS NMR can be used at this stage to study the chemical environment of the framework atoms (^{29}Si, ^{27}Al, ^{31}P) or the integrity of the occluded OSDA (^{13}C). TG can be used to assess the temperature needed for the removal of hydration water and of the occluded organics. Anyhow, the relevant characterization results are the ones obtained after the removal of the OSDA, as this is the final solid that will be used for further experimentation. As said before, XRD is used to confirm the identity of the phase, MAS NMR helps determine the connectivity defects amount and, together with ICP-OES, the framework charge. SEM allows us to determine the crystal size and shape, which may have an important effect on the diffusivity of adsorbates. Finally, the textural characterization gives insight into the crystallinity, pore size and available adsorption surface. The characterization results relevant to each chapter can be found in tables 4.1, 5.1, 6.2, 7.1 and 8.2.

3.3   Adsorption experiments

In order to study the materials' adsorption properties and applicability as adsorbents in separation processes, different types of experiments have been carried out, such as adsorption isotherms, adsorption kinetics and dynamic mixture adsorption experiments.

3.3.1   Gases and vapors used

All the gases used for carrying out adsorption experiments have a purity above 99.995 %.   The vapors had purities above 99.9% and were subjected to freeze-pump-thaw cycles before being used to ensure the absence of gaseous impurities.

3.3.2   Adsorption isotherms of pure compounds

Adsorption isotherms of pure gases have been measured in a set of different devices, depending on the conditions required for the measurement.

A Hiden IGA3 gravimetric device has been used for measuring isotherms of gases and vapors at temperatures between 10 and 60 °C and pressures up to 2000 kPa. The adsorbed amounts are calculated taking into account the flotability of the sample.

A Quantachrome iSorbHP volumetric device has been used to measure adsorption isotherms of permanent gases at temperatures between -196 and 60 °C and pressures up to 5000 kPa. In this case, it is important to define the concept of excess adsorbed amount and excess isotherm, as it will be the standard way of presenting the data. At low temperatures and high pressures, the density of the adsorptive present in the gas phase increases and becomes comparable to that of the adsorbed phase, sometimes even larger. Thus, the adsorption isotherms need to be corrected by subtracting a blank measurement. The result of this correction is the excess isotherm (see fig. 3.13). At temperatures above

0 °C, the blank is negligible and thus, the measured isotherm does not need to be corrected. Excess isotherms may present a maximum excess adsorbed amount and may even decrease to negative excess adsorbed amounts above certain pressures. This happens in cases where the density of the gas phase is larger than that of the adsorbate. Furthermore, to describe the adsorptives at these conditions, the use of real gas equations of state instead of the ideal gas law is necessary. This way, the Helmholtz equation was used to describe H_2 [470], D_2 [471], CO_2 [472], N_2 [473] and CH_4 [474]; and the mBWR-Jacobsen equation was used to describe CO [475] and He [476]. This procedure is automatically performed during data measurement by iSorbHP.
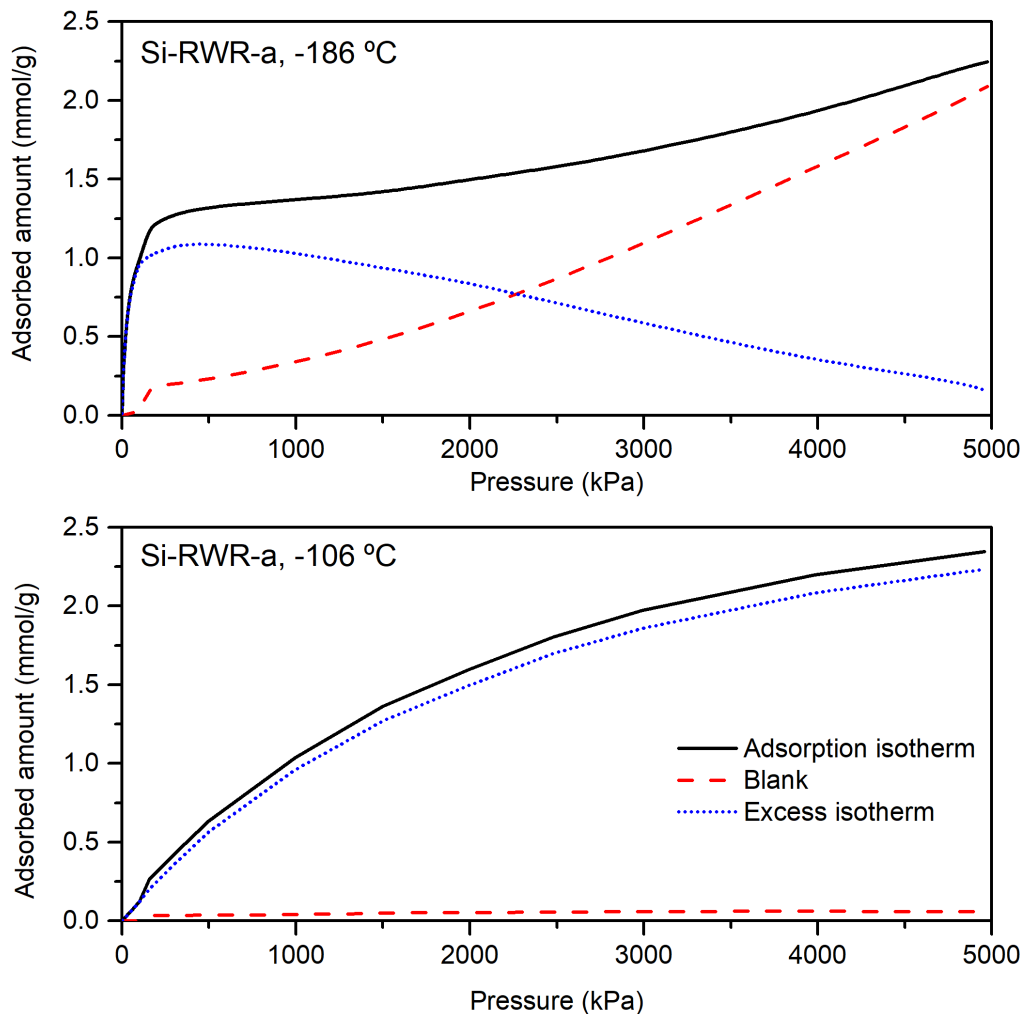

Figure 3.13: *Example of H_2 adsorption isotherms on Si-RWR-a, measured on Quantachrome iSorbHP.*

A Micromeritics ASAP2010 volumetric device has been used to

measure adsorption isotherms of permanent gases at temperatures between 0 and 60 °C and pressures up to 100 kPa.

A Bel BelSorp II Max volumetric device has been used to measure adsorption isotherms of vapors at temperatures between 25 and 60 °C and pressures below 100 kPa.

A VTI SGA 100H gravimetric flow device has been used to measure adsorption isotherms of vapors at 40 °C and pressures below 100 kPa, with N_2 as carrier gas.

Ideal thermodynamic selectivities, also called pure component selectivities, can be calculated from the ratio of adsorbed amounts of different adsorbates at a defined temperature and pressure:

$$\alpha_{a,b}^{eq} = \frac{Q_a\,(P,\,T)}{Q_b\,(P,\,T)} \tag{3.2}$$

Where subindexes "a" and "b" refer to different adsorbates, with "a" usually being the component adsorbed to a greater extent.

3.3.2.1 Fitting experimental isotherms to a model: Langmuir adsorption isotherm

Sometimes, in order to analyse adsorption isotherms more easily, it is useful to find a suitable model to fit the experimental data points. Type I isotherms may be fitted using a variety of equations, such as Langmuir [477], Freundlich [478], Toth [479], Dual-Site-Langmuir or Virial [480]. In this thesis I have only made use of the Langmuir fit for some specific parts of the discussion and thus, I will explain and present it here.

Langmuir derived one of the most fundamental equations in adsorption by considering a kinetic equilibrium of a single substance (fluid phase) on a plane surface (interface with a solid) [477]. The adsorbate gets adsorbed at a rate k_1 and the kinetic equation that describes its adsorption rate v_1 is:

$$v_1 = k_1 P_1 (1 - \Theta) \tag{3.3}$$

Where k_1 is the adsorption rate constant, P_1 is the pressure of the

adsorptive in the fluid phase and Θ is the fraction of occupied adsorption sites or fractional loading and equals Q/Q_{max}. Similarly, the kinetic equation that describes desorption is:

$$v_{-1} = k_{-1}\Theta \tag{3.4}$$

Where v_{-1} is the desorption rate and k_{-1} is the desorption rate constant. By assuming that the equilibrium has been reached, and thus, $v_1 = v_{-1}$ and we get:

$$k_1 P_1 (1 - \Theta) = k_{-1}\Theta \tag{3.5}$$

Which by rearranging turns into:

$$\Theta = Q/Q_{max} = \frac{K_1 P_1}{1 + K_1 P_1} \tag{3.6}$$

Where $K_1 = k_1/k_{-1}$ is the equilibrium constant of the process.

3.3.2.2 Isosteric heat of adsorption

By measuring adsorption isotherms at different temperatures in a certain adsorbate-adsorbent pair, the isosteric heat of adsorption of that compound on said adsorbent can be calculated thanks to the Clausius-Clapeyron relation (eq. (3.7)). The complete process is described below:

1. Measuring adsorption isotherms of a given adsorbate-adsorbent pair at ≥ 3 different temperatures.

2. Fitting the isotherms to an arbitrary model that allows to carry out an interpolation between the measured points. Alternatively, a linear interpolation between each point can be carried out.

3. Obtaining the corresponding pressure (P) values for selected loading/adsorbed amount (Q) values at each temperature (T), i.e. defining the isosteres of the system.

4. Plotting the adsorption isosteres for each value of the adsorbed amount. In this case, P is plotted against $1/T$.

5. Fitting the isosteres to a linear equation, from the slope of which the isosteric heat is obtained according to the Clausius-Clapeyron equation:

$$q_{st} = \left(\frac{\partial \ln P}{\partial \frac{1}{T}} \right)_Q \tag{3.7}$$

6. Plotting the obtained q_{st} values against their corresponding Q values.

The calculated trend of isosteric heat of adsorption against the amount adsorbed gives us information on the system, as explained in fig. 1.7. Furthermore, the value of q_{st} at zero (low) loading, i.e. $q_{st,0}$, is related with the intrinsic strength of the interaction between the adsorbate and the surface of the adsorbent. In order to improve comparability between samples, I have obtained the P values for the isosteres by linear interpolation between experimental points. For avoiding extrapolation issues, $q_{st,0}$ has been approximated as the q_{st} corresponding to the lowest adsorbed amount measured for said system.

3.3.3 Adsorption kinetics of pure compounds

The kinetics of adsorption of pure compounds in different adsorbents has been assessed by carrying out uptake rate measurements. In these measurements, which can be carried out in volumetric and gravimetric adsorption systems, a fresh sample is used and the pressure of the desired adsorptive in the system is (rapidly*) increased from vacuum to a defined value that is afterwards kept constant or varies only slightly. The adsorbed amount is recorded against time. The uptake curve obtained is then fitted with the solution of the transient diffusion equation assuming micropore diffusion control and spherical particles (see eq. (3.8), [162, 481]).

$$\frac{Q_t}{Q_\infty} = 1 - \frac{6}{\pi^2} \sum_{n=1}^{\infty} \frac{1}{n^2} \exp\left(-\frac{n^2 \pi^2 D t}{r^2} \right) \tag{3.8}$$

---

*If the dosing time required for reaching the desired pressure is longer than the time needed for reaching the equilibrium in the system, the study of diffusion will not be possible using this technique.

Where Q is the loading, t is the time, n is the number of terms of the solution, D is the diffusion coefficient and r is the radius of the particle. The only fittable parameter is the diffusional time constant, which equals the quotient D/r^2. I have taken 20 terms of n for obtaining experimental diffusional time constants. This approach is an approximation, as most of the materials of this thesis do not present spherical shape, but it is generally accepted as a good approximation to compare the diffusivities of different materials. In the analysis of Si-RWR data, the solution for slab-shaped particles was used, as well, but it did not provide a better fit nor a considerably different value of the diffusional time constant. Furthermore, in order to be able to compare, in the cases where equilibrium had not been reached, the highest value of adsorbed amount recorded is taken as the equilibrium loading. Ideal kinetic selectivities or separation factors can be calculated from the ratio of diffusional time constants of different adsorbates at a defined temperature and pressure:

$$\alpha_{a,b}^{kin} = \frac{D_a\,(P,\,T)}{D_b\,(P,\,T)} \tag{3.9}$$

Where subindexes "a" and "b" refer to different adsorbates, with "a" usually being the fastest adsorbed component.

3.3.4 Dynamic mixture adsorption experiments

In order to test the materials in conditions similar to those in a real separation system, dynamic mixture adsorption experiments, i.e. breakthrough adsorption experiments, have been carried out. In these experiments, the adsorbent is placed in a fixed bed or column and, after activation under inert gas flow and at high temperature, it is exposed to a flow of an adsorptive or mixture of adsorptives. The concentration/molar flow at the exit of the column is recorded against time (see fig. 3.14). From the concentration/molar flow profile, thermodynamic and kinetic parameters can be obtained. The experimental devices used in this thesis and the corresponding data analysis are explained in the following

sections.
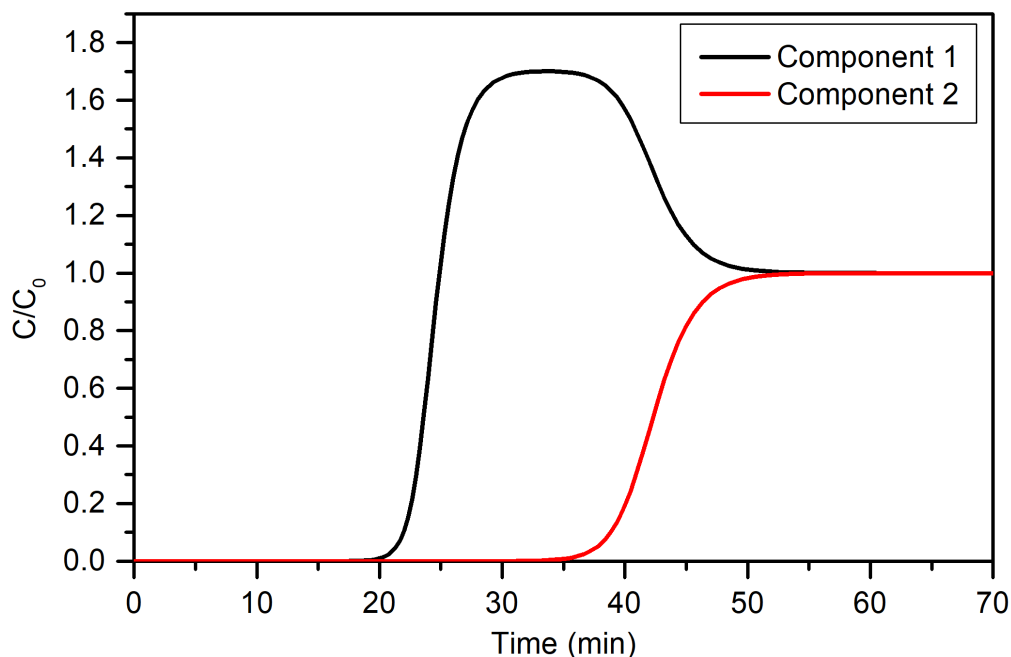
Figure 3.14: *Example of a breakthrough profile of a binary mixture of compounds on an adsorbent that preferably adsorbs compound 2.*

3.3.4.1 Setup for permanent gases separation

Breakthrough experiments of permanent gases (CO_2 and CH_4) were carried out on a device developed at the ITQ, a scheme of which is depicted below (fig. 3.15).

In a typical experiment, a stream (25 cm^3 STP/min) of either pure CO_2, CH_4 or mixtures of those was passed through a bed of fresh adsorbent and the outcome of the bed was analysed with a Coriolis mass flow meter (MFM) and a mass spectrometer (MS), sequentially. Argon (ca. 300 cm^3 STP/min) was used as dilution/makeup gas at the exit of the bed, just before the MS and helium was used as a regeneration gas. The said mixtures of CO_2 and CH_4 have compositions analogous to both natural and landfill gas (20:80 CO_2/CH_4 and 50:50 CO_2/CH_4, respectively). A constant mass of adsorbent was used for the different samples (ca. 0.65 g). The adsorbent particle size was of 0.2-0.4 mm and it was diluted with SiC of larger particle size (0.6 - 0.8 mm) in order to adjust the bed
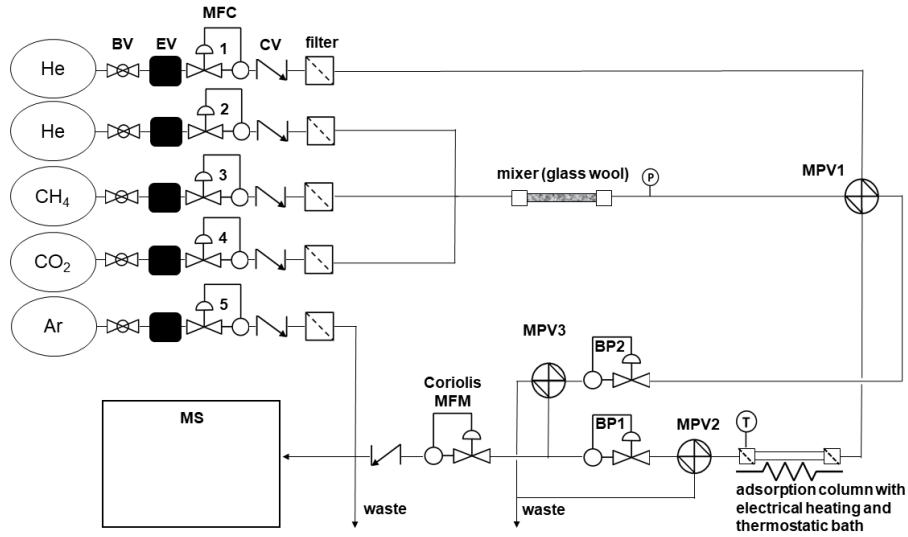
Figure 3.15: *Scheme of the breakthrough experiments setup for permanent gases developed at the ITQ.*

length properly to values between 11 and 13 cm. These experiments were carried out at 25 °C and at pressures relevant to this separation, i.e. between 200 and 700 kPa. The temperature was kept constant using an isothermal bath and the pressure was kept constant using backpressure regulators (BP). At the end of the adsorption experiments, A He flow of 25 cm³ STP/min) was used to isothermally regenerate the adsorption bed for 20 min. After that time, the temperature of the bed was increased still under He flow at ca. 2 °C/min up to 400 °C.

The breakthrough experiments data were analyzed following procedures described previously [265, 482, 483] and adapting them to this case. The equations used to calculate the adsorbed amount of component "i" at the equilibrium, $Q_{i,eq}$, were:

$$Q_{i,eq} = \frac{\dot{n}_0 y_{i,0} \tau_i - \dfrac{\epsilon V_{bed}}{RT} P y_{i,0} - n_d}{m_{ads}} \tag{3.10}$$

Where $\dot{n}_0$ is the total inlet molar flow, $y_{i,0}$ is the molar fraction of component "i" in the feed stream, ϵ is the void fraction or voidage of the adsorbent bed, calculated as described in [484], V_{bed} is the volume of the adsorbent bed, R is the ideal gas constant, T is the temperature (in K), P is the

119

pressure in the column, n_d is a term that takes into account the amount of adsorptive accumulated in the dead volume of the system and will be discussed below and m_{ads} is the adsorbent mass. The first moment of a component τ_i has units of time and can be understood as a mean residence time in the bed. In systems with only 1 component, it equals its average breakthrough time. It is calculated as:

$$\tau_i = \int_0^{t_\infty} \left(1 - \frac{y_i \dot{n}}{y_{i,0} \dot{n}_0} \right) dt \tag{3.11}$$

Where t_∞ is a time value above the equilibration time, y_i is the molar fraction of component i at the exit of the column and $\dot{n}$ is the total molar flow at the exit of the column. This integral was calculated numerically by using the trapezoidal rule, i.e.:

$$\tau_i = \sum_{j=0}^{k-1} \frac{\left(1 - \frac{y_{i,j} \dot{n}_j}{y_{i,0} \dot{n}_0} \right) + \left(1 - \frac{y_{i,j+1} \dot{n}_{j+1}}{y_{i,0} \dot{n}_0} \right)}{2} \left(t_{j+1} - t_j \right) \tag{3.12}$$

Where k is the total number of experimental data points and corresponds to a time value above equilibration time, and j is the number of the experimental point. On the other hand, the term n_d from eq. (3.10) is necessary for a more precise calculation of the adsorbed amount in this case. The column is a stainless steel tube with 2 mm of internal radius and 46.4 cm height. It is filled only partially with the adsorbent bed (ca. 12 cm height), while the rest is filled with SiC beads of sizes between 0.6 and 0.8 mm. Thus, there is 1) a dead volume $V_{d,1}$ which includes the dead volumes between MPV1 and the adsorbent bed and between the adsorbent bed and BP1 and the pressure of which is defined by BP1 and 2) a dead volume $V_{d,2}$ between BP1 and the checkvalve (CV) after the Coriolis MFM, which is at a pressure P_{out} corresponding to the atmospheric pressure plus the pressure drop due to MFM and the CV (ca. 160 kPa). The dead volume between this checkvalve and the mass

spectrometer is considered negligible.

$$Q_{i,eq} = \frac{\dot{n}_0 y_{i,0} \tau_i - \dfrac{\epsilon V_{bed}}{RT} P y_{i,0} - \dfrac{V_{d,1}}{RT} P y_{i,0} - \dfrac{V_{d,2}}{RT} P_{out} y_{i,0}}{m_{ads}} \qquad (3.13)$$

The values of $V_{d,1}$ and $V_{d,2}$ were determined by measuring the time t_d needed for pressurizing the system with He from 200 to 700 kPa at a known molar flow, installing a plug either after BP1 or after the checkvalve, respectively. In this case, instead of the adsorbent bed, 12.5 cm of the column were left empty. The dead volumes were calculated as:

$$V_{d,1} = \frac{\dot{n}_0 \, t_{d,BP1}}{\Delta P} RT - V_{bed} \qquad (3.14)$$

$$V_{d,2} = \frac{\dot{n}_0 \, t_{d,CV}}{\Delta P} RT - V_{d,1} - V_{bed} \qquad (3.15)$$

Once the adsorbed amounts are obtained, the real mixture selectivity can be calculated according to:

$$\alpha_{a,b}^{mix,eq} = \frac{Q_a / y_a}{Q_b / y_b} \qquad (3.16)$$

The performance of different materials in the separation of CO_2 from CH_4 was analyzed in terms of said mixture CO_2/CH_4 selectivities, adsorbent productivity and purity and recovery of both adsorbates [168]. These were presented in section 1.2.2. Taking into account that my dataset implies that regeneration is carried out at least partly isothermally after reaching equilibrium and under He flow, it can be assumed that these experiments are a laboratory analogue of a single bed PSA/TSA process comprising 3 steps:

1. **Adsorption:** The mixture is flown through a clean bed of adsorbent and both components are adsorbed to some extent. The more strongly adsorbed component (CO_2) is adsorbed to a greater extent and displaces part of the more weakly adsorbed component (CH_4). This results in a product stream enriched in the more weakly

adsorbed compound coming out of the column (product 1). In this case, and following natural gas specifications, the purity of that methane-rich product needs to be $> 97\%$ [485], and that defines the duration of that step. Before the overall composition of the effluent is $\leq 97\%$ CH_4, the step of adsorption is finished.

2. **Recycle:** Once the methane-enriched product's purity standard cannot be met anymore (product 2), the stream coming out of the column is recycled to the front of the bed. Product 2 is still enriched in CH_4 with respect to the original feed, and thus, by recycling it the overall CH_4 productivity of the process is increased. This step ends when equilibrium is reached and the adsorbed amount of any component does not vary anymore.

3. **Desorption:** After equilibrium is reached, the bed is regenerated by:

   (a) Countercurrent displacement of the equilibrated gas phase.

   (b) Flowing an inert gas* and/or decreasing pressure during 20 min.

   (c) Increasing temperature to desorb strongly adsorbed species, if necessary.

   A stream is obtained that is enriched in CO_2, i.e. product 3 (He is disregarded).

   For the sake of simplicity, step 2 is not considered in the calculation of the relevant parameters. For the same reason, countercurrent displacement/depressurization of the gas phase at the beginning of step 3 is assumed to be immediate and to result in the complete recycle of the adsorptives present in the gas phase. Steps 1 and 2 are isothermal and step 3 may be isothermal, too, if after < 20 minutes of He flow regeneration is complete. Steps 1-3 are realized at constant pressure.

---

*Flowing He has the same effect as reducing the pressure of the adsorptives in the bed, i.e. reducing their partial pressure.

This is only a way of extrapolating the experimental data to a real process, in order to compare the materials from a practical perspective. Obviously a process comprising more that 1 bed and more steps would be much better integrated. Also, it would probably not be necessary to wait until equilibration to start the regeneration step.

For calculating the adsorbent productivity ($\overline{Prod}$) referred to pure methane processed, I integrated numerically (trapezoidal rule) the methane flow over the duration t_1 of step 1 and divided it by the amount of adsorbent and the duration of the whole cycle (t_{cycle}).

$$\overline{Prod} = \frac{\int_0^{t_1} \dot{n}_{CH_4}\, dt}{m_{ads}\, t_{cycle}} \tag{3.17}$$

Where t_1 was determined by integrating the CH_4 molar flow until the composition of the total effluent was just above 97% methane and taking that as t_1. The cycle time t_{cycle} was obtained by adding the durations of steps 1, 2 and 3, in which t_2 was determined by visual examination of the breakthrough curve (ends when $\dot{n} = \dot{n}_0$ for both components) and t_3 was 20 min or less, ending when $\dot{n} = 0$ for both components. If after reaching 0, the increase of the temperature after 20 min lead to $\dot{n} \neq 0$ for either CO_2 or CH_4, t_3 was considered equal to 20 min and the temperature needed for complete regeneration was written down.

The recovery of methane was calculated as the fraction of CH_4 that is obtained as part of product 1 divided by the sum of that plus CH_4 that is discarded along with product 3:

$$\overline{R}_{CH_4} = \frac{\int_0^{t_1} \dot{n}_{CH_4}\, dt}{\int_0^{t_1} \dot{n}_{CH_4}\, dt + Q_{CH_4,eq} m_{ads}} \tag{3.18}$$

Where $Q_{CH_4,eq}$ is obtained from eq. (3.13). As explained above, the amount of methane present in the gas phase is assumed to be recycled and disregarded for the sake of simplicity.

The recovery of carbon dioxide was calculated as the fraction of CO_2 that is obtained as part of product 3 divided by the sum of that plus CO_2

that is discarded along with product 1:

$$\overline{R}_{CO_2} = \frac{Q_{CO_2,eq} m_{ads}}{\int_0^{t_1} \dot{n}_{CO_2}\, dt + Q_{CO_2,eq} m_{ads}} \tag{3.19}$$

Where $Q_{CO_2,eq}$ is obtained from eq. (3.13). The CO_2 purity in product 3 is calculated as:

$$\overline{Pur}_{CO_2} = \frac{Q_{CO_2,eq}}{Q_{CH_4,eq} + Q_{CO_2,eq}} \tag{3.20}$$

The calculated values of productivity, recovery and purity are orientative and intended to serve as an aid in the comparison between different adsorbents.

3.3.4.2 Setup for vapor phase separation

Breakthrough experiments of vapor mixtures (butanol, ethanol, acetone and water) were carried out on a device developed at the Vrije Universiteit Brussel's Department of Chemical Engineering, a scheme of which is depicted below (fig. 3.16).
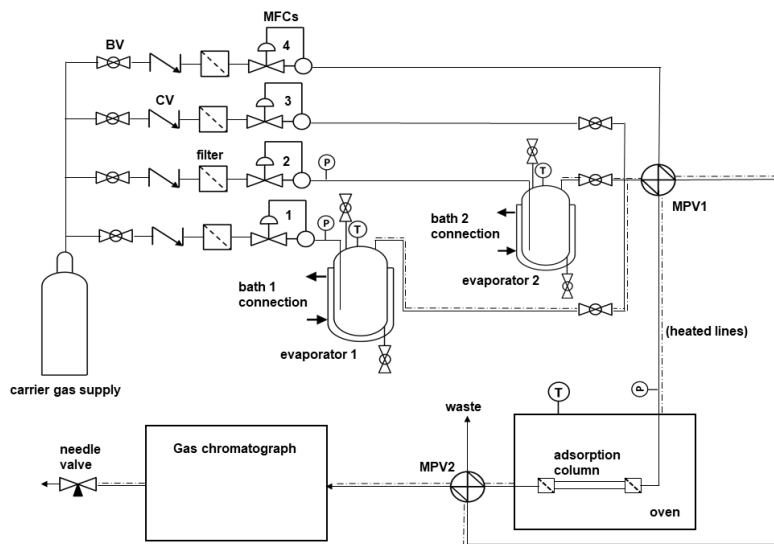

Figure 3.16: *Scheme of the breakthrough experiments setup for vapors developed at the VUB.*

The carrier gas (either He or CO_2) is dosed into the system through 4 different MFCs. MFCs 1 and 2 dose the carrier gas into the evaporators

1 and 2, respectively. Through MFC3, the carrier gas is used to dilute the stream coming out of the evaporators. MFC4 is used in the regeneration step. The pressure in the evaporators is measured upstream of them and their temperature is set thanks to a thermostatic bath. A first MPV allows for either pure carrier gas coming from MFC4 or the vapor-containing stream to flow through either the adsorption column or the bypass. The pressure in the column is measured just before it, and the temperature is set constant (40 - 200 °C) by placing it inside an oven. A second MPV directs the flow coming from either the column or the bypass to either the gas chromatograph (GC) or the waste. After the GC, a needle valve is used to equal the pressure before and after the column at the beginning of the experiment. All the tubing through which vapor is going to flow is heated at 60 °C.

An Agilent 6890N GC was used for analyzing the stream coming out of the experimental setup. This GC is equiped with an automatic gas injection valve which injects 1 ml of sample at selected time intervals. A Stabilwax® capillary column with 15 m in length, an internal diameter of 250 μm and a solid phase with 0.5 μm thickness was used. Detection was done either by a flame ionization detector (FID), which only detects flammable compounds and a thermal conductivity detector (TCD), which detects changes in thermal conductivity. The TCD is more generic despite its lower detection limit and precision.

The columns used were 10 cm long and had an internal diameter of 2.16 mm. The materials used as adsorbents were pelletized and sieved to achieve a particle diameter d_p between 0.25 mm and 0.425 mm. Approximately 0.1 g of each sample was introduced in different columns. Before starting any experiment, the column is regenerated at 200 °C under He flow. After regeneration, the temperature in the oven is set as desired. Meanwhile, the feed stream composition is left to stabilize and checked by flowing it through the bypass and the GC. Once stabilized, MPV2 is switched for the GC to receive the flow from the column and the feed stream to go to waste. At this stage, the carrier gas is flowing through

Table 3.1: Composition of the fermentor liquid and vapor phases at the end of the fermentation process, as simulated by Van der Perre et al (see supplementary information of [398]).

Component	Concentration (g/L)	Pressure (Pa)	Ratio to ethanol
Acetone	7.04	146	4
Butanol	13.75	215	6
Ethanol	2.56	37	1
Butyric acid	0.39	< 0.7	-
Acetic acid	0.38	< 0.4	-
Glucose	14.5	0	-
Water	960.69	5572	150

the column from MFC4 and the pressure downstream of the column is regulated using the needle valve after the GC. At this point the experiment may be started by switching the MPV1 so that the feed stream flows through the column.

The experimental feed stream used for these experiments had a composition representative of the fermentor overhead vapor phase (see table 3.1). For this purpose, the temperature, pressure, and carrier gas flow in the evaporators needs to be carefully set. A liquid mixture of acetone, butanol and ethanol in molar proportions 1:50:1 (see table 3.2) of was placed in evaporator 1 at 30 °C and pure water was placed in evaporator 2 at 35 °C. The carrier gas flow was set at 2.2 and 6.4 cm^3 STP/min, respectively. A dilution flow of 6.5 cm^3 STP /min of carrier gas was sent through the MFC3 to prevent oscillation of the signal due to condensation of the vapors in cold spots that may be present in the tubing despite the heated lines.

The partial pressures of each component in the evaporator overhead presented in table 3.2, i.e. $P_{v,i}$, were calculated using Raoult's law (eq. (3.21)):

$$P_{v,i} = P^0_{v,i} x_{l,i} \qquad (3.21)$$

Table 3.2: *Temperature, carrier gas flows and amounts of compounds present in each evaporator.*

Evaporator	T (°C)	Carrier gas flow rate (cm³ STP/min)	Compound	m (g)	P_v (Pa)	Ratio to ethanol
1	30	2.2	Acetone	1.72 ± 0.02	105.2 ± 1.4	3.4
			Butanol	138.2 ± 0.4	175.6 ± 0.2	5.7
			Ethanol	2.31 ± 0.02	30.7 ± 0.3	1.0
2	35	6.4	Water	-	2377.3 ± 0.6	77.4

Table 3.3: *Parameters used for the calculation of the vapor pressure of compounds relevant to the ABE fermentation using the Wagner's equation.*

Compound	a	b	c	d	T_c (K)	P_c (bar)
Water	-7.77224	1.45684	-2.71942	-1.41336	647.3	220.5
Acetone	-7.55098	1.60784	-1.9944	-3.2002	508.1	47.02
Butanol	-8.40615	2.2301	-8.2486	-0.711	563.05	44.24
Ethanol	-8.68587	1.17831	-4.8762	1.588	513.92	61.32

In which $x_{l,i}$ is the molar fraction of component "i" in the liquid mixture. The vapor pressures of the pure components $P^0_{v,i}$ at the desired temperature were calculated using Wagner's equation (see eq. (3.22), [486]) and the corresponding parameters, listed in Appendix A, Section D of ref. [487] and summarized in table 3.3.

$$\ln P^0_{v,i} = \ln P_{c,i} + \frac{T_{c,i}}{T} \left(a\tau + b\tau^x + c\tau^y + d\tau^z \right) \tag{3.22}$$

Where $P_{c,i}$ is the critical pressure of the component, $T_{c,i}$ is a parametric critical temperature, which may differ from the real value, τ is $1 - T/T_{c,i}$ and a, b, c and d are parameters, the values of which are presented in table 3.3 for acetone, butanol, ethanol and water. Exponents x, y and z equal 1.5, 2.5 and 5 for the organic vapors and 1.5, 3 and 6 for water.

The flow going into the column $\dot{n}_0$ is the sum of flows coming out of the evaporators 1 $\dot{n}_{out,1}$ and 2 $\dot{n}_{out,2}$ and the MFC3 $\dot{n}_{MFC3}$:

$$\dot{n}_0 = \dot{n}_{out,1} + \dot{n}_{out,2} + \dot{n}_{MFC3} \tag{3.23}$$

To calculate the molar flow of each component i, $\dot{n}_{i,out}$, going out of each evaporator (see fig. 3.17) steady state is assumed to have been reached and thus the carrier flow coming in, $\dot{n}_{c,in}$, and going out, $\dot{n}_{c,out}$, of the evaporator are equal:

$$\dot{n}_{c,in} = \dot{n}_{c,out} = \dot{n}_{out} - \sum_{i=1}^{n} \dot{n}_{i,out} \tag{3.24}$$

With $\dot{n}_{out}$ being the total flow coming out of the evaporator and $\sum_{i=1}^{n} \dot{n}_{i,out}$ the sum of flows of vapors of different compounds coming out of the evaporator. Furthermore, for the flow to be constant, the pressure before $P_{c,in}$ and inside the evaporator overhead P_{head} need to be equal. Assuming the pressure drop is negligible and that the vapor phase in the overhead is in equilibrium with the liquid phase:

$$P_{c,in} = P_{head} = P_{c,ev} + \sum_{i=1}^{n} P_{v,i} \tag{3.25}$$

Where $P_{c,ev}$ is the carrier partial pressure inside the evaporator and $\sum_{i=1}^{n} P_{v,i}$ is the sum of vapor pressures inside the evaporator.
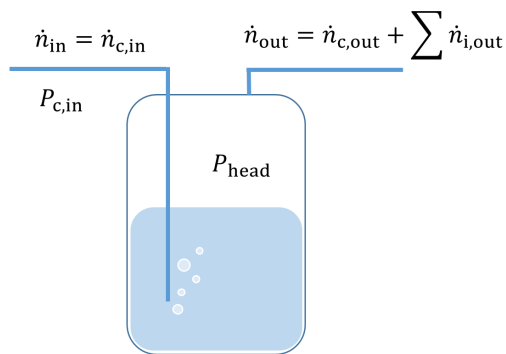

Figure 3.17: *Scheme of the evaporator used for the breakthrough setup at the VUB.*

The molar fractions in the gas phase of each vapor component y_i and the carrier y_c can be defined according to their pressures or flows indistinctly, as:

$$y_i = \frac{\dot{n}_{i,out}}{\dot{n}_{out}} = \frac{P_{v,i}}{P_{head}} \tag{3.26}$$

$$y_c = \frac{\dot{n}_{c,out}}{\dot{n}_{out}} = \frac{P_{c,ev}}{P_{head}} \qquad (3.27)$$

By combining equations 3.26 and 3.27 as a quotient and taking into account the steady state condition presented in eq. (3.24), one obtains:

$$\frac{y_i}{y_c} = \frac{P_{v,i}}{P_{c,ev}} = \frac{P_{v,i}}{P_{head} - \sum_{i=1}^{n} P_{v,i}} = \frac{\dot{n}_{i,out}}{\dot{n}_{c,out}} = \frac{\dot{n}_{i,out}}{\dot{n}_{c,in}} \qquad (3.28)$$

Which can be transformed into:

$$\dot{n}_{i,out} = \dot{n}_{c,in} \frac{P_{v,i}}{P_{head} - \sum_{i=1}^{n} P_{v,i}} \qquad (3.29)$$

$$\dot{n}_{out} = \dot{n}_{c,in} \frac{P_{head}}{P_{head} - \sum_{i=1}^{n} P_{v,i}} \qquad (3.30)$$

Thus allowing us to calculate the total and individual molar flows going out of the evaporators and into the column. The composition of the feed can be calculated from the individual flows.

The breakthrough curves were analyzed to obtain the adsorbed amounts of the different components of the mixture. The first moment τ_i was calculated according to eq. (3.31). In this case the diluted stream allows for integrating molar fractions/concentrations instead of flows, and the total flow is considered to be constant and equal at the inlet and exit of the column. This integration was done numerically, using again the trapezoidal rule.

$$\tau_i = \int_0^{t_\infty} \left(1 - \frac{y_i}{y_{i,0}} \right) dt \qquad (3.31)$$

Furthermore, the dead volumes were negligible and the adsorbed amount expression becomes simpler:

$$Q_{i,eq} = \frac{\dot{n}_0 y_{i,0} \tau_i}{m_{ads}} \qquad (3.32)$$

After some experiments, desorption data were obtained by flowing pure carrier gas (He in most cases) at 40 °C during 20 min and then increasing the temperature at 1 °C / min to 120 °C. This temperature was kept for 5 h and finally, it was increased at 1 °C / min ramp to 200 °C and kept at that

temperature for 2 h to ensure complete regeneration. These desorption data were used for calculating butanol recoveries and purities, similarly to what was done previously by Van der Perre et al [398]. 1-Butanol (BuOH) recovery was calculated as:

$$\overline{R}_{BuOH} = \frac{\int_{t_1}^{t_{reg}} \dot{n}_{BuOH}\, dt}{\int_{0}^{t_{reg}} \dot{n}_{BuOH}\, dt} \tag{3.33}$$

Where t_1 is the time at which the butanol-rich product starts to be collected and t_{reg} is the time at which regeneration of the column is complete. Thus, the divisor in eq. (3.33) is fixed and comprises the whole regeneration step. The product composition, and more specifically the purity of this product referred to the molar fraction of butanol may be calculated by dividing the desorbed amount of the compound of interest between the sum of desorbed amounts:

$$\overline{Pur}_{BuOH} = \frac{\int_{t_1}^{t_{reg}} \dot{n}_{BuOH}\, dt}{\sum_{i} \int_{t_1}^{t_{reg}} \dot{n}_{i}\, dt} \tag{3.34}$$

Chapter 4

Zeolite Si-RWR for the separation of light gases

The separation of hydrogen isotopes and the purification of hydrogen are processes of high industrial importance and scientific interest (see sections 1.3.2 and 1.3.1).

Improvements in the separation of hydrogen isotopes could lead to an easier reduction of the volume of radioactive waste in nuclear plants and a more economic production of these compounds [199, 205, 206]. Quantum sieving by microporous materials has been widely studied as a way to separate H_2 from D_2 and T_2 using different kinds of adsorbents [201]. Small pore zeolites with pore openings below 4.1 Å are promising for this purpose [199, 230, 240, 241].

Furthermore, the purification of H_2 from steam methane reformer off-gas (SMROG, a mixture of H_2, CO, CO_2, CH_4 and N_2, as presented in section 1.3.3), and more specifically, its separation from mixtures containing CO_2 and/or CO is of high importance in the production of highly pure hydrogen. In this case, PSA units using zeolite 5A as the adsorbent are state-of-the-art [184], and research is more focused on improving the process rather than the adsorbent [188]. However, finding new adsorbents which can carry out a separation is always positive and may be advantageous for future applications.

Pure silica RWR zeolite consists of a 1-D (2-D, but non-intersecting)

channel system with 8R openings with elliptical cross-section and perpendicular dimensions of 2.8 and 5.0 Å (see figs. 4.1 and 4.2).
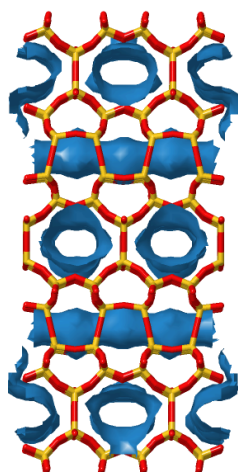

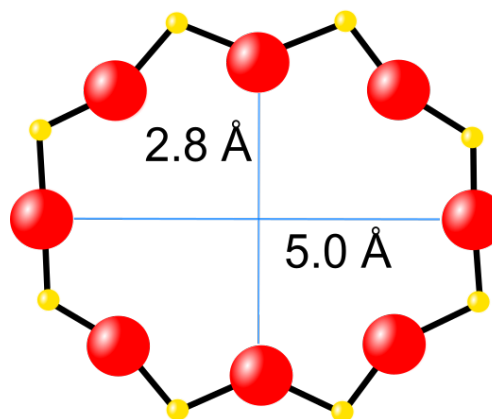**Figure 4.1:** *Channel system of Si-RWR.*

Figure 4.2: *Schematic representation of the pore opening of Si-RWR.*

The topology of this structure is channel-like. The small elliptic pore openings point at the possibility of this material presenting a molecular sieving effect of very small molecules, which is the reason why its adsorption properties of H_2, D_2, CO, N_2, CO_2 and CH_4 are studied here (see table 1.1) with special focus on the separation of hydrogen isotopes (section 4.2) and the purification of hydrogen from SMROG (section 4.3).

The adsorption properties have been studied by measuring and analyzing adsorption isotherms and kinetics data. The loadings displayed in the adsorption isotherm plots correspond to excess adsorbed amounts which have been corrected taking into account blank adsorption measurements (see section 3.3.2). Pure component selectivities were calculated from the isotherms, as well as isosteric heats of adsorption, when possible. Diffusional time constants were obtained and, additionally, a qualitative comparison of the kinetic measurements has been established.

4.1 Characterization of Si-RWR samples

Two samples of Si-RWR were used for this study, namely Si-RWR-a and Si-RWR-b. They were characterized by XRD (fig. 4.3), NMR(fig. 4.4), SEM(fig. 4.5) and CO_2 adsorption at 0 °C, the results of which are summarized in table 4.1.

Table 4.1: *Characterization results of the Si-RWR samples after removal of occluded species.*

Sample	Si defects amount (% Q_3)	Crystal shape	Crystal dimensions (μm)	DA surface area (m²/g)
Si$-$RWR$-$a	1	sheets	$a \times a \times b$ ($1 < a < 6$; $b = 0.1$)	180
Si$-$RWR$-$b	0	sheets	$a \times a \times b$ ($0.5 < a < 2$; $b = 0.1$)	304

As can be seen from the table and figs. 4.4 and 4.5, the samples differ in their crystal size and the amount of connectivity defects. The extremely narrow pores of these samples made it impossible to measure adsorption isotherms of Ar at -186 °C or N_2 at -196 °C due to the very slow diffusion and thus, CO_2 isotherms at 0 °C were used to obtain the Dubinin-Astakhov (DA) surface area. Sample Si-RWR-b apparently presents a larger DA surface area, but it is probably due to kinetic hindrances in Si-RWR-a, as will be discussed below.

The normalized diffractograms of both samples are presented in fig. 4.3. Si-RWR-b presents much lower intensities than Si-RWR-a and broader peaks. These observations may be explained by a smaller size of the crystalline domains in Si-RWR-b, which in turn leads to a lower crystalline order at a large scale, i.e. a lower crystallinity. This is coherent with the crystal size obtained by visual examination of the SEM images (see fig. 4.5). Additionally, a slight increase in the baseline from 22 to 32° is observed in the diffractogram of Si-RWR-b in comparison to Si-RWR-a, which could be due to a small amount of amorphous silica present
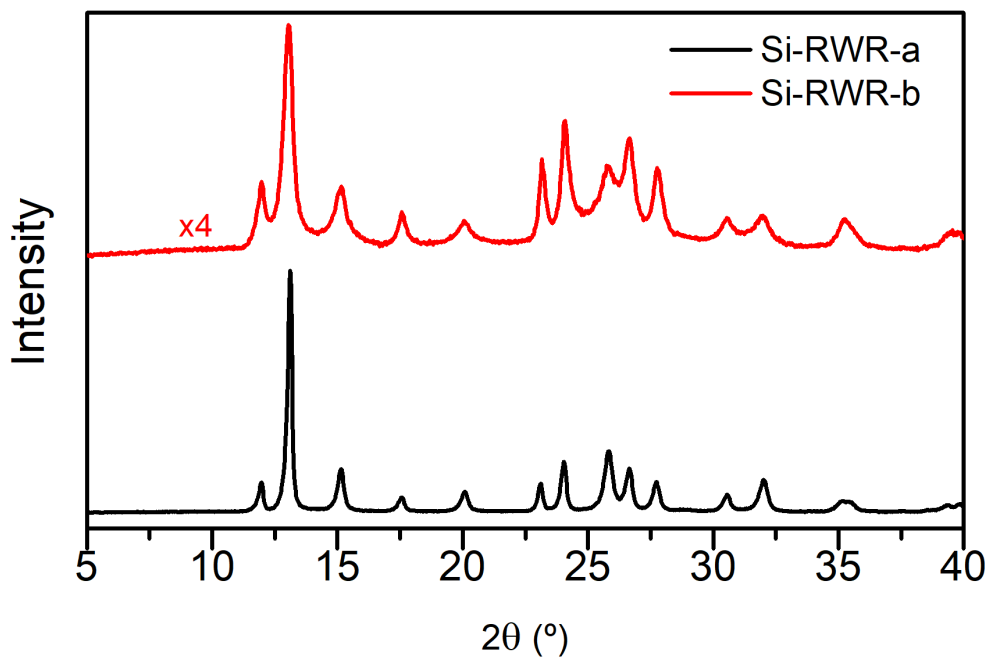
Figure 4.3: *X-Ray diffractograms of Si-RWR samples.*

in the former. Nonetheless, this was not observed by SEM and thus, cannot be confirmed. The ^{29}Si MAS NMR spectra are notably different, in which the resonances can be more easily differentiated in Si-RWR-a. None of the samples present a significant amount of connectivity defects. However, the better resolution of the spectrum of Si-RWR-a confirms that this sample possesses a higher degree of crystalline order than Si-RWR-b.
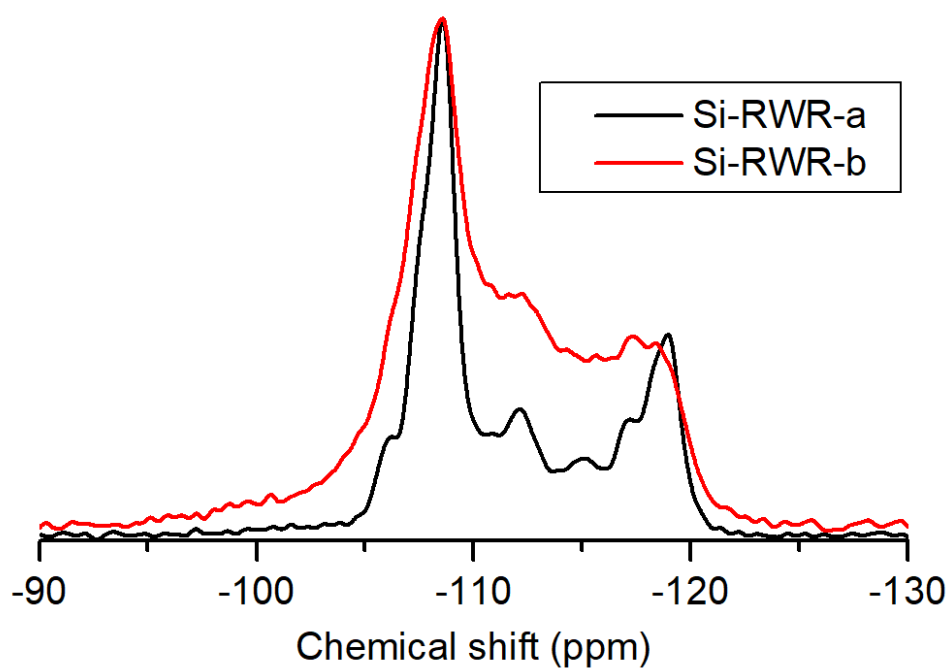
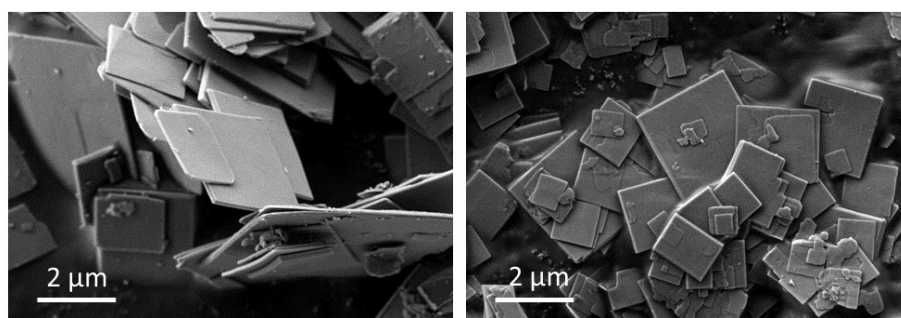**Figure 4.4:** ^{29}Si MAS NMR spectra of Si-RWR samples.

Figure 4.5: SEM images of Si-RWR samples. On the left, Si-RWR-a, on the right, Si-RWR-b.

4.2   Separation of hydrogen isotopes

The adsorption of H_2 and D_2 and the possibility of separating them using Si-RWR materials was studied by measuring their adsorption isotherms (-196 to -106 °C, up to 5000 kPa, see fig. 4.6) and kinetics (-196 to -106 °C, at 500 kPa, see fig. 4.9).

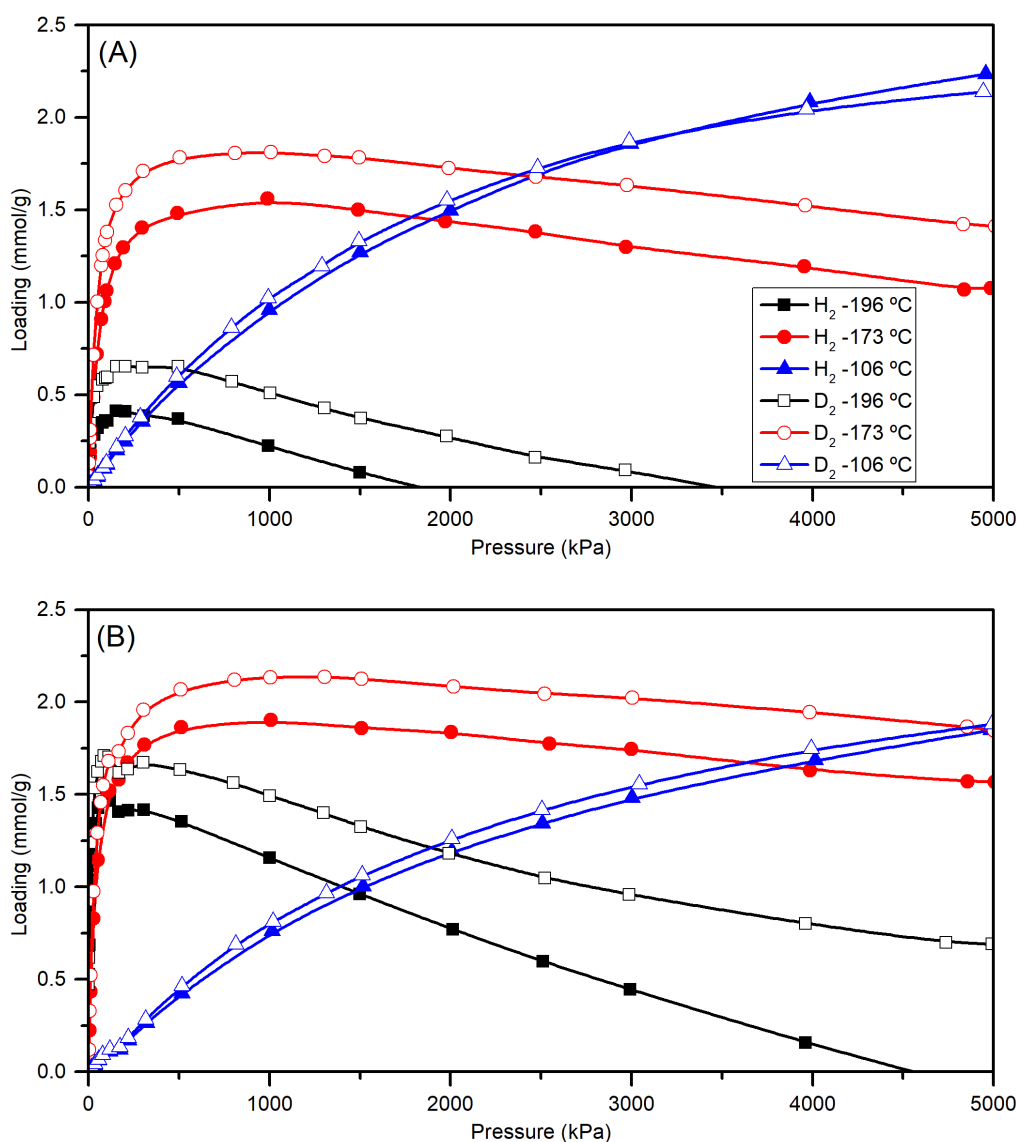**Figure 4.6:** *Adsorption isotherms of D_2 and H_2 on (A) Si-RWR-a and (B) Si-RWR-b samples at low temperatures. Lines are guides to the eye.*

The isotherms displayed in fig. 4.6 show that D_2 is adsorbed to a greater extent than H_2 at temperatures below -106 °C in both Si-RWR samples at all studied pressures.   At -106 °C the isotherms become practically equivalent and there is no selectivity in any of the samples.

Probably due to kinetic restrictions in Si-RWR-a, the adsorbed amounts below -106 °C are lower in this material than in Si-RWR-b, especially at the lowest temperature of -196 °C. Oppositely, at -106 °C, the adsorbed amount on Si-RWR-a is larger, which could be due to the higher degree of crystalline ordering.
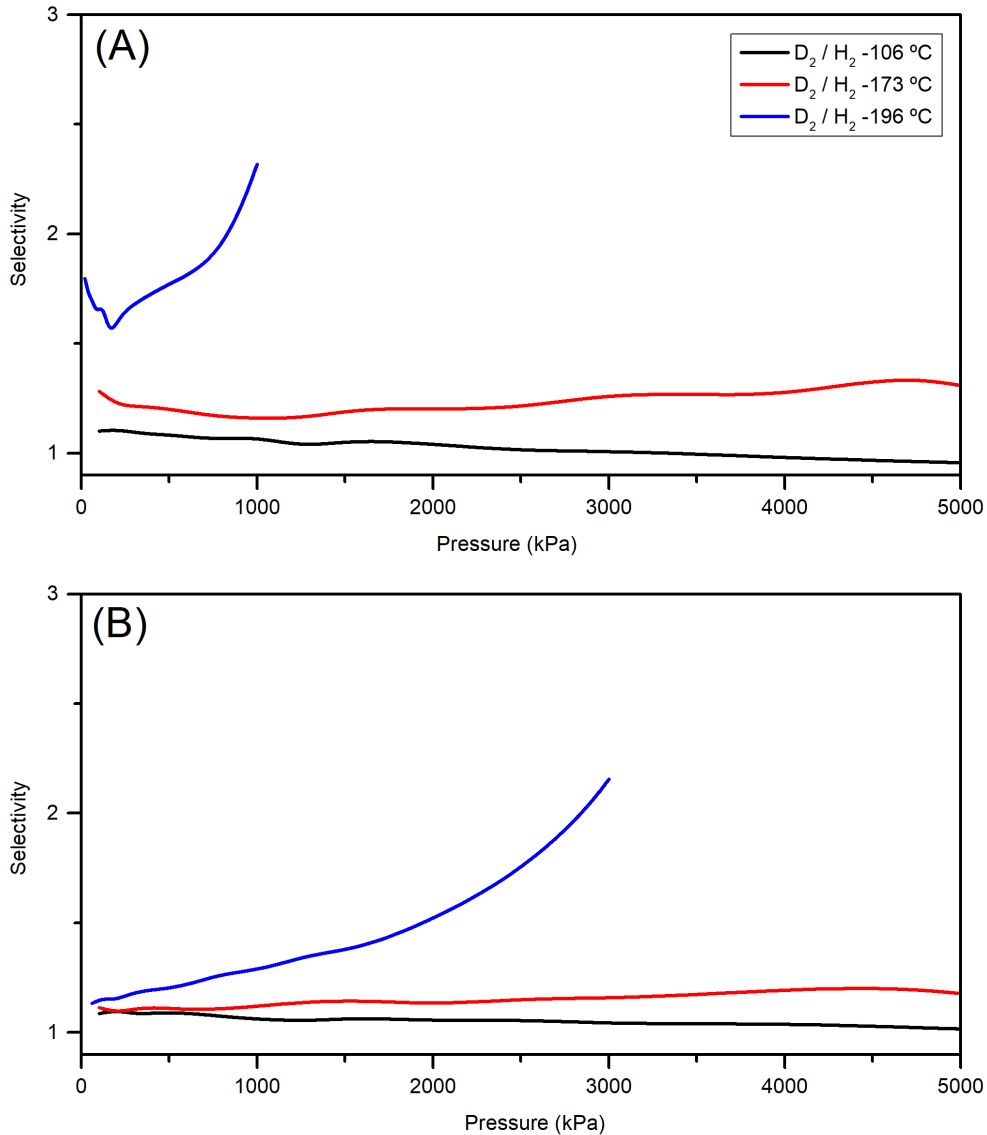
Figure 4.7: *Pure component selectivities of D_2/H_2 on (A) Si-RWR-a and (B) Si-RWR-b samples at low temperatures. Note that selectivities at -196 and -173 °C are apparent, as equilibrium has not been fully reached.*

The pure component selectivities of D_2 over H_2 calculated according to eq. (3.2) are low in both samples at all studied temperatures (see fig. 4.7), and seemingly not applicable to an adsorptive separation process, where the adsorption kinetics need to be fast to maximize the productivity.

137

Furthermore, as depicted in fig. 4.8, the heats of adsorption of hydrogen and deuterium on these materials are low and very similar, which means that they present similar affinities towards them.

Figure 4.8: *Isosteric heats of adsorption of D_2 and H_2 on Si-RWR-a and of H_2 on Si-RWR-b calculated according to Clausius-Clapeyron's method.*

The kinetic restrictions in Si-RWR-a mentioned above are confirmed by the uptake rate measurements presented in fig. 4.9, where it can be seen that at similar times, the kinetics in Si-RWR-b are much clos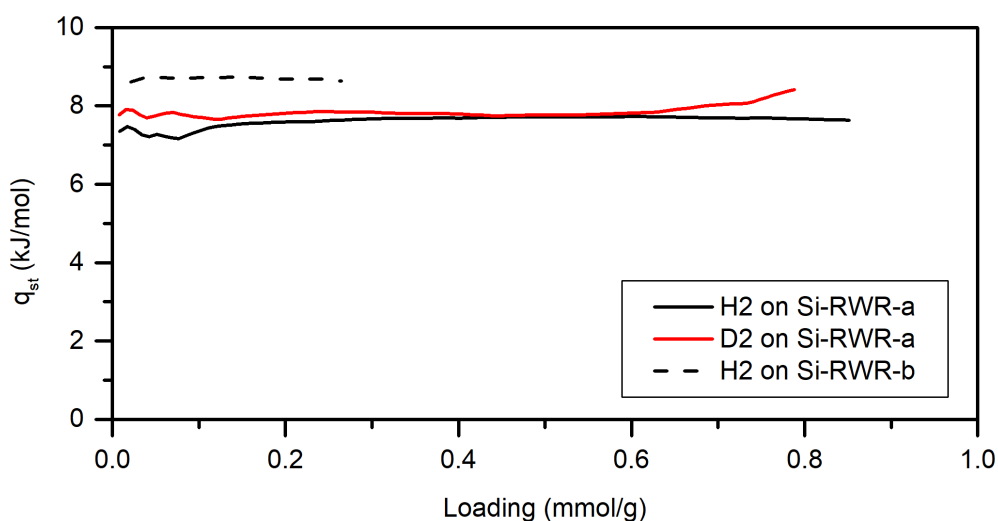er to equilibrium. Visual evaluation of the uptake curves allows us to discard the posibility of carrying out a kinetic separation of D_2 and H_2 on Si-RWR materials, as the kinetics of both compounds are very similar. The diffusional time constants calculated by fitting Crank's curve (eq. (3.8)) to the uptake rate curves[*] and the kinetic selectivities calculated according to eq. (3.9) are presented in table 4.2.

The results obtained indicate that this material is not likely to be applicable to a D_2/H_2 separation method. In coherence with the computational results presented in [199], the selectivities in this material are very low in order to compete with other zeolitic adsorbents proposed for this separation.

---

[*]The solution for spherical particle shape was used in all cases, as the solution for slab particle shape did not provide a better fit nor a significantly different value.
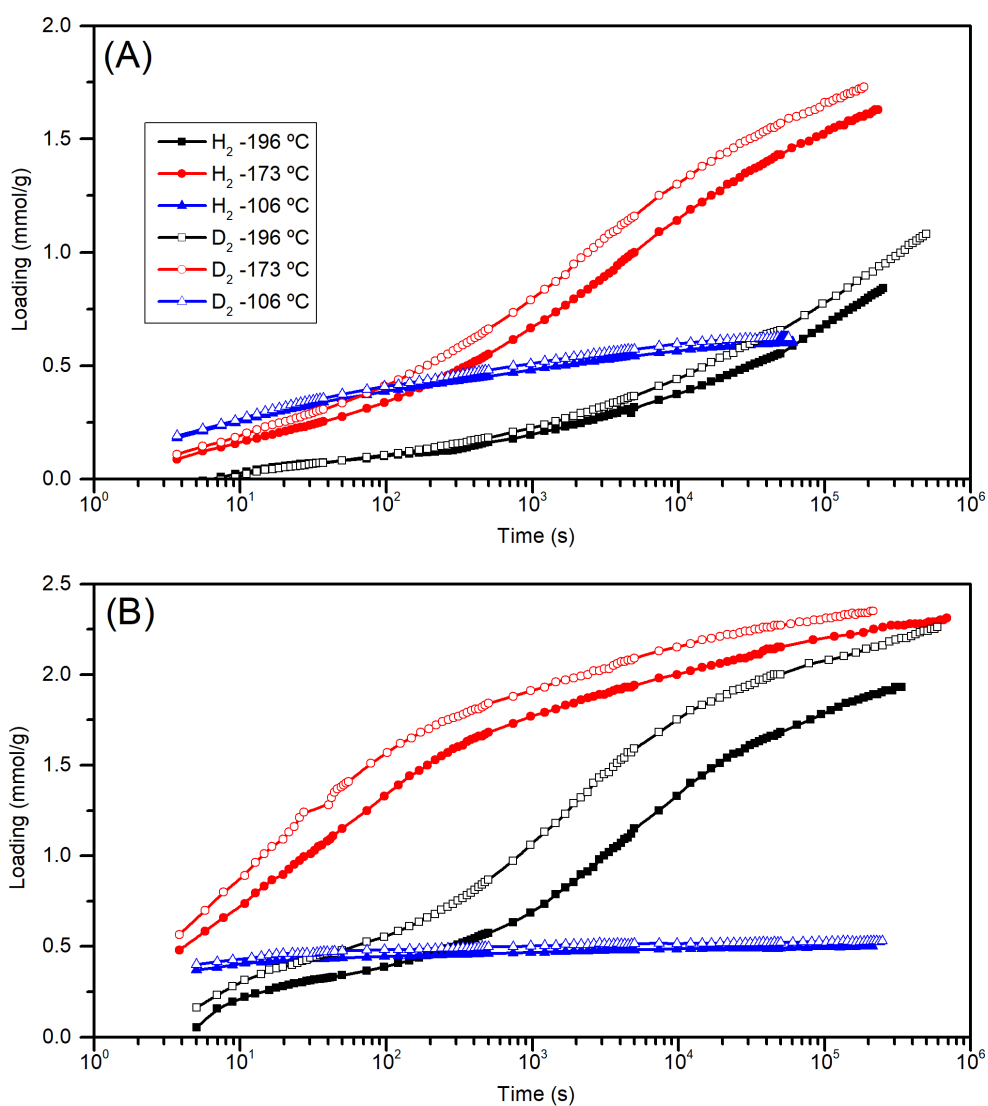
Figure 4.9: *Kinetics of adsorption at 500 kPa of D_2 and H_2 on (A) Si-RWR-a and (B) Si-RWR-b samples at low temperatures.*

Table 4.2: *Diffusional time constants obtained from fitting of eq. (3.8) to uptake rate curves and kinetic D_2/H_2 selectivities.*

	Si-RWR-a			Si-RWR-b		
T (ºC)	D_2	H_2	$\alpha^{kin}_{D_2,H_2}$	D_2	H_2	$\alpha^{kin}_{D_2,H_2}$
-196	$1.33 \cdot 10^{-6}$	$1.31 \cdot 10^{-6}$	1.01	$2.16 \cdot 10^{-5}$	$9.49 \cdot 10^{-6}$	2.28
-173	$1.86 \cdot 10^{-5}$	$1.20 \cdot 10^{-5}$	1.55	$6.10 \cdot 10^{-4}$	$3.33 \cdot 10^{-4}$	1.83
-106	$6.59 \cdot 10^{-4}$	$5.90 \cdot 10^{-4}$	1.12	$8.12 \cdot 10^{-3}$	$7.70 \cdot 10^{-3}$	1.05

4.3 Separation of components present in steam methane reformer off gas and refinery off gas

The adsorption of the components of SMROG and ROG (i.e. CO, H_2, CH_4, CO_2, H_2O and N_2) has been studied at either room temperature (0 - 25 °C) or low temperatures (-106 to -36 °C), focusing on the separation of CO_2 from the other components (H_2, CO, CH_4, N_2) or on the separation of H_2 from CO, respectively.

4.3.1 Carbon dioxide from other SMROG components

Adsorption of CO_2, H_2, CO, CH_4, H_2O and N_2 on Si-RWR materials was studied at temperatures close to room temperature by measuring adsorption isotherms (figs. 4.10 and 4.11) and kinetics (fig. 4.15). Isosteric heats of adsorption of CO_2 and other compounds were calculated when possible (fig. 4.13), as well as equilibrium and kinetic selectivities (fig. 4.12 and table 4.3).

Both samples adsorb moderate quantities of CO_2 at pressures above 1000 kPa, and present much lower adsorption capacities for CO, N_2, H_2 and CH_4 in decreasing order (fig. 4.10). Methane is adsorbed at a very slow rate on both materials and does not reach equilibrium at practical isotherm measurement times (ca. 1 week). The same happens with CO_2 on Si-RWR-a, which is not equilibrated, as evidenced by comparing the loading of the adsorption measurement at 500 kPa with the last measured loading from the uptake rate measurement at the same pressure. The difference between both data points is large on Si-RWR-a, and very small on Si-RWR-b, indicating that this material's isotherm is at equilibrium or close to it. Additionally, the adsorption of water at 25 °C was studied on Si-RWR-a by measuring its adsorption isotherm, presented in fig. 4.11. It may be seen that only a small amount of water (ca. 0.8 mmol/g) is adsorbed on Si-RWR-a at relative humidities close to 85%. In general

terms, Si-RWR-a adsorbs larger quantities of all compounds than Si-RWR-b, which may again be explained by its higher crystallinity. Si-RWR-a also seems to present more important kinetic restrictions than Si-RWR-b, which will be further discussed below.
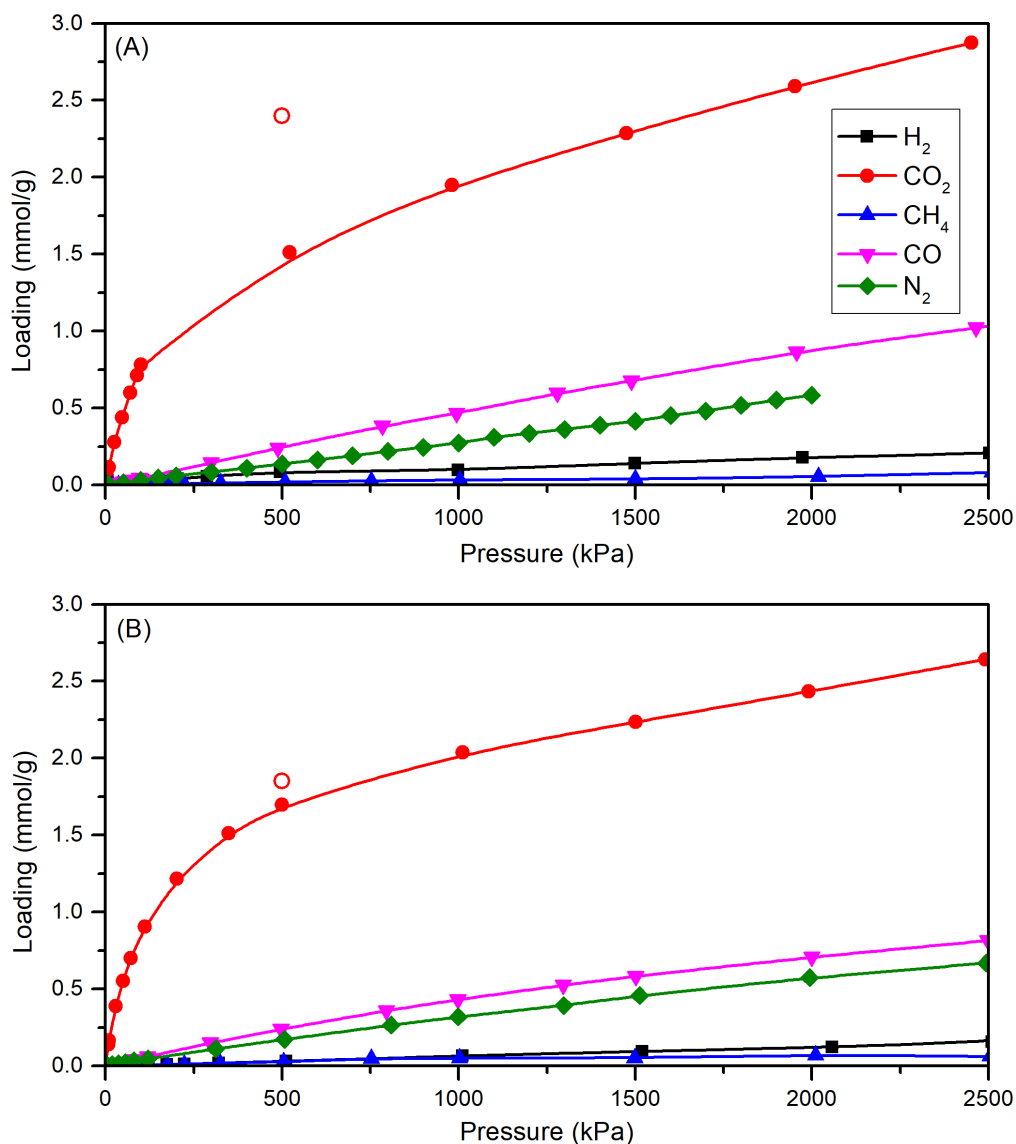
Figure 4.10: *Adsorption isotherms of H_2, CO_2, CH_4, CO and N_2 on (A) Si-RWR-a and (B) Si-RWR-b samples at ambient temperature (i.e. 25 °C, save for H_2 in Si-RWR-a, which was measured at 0 °C). Methane isotherms were not fully equilibrated. Red open circles at 500 kPa correspond to the last CO_2 loading obtained from the kinetic measurement. Lines are guides to the eye.*

The equilibrium selectivities[*] calculated from the pure component isotherms show that these materials preferentially adsorb CO_2 over other SMROG components over the entire pressure range covered at room

---
[*]Apparent selectivities in the cases where the isotherm is not fully equilibrated.

Figure 4.11: *Adsorption isotherm of H_2O on Si-RWR-a at 25 °C. The line is a guide to the eye.*

temperature. Selectivities of CO_2 over CH_4 or H_2 are particularly high (far above 10), while selectivities over N_2 or CO are lower (between 10 and 3). These results indicate that Si-RWR could be used as a selective CO_2 adsorbent.

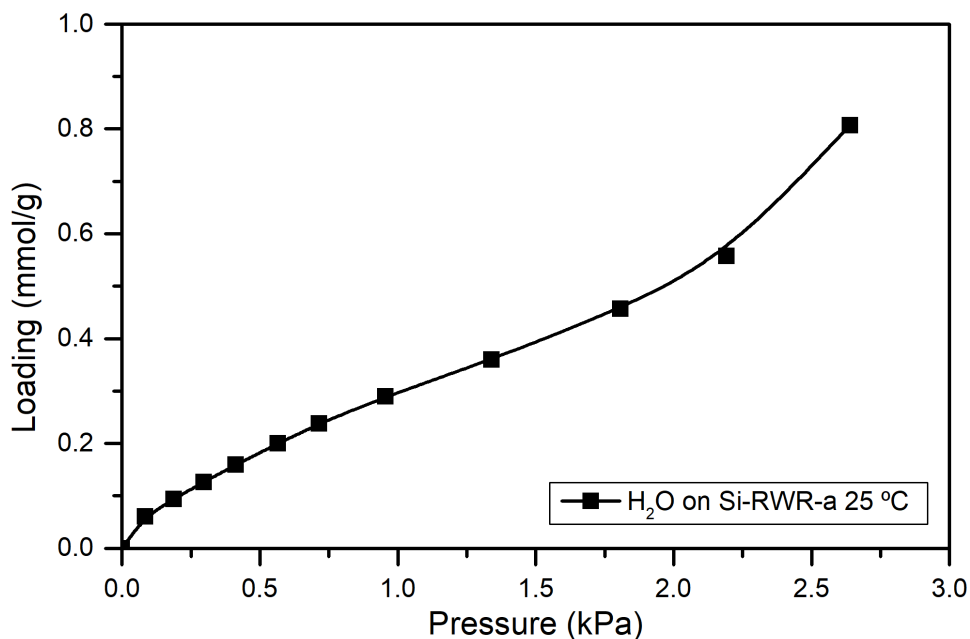The isosteric heats of adsorption of some of the components on the materials are depicted on fig. 4.13. CO_2 presents a much larger adsorption heat than H_2 on both materials. The difference is of ca. 10 kJ/mol on Si-RWR-a and of ca. 20 kJ/mol on Si-RWR-b. Furthermore, on Si-RWR-b, the isosteric heat of adsorption of CO is ca. 10 kJ/mol above that of hydrogen and 10 kJ/mol below that of CO_2.

On Si-RWR-b, the $q_{st}^{CO_2}$ is quite high for a pure silica material, but it may be explained by taking into account the enhanced interactions of the adsorbate with this material's walls, i.e. confinement effect [278, 488]. However, the difference between the $q_{st}^{CO_2}$ on both materials is large (ca. 10 kJ/mol) and none of the physical characteristics of Si-RWR-a, i.e. the higher degree of crystalline order, larger crystal size, can account for that. Furthermore, the fact that the heats of adsorption of H_2 are comparable in both materials, but there is a 10 kJ/mol difference between the trend for
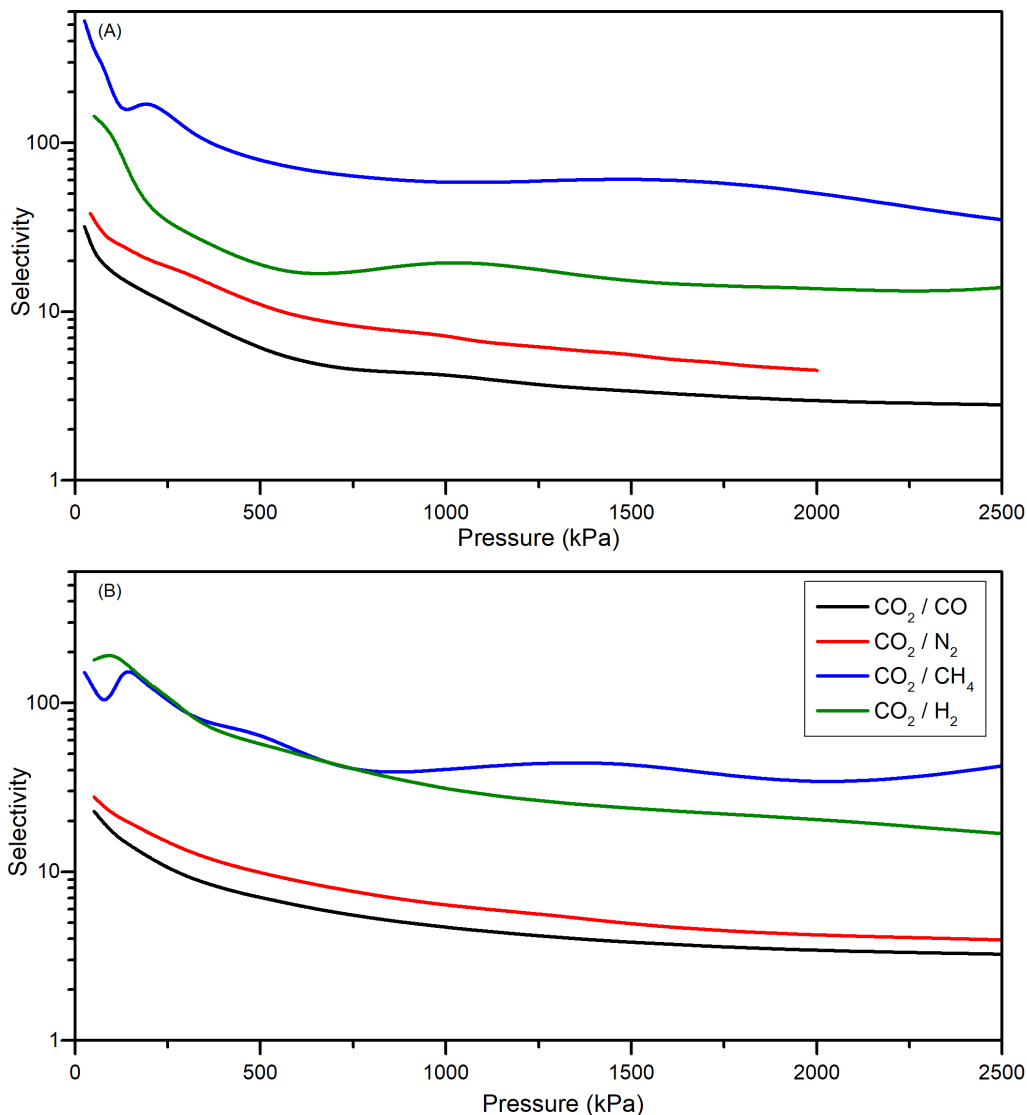
Figure 4.12: *Pure component selectivities of CO_2 over the other components on (A) Si-RWR-a and (B) Si-RWR-b samples at 25 °C, with the exception of $\alpha^{eq}_{CO_2,H_2}$, which was calculated from isotherms measured at 0 °C. Note that selectivities over methane are apparent, as equilibrium has not been fully reached.*

CO_2 on the two materials is worth of discussion.

The most suitable explanation for this difference in $q_{st}^{CO_2}$ is probably the fact that the CO_2 adsorption isotherm measurements carried out are not fully equilibrated, as was evidenced in fig. 4.10. The set of isotherms that were used for the calculation of the heat of adsorption follow the expected order (increasing loading with decreasing temperature, see fig. 4.14A). Nonetheless, the isotherms measured at 0 and 25 °C were measured several times giving substantially different results fig. 4.14B. In fig. 4.14C, the choice of isotherms used for the calculation of the isosteric heat of
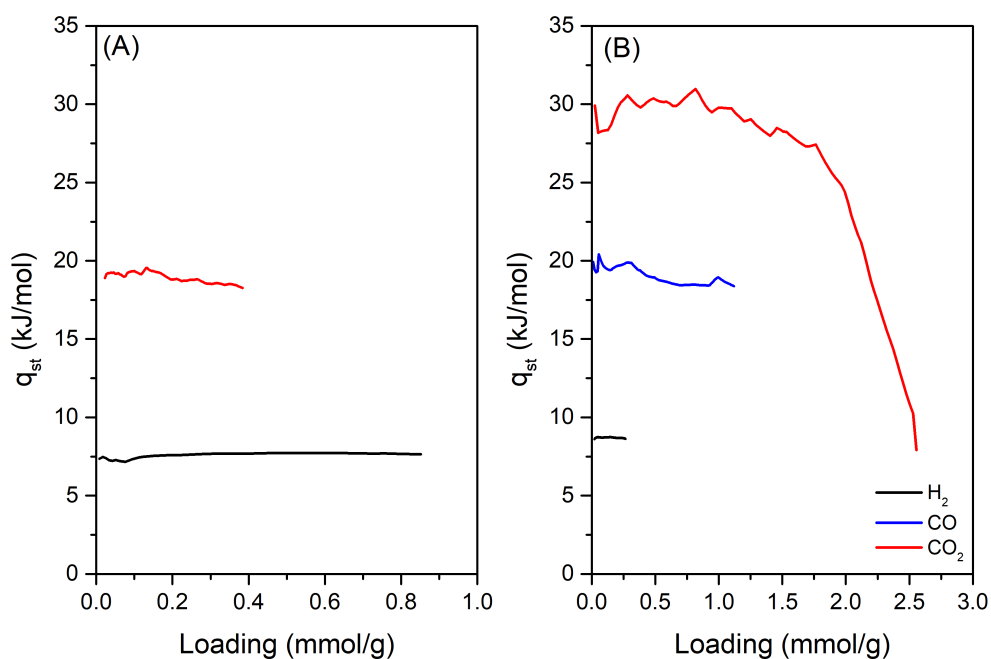
Figure 4.13: *Isosteric heats of adsorption of (A) H_2 and CO_2 on Si-RWR-a and (B) of H_2, CO and CO_2 on Si-RWR-b samples calculated according to Clausius-Clapeyron's method.*

adsorption is modified to see the effect that taking or not some isotherms into account has on the final $q_{st}^{CO_2}$ trend. When disregarding the isotherms measured at 0 and 10 °C, the heat of adsorption increases ca. 5 kJ/mol, thus being a bit closer to the value on Si-RWR-b. In any case, both the $q_{st}^{CO_2}$ and the CO_2 adsorption isotherms on Si-RWR-a are not to be considered fully trustworthy.

The uptake rate measurements presented in fig. 4.15 confirm the reduced diffusivities on Si-RWR-a compared to Si-RWR-b. The uptake rate measurement of CO_2 on Si-RWR-a reaches a considerably high loading (2.4 mmol/g) at long times. As previously explained, the CO_2 isotherm is far away from equilibrium, presenting a loading of 1.5 mmol/g at the same pressure (see fig. 4.10A), which indicates that the isotherm is far away from equilibrium. In the case of Si-RWR-b, the maximum loading of the isotherm and the uptake rate measurements are comparable (ca. 1.8 mmol/g). Furthermore, in Si-RWR-b CO_2 diffuses faster and reaches higher maximum loadings than the other components.

Coinciding with the conclusions obtained from the visual evaluation
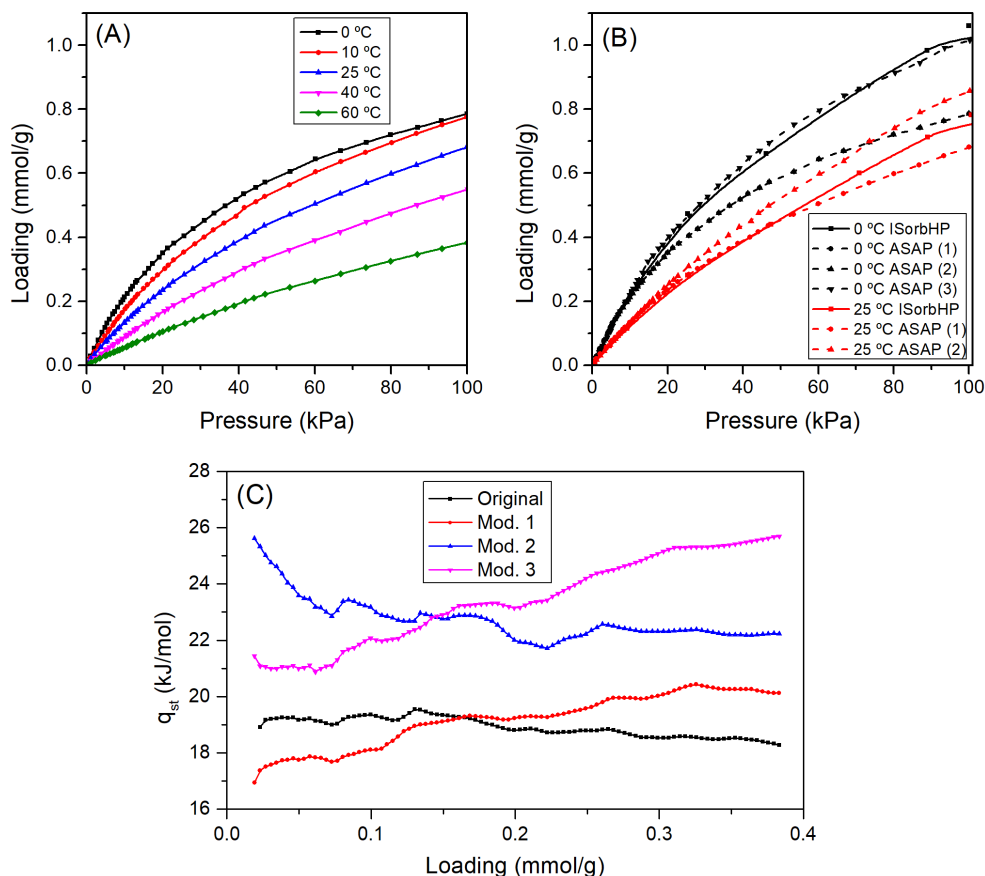
Figure 4.14: *Particularities in the adsorption of CO_2 on Si-RWR-a: (A) isotherms up to 100 kPa measured in an ASAP2010 device, used for the calculation of the isosteric heat of adsorption, (B) repetitions of isotherms at 0 and 25 °C and (C) calculated trends of the isosteric heat of adsorption. The trend labeled as "Original" in (C) was calculated using the isotherms depicted in (A). For the calculation of "Mod. 1", the isotherm at 0 °C used was the one labeled as "0 °C ASAP (3)" in (B). For the calculation of "Mod. 2" only isotherms above 25 °C in (A) were used, thus excluding the lowest temperatures, in which supposedly the kinetic restrictions are stronger. "Mod. 3" only differs from "Mod. 2" in which the isotherm at 25 °C used was the one labeled as "25 °C ASAP (2)" in (B). Lines in (A) and (B) are guides to the eye.*

of the uptake rate experiments, the diffusional time constants obtained from fitting the curves to eq. (3.8) indicate a much slower diffusion of most components in Si-RWR-a compared to Si-RWR-b, with methane being practically non-adsorbed in both materials (see table 4.3). It is also noteworthy that the diffusional time constant of CO_2 is ca. 300 times lower in Si-RWR-a than in Si-RWR-b. Thus, kinetic selectivities present considerably different values in the two materials, with Si-RWR-a not being applicable for the kinetic separation of these compounds and,

on the contrary, Si-RWR-b being promising for kinetic separation of CO_2 from CH_4 and, to a lesser extent, from N_2 and CO.
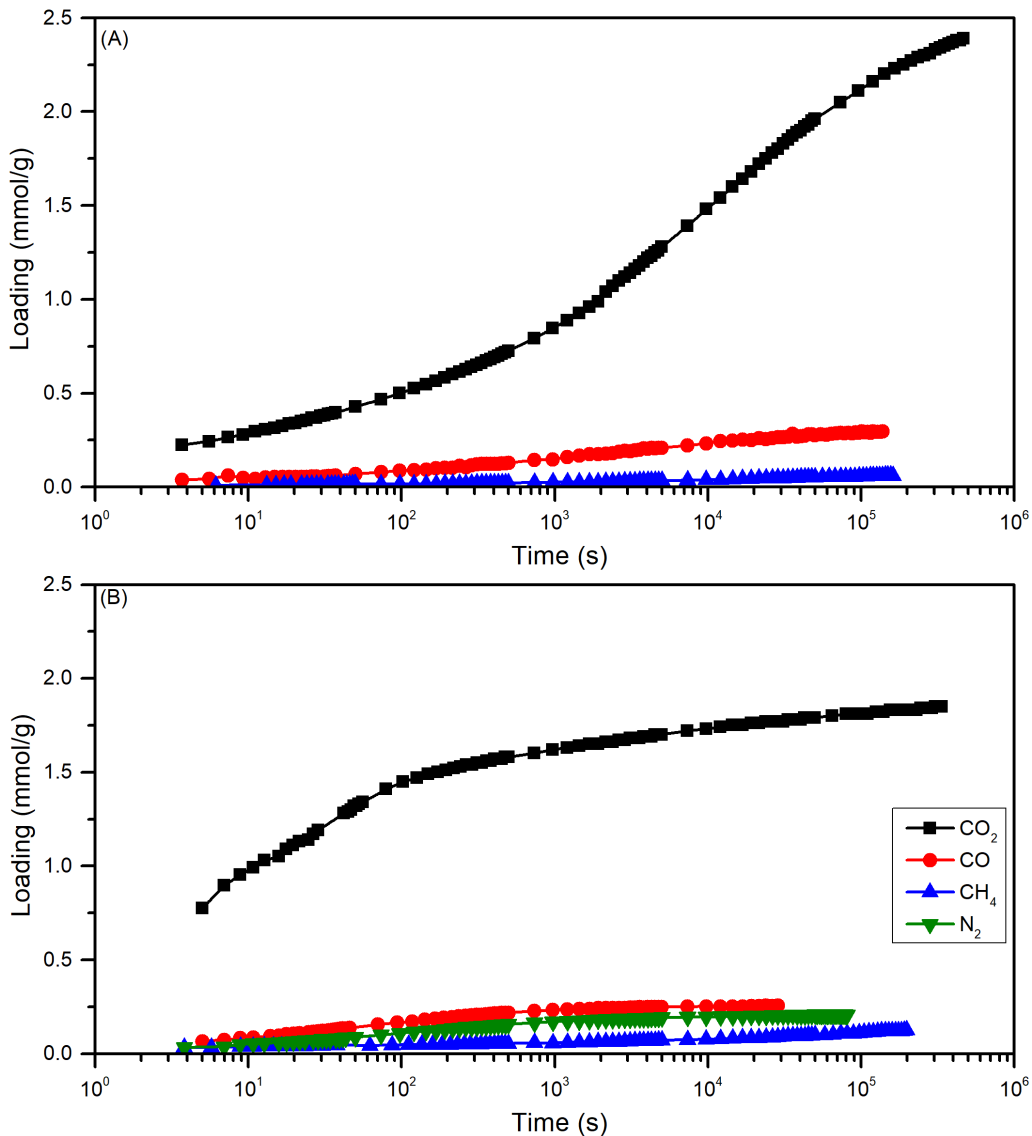
Figure 4.15: *Kinetics of adsorption at 500 kPa of SMROG components on (A) Si-RWR-a and (B) Si-RWR-b samples at 25 °C.*

Overall, it is clear that the preparation method of the lamellar precursor (RUB-18) is very relevant to the adsorption properties of the final Si-RWR material. A material similar to Si-RWR-a would be less applicable to a separation process due to the extreme kinetic hindrances it imposes on the studied adsorbates. On the contrary, Si-RWR-b seems a promising material to separate CO_2 from the other components of the mixture, both under thermodynamic or kinetic control[*]. In comparison to the well-

---

[*]A combined effect of kinetics and thermodynamics is not excluded in industrial PSA

Table 4.3: *Diffusional time constants obtained from fitting of eq. (3.8) to uptake rate curves at 25 °C and kinetic selectivities of CO_2 over other compounds present in SMROG and ROG streams.*

	Si-RWR-a		Si-RWR-b	
Compound	D/r^2 (s^{-1})	$\alpha_{CO_2,n}^{kin}$	D/r^2 (s^{-1})	$\alpha_{CO_2,n}^{kin}$
CO_2	$6.35 \cdot 10^{-6}$	-	$1.75 \cdot 10^{-3}$	-
CH_4	$9.47 \cdot 10^{-6}$	0.671	$1.37 \cdot 10^{-5}$	128
CO	$2.65 \cdot 10^{-5}$	0.239	$5.96 \cdot 10^{-4}$	2.93
N_2	-	-	$2.62 \cdot 10^{-4}$	6.68

established zeolite 5A, which presents a high isosteric heat of adsorption of CO_2 (ca. 40 kJ/mol), the moderate heat of adsorption of CO_2 on Si-RWR ($\leq$ 30 kJ/mol) is another factor favoring the feasibility of a process using this material, as the regeneration of the adsorbent would be relatively easy [265]. Furthermore, the preparation of this material does not involve the use of an expensive OSDA and thus, one of the most common drawbacks of this kind of materials is avoided [34].

---

processes, depending on the cycle and contact time with the adsorbent.

4.3.2 Hydrogen from carbon monoxide

The adsorption of H_2 and CO was studied at temperatures below ambient (-106 and -36 °C) by measuring adsorption isotherms up to 4500 - 5000 kPa (fig. 4.16) and kinetics at 500 kPa (fig. 4.18).
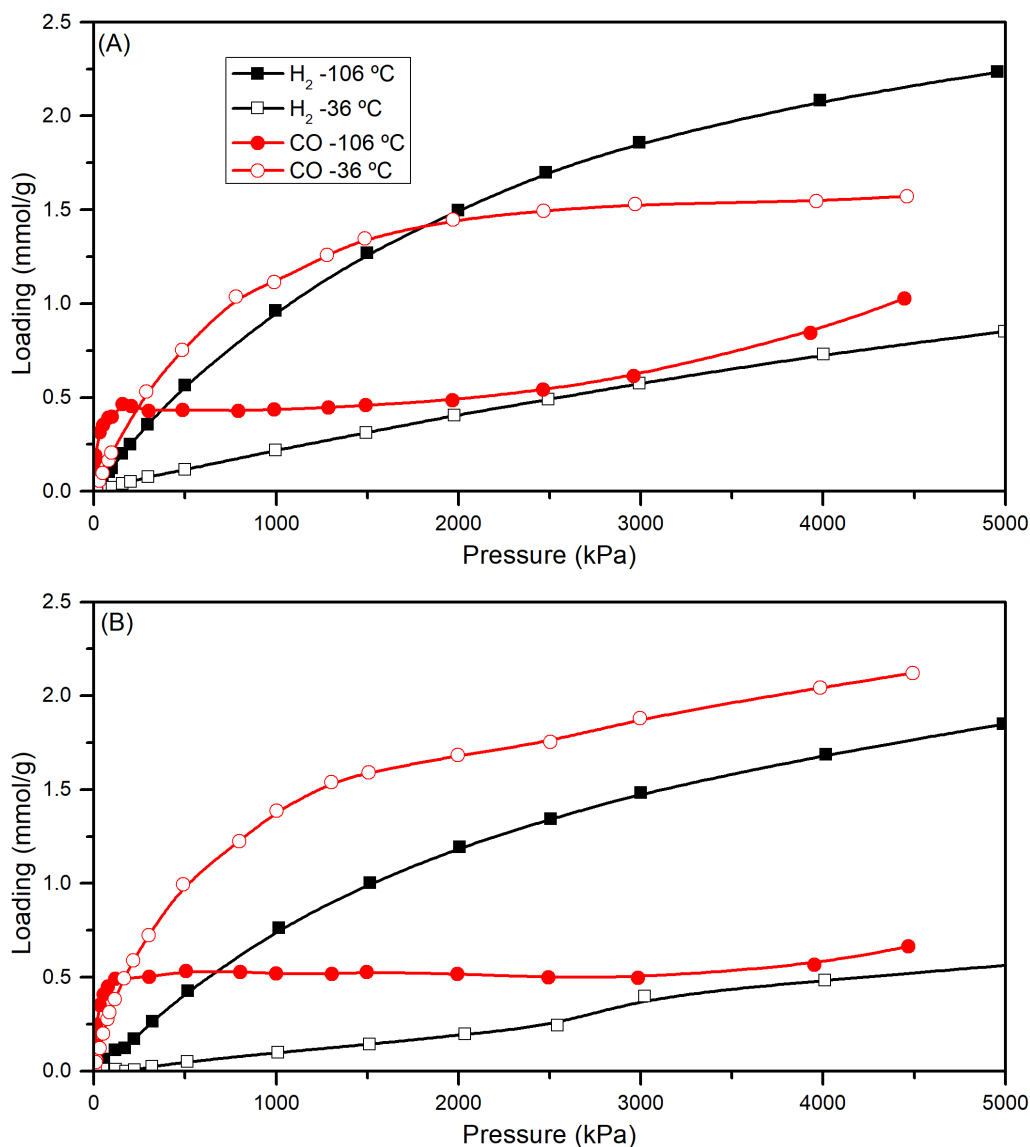
Figure 4.16: *Adsorption isotherms of H_2 and CO on (A) Si-RWR-a and (B) Si-RWR-b samples at low temperatures. Lines are guides to the eye.*

Si-RWR adsorbs moderate amounts of H_2 at -106 °C, and much lower amounts at -36 °C (see fig. 4.16). As in the previous cases, the adsorption capacity of Si-RWR-a surpasses that of Si-RWR-b and the reason for that is the higher crystallinity of the first sample. The adsorption of CO in both samples is kinetically limited at -106 °C, something that is evident from

148

the intersection of these with the isotherms at -36 °C. In the case of CO, it reaches higher loadings in Si-RWR-b, which is again explained by more severe kinetic barriers in Si-RWR-a.

Apparent thermodynamic selectivities are presented in fig. 4.17, but due to the CO isotherms not being equilibrated, these are only of qualitative interest. As can be seen, the selectivity is inverted from H_2 to CO when going from -106 to -36 °C. At the lower temperature, due to the hindered adsorption of CO, the adsorbed amount of H_2 is > 2 larger than that of CO above 1000 kPa. However, at -36 °C, the material is selective towards CO.
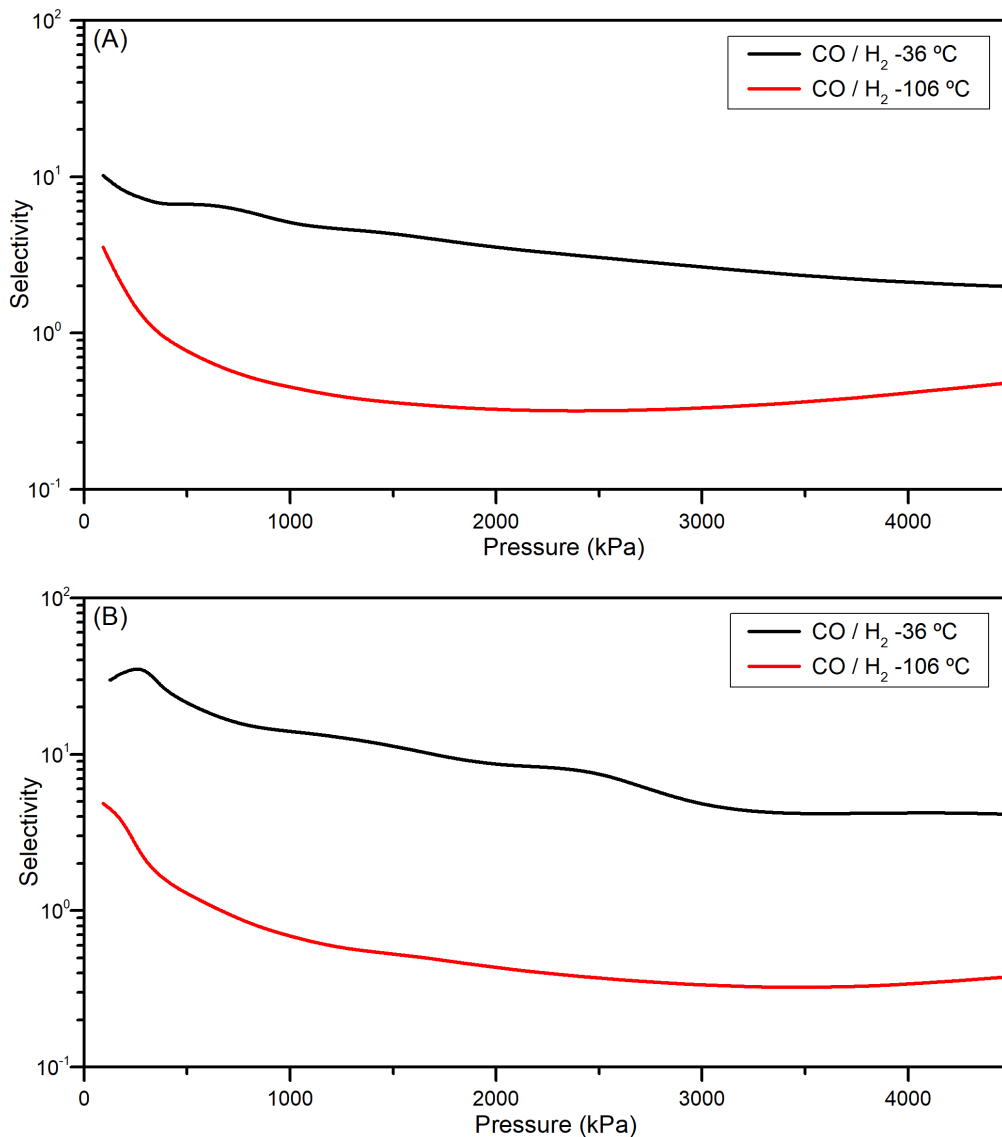
Figure 4.17: *Apparent pure component selectivities of CO/H_2 on (A) Si-RWR-a and (B) Si-RWR-b samples at low temperatures.*

By comparing the maximum loadings reached at 500 kPa in the uptake rate measurements (fig. 4.18), it is confirmed that the CO isotherms presented in fig. 4.16 are not equilibrated. The diffusional time constants[*] and kinetic selectivities of H_2 over CO are presented in table 4.4.
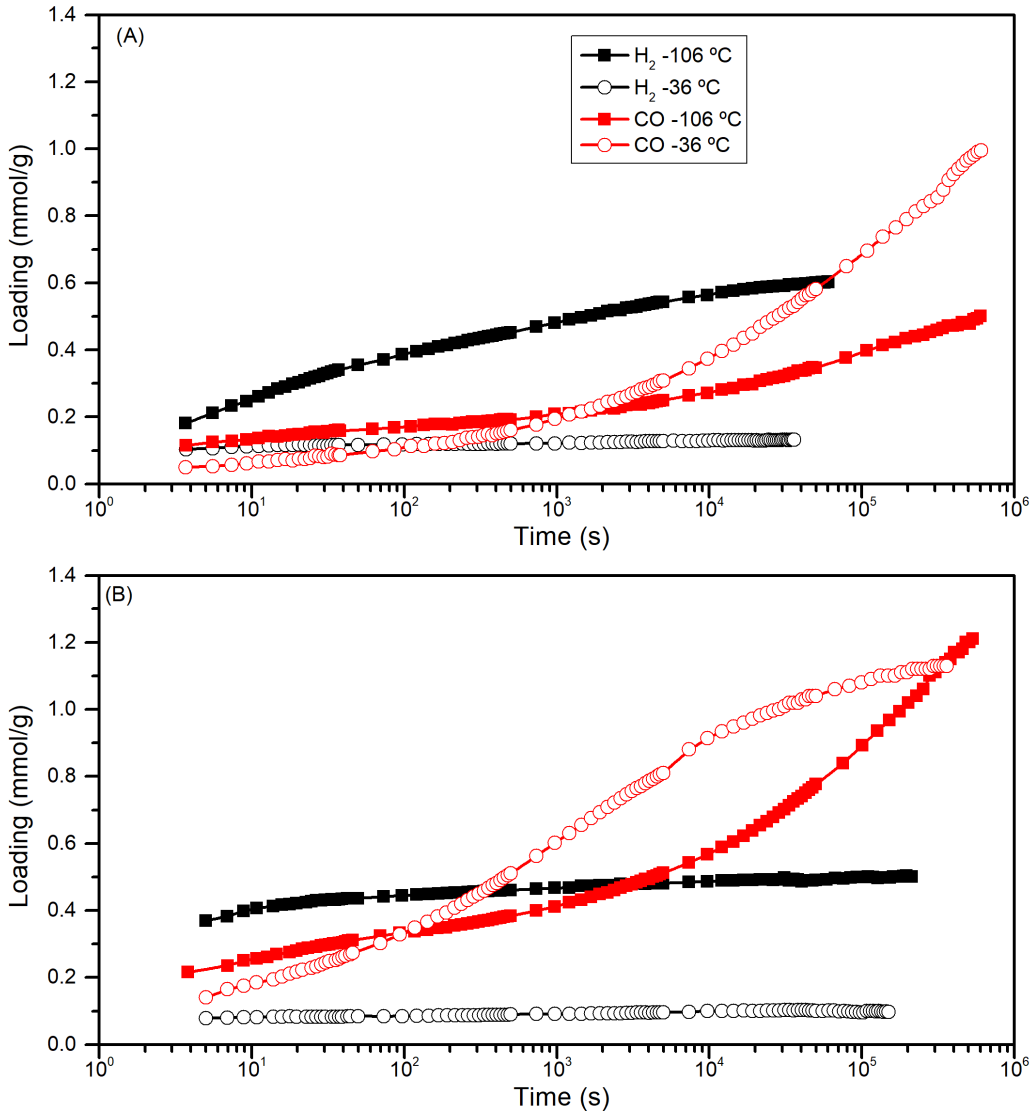
Figure 4.18: *Kinetics of adsorption at 500 kPa of H_2 and CO on (A) Si-RWR-a and (B) Si-RWR-b samples at low temperatures.*

In coherence with what can be observed in fig. 4.18, kinetic H_2/CO selectivities are very high, as hydrogen diffuses much faster than CO at the selected temperatures. However, when taking into account the adsorbed amounts, it is also obvious that despite the high kinetic

---

[*]Note that not having reached the equilibrium loadings, these values need to be analyzed carefully and therefrom derived conclusions are only qualitative.

Table 4.4: *Diffusional time constants obtained from fitting of eq.* (3.8) *to uptake rate curves and kinetic H$_2$/CO selectivities.*

	Si-RWR-a			Si-RWR-b		
T (ºC)	H$_2$	CO	$\alpha_{H_2,CO}^{kin}$	H$_2$	CO	$\alpha_{H_2,CO}^{kin}$
-106	$5.90 \cdot 10^{-4}$	$4.02 \cdot 10^{-6}$	147	$7.70 \cdot 10^{-3}$	$2.23 \cdot 10^{-6}$	3444
-36	$1.30 \cdot 10^{-2}$	$1.08 \cdot 10^{-6}$	12079	$7.36 \cdot 10^{-3}$	$3.00 \cdot 10^{-5}$	246

selectivities, no efficient kinetic separation could be carried out in Si-RWR-b at these temperatures. At -106 °C the amount of adsorbed H$_2$ (ca. 0.45 mmol/g) is equilibrated after ca. 10 s, but the CO loading is also important at that time (ca. 0.3 mmol/g). At -36 °C, the kinetic of CO is above that of H$_2$ at all times. However, on Si-RWR-a, and presumably thanks to the reduced diffusivities of adsorbates in general, the differences in the adsorbed amounts of H$_2$ and CO are more favorable for allowing a kinetic separation of these, especially at -106 °C. Overall, these observations lead to believe that Si-RWR could be used at low temperatures to separate H$_2$ from CO, if a material with the right crystal size and degree of crystalline order is prepared. As has been demonstrated, depending on the selected temperature and controlling factor (thermodynamics or kinetics), the selectivity may be shifted from H$_2$ to the other components of the mixture.

4.4 Conclusions regarding the adsorption properties of zeolite Si-RWR

- Si-RWR poses as a promising and versatile material to purify hydrogen from SMROG and ROG streams, by selectively adsorbing the other components of these mixtures at ambient temperature and kinetically excluding those at lower temperatures.

- Si-RWR acts as a molecular sieve, in which it does not adsorb methane at a relevant amount at any temperature

- The adsorption properties of Si-RWR may be tailored in detail by controlling the synthesis conditions and procedure of its lamellar precursor RUB-18.

- Si-RWR materials are cheap compared to other pure silica materials, as no OSDA is used for their synthesis and the N-methyl formamide used for refluxing may be recycled.

Chapter 5

AlPOs and SAPOs as carbon dioxide adsorbents

Materials that present low heats of adsorption of CO_2 but still high selectivities are especially interesting as adsorbents for its separation from relevant mixtures, such as natural gas, biogas or post-combustion gases. The main advantage of such materials is the reduced amount of energy required for the regeneration of the adsorbent. At the ITQ, it was observed that several SAPOs with LTA structure (the ones reported in [52]) present unusually low isosteric heats of adsorption of CO_2 and, with that as a start, the decission was made to carry out a study comprising SAPOs and AlPOs of LTA, CHA and AFI structures and their zeolitic counterparts. CHA was chosen as another small pore structure extensively reported as CO_2 adsorbent [242, 312, 314, 489], and AFI was chosen to see if these observations apply also to large pore zeotypes. The study is focused on the trends of the isosteric heat of adsorption of CO_2 on these materials, and on the dependance of these values with the framework charge. In this way, the existing study by Palomino et al. [279] on LTA zeolites is expanded to other compositions and structures. Additionally, a first comparison of some of these materials is made in terms of their CO_2/CH_4 selectivities and CO_2 and CH_4 isosteric heats of adsorption.

Table 5.1: *Characterization results of the samples after removal of occluded species. Light blue background is for LTA, white is for CHA and light red is for AFI-structured materials.*

Sample	Si defects amount (% Q_3)	Crystal shape	Crystal dimensions (μm)	BET surface area (m²/g)	DA surface area (m²/g)	Micropore volume (cm³/g)
AlPO–LTA	-	cubes	5	774	-	0.290
SAPO–LTA–104	-	cube fractions	3	797	-	0.301
SAPO–LTA–24	-	cube fractions	0.5 - 4	776	-	0.289
SAPO–LTA–13	-	truncated octahedra	1 - 2	743	-	0.275
Si–LTA	0	cubes	0.3	811	-	0.320
LTA–31	-	-	-	777	-	0.305
LTA–6	-	cubes	0.4	806	-	0.297

Table 5.1 continued from previous page

Sample	Si defects amount (% Q_3)	Crystal shape	Crystal dimensions (μm)	BET surface area (m²/g)	DA surface area (m²/g)	Micropore volume (cm³/g)
LTA−4.5	-	-	-	799	680	0.304
LTA−3	-	-	-	794	609	0.295
AlPO−CHA	-	indefinite	5 - 10	-	-	0.226
SAPO−CHA−10	-	cubes	0.5	595	-	0.210
SAPO−CHA−7	-	indefinite	1 - 5	699	-	0.242
Si−CHA	8	cubes	2 - 10	821	-	0.296
CHA−19	-	-	-	869	-	0.305
CHA−18	-	-	-	801	-	0.293

Table 5.1 continued from previous page

Sample	Si defects amount (% Q_3)	Crystal shape	Crystal dimensions (µm)	BET surface area (m²/g)	DA surface area (m²/g)	Micropore volume (cm³/g)
CHA−6	-	-	-	749	600	0.273
CHA−3[a]	-	-	-	-	470	-
AlPO−AFI	-	hexagonal prisms	5	310	-	0.117
SAPO−AFI−46	-	hexagonal prisms	7	383	-	0.141
SAPO−AFI−34	-	hexagonal prisms	7	355	-	0.119

Table 5.1 continued from previous page

Sample	Si defects amount (% Q_3)	Crystal shape	Crystal dimensions (μm)	BET surface area (m²/g)	DA surface area (m²/g)	Micropore volume (cm³/g)
Si–AFI	10	rounded cylinder	$l = 6$, $d = 3$	359	-	0.130

[a] The extremely narrow pores of this sample made it impossible to measure adsorption isotherms of N_2 at -196 °C due to the very slow diffusion.

5.1 Characterization of the materials selected for this study

The materials included in this chapter are listed in table 5.1, together with their most relevant characterization results.
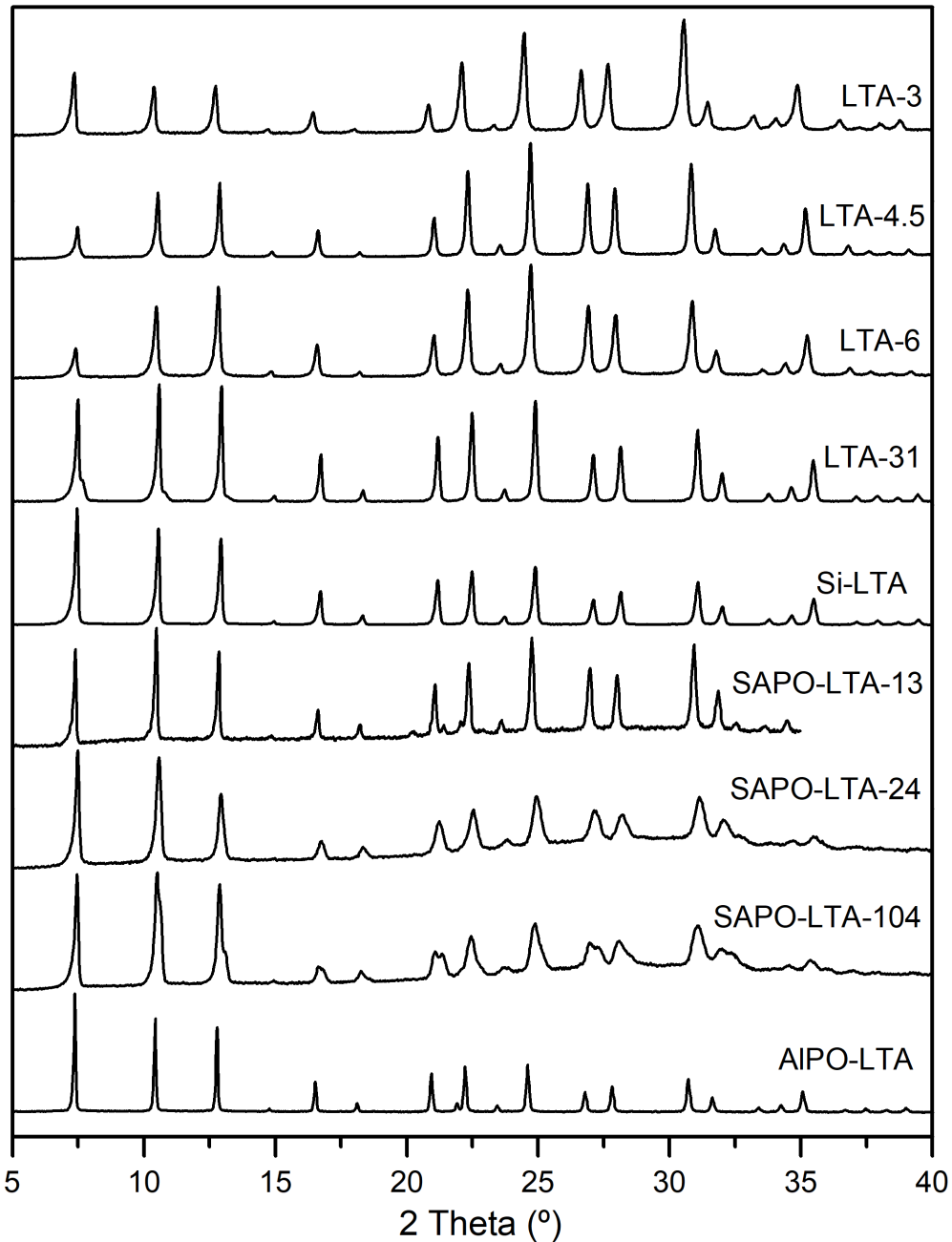

Figure 5.1: *Normalized X-Ray diffractograms of the calcined materials with LTA structure.*

The XRD patterns of said materials are depicted in figures 5.1 - 5.3. Some LTA and CHA SAPOs present lower signal/noise ratios than other

isostructural materials, which may be due to a lower degree of crystalline order caused by partially reversible hydration processes[*] after calcination [83] or even by partial loss of crystallinity. A broad signal of low intensity in the range of 20 - 35° in some of the spectra evidences the lower crystallinity of those samples, i.e. SAPO-LTA-13, SAPO-LTA-24, SAPO-LTA-104, SAPO-CHA-10. However, they were proven to be stable and to have an acceptable value of micropore volume (see table 5.1). It is also worth saying that other structures (RHO, FAU) with SAPO composition were tested, but these materials did not remain stable upon calcination and rehydration and thus, were not included in this study.
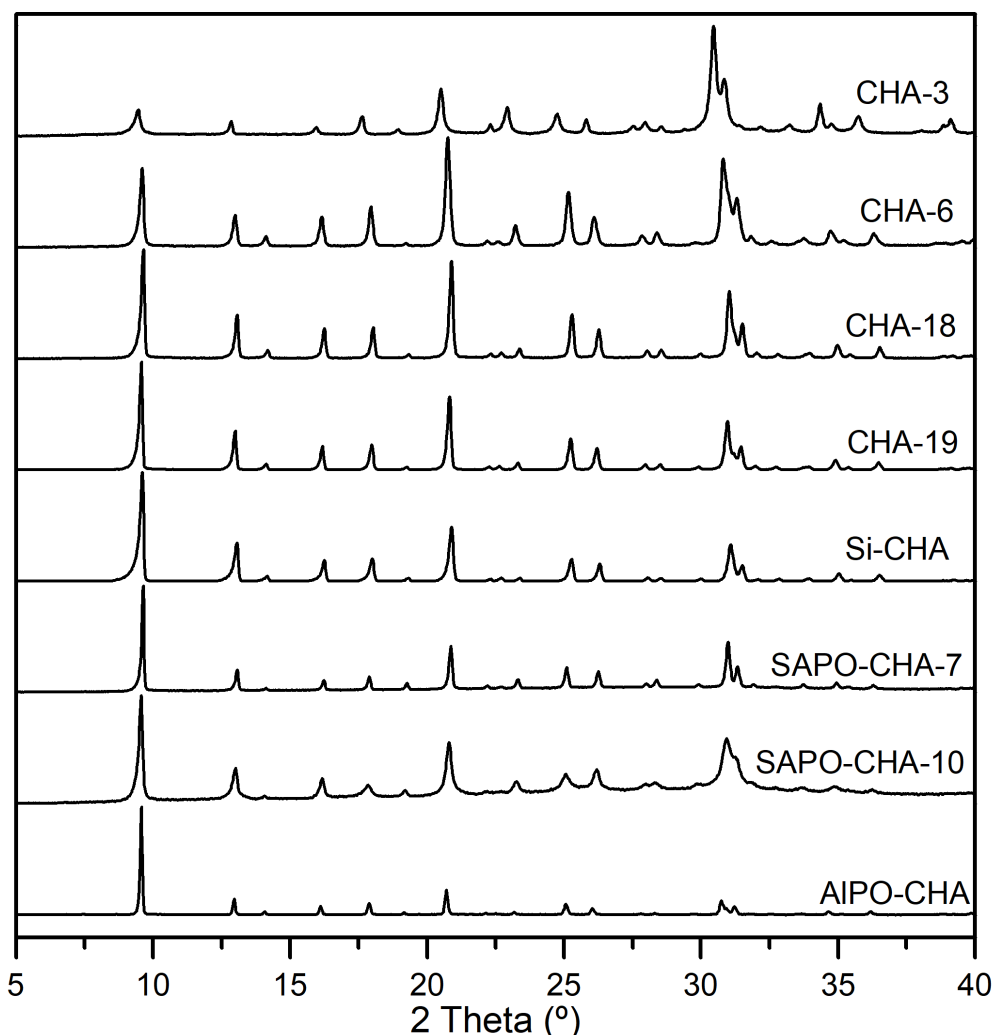

Figure 5.2: *Normalized X-Ray diffractograms of the calcined materials with CHA structure.*

---

[*]These materials hydrate readily and may therein undergo slight unit cell symmetry and connectivity changes, which may be fully or partially reversible. An example of that is SAPO-34 [83], referred to as SAPO-CHA according to this thesis' nomenclature system.
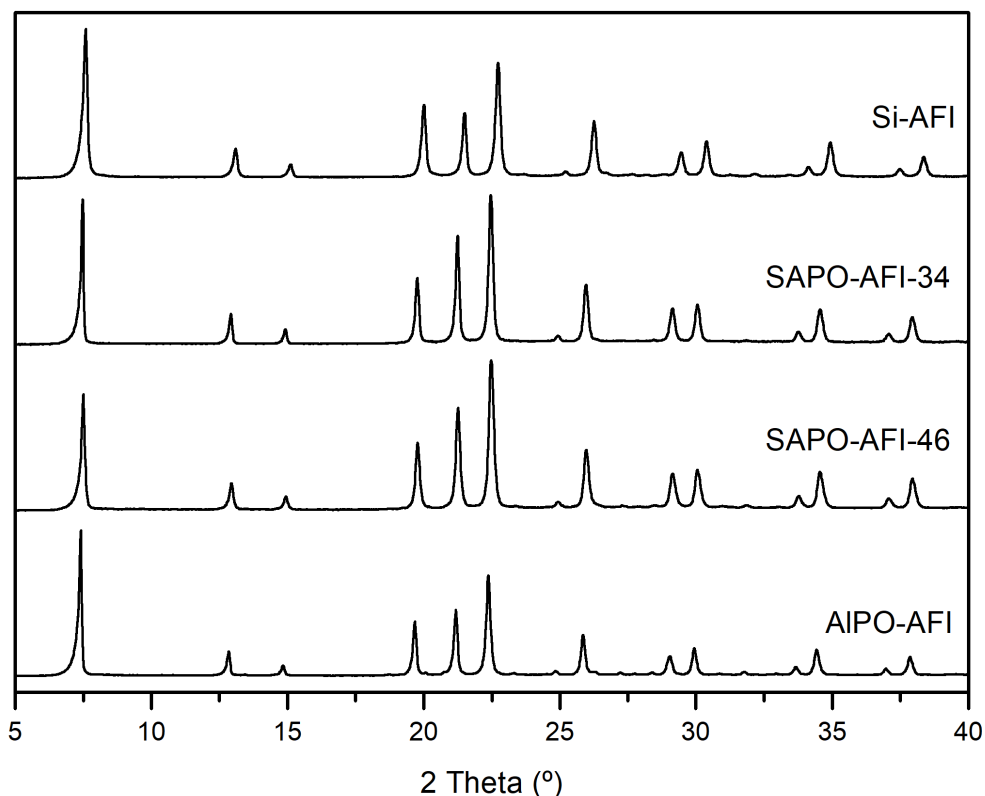
Figure 5.3: *Normalized X-Ray diffractograms of the calcined materials with AFI structure.*

The ^{29}Si MAS NMR spectra of the SAPOs are presented in fig. 5.4. As can be seen, notably different Si species may be found in materials with the same structure. Signals in the -100 to -120 ppm range belong to Si-rich domains and signals centered around -90 ppm correspond to isolated Si species in SAPO materials [50, 52]. Thus, as can be observed, CHA-structured SAPOs and SAPO-LTA-24 and SAPO-LTA-13 present a larger fraction of isolated Si, whilst AFI-structured SAPOs present similar amounts of both types of Si and SAPO-LTA-104 presents a larger fraction of Si-rich domains.

These spectra were analyzed in detail as explained in section 3.1.2.2 in order to determine the fraction of isolated Si species, needed for the obtention of the estimated framework negative charge. This way, the spectra were fitted using a sum of two gaussian functions, one for each silicon signal. An example of fitting to the ^{29}Si MAS NMR spectra of AFI-structured SAPOs is presented in fig. 5.5. The obtained fraction of isolated
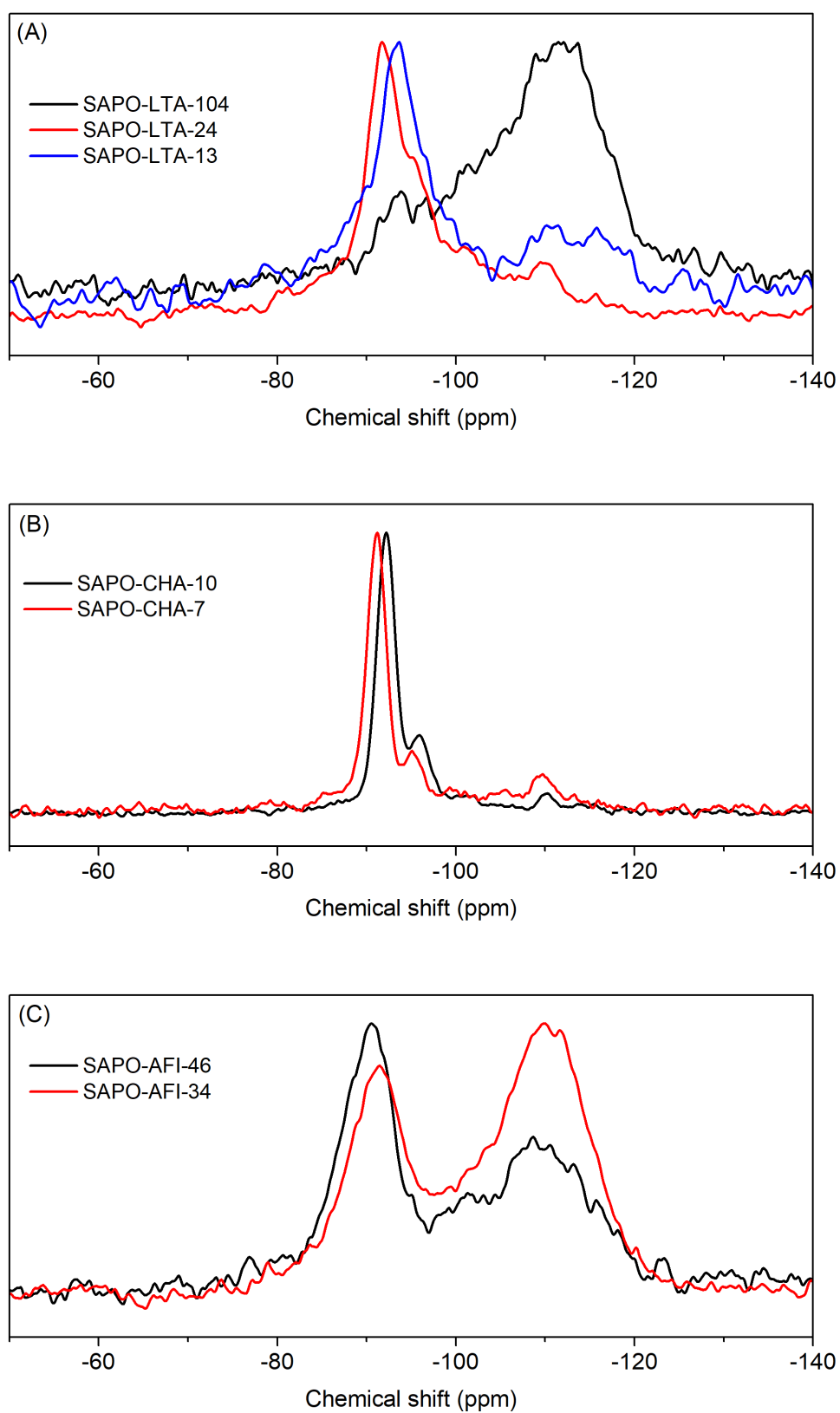
Figure 5.4: ^{29}Si MAS NMR spectra of calcined (A) LTA, (B) CHA and (C) AFI-SAPOs.

Si was multiplied by the molar fraction of Si in order to obtain the estimated framework negative charge of the SAPOs. The framework charge of zeolites is assumed to be equal to their aluminium molar fraction. The composition, Si distribution and estimated framework negative charge of the materials relevant to this chapter can be found in table 5.2.
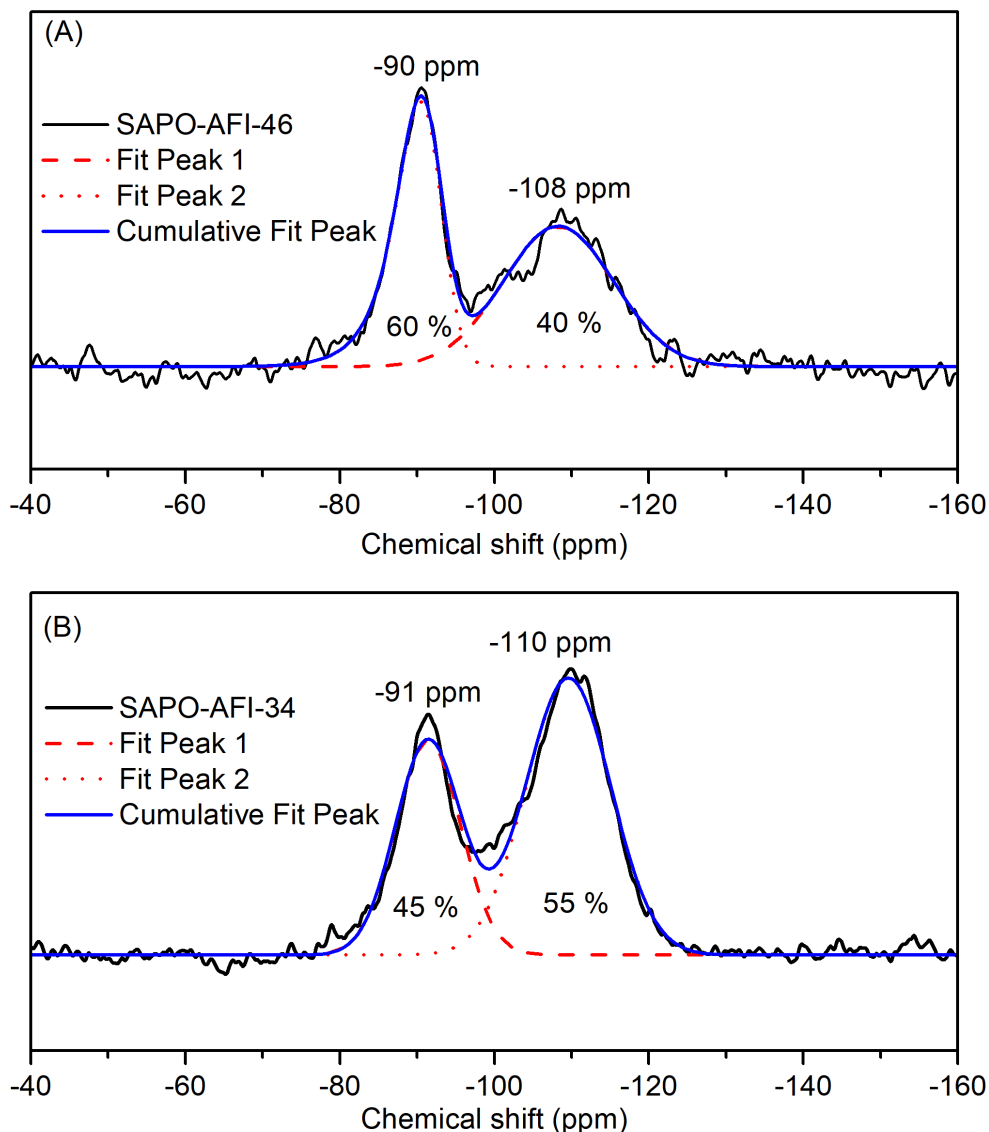
Figure 5.5: *Fitting example performed on the ^{29}Si MAS NMR spectra (A) SAPO-AFI-46 and (B) SAPO-AFI-34. The peak center and the fractional area are indicated close to every peak.*

In what refers to the textural analysis of said samples, some anomalies are worth mentioning. Routine N$_2$ isotherm at -196 °C was not successfully measured on CHA-3, due to a decreased effective pore size having its origin in the presence of K$^+$ as charge-balancing ion in this

Table 5.2: *Framework composition as determined per ICP, isolated Si fraction as determined from* ^{29}*Si MAS NMR spectra and the estimated framework negative charge. Light blue background is for LTA, white is for CHA and light red is for AFI-structured materials.*

Sample	x_{Si}	x_{Al}	x_{P}	Isolated Si Fraction	Estimated Framework Negative Charge
AlPO-LTA	-	0.53	0.47	-	0
SAPO-LTA-104	0.04	0.5	0.46	0.24	0.010
SAPO-LTA-24	0.05	0.52	0.43	0.82	0.041
SAPO-LTA-13	0.1	0.54	0.36	0.8	0.08
Si-LTA	1	-	-	-	0
LTA-31	0.97	0.03	-	-	0.032
LTA-6	0.83	0.17	-	-	0.17
LTA-4.5	0.78	0.22	-	-	0.22
LTA-3	0.67	0.33	-	-	0.33
AlPO-CHA	-	0.57	0.43	-	0
SAPO-CHA-10	0.10	0.55	0.35	0.975	0.097
SAPO-CHA-7	0.18	0.51	0.31	0.814	0.15
Si-CHA	1	-	-	-	0
CHA-19	0.95	0.05	-	-	0.052
CHA-18	0.94	0.06	-	-	0.055
CHA-6	0.84	0.16	-	-	0.16
CHA-3	0.65	0.35	-	-	0.35
AlPO-AFI	-	0.54	0.46	-	0
SAPO-AFI-46	0.04	0.53	0.43	0.6	0.022
SAPO-AFI-34	0.06	0.54	0.40	0.45	0.030
Si-AFI	1	-	-	-	0

material. Therefore, Dubinin Astakhov's method was used to determine the surface area from the CO_2 adsorption isotherm measured at 0 °C. DA surface areas tend to be systematically lower than their respective BET surface areas, as evidenced by comparing both calculated values in materials where the two were obtainable. This means that probably, the displayed DA surface area value of CHA-3 (470 m^2/g) would translate to

a larger value of BET surface area.

5.2 Adsorption isotherms and isosteric heats of adsorption of carbon dioxide

The adsorption of CO_2 on these materials was studied by measuring isotherms at temperatures ranging from 0 to 60 °C and pressures up to 100 kPa, generally. In some cases, higher pressures were reached. The measured CO_2 isotherms at 25 - 30 °C are presented in fig. 5.6. Materials with a higher framework charge present steeper low-pressure regimes in their isotherms and reach saturation at lower values of pressure (above 100 kPa), which is reasonable, as it is a sign of the stronger adsorption that can take place when the quadrupole of CO_2 interacts with charged moieties. This is the case of zeolites with low Si/Al ratio, such as CHA-3 and LTA-3. The isotherms of materials with low framework negative charge, i.e. AlPOs, SAPOs and high- and pure silica zeolites are similar and reach saturation at higher pressures (above 500 kPa, see fig. 5.7). The saturation loading of materials that share the same structure is comparable, and in the case of LTA and CHA materials, around 5 mmol/g.

By applying Clausius-Clapeyron's method to sets of at least 3 isotherms measured at temperatures ranging from 0 to 60 °C, the isosteric heat of adsorption of CO_2 at different loadings was calculated for each material (see fig. 5.8). In most AlPO and SAPO materials, an initial drop in the trend of the q_{st} with the adsorbed amount is observed, which has its origin in energetic inhomogeneities on the surface of the adsorbent. Another possibility, especially for LTA and CHA is that, at low loadings an optimal fitting of the molecules with the surface takes place [488]. At higher loadings, the q_{st} rises slowly, due to the lateral interactions between adsorbate molecules becoming more important [160]. Zeolites with high negative framework charge, such as LTA-3 or CHA-3, present the opposite behavior.

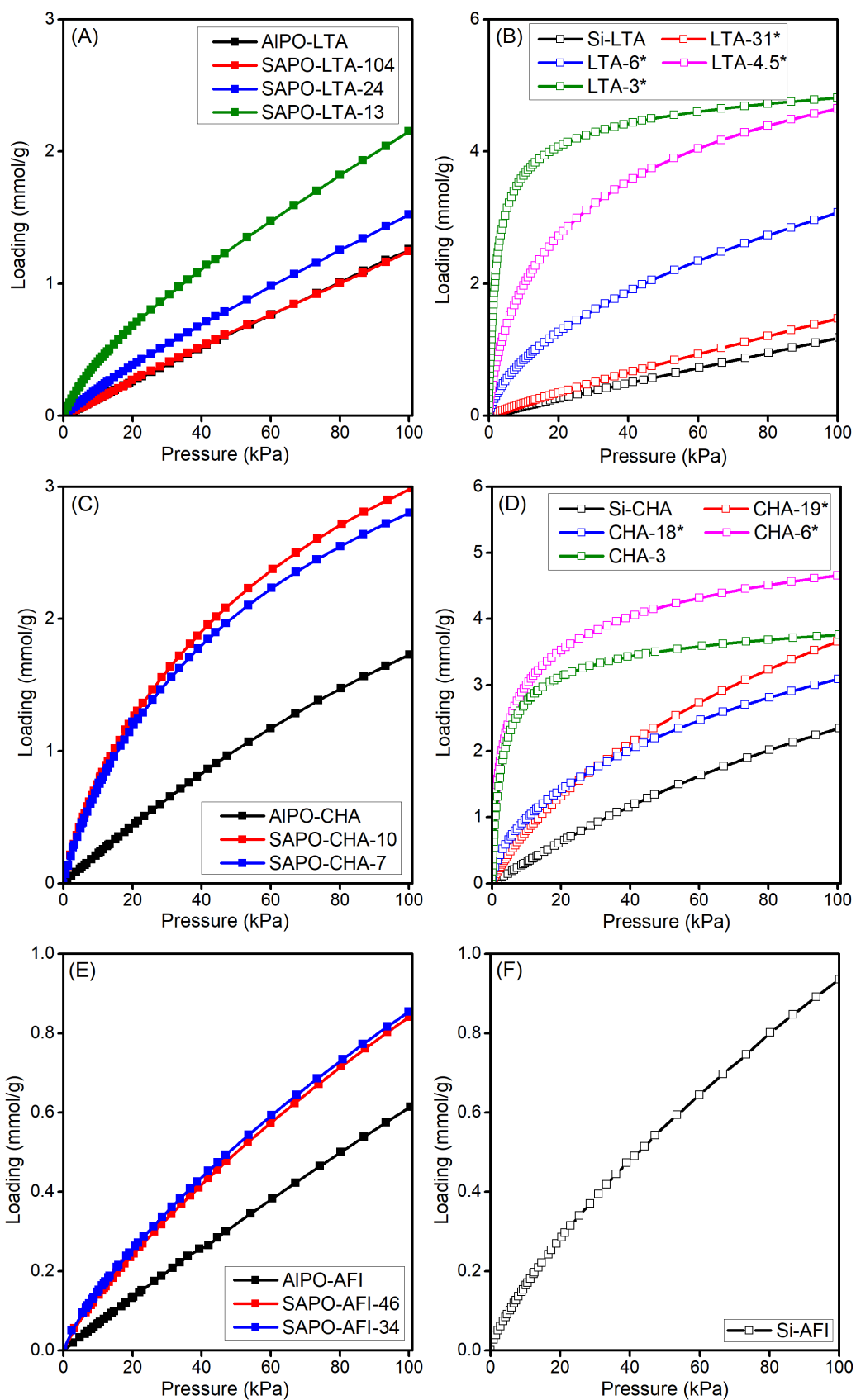Interestingly, in the materials studied in this chapter, which are either

Figure 5.6: *CO₂ adsorption isotherms at 25 °C (*30 °C) and up to 100 kPa on LTA (A, B), CHA (C, D) and AFI (E, F) materials. The lines are guides to the eye.*
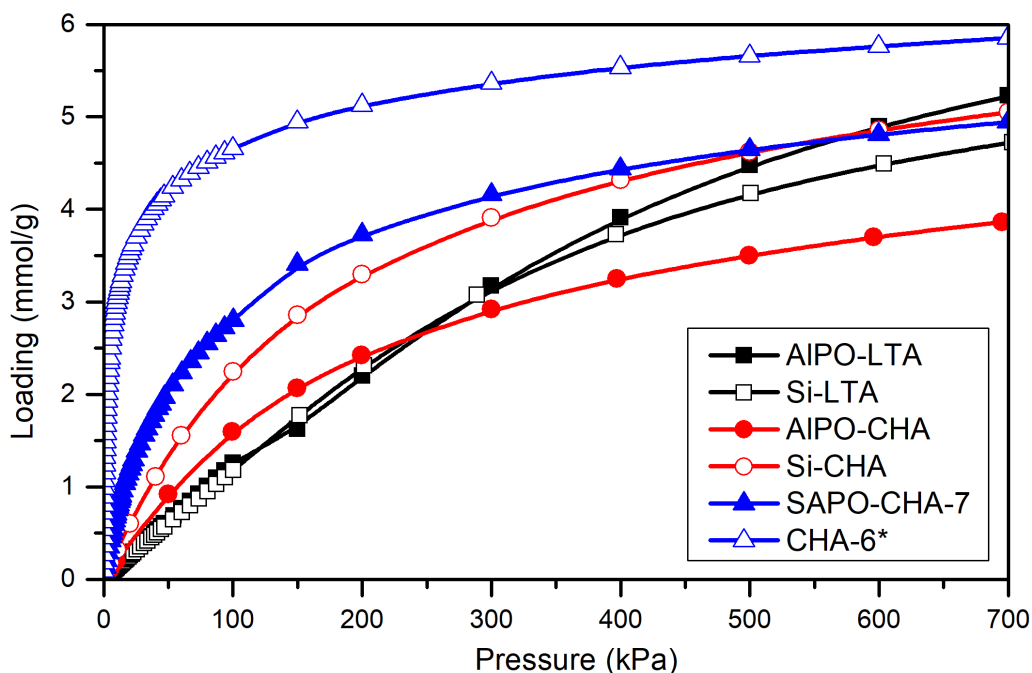
Figure 5.7: *CO_2 adsorption isotherms at 25 °C (*30 °C) and up to 700 kPa on selected LTA and CHA materials. The lines are guides to the eye.*

channel-like large-pore (AFI) or cavity-like small-pore zeolites (LTA, CHA), the value of the CO_2 q_{st} approaches values between 25 and 30 kJ/mol at high loadings, which are close to the sublimation enthalpy of CO_2. This means that, under these conditions, the lateral interactions between adsorbate molecules* resemble those characteristic of solid CO_2 [490].

AlPO-LTA and SAPO-LTA-104 present very similar adsorption isotherms and isosteric heats (starting at ca. 12 kJ/mol), which may be understood, as this SAPO presents Si mainly as Si-islands. The q_{st} of Si-LTA is ca. 10 kJ/mol above that of AlPO-LTA at all loadings. SAPO-LTA-13 and SAPO-LTA-24 present very similar initial values around 20 kJ/mol, but the q_{st} of the latter drops to ca. 3 kJ/mol below the trend of the first. The fact that SAPO-LTA-24 presents a lower q_{st} is easily explained by taking into account it has half the amount of isolated Si that SAPO-LTA-13 has. The LTA zeolites present the expected sequence in this sense, with the lowest initial q_{st} value belonging to Si-LTA and the highest to the material presenting the highest negative charge, which is LTA-3.

---

*In materials with tighter pores, this would probably not be the case, as was seen for Si-RWR-b in fig. 4.13 and will be seen for Si-ITW in chapter 6.
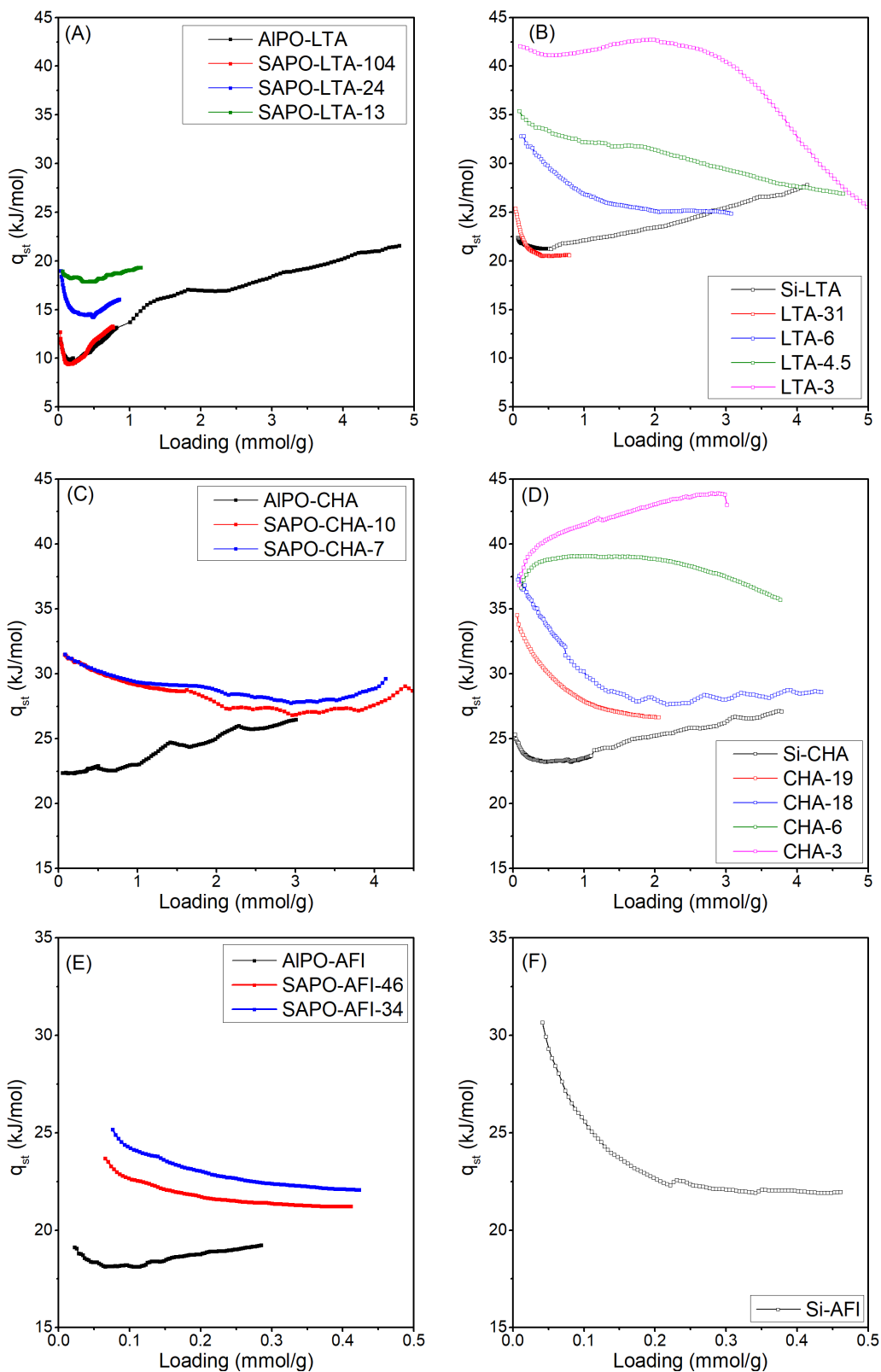
166

Figure 5.8: *Isosteric heat of adsorption of CO_2 against the adsorbed amount on materials with LTA (A, B), CHA (C, D), and AFI (E, F) structures.*

In the case of CHA-structured materials, the AlPO and the pure silica materials present similar trends of the q_{st} despite their initial values

differ (22 and 25 kJ/mol, respectively). However, those are notably different to those of the other CHA materials (32-38 kJ/mol). SAPO-CHA-10 and SAPO-CHA-7 present similar trends, which start at 32 kJ/mol and decrease slowly to 27 and 28 kJ/mol, respectively. The trends in CHA zeolites present the expected order, with the low Si/Al materials presenting the highest q_{st}. It is noteworthy that CHA-18, CHA-6 and CHA-3 have a very similar starting value, which could be due to energetically similar adsorption sites being occupied first.

All AFI materials present q_{st} trends with an initial decrease. Si-AFI presents a notably higher value of q_{st} at low loading (31 kJ/mol) than AlPO-AFI (19 kJ/mol). This high starting value for Si-AFI may be related to the relatively high concentration of connectivity defects (10 %, see table 5.1) in this material as determined by ^{29}Si MAS NMR. SAPO-AFI-46 presents a slightly lower q_{st} than SAPO-AFI-34 in all the range of loadings studied, which seems reasonable from their respective framework charges.

From all these results, the fact that all AlPOs and even some SAPOs present lower heats of adsorption of CO_2 than even pure silica zeolites is especially interesting. By taking the q_{st} at low loadings, i.e. $q_{st,0}$, and plotting it against the estimated negative framework charge* (see fig. 5.9), a highly informative way of analyzing these data arises. In this kind of plot, materials of different chemical composition may be compared in terms of their intrinsic affinity towards a specific adsorbate (in this case CO_2). LTA zeolites, as reported in [279], present a linear relationship (black coninuous line) between the $q_{st,0}$ and the framework charge. This trend is also observed for LTA-AlPO and SAPOs and for AFI-AlPO and SAPOs (discontinuos blue and black lines). In LTA and AFI, all AlPO and SAPO materials studied present lower $q_{st,0}$ than the pure silica zeolite (and other zeolites) with the same structure. In AFI this can be attributed to the presence of a 10% Q^3 environments, i.e. silanol groups, as mentioned above, but in LTA, this is surely not the explanation, as Si-LTA is free of

---

*This plot was originally designed for zeolites, and used the Si/Al ratio as the horizontal axis. It receives the name of Palomino's Plot [279].

168

defects. CHA-AlPO and SAPOs also present lower $q_{st,0}$ than CHA-zeolites at similar values of framework charge, and their $q_{st,0}$ increases with the charge, but their relationship is clearly not linear.

On the whole, this indicates that SAPOs and AlPOs present an intrinsically lower heat of adsorption of CO_2 compared to zeolites and this could be practical for separation of CO_2 from relevant mixtures, as the regeneration would be less energy intensive, given that materials with the right selectivity, i.e. preferably small pore zeolites, are selected.
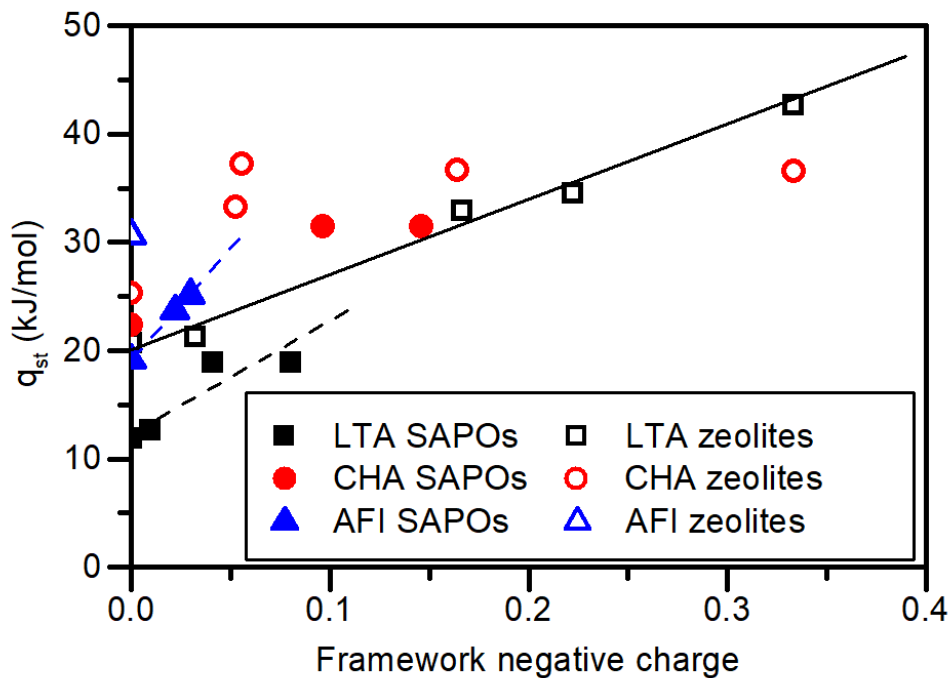

Figure 5.9: *Isosteric heats of adsorption of CO_2 on zeolites (open symbols), AlPOs and SAPOs (filled symbols) of LTA (black squares), CHA (red circles), and AFI (blue triangles) structures at low loadings plotted against the estimated negative framework charge. The points labeled as SAPOs that fall in the vertical axis (zero framework charge) correspond to AlPOs.*

5.3 Comparison of SAPOs, AlPOs and zeolites as adsorbents for the separation of CO_2 from CH_4

To bring these observations to a further level of significance, I compared AlPO/SAPO materials with their zeolitic analogues at similar values of estimated negative framework charge in the context of the CO_2/CH_4 separation. More specifically, the pairs AlPO-LTA/Si-LTA, AlPO-CHA/Si-CHA and SAPO-CHA-7/CHA-6 were chosen. From sets of isotherms measured at different temperatures and up to 700 kPa, the q_{st} of CO_2 and CH_4 and the CO_2/CH_4 ideal selectivities at 25 °C were calculated and are shown in fig. 5.10. Furthermore, the ideal working capacities of CO_2 at 25 °C were estimated for a PSA process that operates between 500 and 100 kPa and are presented in table 5.3. It must be noted, that the studied parameters give information on the ideal separation ability of these materials. A dynamic CO_2/CH_4 mixture adsorption study on these materials would give more accurate information on their real performance.

Table 5.3: *Carbon dioxide loadings at 100 and 500 kPa of some adsorbents and their PSA working capacity.*

Sample	Q_{100} (mmol/g)	Q_{500} (mmol/g)	$WC_{PSA}^{500-100kPa}$ (mmol/g)
AlPO-LTA	1.26	4.47	3.21
Si-LTA	1.18	4.17	2.99
AlPO-CHA	1.60	3.50	1.90
Si-CHA	2.24	4.62	2.38
SAPO-CHA-7	2.80	4.64	1.84
CHA-6	4.65	5.66	1.01

As can be seen in fig. 5.10A, C and E the isosteric heat of adsorption of CO_2 is higher than that of CH_4 on almost all of the selected materials, which denotes a favorable thermodynamical selectivity towards CO_2. The exception to that is only AlPO$-$LTA at low loadings, but in the end this does not lead to a lower selectivity in comparison to Si-LTA. From fig. 5.10A, it can be seen that Si-LTA presents higher heats of adsorption
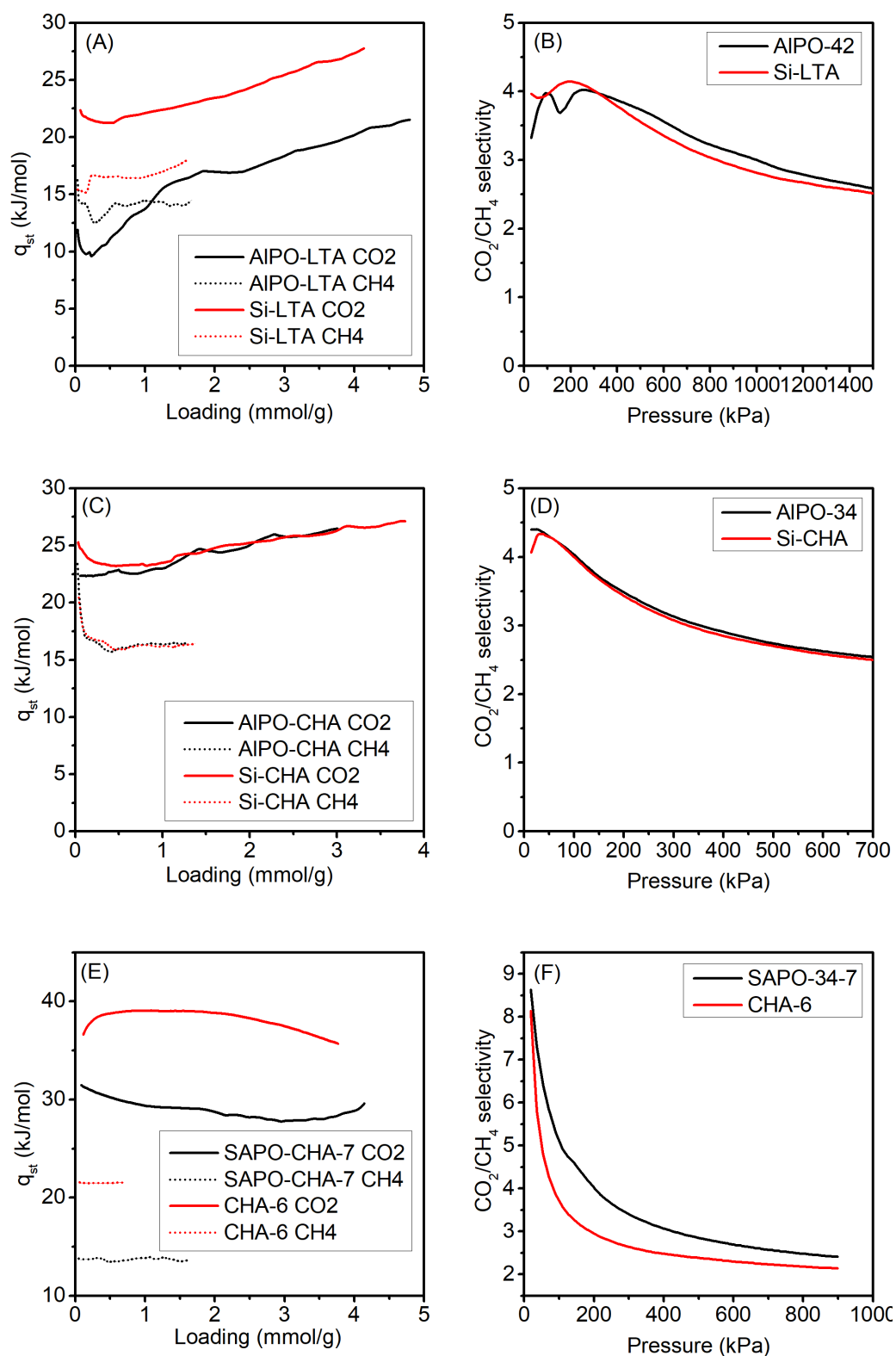
Figure 5.10: *Isosteric heats of adsorption (A, C, E) and CO₂/CH₄ pure component selectivities at 25 °C (B, D, F) on relevant AlPO/SAPO (black) and zeolite (red) pairs.*

171

of both CH_4 and CO_2 than AlPO-LTA. However, their CO_2/CH_4 ideal selectivities and working capacities are very similar. In the case of AlPO-CHA and Si-CHA, their isosteric heats and ideal selectivities are almost identical (fig. 5.10C and D), and Si-CHA surpasses AlPO-CHA in terms of working capacity. When comparing SAPO-CHA-7 and CHA-6, it can be appreciated that the zeolite has higher heats of adsorption of CO_2 and CH_4 by 7 kJ/mol in both gases. Interestingly, the selectivity is higher on the SAPO at all studied pressures. The working capacity is 80% higher on the SAPO, which together with the higher selectivity and easier regenerability, makes this material far more appealing as a CO_2 sorbent than the zeolite. This is in accordance to the fact that SAPO-CHA has previosuly been proposed as a CO_2 adsorbent/membrane for the separation of CO_2 from CH_4 [491–493].

Overall, it is concluded that, at similar values of the estimated negative framework charge, SAPOs can present advantages over zeolites in the CO_2/CH_4 separation. Frequently these advantages are related to lower isosteric heats of adsorption and equally good selectivities and similar working capacities, which could translate to significant energetic savings when using SAPOs as CO_2 adsorbents in separation processes. In some cases, selectivities and working capacities may be even more favorable on SAPOs than zeolites. Nonetheless, a possible issue that could arise when working with SAPOs and AlPOs in these processes is the adsorption of water and its effect on the material and the process itself.

5.4 Conclusions regarding AlPOs and SAPOs as carbon dioxide adsorbents

- AlPO and SAPO materials of LTA, CHA and AFI structure present lower isosteric heats of adsorption of CO_2 than their zeolitic counterparts.

- The selectivity in small-pore zeotypes is maintained when going from a zeolite to its isostructural AlPO/SAPO material.

- AlPOs and SAPOs are promising candidates to be applied as adsorbents in CO_2 separation processes, lowering the energy needed for regeneration while keeping similar selectivities in comparison to zeolites.

- Future research on this topic should be directed to finding other CO_2 selective AlPOs and SAPOs with appropriate chemical and thermal stability.

Chapter 6

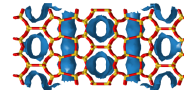# Influence of zeolite framework topology on the separation of carbon dioxide from methane
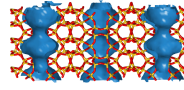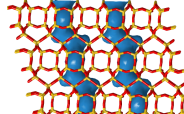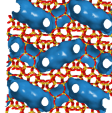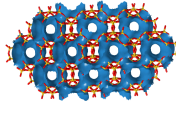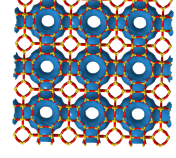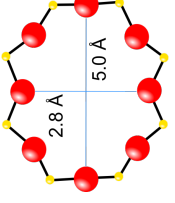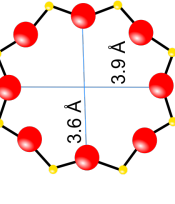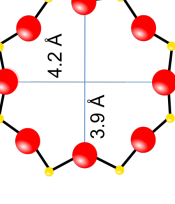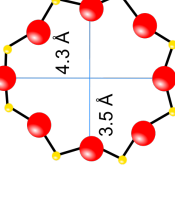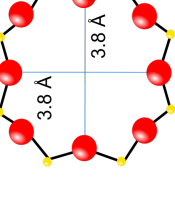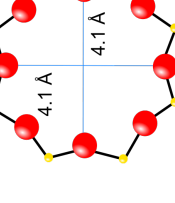
Many zeolitic materials are known that can act as adsorbents for separating CO_2 from its mixtures with CH_4 and N_2. Zeolite 13X is the one that has received most attention in this respect [243, 302–304, 307, 308], probably because of its low price and commercial availability. In this case, a high selectivity is achieved mainly through the differences in the specific interactions of CO_2 and CH_4 or N_2 with the cations present in the material. The main drawbacks of zeolite 13X are its energetically demanding regeneration and its hydrophilicity, which have their origin, too, in the presence of cations. Therefore, it may be understood that there are other materials, such as high- and pure silica zeolites, that are much more convenient for this separation, in which they present lower isosteric heats of adsorption and larger working capacities [265, 278–280, 489]. In these cases, selectivity may be achieved not only through the specific interactions with charged species, but also through the maximization of disperse interactions with the surface, i.e. close-fitting of the molecules in the pores [278, 488] or through molecular sieving [290, 292].

Inspired by these findings and with the objective to expand the range of tested materials and to see how these properties affect their applicability

to the CO_2/CH_4 separation, Miguel Palomino carried out an adsorption study of CO_2 and CH_4 on pure silica small pore zeolites with CHA, IHW, ITW and LTA structures [494]. Pure component isotherms were used in the calculations of the isosteric heats of adsorption of both compounds and the CO_2/CH_4 ideal selectivity. These materials present diverse framework topologies, with the channel system of CHA and LTA being tridirectional and possessing cavities (herefrom referred to as cavity-like), while IHW is bidirectional and also cavity-like and ITW is unidirectional and channel-like (see table 6.1). Coinciding with the observations made by Grajciar et al [278], channel-like Si-ITW was a material showing relatively high CO_2 q_{st} and this, combined with a lower adsorption of methane resulted in a high CO_2/CH_4 selectivity. I expanded this work by adding two other materials to the study, which are Si-RWR-a* (1D, channel-like) and Si-MTF (1D, cavity-like), and carrying out dynamic mixture adsorption experiments. Aluminosilicate zeolite LTA-6 was included as a reference material [265, 279] to compare its performance to the pure silica materials.

---

*It would have been better to include Si-RWR-b instead, as it is better suited for CO_2/CH_4 separation, but at the time that this study was carried out, I did not have enough amount of the Si-RWR-b sample.

Table 6.1: *Pore shape, opening size and framework topology of zeolites studied as CO$_2$ adsorbents in this chapter.*

Descriptor	Si-RWR	Si-MTF	Si-ITW	Si-IHW	Si-CHA	Si-LTA
Dimensionality	1D	1D	1D	2D	3D	3D
Topology	Channels	Cavities	Channels	Cavities	Cavities	Cavities
View 1						
View 2						
Pore Opening Size (Å)	2.8 × 5.0	3.6 × 3.9	3.9 × 4.2	3.5 × 4.3	3.8 × 3.8	4.1 × 4.1
Framework Density (T/1000 Å^3)	19.2	20.7	17.7	18.5	15.1	14.2

177

6.1 Materials description and characterization

As can be seen from table 6.1, most of the selected structures have approximately circular pore openings of ca. 4 Å diameter, except for RWR, which presents a clearly elliptical opening of dimensions 2.8×5.0 Å and IHW, which is ovoid, with a size of 3.5×4.3 Å. RWR presents a unidirectional (1D) channel system, which consists of two perpendicular but non-intersecting 1D channel systems, with a clear channel-like topology. MTF presents a 1D channel system and a cavity-like topology. ITW presents a 2D channel system but the pore openings in the [100] direction are too small for molecules to diffuse along, which practically renders this material as 1D. Its channel topology is channel-like, with side pockets. IHW is 2D and cavity-like, with elongated cavities. CHA is 3D and cavity-like, with elongated cavities. LTA is 3D and cavity-like, with spherical cavities. The framework density was another parameter described by Grajciar et al [278] to have a relevant effect on the heat of adsorption of CO_2 and thus, this parameter has been included in table 6.1. MTF presents a high density, closely followed by RWR, IHW, ITW and finally, CHA and LTA, with notably lower framework densities.

The samples used for this study were fully characterized and the results are presented in table 6.2, XRD and NMR spectra can be found in appendix A.1. As calculated from the ^{29}Si MAS NMR spectra, the only sample presenting a relevant amount of connectivity defects was Si-CHA, with 8 % of Si in the form of silanol groups. The highly variable particle size of the Si-ITW sample is due to repeated pelletization and usage throughout the years. Despite of that, the sample retains the same XRD and textural properties as when it was first calcined, which is a clear example of the high stability of pure silica zeolites. The DA surface area of Si-RWR-a is not fully trustworthy, due to the diffusional restrictions of CO_2 on this material, as discussed in section 4.3.

Table 6.2: *Characterization results of the samples after removal of occluded species.*

Sample	Si defects amount (% Q_3)	Crystal shape	Crystal dimensions (µm)	Pore diameter[a] (Å)	BET surface area (m^2/g)	DA surface area (m^2/g)	Micropore volume (cm^3/g)
Si−CHA	8	cubes	2 - 10	5.4	821	-	0.30
Si−IHW	0	needles	$2 \times 0.2 \times 0.2$	5.3	393	-	0.16
Si−ITW	0	indefinite	2 - 30	4.8	356	-	0.18
Si−LTA	0	cubes	0.3	6.4	811	-	0.32
Si−MTF	0	sheets	$5 \times 2 \times 0.1$	4.8	232	241	0.07
Si−RWR−a	1	sheets	$a \times a \times b$ ($1 < a < 6$; $b = 0.1$)[b]	-	-	180	-
LTA−6	-	cubes	0.4	-	806	-	0.30

[a]Obtained by applying Horwatz-Kawazoe to the Ar adsorption isotherm at -186 °C.

6.2 Pure component isotherms analysis

Adsorption isotherms of CO_2 and CH_4 at temperatures ranging from 0 to 60 °C and up to 100 kPa were measured on a volumetric Micromeritics ASAP2010 and isotherms at 10 - 60 °C and up to 700 kPa were measured on a gravimetric Hiden IGA3 device. The isotherms measured in the ASAP2010 were preferably used for the calculation of the isosteric heats of adsorption, as they are better defined in the low pressure regime, and the ones measured up to 700 kPa, for the calculation of ideal CO_2/CH_4 selectivities. Additionally, water isotherms were measured on Si-ITW, Si-RWR-a and LTA-6 on a volumetric BelSorp II Max device.

The first comparison between the selected materials is done in terms of their adsorption isotherms of CO_2 and CH_4 at 25 - 30 °C and up to 700 kPa, and is presented in fig. 6.1. As can be seen from fig. 6.1A, the aluminosilicate material LTA-6 presents the largest adsorption capacity of CO_2 followed by Si-CHA and Si-LTA. Out of these materials, Si-LTA presents a very favorable isotherm shape, which is close to linear up to 400 kPa, thus favoring a large working capacity. Si-ITW follows with a moderate CO_2 adsorption capacity and, finally, there are Si-IHW, Si-MTF and Si-RWR-a[*]. From fig. 6.1B, it is seen that Si-CHA, LTA-6 and Si-LTA present the highest CH_4 uptakes in the relevant range of pressures studied. They are followed by Si-IHW, Si-MTF and Si-ITW and, far below, by Si-RWR-a. These results point towards the channel-like materials, i.e. Si-RWR-a and Si-ITW, presenting the highest CO_2/CH_4 selectivities.

Additionally, the adsorption of CH_4 is kinetically hindered on Si-ITW and practically zero on Si-RWR-a. In fact, the CH_4 isotherm on Si-ITW is not fully equilibrated, as confirmed by comparing the isotherms measured on two devices at different temperatures (see fig. 6.2). Note that the differences between isotherms measured on the two devices are larger at lower temperatures, where equilibrium is further away from being reached. Additionally, the isotherms measured on the IGA overlap at low

---

[*]The isotherm of CO_2 on Si-RWR-a was measured on a high pressure volumetric Quantachrome ISorbHP device. Additionally, it is not fully equilibrated (see discussion in chapter 4).
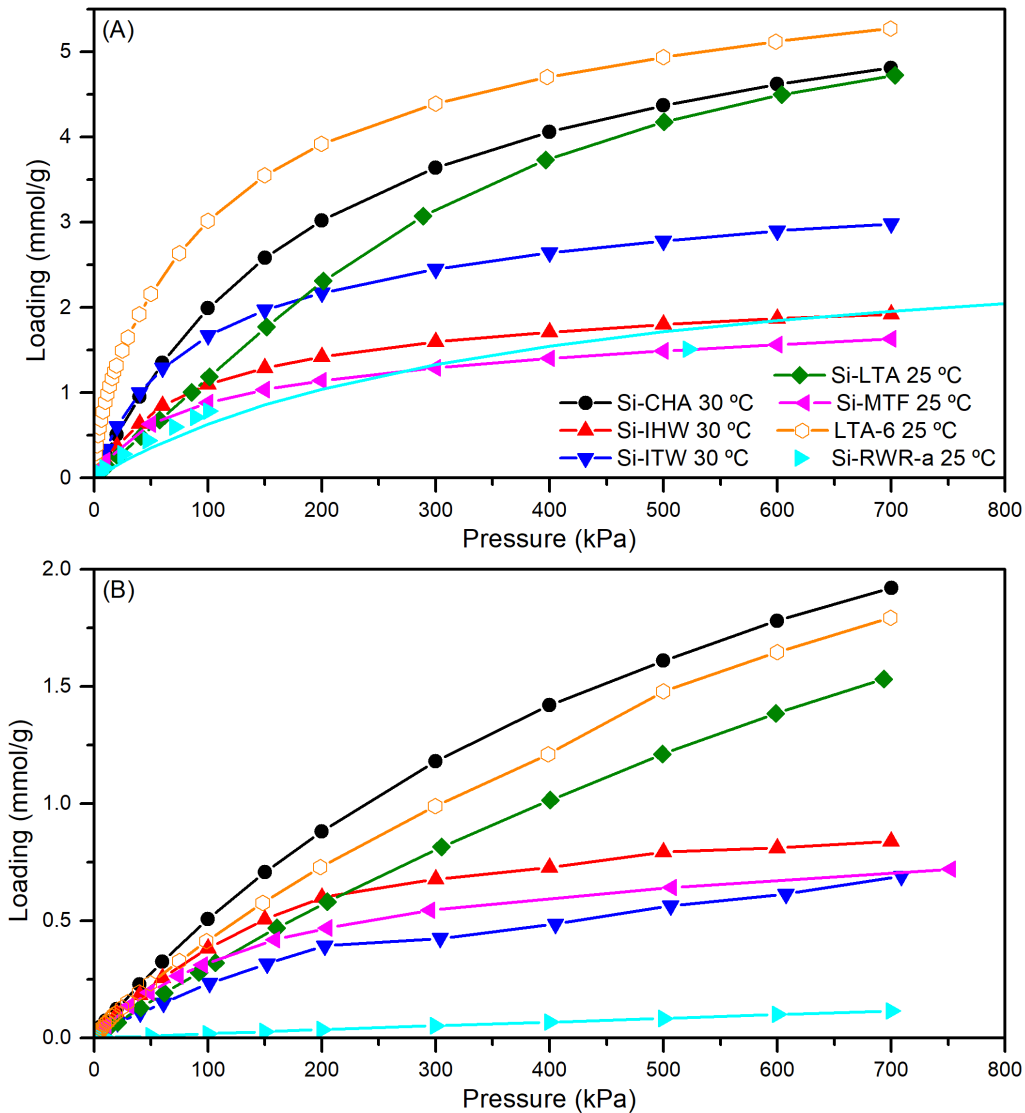
Figure 6.1: *Adsorption isotherms of (A) CO$_2$ and (B) CH$_4$ at ambient temperature on the selected pure silica zeolites. The lines are guides to the eye, save for CO$_2$ on Si-RWR-a, in which case the line corresponds to the Langmuir fit (eq. (3.6)).*

pressures.

The calculated pure component selectivities are presented in fig. 6.3. In this figure, Si-RWR-a comes forward as the material possessing the largest ($>$ 13) CO$_2$/CH$_4$ ideal selectivity at all studied pressures. In the embedded graph in fig. 6.3, the selectivities on the other materials can be observed with better definition. LTA-6 and Si-ITW present large selectivities ($>$ 5) below 200 kPa. After that, Si-ITW holds values around 5, while the selectivity on LTA-6 decreases to ca. 3. Zeolites Si-LTA and Si-CHA begin with values around 4 at pressures $<$ 100 kPa, which Si-LTA
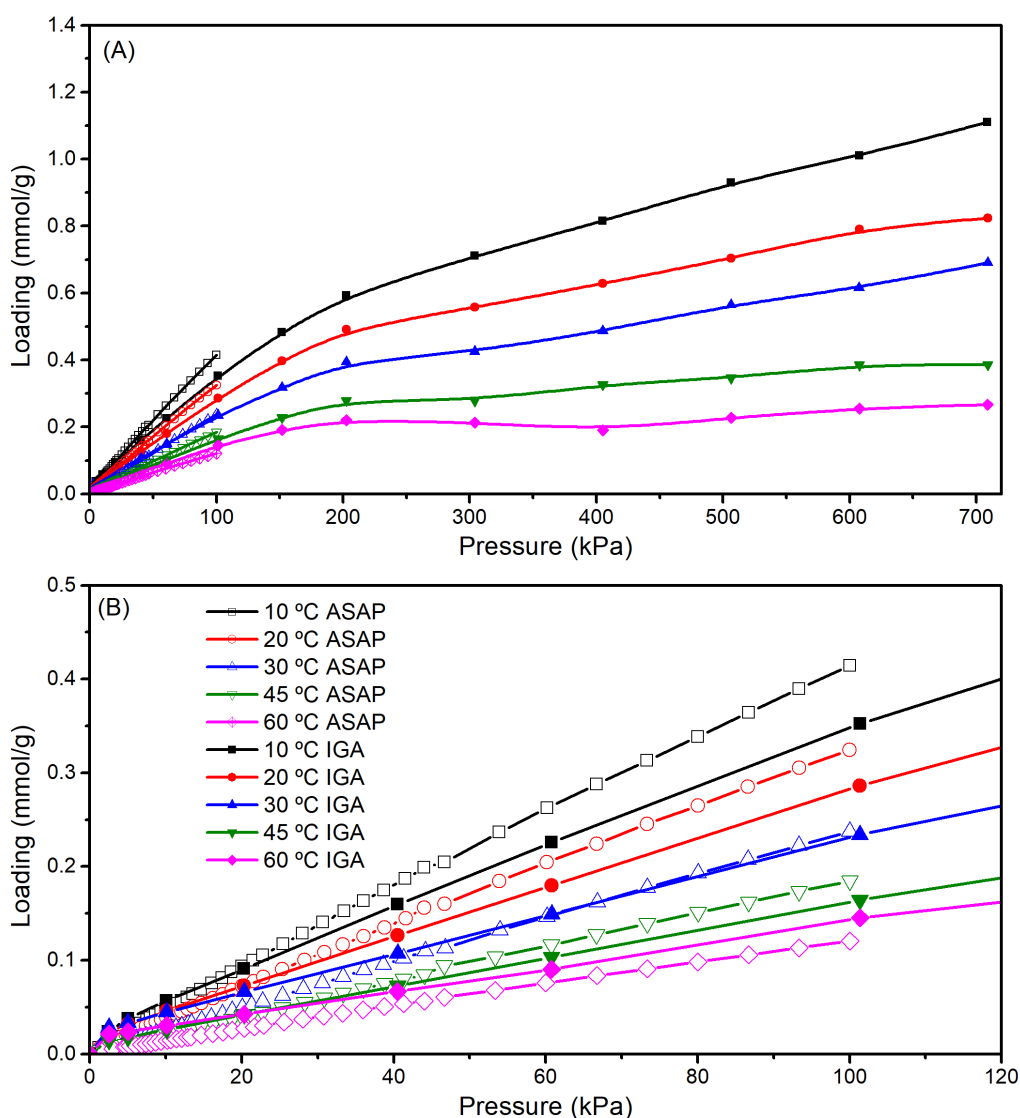
Figure 6.2: *Methane adsorption isotherms on Si-ITW measured on two different devices (A) up to 700 kPa and (B) zoomed in.*

holds up to 300 kPa, and then decrease to 3 and 2.5, respectively. It is noteworthy that, above 400 kPA, the selectivities on the two materials with LTA structure are very similar. The lowest CO_2/CH_4 selectivities are observed on Si-IHW and Si-MTF. These results confirm the idea that channel-like structures favor CO_2/CH_4 selectivity and that careful selection not only of the adsorbent composition or pore size, but also of its topology is important to a separation process.

The isosteric heats of adsorption of CO_2 and CH_4 are presented in fig. 6.4 and their values at low loadings in table 6.3. As can be seen, the heat of adsorption of carbon dioxide at low loading on each material,
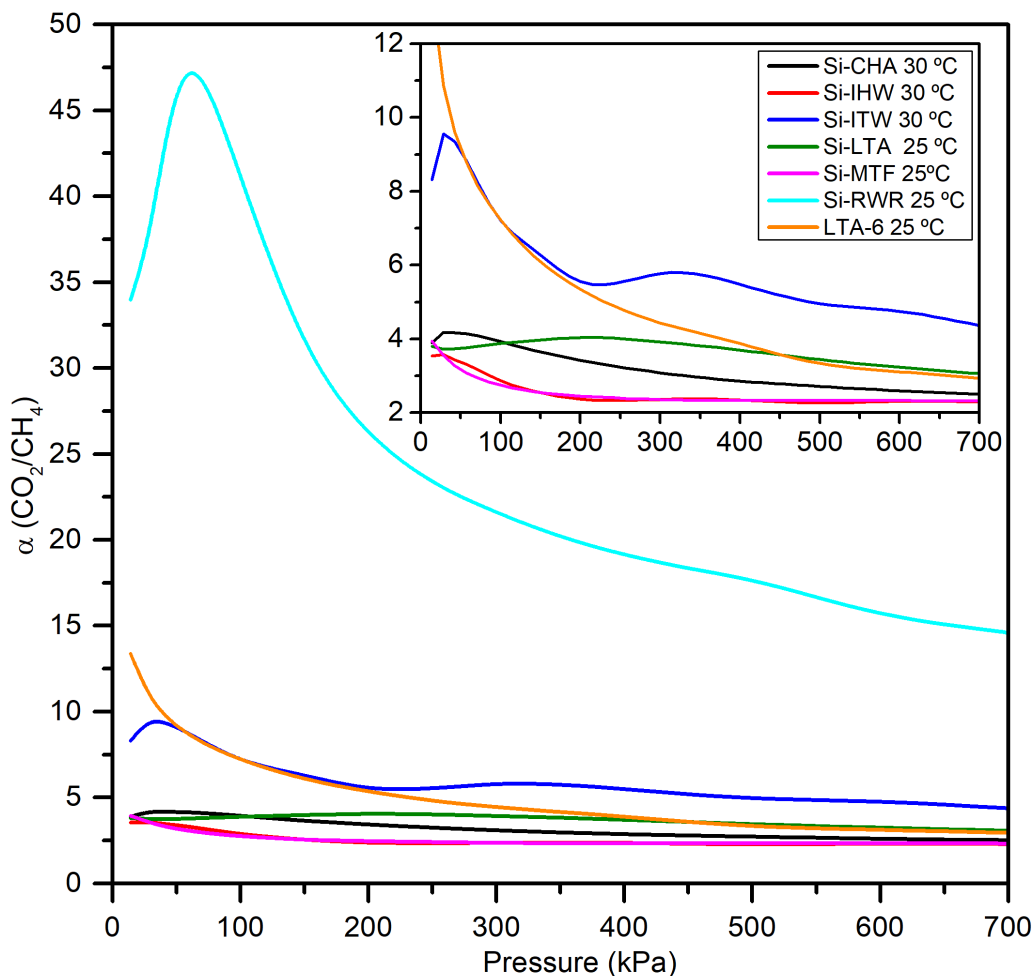
Figure 6.3: *Ideal CO$_2$/CH$_4$ selectivities on the selected pure silica zeolites plotted against the pressure. The embedded plot is a zoom on the Y-axis, leaving out Si-RWR-a.*

except Si-ITW, is ca. 5 kJ/mol larger than that of methane, indicating a stronger interaction of the first with the zeolite surface. In the case of LTA-6, the difference is of 18 kJ/mol. The zeolite presenting the largest CO$_2$ and CH$_4$ $q_{st,0}$ values is Si-ITW, even though the value for methane is subject to error due to not fully equilibrated isotherms, as explained above. The enhanced interactions with the surface of the channel-like material, i.e. the confinement effect, may be responsible for these relatively high values of q_{st} [278, 488]. The isosteric heat of adsorption of CO$_2$ on Si-RWR-a is also of doubtful validity, since the isotherms are not fully equilibrated (see chapter 4).

Table 6.3: *Isosteric heats of adsorption at low coverage of CO_2 and CH_4 on the studied materials.*

Sample	$q_{st,0}^{CO_2}$ (kJ/mol)	$q_{st,0}^{CH_4}$ (kJ/mol)
Si-CHA	25.3	20.5
Si-IHW	22.0	15.7
Si-ITW	27.6	26.5[a]
Si-LTA	22.4	15.4
Si-MTF	25.3	20.2
Si-RWR-a	18.9[a]	-[b]
LTA-6	25.9	7.8

[a] These values are not precise, as the isotherms were not fully equilibrated. [b] This value was not obtainable, as Si-RWR does not adsorb a quantifiable amount of CH_4.
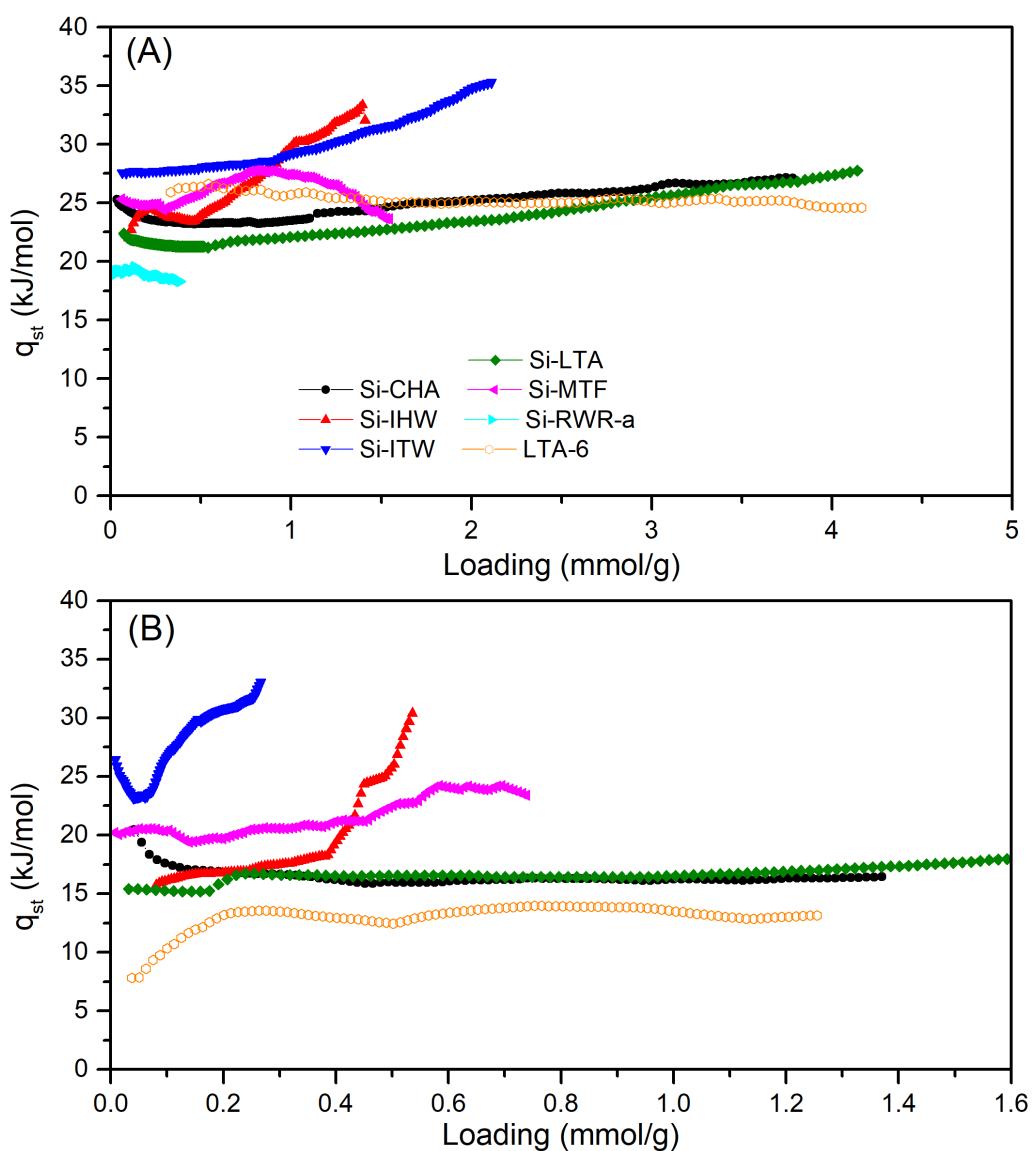
Figure 6.4: *Isosteric heats of adsorption of (A) CO_2 and (B) CH_4 on the selected pure silica zeolites plotted against the loading.*

Finally, and related to what will be discussed in the next section, the water isotherms on Si-ITW and LTA-6 are presented in fig. 6.5. As can be seen, Si-ITW is very hydrophobic and adsorbs a very small amount of water, whilst LTA-6 is considerably hydrophilic and adsorbs a large amount of water. These results are expected, considering that defect-free pure silica zeolites, such as Si-ITW, tend to be hydrophobic and the opposite applies for aluminosilicate zeolites, such as LTA-6. This is meaningful, in which water adsorption decreases the efficiency of the separation of CO_2, by competing with it or even reacting with it [272, 273, 276, 277], and thus, a hydrophobic sorbent, such as a pure silica zeolite, will circumvent these problems.
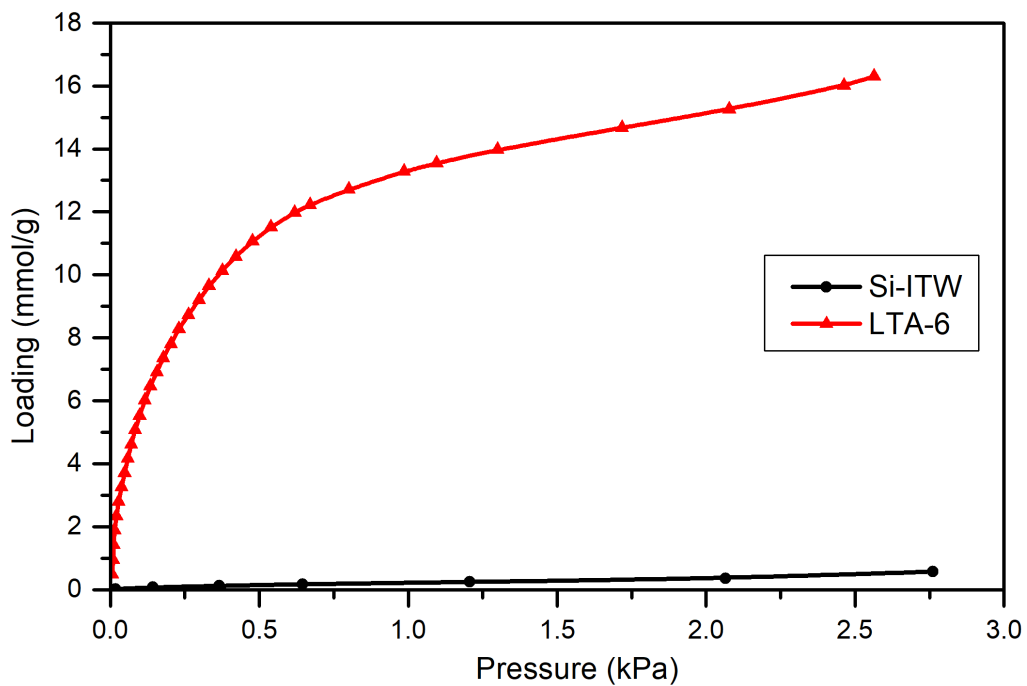
Figure 6.5: *Water adsorption isotherms on Si-ITW and Si-LTA-6.*

6.3 Breakthrough adsorption experiments

The materials presenting the highest ideal CO_2/CH_4 selectivities, i.e. Si-RWR-a, Si-ITW and Si-LTA, were further studied by carrying out breakthrough adsorption experiments of pure components and of CO_2/CH_4 mixtures in 1:1 and 1:4 molar ratios. An amount of ca. 0.66 g of material pelletized to sizes from 0.2 to 0.4 mm was diluted with SiC and packed into a cylindrical column of 4 mm internal diameter, achieving adsorbent bed lengths of ca. 12.5 cm (see table 6.4).

Table 6.4: *Adsorbent amounts (m) and bed lengths (l) used for the breakthrough experiments.*

Material	m (g)	l (cm)
Si-LTA	0.6535	12.9
LTA-6	0.6618	12.5
Si-ITW	0.6652	12.5
Si-RWR-a	0.6550	11.7

Table 6.5: *Feed compositions used for the breakthrough experiments of permanent gases in this study.*

Feed	y_{CO_2}	y_{CH_4}	F_{CO_2} (mL STP/min)	F_{CH_4} (mL STP/min)	$F_{Ar,dil}$ (mL STP/min)
pure CO_2	1	0	25	0	269 ± 3
pure CH_4	0	1	0	25	269 ± 3
CO_2/CH_4 20:80	0.2	0.8	5	20	269 ± 3
CO_2/CH_4 50:50	0.5	0.5	12.5	12.5	269 ± 3

The temperature was kept at 25 °C and the system pressures were 200 and 700 kPa for the mixture experiments and 200 kPa for the pure component experiments. A reportedly promising aluminosilicate material, i.e. LTA-6 (LTA-5 in [265, 279]) was added to this part of the study for comparison. As presented in section 3.3.4.1, a total volumetric flow of

gas mixture of 25 mL STP/min was fed to the column, and was diluted with ca. 270 mL STP/min of Ar. The mixtures and corresponding flows are presented in table 6.5.

In fig. 6.6 the amounts adsorbed calculated from the breakthrough curves of the pure components are compared with the isotherms. As can be seen, the adsorbed amounts calculated from the BT experiments match qualitatively well with the adsorption isotherms. In most cases, these are above the loadings given by the isotherm and the deviation is relatively larger for CH_4 than for CO_2. This analysis is important in order to contextualize the results and the conclusions to be drawn from them, which are mainly of qualitative nature, as an exact quantitative analysis will probably not be fully reliable. Luckily, I have used an almost constant amount of adsorbent and bed length in all the experiments (see table 6.4), which allows for comparison between the experiments carried out with the different materials.

The experiments using mixtures of gases allow for analyzing the suitability of the selected adsorbents for separation processes of CO_2 and CH_4. By carrying out experiments at different feed compositions (CO_2/CH_4 20:80 and 50:50) and pressures (200 and 700 kPa), the best adsorbent for each set of conditions may be selected. The most relevant experimental breakthrough and regeneration profiles are presented in figures 6.7 - 6.10 and the whole set of experiments is available in appendix A.3. In these, normalized flows (I have simplified the notation from $y_i \dot{n} / y_{i,0} \dot{n}_0$ to $\dot{n}_i / \dot{n}_{i,0}$) are plotted against time.

Visual examination of the plots already allows for the obtention of key qualitative conclusions. As can be seen, despite of possible competition between the adsorbates, in all the experiments CH_4 is the least and less strongly adsorbed component of the mixture and therefore breaks through in the first place. Being the first component to break through, it is not surprising that most of its flow profiles present a roll-up, in which the flow coming out of the column is higher than that in the feed. This is due to methane being adsorbed and afterwards displaced by carbon
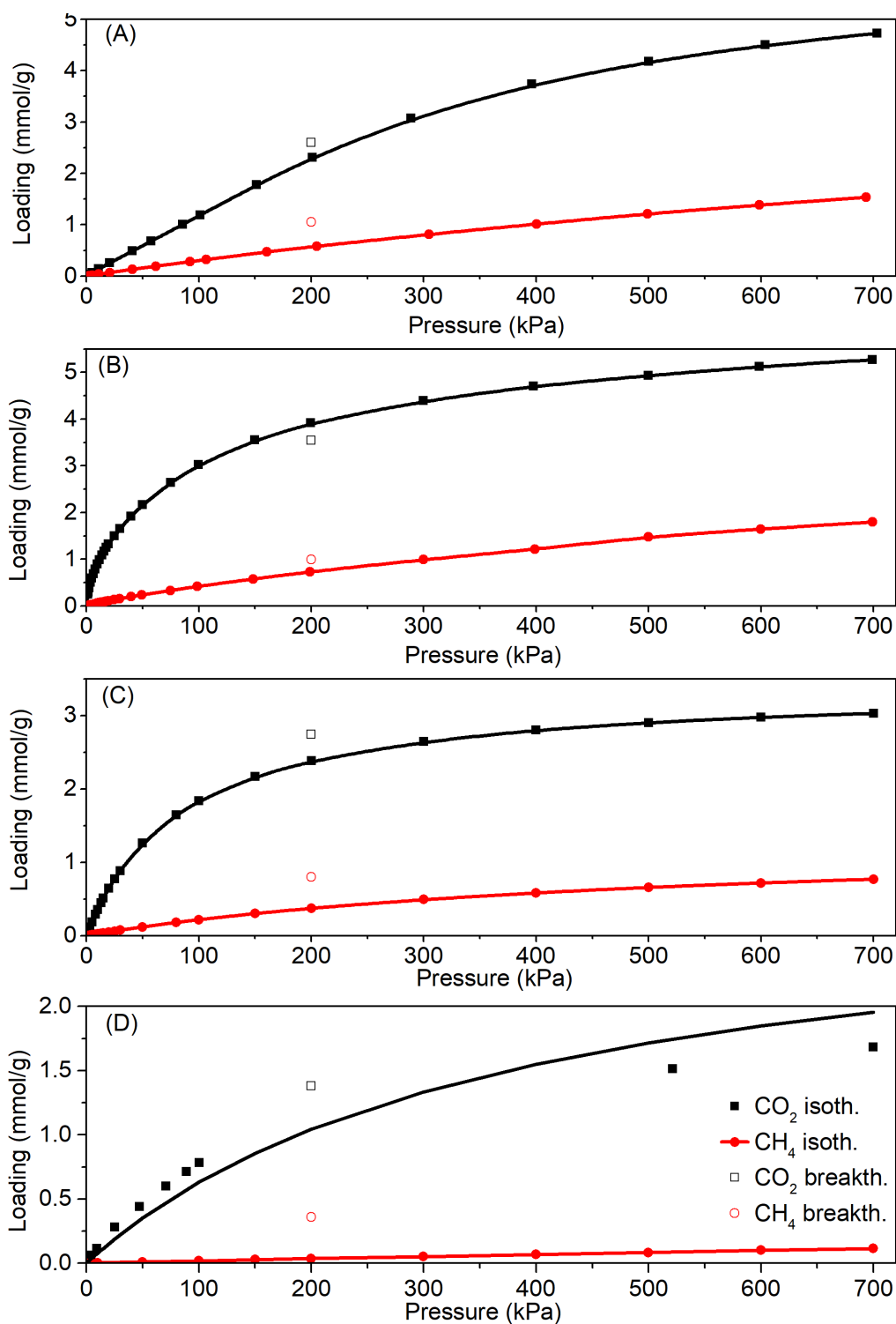
Figure 6.6: *Adsorption isotherms of CO_2 and CH_4 on (A) Si-LTA, (B) LTA-6, (C) Si-ITW and (D) Si-RWR-a at 25 °C compared with the amounts adsorbed calculated from pure component breakthrough adsorption experiments. Lines are guides to the eye, save for Si-RWR-a, where they correspond to the Langmuir fit of the CO_2 isotherm. The ITW isotherm at 25 °C was estimated as explained in appendix A.2.*
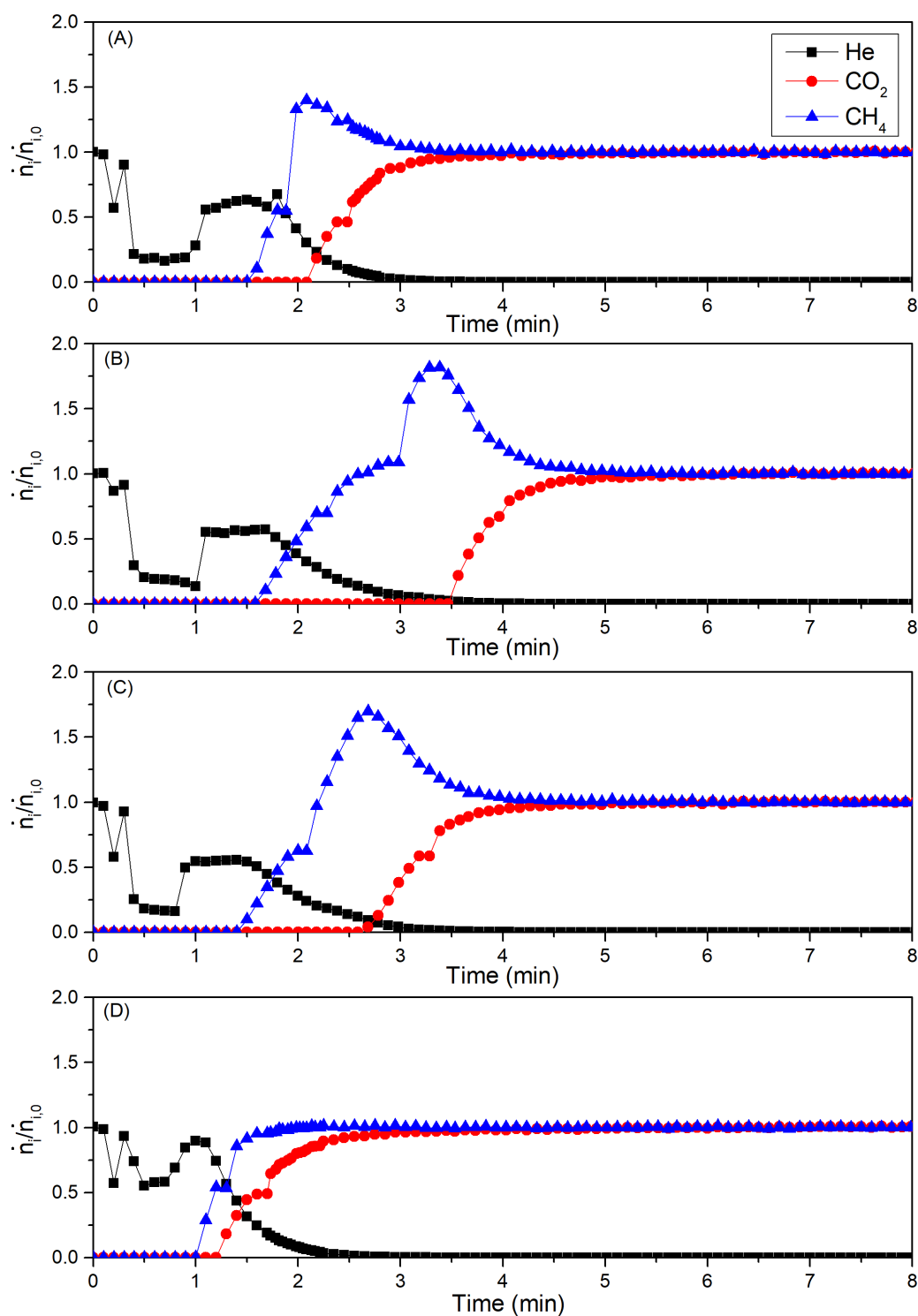
Figure 6.7: *Breakthrough curves at 25 °C and 200 kPa of a 50:50 CO₂/CH₄ mixture on (A) Si-LTA, (B) LTA-6, (C) Si-ITW and (D) Si-RWR-a.*

dioxide, which is adsorbed more strongly. Another general feature of these breakthrough profiles is that there are cases in which, prior to breakthrough of CH_4 the total flow coming out of the column (consisting purely of He at these early times) decreases temporarily. This is seen as
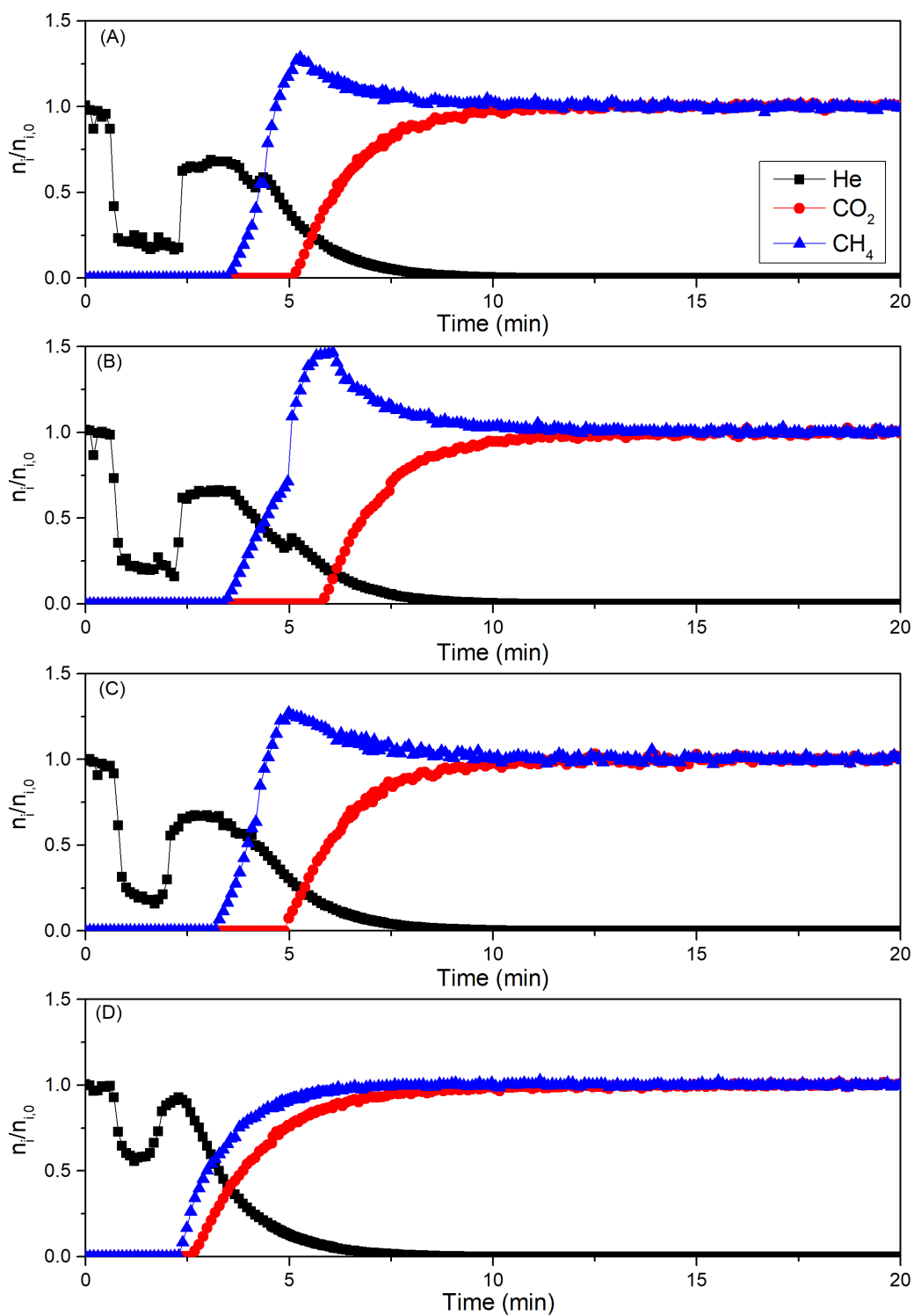
Figure 6.8: *Breakthrough curves at 25 °C and 700 kPa of a 50:50 CO₂/CH₄ mixture on (A) Si-LTA, (B) LTA-6, (C) Si-ITW and (D) Si-RWR-a.*

a drop in the flow and comes from the fact that a substantial part of the incoming CO_2/CH_4 feed is being adsorbed. If these experiments had been carried out with a diluted mixture, this effect would be much less notorious. These observations are qualitatively applicable to all the experiments.
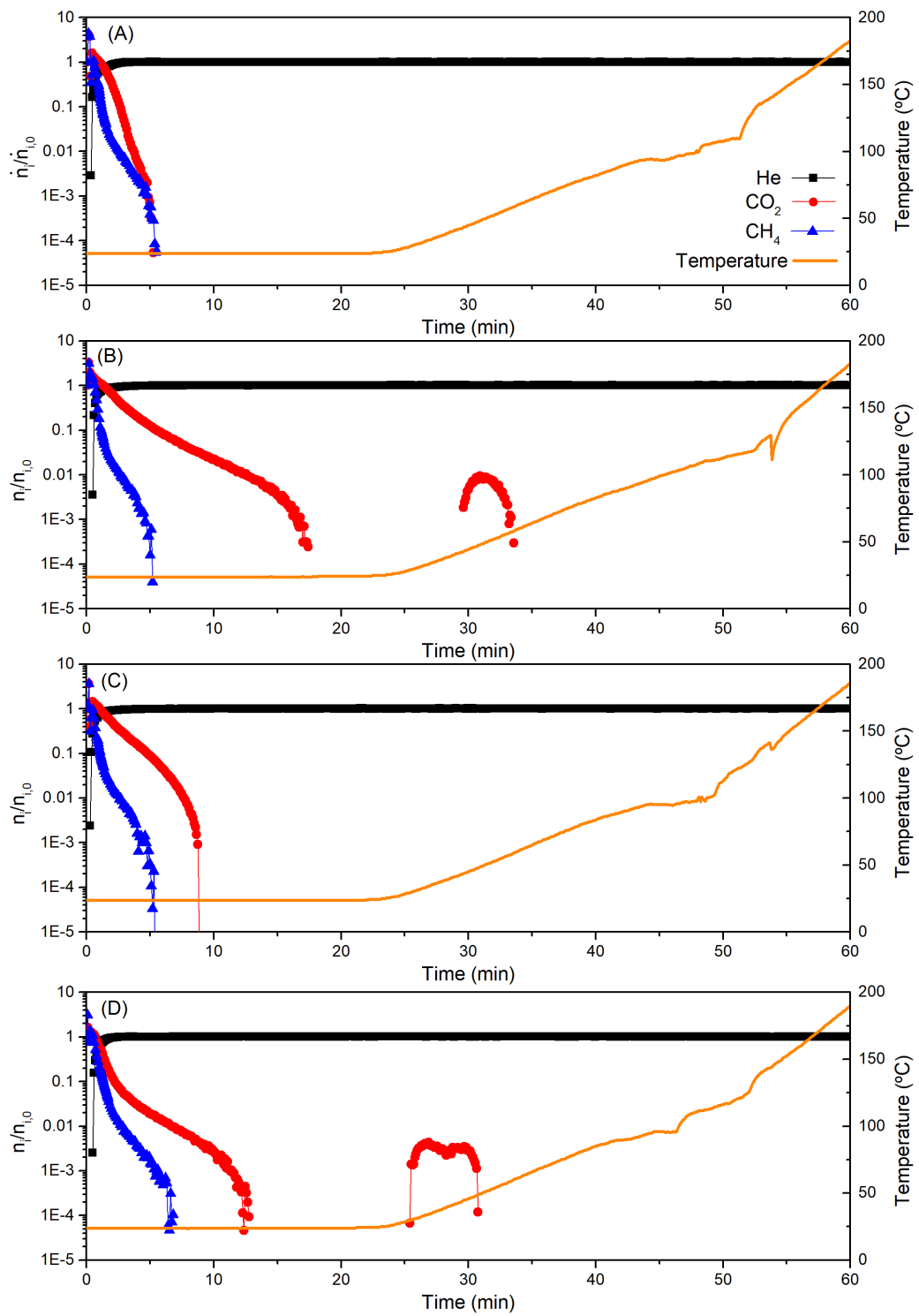
Figure 6.9: *Regeneration profiles at 25 °C and 200 kPa of a 50:50 CO₂/CH₄ mixture on (A) Si-LTA, (B) LTA-6, (C) Si-ITW and (D) Si-RWR-a.*

191
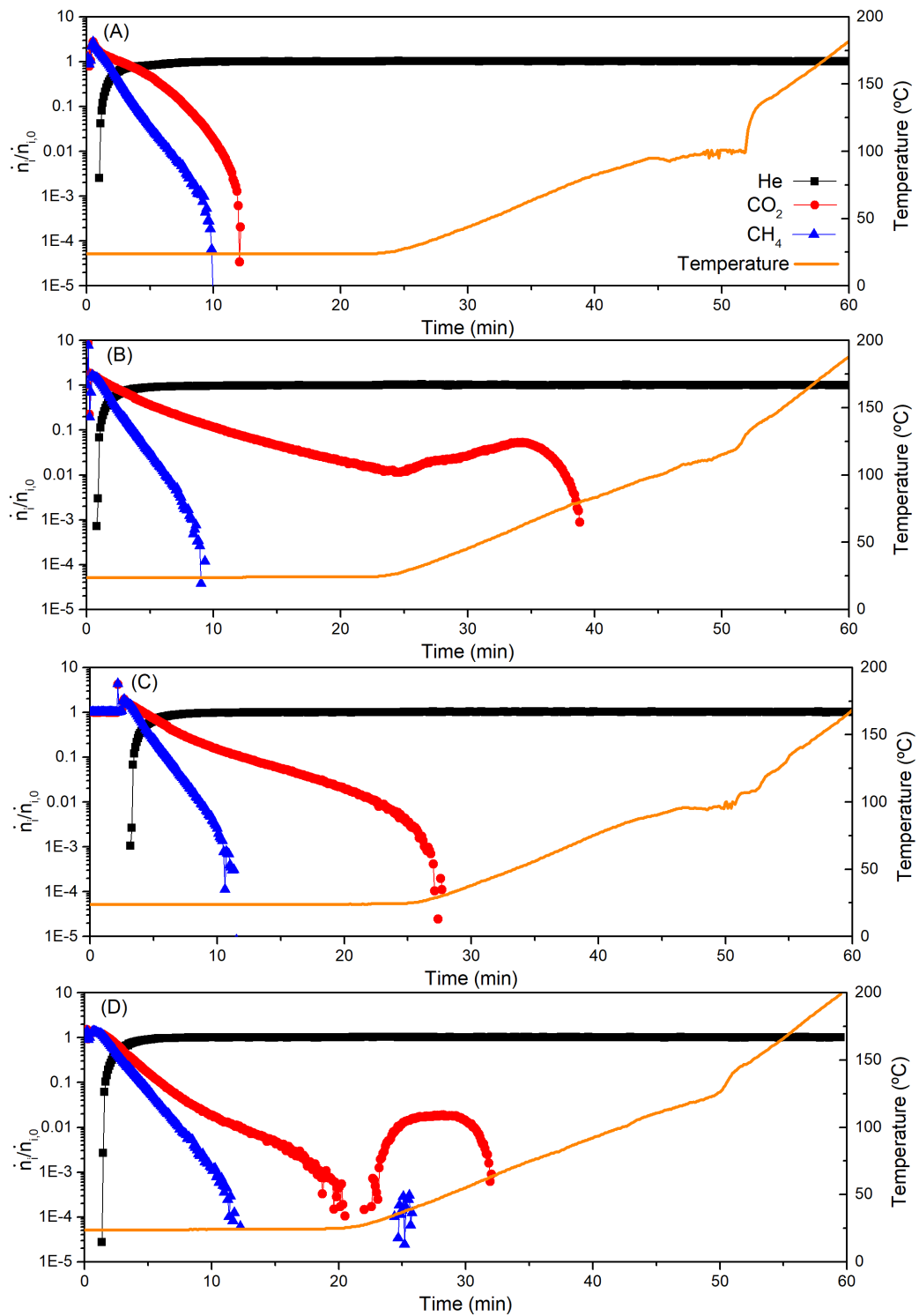
Figure 6.10: *Regeneration profiles at 25 °C and 700 kPa of a 50:50 CO₂/CH₄ mixture on (A) Si-LTA, (B) LTA-6, (C) Si-ITW and (D) Si-RWR-a.*
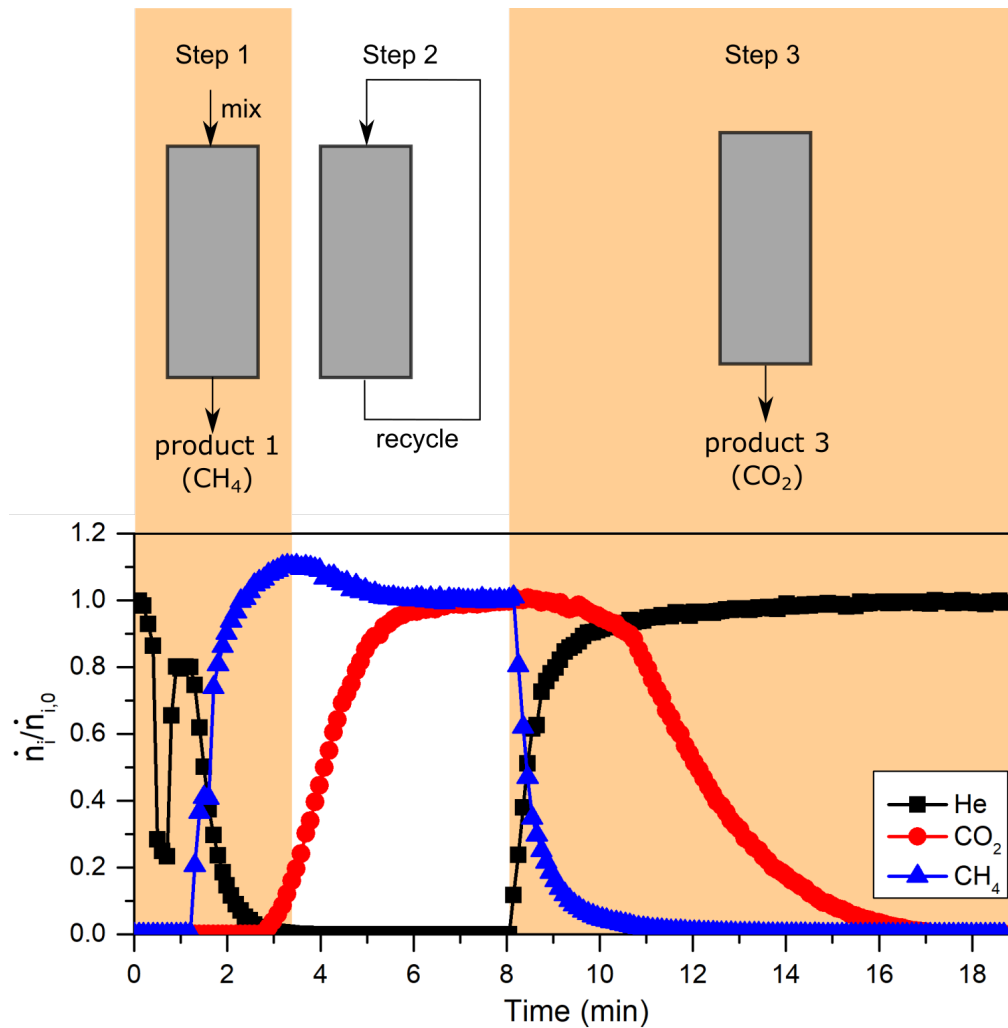
Figure 6.11: *Breakthrough and regeneration curves at 25 °C and 200 kPa of a 20:80 CO_2/CH_4 mixture on Si-ITW and schematic representation of their relationship with the hypothetical process described in section 3.3.4.1. Slightly modified for the sake of clarity.*

In figures 6.7 and 6.8, the general aspect of the adsorption step (steps 1 - 2 of the process, see fig. 6.11) may be observed. Qualitatively, the separation performance of the studied materials follows the trend LTA-6 > Si-ITW > Si-LTA >> Si-RWR-a in terms of the difference of breakthrough times of CO_2 and CH_4, which directly affects the productivity of CH_4 as part of product 1 and the purity of CO_2 in product 3. Si-RWR-a results in a poor adsorbent for carrying out this separation despite its high CO_2/CH_4 ideal selectivity, due to the slow diffusion and low adsorption capacities. The slow diffusion of CO_2 is confirmed, as the normalized flow reaches a value of 1, i.e. equilibrium, at longer times after CO_2 breakthrough than on the other adsorbents. LTA-6 is the adsorbent presenting the

193

largest difference between breakthrough times of both components. Si-ITW separates both components better than Si-LTA at 200 kPa, but at 700 kPa their performance appears to be very similar. Increasing the pressure of the process from 200 to 700 kPa increases the duration of the adsorption and equilibration steps, and the absolute difference between the breakthrough of both components, thus having a positive effect on the productivity of the adsorbent.

Regeneration profiles recorded at the end of the previous adsorption experiments corresponding to the step 3 of the hypothetical process presented in section 3.3.4.1 are presented in figures 6.9 and 6.10. In these, it becomes clear that regeneration is more difficult in LTA-6 and Si-RWR-a compared to Si-ITW and Si-LTA. In the case of Si-LTA, less than 15 minutes under isothermal inert flow are enough to fully regenerate the bed. Increasing the pressure increases the regeneration time of all the adsorbents and the temperatures needed for complete regeneration in Si-RWR-a, Si-ITW and LTA-6.

The data were treated as presented in section 3.3.4.1 and the most relevant results, i.e. adsorbed amounts, mixture selectivities ($\alpha_{CO_2,CH_4}^{mix,eq}$), adsorbent productivity of methane ($\overline{Prod}$), recoveries ($\overline{R_{CO_2}}$, $\overline{R_{CH_4}}$) and purities of the products ($\overline{Pur_{CO_2}}$) * are presented in table 6.6 and discussed below. These results allow for a detailed analysis on the adsorbent performance at each experimental condition. Methane purities in product 1 are fixed at $> 97\%$, according to natural gas specifications [485].

Methane productivities are surprisingly high in general,[†] probably due to the simplified method used to extrapolate the breakthrough results to a hypothetical process, but they will serve for comparison. In most cases, and probably, due to how it is calculated, the CO_2 recovery is relatively high ($> 90\%$).

---

*Note that the purity of the methane-rich product 1 is set $> 97\%$.

[†]My reason to believe thy are "surprisingly high" is that zeolite 13X, a benchmark adsorbent for CO_2 separation, is reported to give a productivity value significantly lower (0.75 mol/kg/h) than the ones I have obtained for most of the adsorbents studied here. Zeolite 13X was studied via numerical simulation in a 6-step PSA for landfill gas processing at total pressures ranging from 100 to 800 kPa and a feed composition of 40:60 CO_2/CH_4 [495].

- **CO_2/CH_4 20%:80% 200 kPa**

  - Si-LTA presents a low mixture selectivity (2.7) and CO_2 purity of product 3 (40 %). Methane productivity is high (7.22 mol/kg/h) and its recovery is relatively low (63 %).

  - LTA-6 presents a high mixture selectivity (9.5) and, accordingly, a relatively high CO_2 purity in product 3 (70 %). Its methane productivity (12.4 mol/kg/h) and recovery (90 %) are high, too. Heating to 58 °C is necessary to regenerate the bed.

  - Si-ITW presents a moderate selectivity (7.5), a purity of CO_2 (65 %) slightly lower than for LTA-6 and a larger CH_4 productivity (15.3 mol/kg/h) than LTA-6 due to the easier regeneration which leads to an overall lower cycle time.

  - Si-RWR-a presents low selectivity (1.91), CO_2 purity (42 %), relatively low CH_4 productivity (1.91 mol/kg/h) and CH_4 recovery (47 %).

- **CO_2/CH_4 20%:80% 700 kPa**

  - **Si-LTA** presents a low mixture selectivity (1.9) and a very low CO_2 purity (33 %). Methane productivity is high (10.5 mol/kg/h), but its recovery is relatively low (43 %).

  - **LTA-6** presents a high mixture selectivity (10.4) and a moderate CO_2 purity (72 %). Its methane productivity (16.0 mol/kg/h) and recovery (91 %) are very high. Heating to 74 °C is necessary to regenerate the bed.

  - **Si-ITW** presents a high selectivity (10.9), a purity of CO_2 (73 %) slightly higher than for LTA-6 and a large CH_4 productivity (11.8 mol/kg/h) and recovery (90 %, slightly lower than LTA-6).

  - **Si-RWR-a** presents a low selectivity (3.7) and CO_2 purity (48 %), CH_4 productivity (1.2 mol/kg/h) and CH_4 recovery (55 %). Additionally, heating up to 57 °C is necessary to regenerate the bed.

- **CO$_2$/CH$_4$ 50%:50% 200 kPa**

  - **Si-LTA** presents a low mixture selectivity (2.9) but still a moderate CO$_2$ purity (74 %). Methane productivity (2.3 mol/kg/h) is moderate, but its recovery (47 %) is relatively low.

  - **LTA-6** presents a moderate mixture selectivity (7.1) and a relatively high CO$_2$ purity (88 %). Its methane productivity (4.0 mol/kg/h) is moderate (although relatively high) and its recovery is high (84 %). Heating to 58 °C is necessary to regenerate the bed.

  - **Si-ITW** presents a moderate mixture selectivity (7.5), a high purity of CO$_2$ (88 %) and a relatively large CH$_4$ productivity (4.9 mol/kg/h) and recovery (82 %).

  - **Si-RWR-a** presents a low selectivity (2.9) but still a moderate CO$_2$ purity (74 %). The CH$_4$ productivity (0.1 mol/kg/h) and CH$_4$ recovery (16 %) are extremely low. Heating up to 49 °C is necessary to regenerate the bed.

- **CO$_2$/CH$_4$ 50%:50% 700 kPa**

  - **Si-LTA** presents a moderate mixture selectivity (4.8) and a relatively high CO$_2$ purity (83 %). Methane productivity (3.0 mol/kg/h) is moderate, but its recovery (65 %) is relatively low.

  - **LTA-6** presents a moderately high mixture selectivity (8.3) and a high CO$_2$ purity (89 %). Its methane productivity (3.5 mol/kg/h) is moderate, although the highest in these conditions, and its recovery is high (81 %). Heating to 80 °C is necessary to regenerate the bed.

  - **Si-ITW** presents a moderate mixture selectivity (6.9), a high purity of CO$_2$ (87 %) and a relatively large CH$_4$ recovery (76 %). The productivity is moderate (2.4 mol/kg/h).

  - **Si-RWR-a** presents a low selectivity (2.7) but still a moderate CO$_2$ purity (73 %). The CH$_4$ productivity (0.1 mol/kg/h) and

CH$_4$ recovery (12 %) are extremely low. Heating up to 63 °C is necessary to regenerate the bed.

From these results, it is clear that Si-RWR-a cannot be possibly applied for the separation of CO$_2$ from methane at pressures between 200 and 700 kPa and percentages of CO$_2$ above 20 %. The productivity on this material is the lowest out of the ones studied at every set of conditions and furthermore, its regeneration is not easy, probably due to kinetic restrictions. Its low adsorption capacity is also a limiting factor. Si-LTA, despite presenting large pure gas adsorption capacities, presents comparably low CH$_4$ recoveries in all cases, and low CO$_2$ purities when the composition of the feed is close to 20:80 CO$_2$/CH$_4$. Productivities on this material are moderate, partly due to the easy regeneration that allows for reducing the total cycle duration. LTA-6* and Si-ITW present similar performances, with high productivities, recoveries and purities in most cases. According to said parameters, LTA-6 is the best adsorbent at higher pressure, while Si-ITW stands out at lower pressure. Additionally, the regeneration in Si-ITW doesn't require a significant amount of energy in any case, as does that of LTA-6.

Altogether, it is reasonable to believe that Si-ITW is a promising adsorbent to carry out the separation of CO$_2$ from CH$_4$ at ambient temperature, pressures between 200 and 700 kPa and relevant compositions of natural gas and biogas. The presence of H$_2$O and N$_2$ is an interesting factor which should be looked into for further evaluation of these adsorbents. Even though the presence of other possible components has not been taken into account in the breakthrough experiments, a notably more important effect of moisture on the aluminosilicate material LTA-6 may be expected, as evidenced in fig. 6.5. Ultimately, I have shown that, out of the studied pure silica materials, the channel-like small pore material Si-ITW presents the best features to be applied as an adsorbent for the separation of CO$_2$ from CH$_4$ in

---

*Note that this LTA-6 sample is very similar to the "LTA-5" material reported in [265] and [279] as being in the optimal range of compromise between selectivity and working capacity.

a swing adsorption process. Contrarily, another channel-like material, i.e. Si-RWR-a, presented very high ideal selectivities, but is not truly applicable, due to kinetic restrictions and low adsorption capacity, both features probably stemming from its very small pore opening.

There is another important conclusion I draw from this work. Pure component isotherms on their own may miscarry one in the search of a suitable adsorbent for a separation process. By measuring adsorption kinetics, as well, more firm conjectures can be made. It is, however, breakthrough experiments carried out at relevant process conditions the approach that gives a realistic outlook on the applicability of an adsorbent to a certain adsorption process. In breakthrough experiments, both kinetics and thermodynamics play their part and the interplay can be extrapolated to a real separation.

Table 6.6: *Results obtained from the CO_2/CH_4 mixture breakthrough adsorption experiments.*

Mixture	Material	Q_{CO_2} (mmol/g)	Q_{CH_4} (mmol/g)	$\alpha_{CO_2/CH_4}^{mix,eq}$	$\overline{Prod}$ (mol/kg/h)	$\overline{R}_{CH_4}$	$\overline{Pur}_{CO_2}$	$\overline{R}_{CO_2}$	t_{reg} (min)	T_{reg} (°C)
CO_2/CH_4 20:80 200 kPa	Si-LTA	0.51	0.77	2.7	7.22	63%	40%	94%	6.57	25
	LTA-6	1.49	0.63	9.5	12.40	90%	70%	90%	20	58
	Si-ITW	1.06	0.57	7.5	15.27	86%	65%	91%	8.51	25
	Si-RWR-a	0.29	0.41	2.9	1.91	47%	42%	97%	6.95	25
CO_2/CH_4 20:80 700 kPa	Si-LTA	2.21	4.53	1.9	10.54	43%	33%	95%	11.53	25
	LTA-6	2.33	0.90	10.4	15.98	91%	72%	89%	20	74
	Si-ITW	1.84	0.67	10.9	11.83	90%	73%	90%	20	27
	Si-RWR-a	1.20	0.45	3.7	1.17	55%	48%	96%	20	57
CO_2/CH_4 50:50 200 kPa	Si-LTA	1.34	0.47	2.9	2.35	47%	74%	99%	5.55	25
	LTA-6	2.46	0.35	7.1	3.97	84%	88%	99%	20	58
	Si-ITW	1.81	0.24	7.5	4.86	82%	88%	99%	8.85	25
	Si-RWR-a	0.72	0.25	2.9	0.11	16%	74%	100%	20	49
CO_2/CH_4 50:50 700 kPa	Si-LTA	3.04	0.63	4.8	2.99	65%	83%	99%	12.13	25
	LTA-6	3.73	0.45	8.33	3.46	81%	89%	99%	20	80
	Si-ITW	2.78	0.40	6.9	2.39	76%	87%	99%	20	30
	Si-RWR-a	1.20	0.45	2.7	0.11	12%	73%	100%	20	63

The purity of methane has been fixed at $> 97\%$.

6.4 Conclusions on the influence of zeolite framework topology on the separation of CO_2 from CH_4

- Small pore channel-like pure silica zeolites with the appropriate pore size present higher CO_2/CH_4 selectivities than cavity-like materials sharing composition and similar pore size.

- A compromise between ideal CO_2/CH_4 selectivity, diffusivities and adsorption capacity must be met in order to find a suitable adsorbent.

- Si-ITW stands out as a very promising adsorbent for separating CO_2 from CH_4, being capable of separating bulk mixtures of these gases at relevant conditions of their mixture and with a performance comparable to that of LTA-6 and easier regeneration.

- Breakthrough experiments are a very powerful tool to study adsorbents for their use in industrial separations. They are complementary to isotherm and kinetic measurements and result very convenient for analyzing the potential applicability of an adsorbent.

Chapter 7

Zeolite Si-STW for the separation of linear, branched and dibranched paraffins

The adsorptive separation of multibranched hydrocarbons from linear and monobranched ones is an active field of research that could help to optimize the production of high octane gasoline by hydroisomerization of straight run naphta, as explained in section 1.3.5. A variety of zeolitic materials predominantly featuring medium pore structures (10-rings) have been studied for this purpose, with MFI-structured materials being the ones most frequently brought into discussion [368], probably due to them being commercially available.

In this chapter, I present Si-STW as a material that can perform this separation by excluding multibranched hydrocarbons, and especially those containing quaternary carbon atoms. Si-STW is compared with Si-MFI, taken as a reference material. Two different Si-MFI samples with different crystal size (Si-MFI-a and Si-MFI-b) were used. The results presented here are part of a joint experimental and computational study which I published along with my fellow PhD students Alechania Misturini (responsible for the computational part) and Andrés Sala (responsible for the synthesis and characterization) [496]. I will focus on the results from the adsorption experiments, which I carried out and analyzed. I will refer

to the computational results to discuss the validity of the experimental results.

7.1   Materials description and characterization

The synthesis of Si-STW, si-MFI-a and Si-MFI-b is presented in section 3.2.2.   STW is a medium pore 2D chiral zeolite, in which a helicoidal 10-ring channel (minimum opening 5.2 × 5.7 Å) is perpendicularly intersected by 8-ring channels (minimum opening 3.0 × 4.4 Å). MFI is as well a medium pore zeolite with a 3D* channel system consisting of intersecting 10-ring straight channels (minimum opening 5.3 × 5.6 Å) in one direction and perpendicular 10-ring sinusoidal ones (minimum opening 5.1 × 5.5 Å).

Table 7.1: *Characterization results of the Si-RWR samples after removal of occluded species.*

Sample	Si defects amount (% Q_3)	Crystal shape	Crystal dimensions (µm)	Pore diameter[a] (Å)	BET surface area (m^2/g)	Micropore volume (cm^3/g)
Si−MFI−a	0	rods	80	5.1	386	0.17
Si−MFI−b	10	hexagonal prisms	0.5	5.1	451	0.18
Si−STW	0	elongated	0.5 - 5	5.3	630	0.24

[a]Obtained by applying Horwatz-Kawazoe to the Ar adsorption isotherm at -186 °C.

The characterization results of the samples are summarized in table 7.1 and the SEM images are presented in fig. 7.2. XRD patterns and ^{29}Si MAS NMR spectra can be found in appendix B. The Si-STW sample possesses elongated crystals with lengths of 0.5 to 5 µm and its micropore volume was determined by the t-plot method to be of 0.24 cm^3/g. The pure silica MFI samples were synthesized with very different crystal sizes. Si-MFI-a presents rod-shaped crystals of 80 µm in length and a micropore volume of 0.17 cm^3/g. Si-MFI-b presents much smaller (0.5 µm) crystals with hexagonal prism shape, a micropore volume of 0.18

---

*The fact that molecules can diffuse in 3 directions is what makes it tridirectional, and not the definition of the channels.
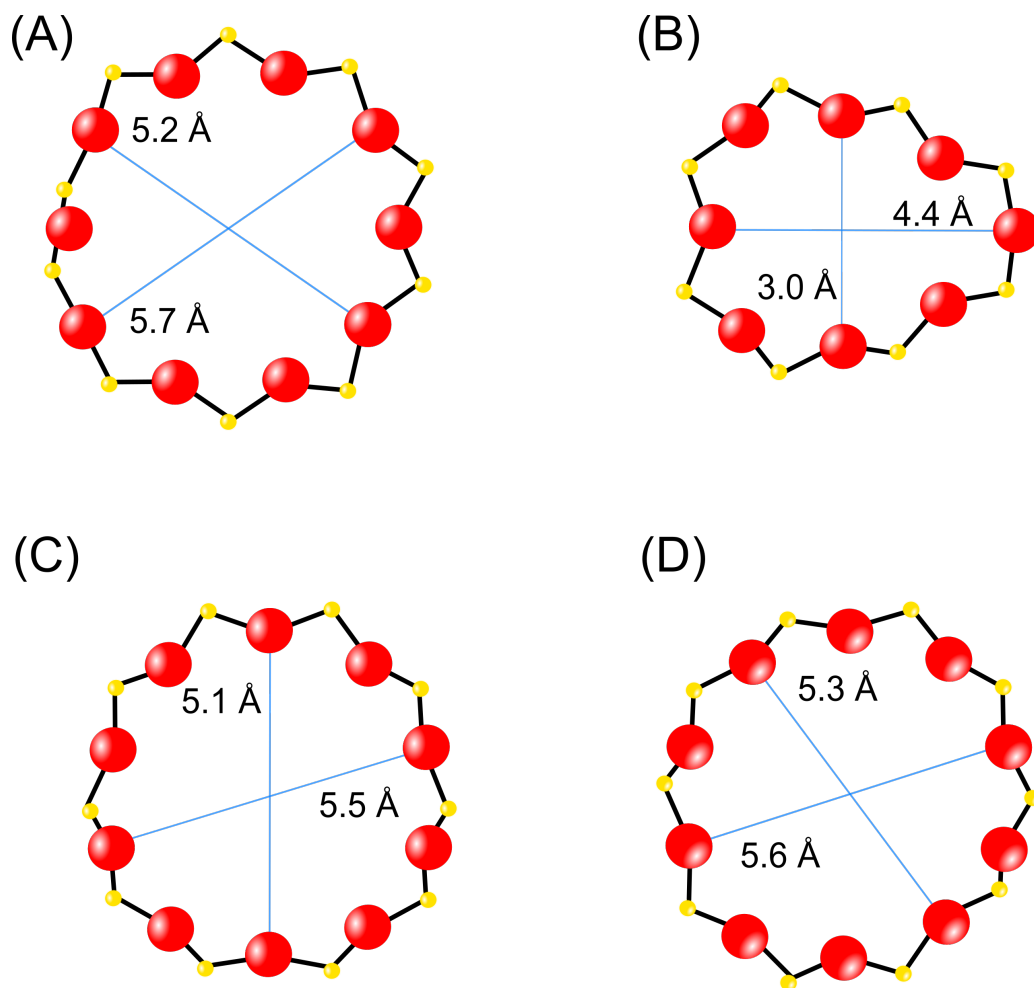
Figure 7.1: *Pore openings of STW and MFI structures. In (A), the 10-ring viewed along [001] and in (B), the 8-ring viewed along [100] characteristic of STW are shown. In (C), the 10-ring viewed along [100] and in (B), the 10-ring viewed along [010] characteristic of MFI are shown.*

cm^3/g and a substantial amount of connectivity defects (10 %) determined by ^{29}Si MAS NMR.

7.2 Selection of model adsorbates and methodology

There is a large number of possible isomers belonging to the gasoline fraction (C5 - C12) and a study including all of them would be highly expensive and time-consuming. Thus, the effort was put into a limited amount of isomers, which are considered to be representative of other isomers in the gasoline fraction and which I will refer to as model
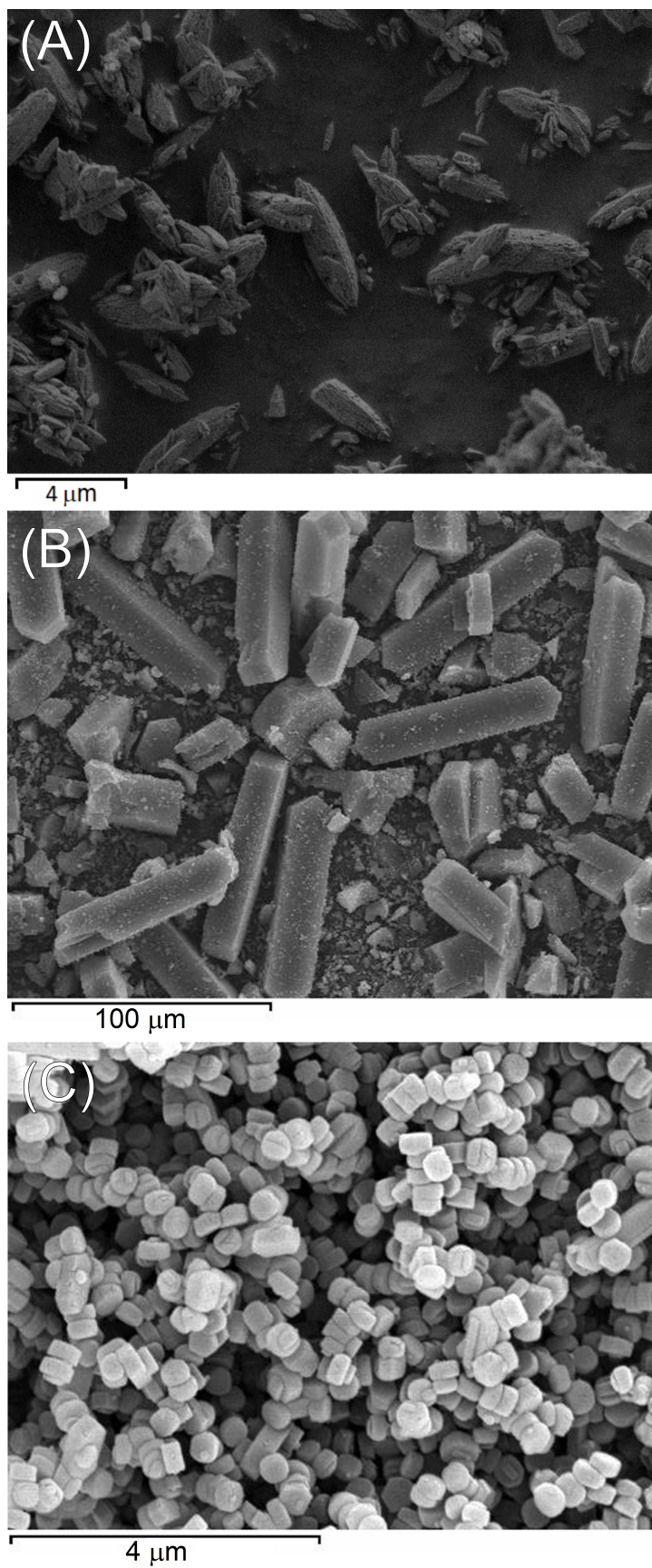
Figure 7.2: *SEM images of (A) Si-STW, (B) Si-MFI-a and (C) Si-MFI-b.*

adsorbates.

The compounds selected as model adsorbates are in the C5 - C7 fractions and are included in fig. 7.3 along with their respective abbreviation and octane numbers. For the C5 and C6 fractions, all the possible isomers were studied, i.e. nC5, 2MB, 22DMPr, nC6, 2MPe, 22DMB and 23DMB. For the C7 fraction the number of possible isomers is larger and only nC7, 3MH, 23DMPe and 24DMPe were included. This way, a linear and a monobranched isomer from each fraction have been selected and a variety of kinds of dibranched isomers is covered, which allows us to assess the effect of the respective position of the branches on their adsorptive behavior. Due to the size of these molecules ($4.3 \leq d_{kin} \leq 4.5$ for linear, $5.0 \leq d_{kin} \leq 5.9$ for monobranched and $5.8 \leq d_{kin} \leq 6.5$ for dibranched),[40, 177, 183] only the 10-ring channel of Si-STW and the two 10-ring channels of Si-MFI will be available for adsorption (see fig. 7.1).

The adsorption properties of the different adsorbate-adsorbent systems were studied by measuring adsorption isotherms at 10 - 60 °C and adsorption kinetics at 25 °C. In the isotherms, pressures up to 30, 15 and 5 kPa were reached for the C5, C6 and C7 fractions, respectively. These were chosen in order to remain below their vapor pressures at all the temperatures studied. The kinetic experiments were carried out at these maximum pressures, but also at 0.1 kPa. From these experimental data, isosteric heats of adsorption, ideal equilibrium selectivities, diffusional time constants and ideal kinetic selectivities were calculated. The adsorption properties of the C5 fraction was studied on Si-STW, Si-MFI-a and Si-MFI-b, in order to compare the adsorbents. The adsorption properties of the C6 and C7 fractions was studied on Si-STW.

n-pentane, nC5
RON = 61.8,
MON = 63.2

n-hexane, nC6
RON = 24.8,
MON = 26.0

n-heptane, nC7
RON = 0,
MON = 0

2-methylbutane, 2MB
RON = 93.0,
MON = 89.7

2-methylpentane, 2MPe
RON = 73.4,
MON = 73.5

3-methylhexane, 3MH
RON = 52.0,
MON = 55.0

2,2-dimethylpropane,
22DMPr
RON = 85.5,
MON = 80.2

2,2-dimethylbutane,
22DMB
RON = 91.8,
MON = 93.4

2,3-dimethylpentane,
23DMPe
RON = 91.1,
MON = 88.5

2,3-dimethylbutane,
23DMB
RON = 104.3,
MON = 94.2

2,4-dimethylpentane,
24DMPe
RON = 83.1,
MON = 83.8

Figure 7.3: *Compounds used as adsorbates for this study, their abbreviation and motor and research octane numbers (MON and RON, respectively).*

7.3 Comparison between Si-STW and Si-MFI materials as adsorbents for the separation of pentane isomers

7.3.1 Adsorption isotherms and selectivities of C5 isomers on Si-STW and Si-MFI materials

The isotherms of the pentane isomers on Si-STW, Si-MFI-a and Si-MFI-b at 25 °C are depicted in fig. 7.4. Si-STW presents a larger maximum adsorption capacity of the components of the C5 fraction in general than Si-MFI-a or Si-MFI-b. In both zeolites the different isomers are

adsorbed to amounts which follow the order linear > monobranched > dibranched, with the difference between mono- and dibranched being larger on Si-STW. In fig. 7.4B, it may be observed that Si-MFI-b presents slightly larger adsorption capacities of the linear and monobranched isomers than Si-MFI-a, which is coherent with its slightly larger micropore volume. In the case of the dibranched isomer, the isotherms on both Si-MFI materials differ largely due to the isotherm on Si-MFI-a having not reached equilibrium. The reasons behind this are its larger crystal size if compared to Si-MFI-b (ca. 100 times larger) and a slow diffusion of 22DMPr in Si-MFI.
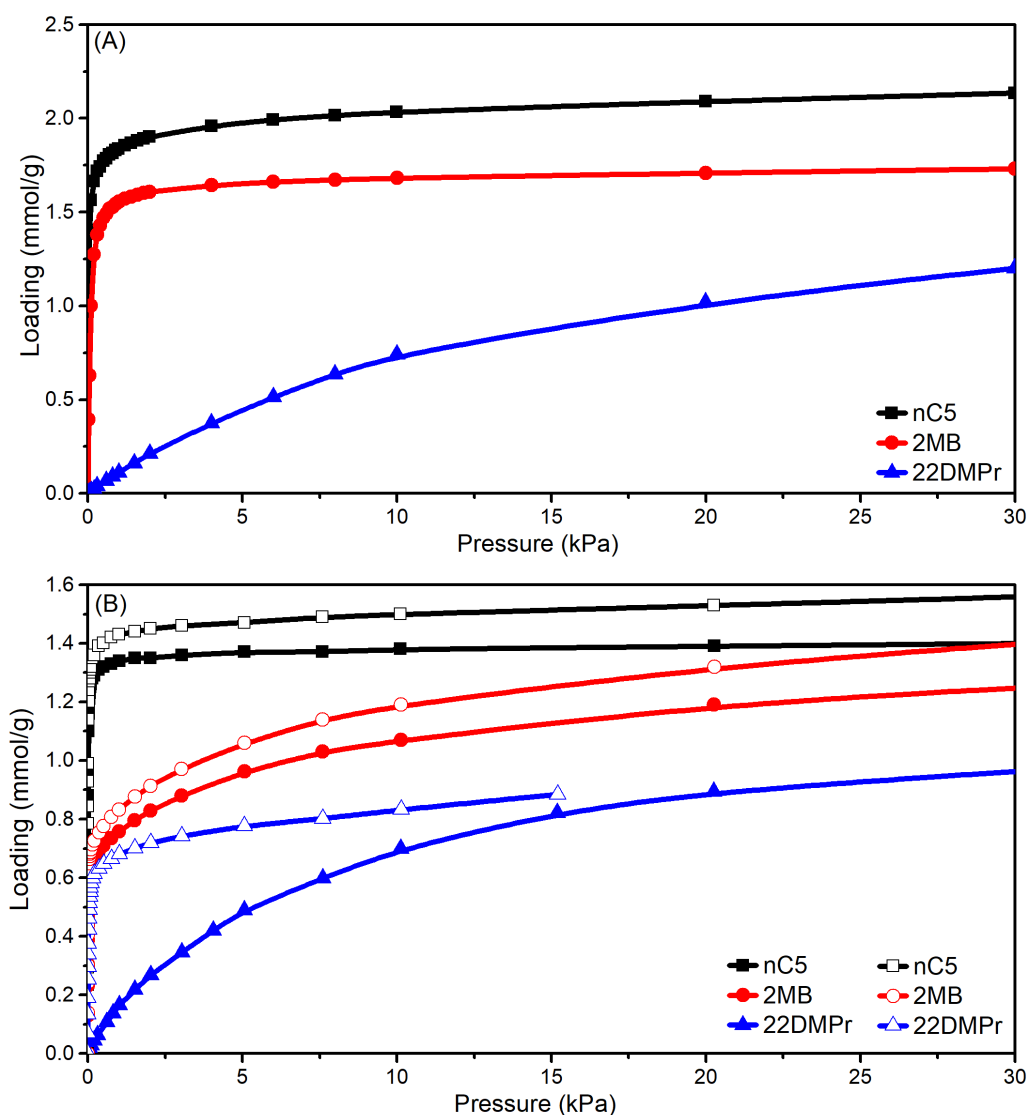
Figure 7.4: *Adsorption isotherms at 25 °C of C5 isomers (A) on Si-STW, (B) on Si-MFI-a (closed symbols) and on Si-MFI-b (open symbols). Note that the vertical axes' scales differ.*

The ideal selectivities of 2MB over 22DMPr, i.e. of the monobranched over the dibranched isomer of the C5 fraction, on the three materials are plotted in fig. 7.5. The 2MB/22DMPr selectivity trend on Si-MFI-a is an apparent selectivity, as the 22DMPr isotherm on this material is not equilibrated. At low pressure, a selectivity of ca. 30 is attainable with Si-STW and lower selectivities are attainable with Si-MFI-a (ca. 15) and Si-MFI-b (ca. 1). When going to pressures > 5 kPa, the selectivity rapidly decreases to values below 4 for Si-STW, 2 for Si-MFI-a and it slightly increases for Si-MFI-b. At pressures above 15 kPa, the selectivity varies only slightly and remains at values between 1.5 and 2 for Si-STW and at values close to 1.5 for Si-MFI materials. Throughout the whole range of pressures studied at 25 °C, Si-STW presents a larger 2MB/22DMPr selectivity than the two Si-MFI materials.

Figure 7.5: *Ideal adsorption selectivities at 25 °C of 2MB/22DMPr on Si-STW, Si-MFI-a and Si-MFI-b. The selectivities on Si-MFI-a are apparent selectivities, as the 22DMPr isotherm is not fully equilibrated.*

7.3.2 Isosteric heats of adsorption of C5 isomers on Si-MFI and Si-STW and comparison with literature data

The isosteric heats of adsorption of the C5 isomers on Si-MFI-a, Si-MFI-b and Si-STW calculated from the experimental isotherms are presented in table 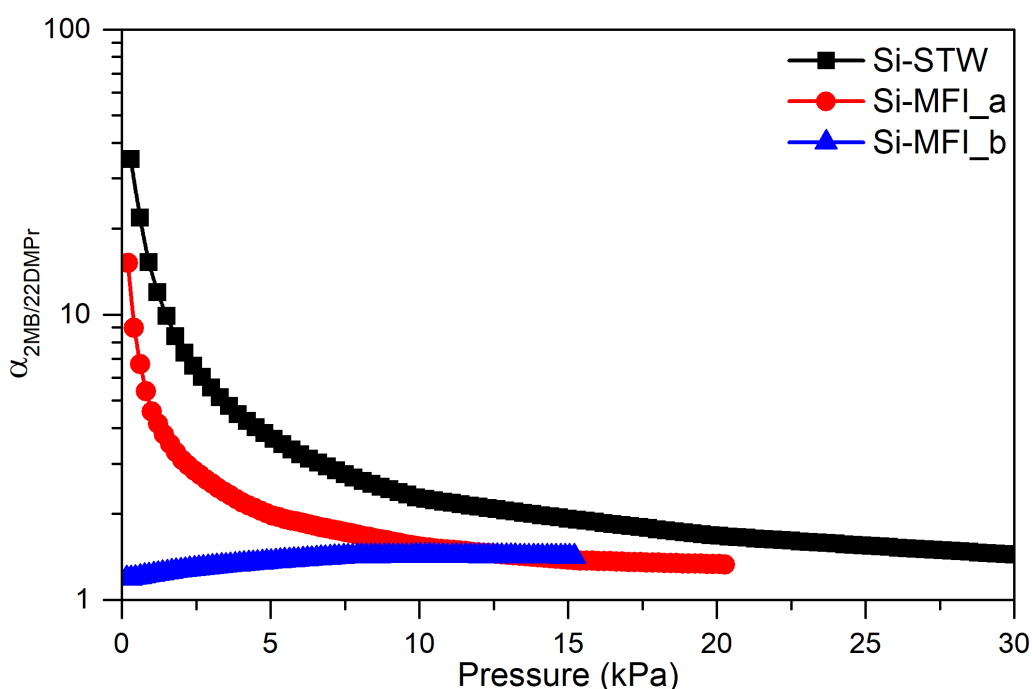7.2. The values calculated from the experimental isotherms are validated by comparing them with values reported in the literature for Si-MFI obtained by chromatographic methods [497], calorimetry [498] or simulations [499] and those obtained from MD simulations carried out by my coworker Alechania Misturini for Si-MFI and Si-STW [496].

Table 7.2: *Experimental and simulated isosteric heats of adsorption of C5 isomers on Si-MFI. The numbers in parentheses next to the experimental values are the lowest loadings (in mmol/g) at which the q_{st} could be obtained. The numbers in brackets indicate the reference from which they have been extracted, i.e. Perez-Botella et al 2020 [496], Dubbeldam et al 2004 [499], Denayer et al 1998 [500] or Ferreira 2007 [498].*

Material	Compound	q_{st}^{exp} (kJ/mol)	q_{st}^{sim} [496] (kJ/mol)	q_{st}^{sim} [499] (kJ/mol)
Si-MFI	nC5	56.1 (0.23)[a], 57.9 (0.29)[b], 57.7[c]	59.5	57.9
	2MB	57.3 (0.13)[a], 53.2 (0.14)[b], 56.1[c]	56.7	55.8
	22DMPr	-	54.1	-
Si-STW	nC5	61.5 (1.5)	63.9	-
	2MB	55.3 (0.9)	62.7	-
	22DMPr	33.3	58.8	-

[a] Si-MFI-a. [b] Si-MFI-b. [c] Taken from ref. [497]

As is presented in table 7.2, the experimental q_{st} values obtained for the C5 fraction on Si-MFI materials in this work are well comparable with others previously reported by Denayer et al [500] and with those simulated by my coworker in [496] and by Dubbeldam et al [499]. The isosteric heat of adsorption of 22DMPr on Si-MFI was not obtainable from the isotherms, as isotherm data were not fully equilibrated. The experimental q_{st} of

nC5 on Si-STW is very close to the one determined by my coworker by simulations. However, when going to the monobranched and dibranched isomers, the differences in the experimental and simulated q_{st} values become larger. The experimental q_{st} of 2MB (55.3 kJ/mol) differs in ca. 7 kJ/mol from the simulated value (62.7 kJ/mol) and the experimental value for 22DMPr (33.3 kJ/mol) is notably discordant with the one obtained from MD simulations (58.8 kJ/mol). In the case of the monobranched isomer, a shortcoming of the MD algorithm may be a possible explanation for the small error (ca. 11%), which may even lay within the acceptable experimental error. Nonetheless, for the dibranched isomer such a large difference may have a different origin. It is possible that the experimental 22DMPr adsorption isotherms used for the calculation of q_{st}^{exp} were not equilibrated, despite seeming so. This could imply two significantly different diffusion regimes upon adsorption of these isomers depending on the coverage. Similar behavior has been described in other zeolites; for instance, Si-ITW presents two different diffusional regimes when adsorbing propane, due to flexibility of the framework [330, 501]. This flexibility in pure silica materials may be induced by adsorbates, the kinetic diameter of which is slightly larger than the pore opening of the material [335], as could be the case of 22DMPr (6.2 Å) on Si-STW (pore opening 5.2 × 5.7 Å).

7.3.3 Kinetics of adsorption of C5 isomers on Si-STW and Si-MFI materials

The adsorption kinetics measurements of C5 isomers on Si-STW, Si-MFI-a and Si-MFI-b at 25 °C and at 0.1 and 30 kPa are plotted in figure 7.6. At 0.1 kPa (fig. 7.6A, C and E) it is evident that the linear and monobranched isomers reach their maximum loading rapidly, i.e. after less than 1000 s, in the three materials. The dibranched isomer needs much longer times to diffuse into the material and thus, its adsorption is negligible on Si-STW and Si-MFI-a even after 2000 - 5000 s. On Si-MFI-b, probably due to

the small crystal size, there is a significant amount of adsorption, even though it is far from reaching equilibrium at times close to 50000 s. At 30 kPa (fig. 7.6B, D and F), the differences between 22DMPr and the other isomers are also large, with nC5 and 2MB reaching equilibrium at 100 to 300 s and 22DMPr reaching equilibrium at times above 10000 s. The slowest diffusion of 22DMPr is on Si-STW, as at times close to 50000 s equilibrium has not been reached still. By the time that linear and monobranched isomers have reached equilibrium, the amount adsorbed of 22DMPr is very small on the three materials (ca. 0.3 mmol/g). On the whole, it may be affirmed that the three adsorbents, i.e Si-STW, Si-MFI-a and Si-MFI-b, kinetically differentiate linear and monobranched from dibranched isomers, and the differences are larger on Si-STW than on the Si-MFI materials.

Table 7.3: *Diffusional time constants of pentane isomers at 25 $^\circ$C and 0.1 and 30 kPa and maximum loadings at 30 kPa.*

Material	Compound	$D_{0.1}/r^2$ (s^{-1})	D_{30}/r^2 (s^{-1})	Q_{30} (mmol/g)
	nC5	$1.3 \cdot 10^{-3}$	$3.0 \cdot 10^{-3}$	2.17
Si-STW	2MB	$9.1 \cdot 10^{-4}$	$1.9 \cdot 10^{-3}$	1.70
	22DMPr	$3.4 \cdot 10^{-5}$	$2.2 \cdot 10^{-5}$	1.22
	nC5	$1.4 \cdot 10^{-3}$	$2.4 \cdot 10^{-3}$	1.40
Si-MFI_a	2MB	$7.4 \cdot 10^{-4}$	$1.1 \cdot 10^{-3}$	1.25
	22DMPr	$2.3 \cdot 10^{-5}$	$3.0 \cdot 10^{-5}$	0.97
	nC5	$1.6 \cdot 10^{-3}$	$1.4 \cdot 10^{-3}$	1.56
Si-MFI_b	2MB	$1.4 \cdot 10^{-3}$	$1.3 \cdot 10^{-3}$	1.22
	22DMPr	$5.5 \cdot 10^{-6}$	$3.3 \cdot 10^{-5}$	0.88

From the uptake curves presented, diffusional time constants were obtained according to eq. (3.8) (see table 7.3) and kinetic selectivities of relevant pairs of isomers were calculated, as presented in table 7.4. The maximum loadings at 30 kPa are indicated in table 7.3, as they
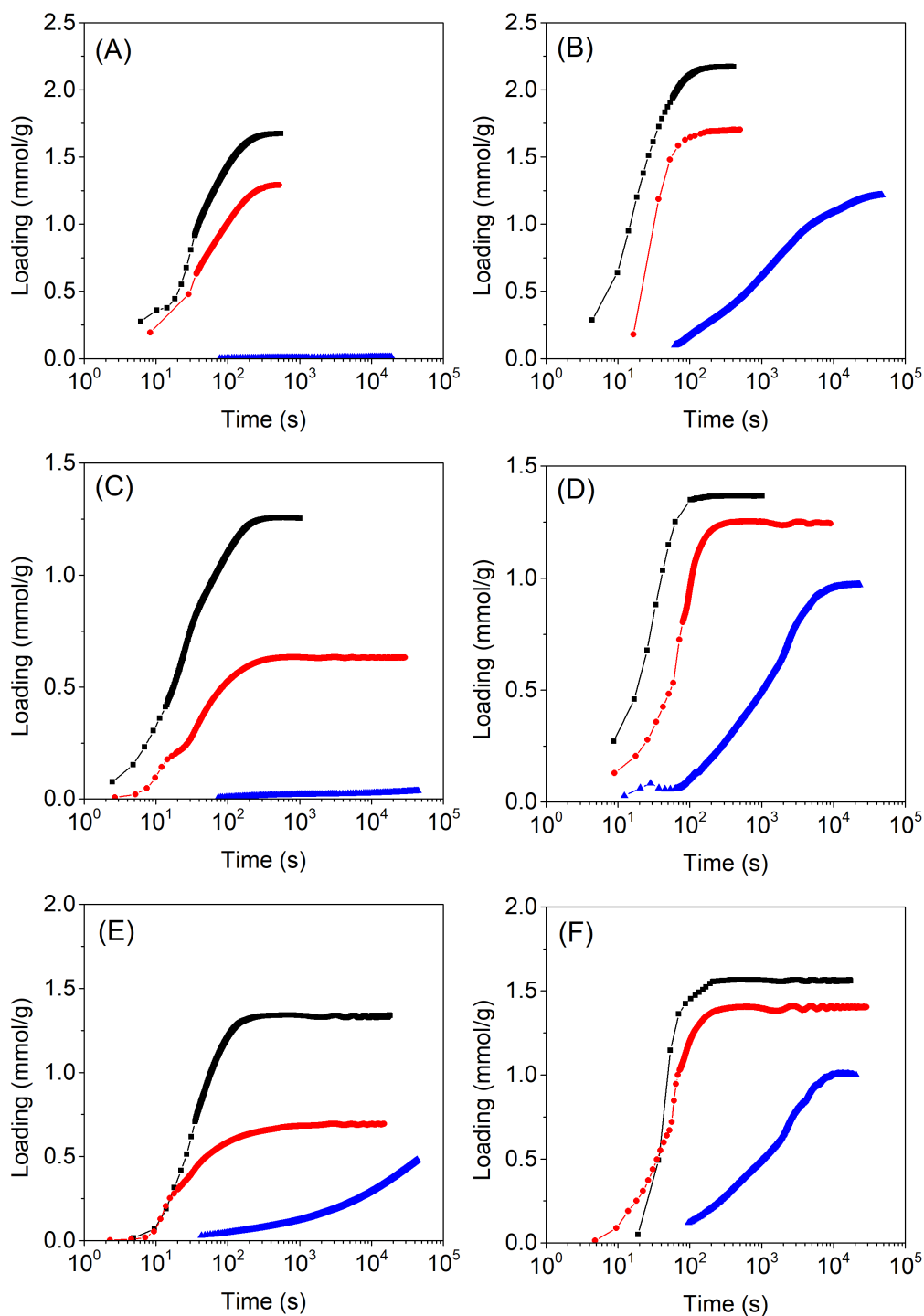
Figure 7.6: *Adsorption kinetics at 25 °C of nC5 (black squares), 2MB (red circles) and 22DMPr (blue triangles) on (A) Si-STW at 0.1 kPa, (B) Si-STW at 30 kPa, (C) Si-MFI-a at 0.1 kPa, (D) Si-MFI-a at 30 kPa, (E) Si-MFI-b at 0.1 kPa and (F) Si-MFI-b at 30 kPa.*

are relevant for both the calculation of the diffusional constants and the comparison between adsorbents. At 25 °C and 30 kPa, Si-STW presents maximum loadings ca. 1.5 times larger than Si-MFI materials, which

would make Si-STW more favorable as an adsorbent for a separation process. Furthermore, at this pressure, it becomes evident that Si-STW is a better adsorbent for this application than Si-MFI, presenting larger selectivities of the linear and monobranched over the dibranched component of the C5 fraction.

Table 7.4: *Kinetic selectivities of relevant compound pairs of the C5 fraction on Si-STW, Si-MFI-a and Si-MFI-b at 30 kPa.*

Material	Compounds	$\alpha^{kin,30}$
Si-STW	nC5/22DMPr	135
	2MB/22DMPr	88
Si-MFI-a	nC5/22DMPr	78
	2MB/22DMPr	36
Si-MFI-b	nC5/22DMPr	43
	2MB/22DMPr	41

7.4 Si-STW as an adsorbent for the separation of hexane and heptane isomers

7.4.1 Adsorption isotherms and selectivities of C6 and C7 isomers on Si-STW

The isotherms of hexane and heptane isomers on Si-STW at 25 °C are presented in fig. 7.7.
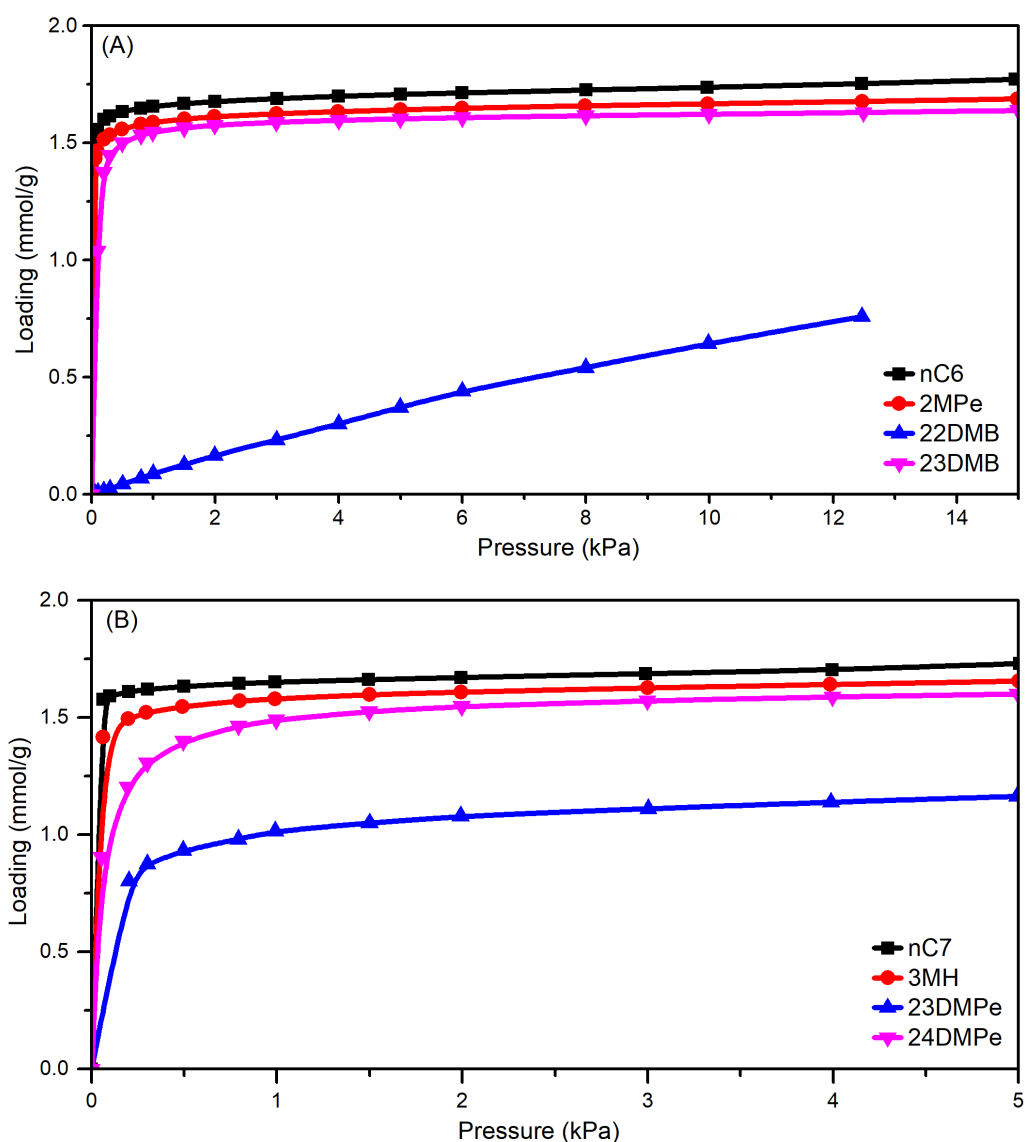
Figure 7.7: *Adsorption isotherms at 25 °C of (A) C6 and (B) C7 isomers on Si-STW.*

In fig. 7.7A, the adsorption isotherms of the C6 fraction are depicted. As can be seen, nC6, 2MPe and 23DMB present notably different

isotherms compared to 22DMB, this meaning that the relative position of the branches in the hydrocarbon chain are very relevant to their adsorptive properties. The 22DMB isotherm is not equilibrated, as confirmed by examining the adsorption kinetics of each point (not shown) and the isotherms measured at 10 and 25 °C, which intersect (see fig. 7.8A). This, together with the findings from section 7.3.1, indicates that dibranched hydrocarbons featuring quaternary carbon atoms are adsorbed on Si-STW at lower amounts than other isomers and that they present strong kinetic hindrances.
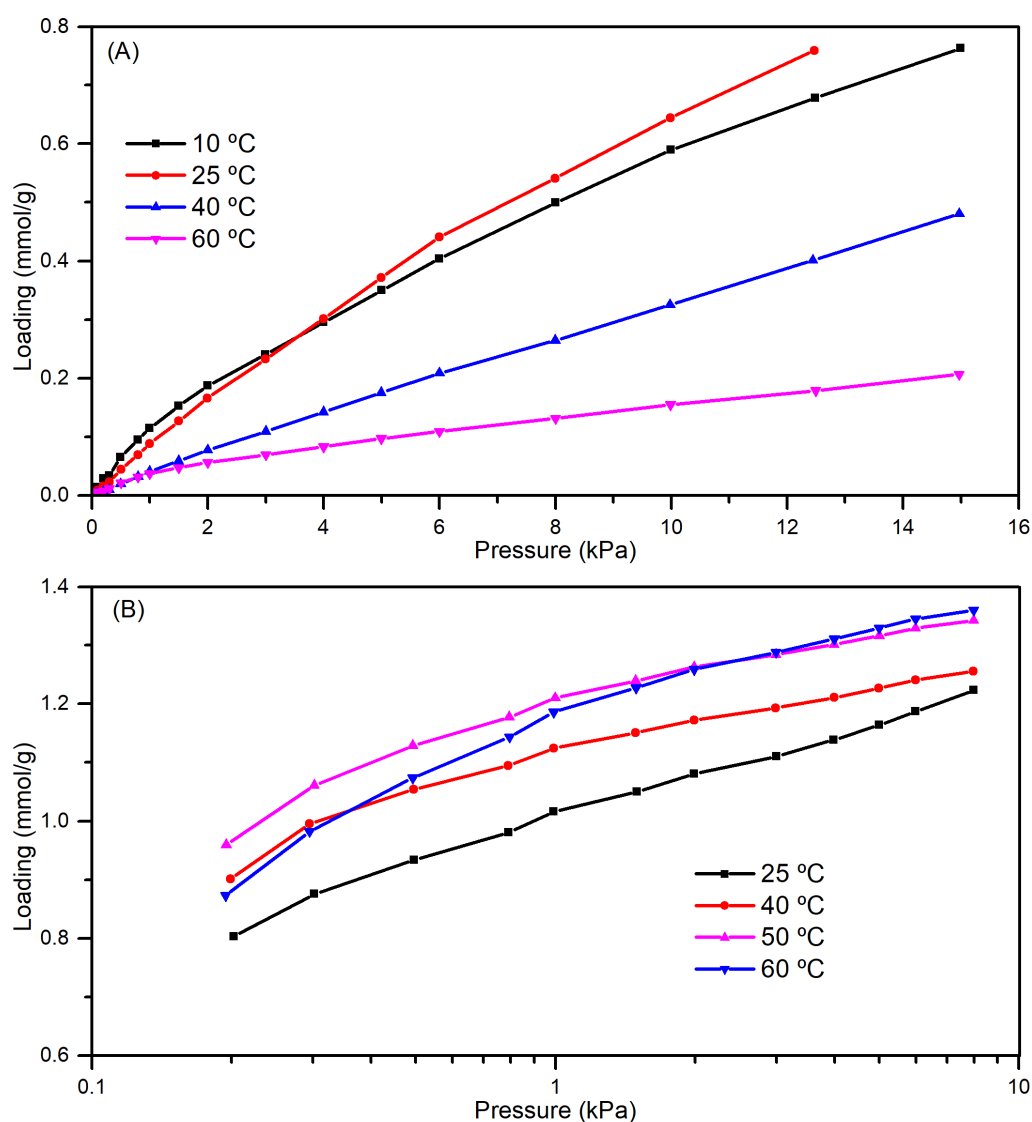
Figure 7.8: *Non equilibrated adsorption isotherms of (A) 22DMB and (B) 23DMPe on Si-STW.*

In what refers to the C7 fraction (see fig. 7.7B), nC7 and 3MH

present very similar isotherms and the dibranched isomers present lower maximum loadings and less steep low-pressure regimes. 24DMPe presents a behavior closer to that of nC7 and 3MH, whereas 23DMPe presents a much lower loading and its isotherm is not equilibrated, as evidenced in fig. 7.8B, where the isotherms measured at different temperatures do not follow the thermodynamic trend. In this case, no quaternary-C-atom containing isomer was studied, but it becomes clear that, the further away from each other the branches of the isomers, the larger their adsorption capacity.
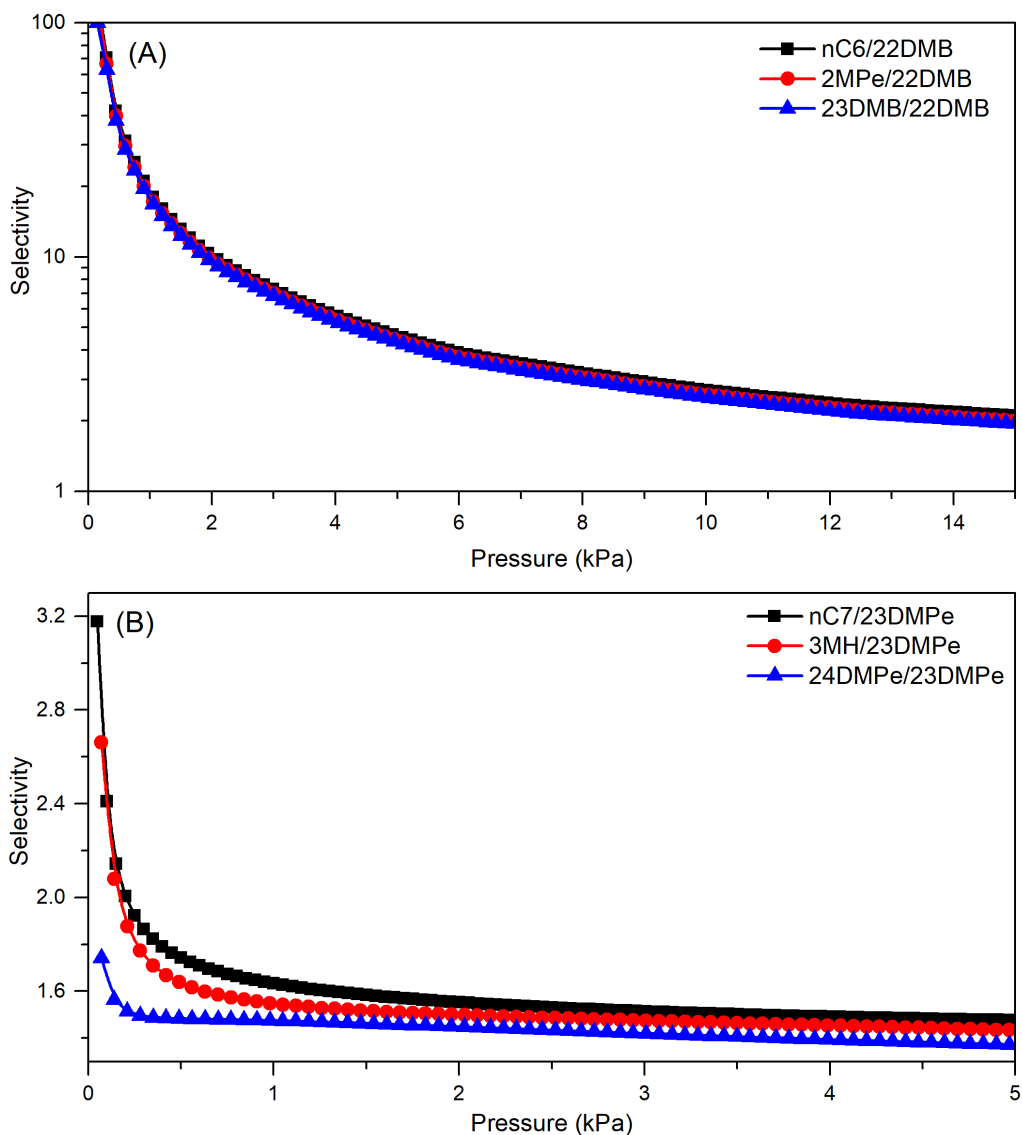
Figure 7.9: *Ideal adsorption selectivities at 25 °C of (A) nC6, 2MPe and 23DMB over 22DMB and (B) nC7, 3MH, 24DMPe over 23DMPe on Si-STW. Note that these are apparent selectivities, as the isotherms of 22DMB and 23DMPe are not fully equilibrated.*

The ideal selectivities were calculated for selected pairs of components on Si-STW and are plotted in fig. 7.9. The selectivities of the components of the C6 fraction over 22DMB (see fig. 7.9A) present very large values at low pressure ($>$ 100) which decrease to ca. 2 at 15 kPa. The selectivity of nC6, 2MPe and 23DMB over 22DMB are very similar, which is understandable, as the isotherms of nC6, 2MPe and 23DMB present similar shapes and maximum loadings. The apparent selectivities of the components of the C7 fraction over 23DMPe (see fig. 7.9B) are below 3.2 (nC7), 2.8 (3MH) and 1.8 (24DMPe) at low pressure and they decrease to values close to 1.5 above 1 kPa.

7.4.2 Isosteric heats of adsorption of C6 and C7 isomers on Si-STW

The isosteric heats of adsorption of the C6 and C7 isomers on Si-STW calculated from the experimental isotherms are presented in table 7.5. These values are compared with the computational ones obtained by my coworker Alechania Misturini in [496].

The experimental and simulated values for the linear hydrocarbons match fairly well. The difference becomes slightly larger for monobranched isomers ($<$ 10%) and there is a large discrepancy between experiment and simulation in the case where dibranched isomers are involved. For instance, the differences between experiment and simulation in the cases of 23DMB and 24DMPe, are of 27 and 23 kJ/mol, respectively. The same explanation as the one given in section 7.3.2 is plausible. A pseudo-equilibrium state may have been reached. In this case, too, the sizes of 23DMB (6.3 Å) and 24DMPe (5.8 Å) are similar to the pore opening of Si-STW (5.2 $\times$ 5.7 Å).

Table 7.5: *Experimental and simulated isosteric heats of adsorption of the studied C6 and C7 isomers on Si-STW. The numbers in parentheses next to the experimental values are the lowest loadings (in mmol/g) at which the q_{st} could be obtained. The simulated values were extracted from [496]. The experimental values for 22DMPB and 23DMPe could not be obtained. Rows with light blue background contain information on the C7 fraction.*

Compound	q_{st}^{exp} (kJ/mol)	q_{st}^{sim} (kJ/mol)
nC6	81.0 (1.6)	77.0
2MP	72.2 (1.4)	73.1
22DMB	-	70.7
23DMB	46.0 (1.4)	72.9
nC7	85.8 (1.6)	85.3
3MH	76.3 (1.41)	85.4
(R)23DMPe	-	82.3
(S)23DMPe	-	85.0
24DMPe	58.9 (0.9)	81.9

7.4.3 Kinetics of adsorption of C6 and C7 isomers on Si-STW

The adsorption kinetics measurements, i.e. uptake curves, at 25 °C of C6 and C7 isomers on Si-STW are plotted in fig. 7.10. As can be seen in fig. 7.10A and C, at 0.1 kPa, the linear and monobranched isomers diffuse very similarly into Si-STW, reaching equilibrium at 200 - 300 s, while the dibranched isomers take longer times. 23DMB reaches equilibrium at ca. 700 s, 24DMPe at ca. 500 s and 22DMB and 23DMPe do not reach equilibrium in the studied time range ($>$ 50000 s). 22DMB presents negligible loadings throughout the uptake curve at 0.1 kPa. At higher pressure (15 kPa, see fig. 7.10B) the diffusive behavior of the dibranched components of the C6 fraction changes slightly, with 23DMB reaching equilibrium after ca. 2000 s and 22DMB presenting a slow but significat uptake (ca. 0.8 mmol/g at 50000 s). 22DMB still does not reach equilibrium in the studied time range. The uptake curves of the

C7 fraction at 5 kPa are presented in fig. 7.10D, where a substantially different trend is observed for 24DMPe and 23DMPe. 24DMPe behaves similarly to the linear and monobranched isomers, reaching equilibrium at times below 1000 s, while 23DMPe does not reach equilibrium at times below 100000 s.
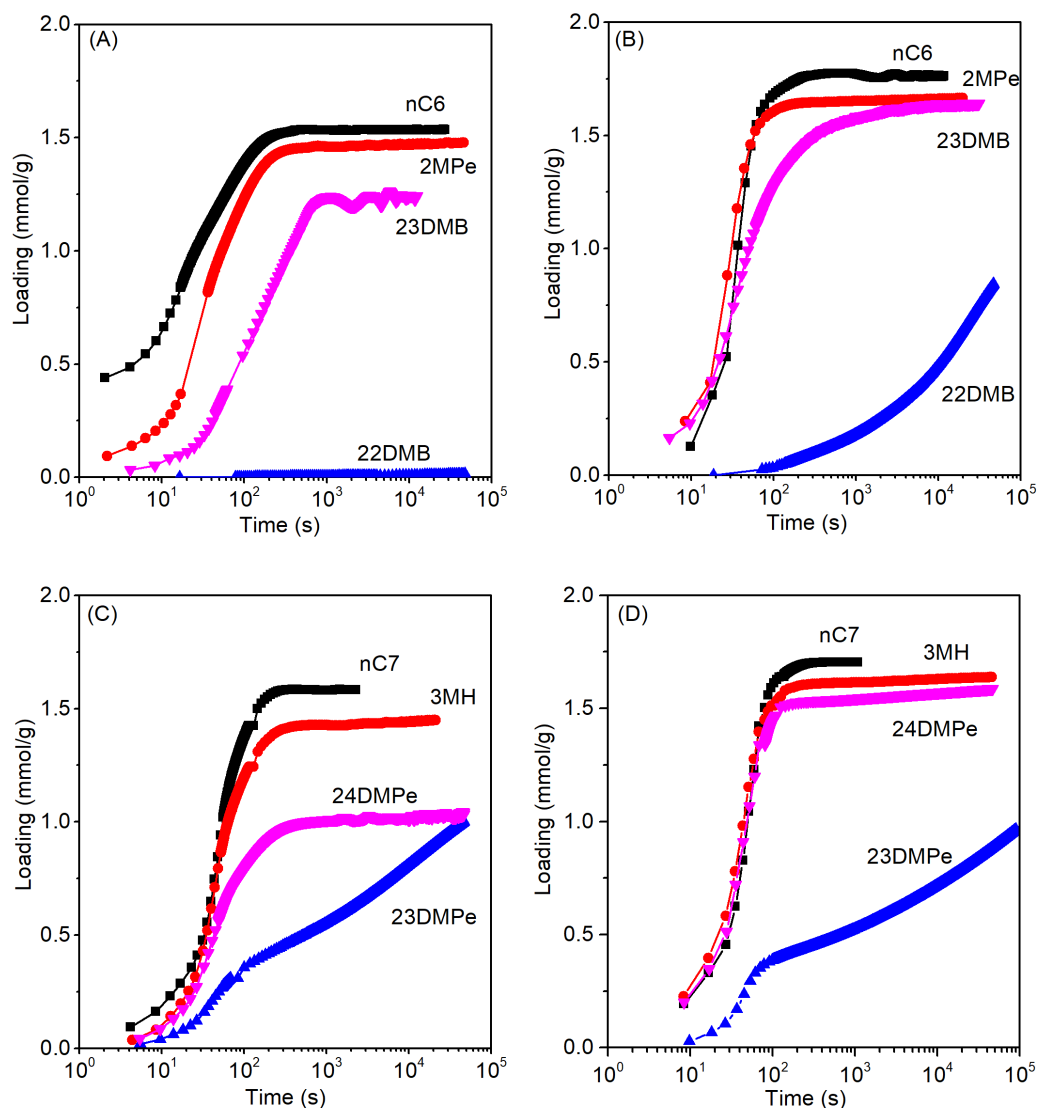
Figure 7.10: *Adsorption kinetics at 25 °C on STW of the components of the C6 fraction at (A) 0.1 kPa and (B) 15 kPa and of the components of the C7 fraction at (C) 0.1 kPa and (D) 5 kPa.*

Therefore, it is evident that Si-STW is an adsorbent that kinetically differentiates linear and monobranched from dibranched isomers, and even between dibranched isomers, depending on the relative positions of the branches. This way, dibranched hydrocarbons featuring quaternary

carbon atoms are kinetically excluded from the zeolite, along with others in which the branches are too close to allow for rotational freedom in the molecule that favors diffusion inside the pores of the material.

Table 7.6: *Diffusional time constants at 25 °C and 0.1 and 15/5 kPa (C6/C7-fractions) and maximum loadings at "high" pressure on Si-STW. Rows with light blue background contain information on the C7 fraction.*

Compound	$D_{0.1}/r^2$ (s^{-1})	D_{high}/r^2 (s^{-1})	Q_{high} (mmol/g)
nC6	$1.9 \cdot 10^{-3}$	$1.7 \cdot 10^{-3}$	1.77
2MP	$1.2 \cdot 10^{-3}$	$2.2 \cdot 10^{-3}$	1.66
22DMB	$3.5 \cdot 10^{-6}$	$2.9 \cdot 10^{-6}$	1.00
23DMB	$3.0 \cdot 10^{-4}$	$9.5 \cdot 10^{-4}$	1.64
nC7	$1.2 \cdot 10^{-3}$	$1.7 \cdot 10^{-3}$	1.70
3MH	$1.0 \cdot 10^{-3}$	$1.8 \cdot 10^{-3}$	1.64
23DMPe	$< 5 \cdot 10^{-6}$	$< 5 \cdot 10^{-6}$	> 1
24DMPe	$0.9 \cdot 10^{-3}$	$1.8 \cdot 10^{-3}$	1.60

As was done for the C5 fraction, diffusional time constants were obtained for the C6 and C7 fractions on Si-STW (see table 7.6) and kinetic selectivities of relevant pairs of isomers were calculated, as presented in table 7.7. The maximum loadings at "high" pressure are indicated in table 7.6. At 25 °C and said pressures (15 and 5 kPa for the C6 and C7 fractions, respectively), the difference between the slowest diffusing isomers (22DMB and 23DMPe) and the fastest ones is very large, with selectivities reaching values above 500. These are far above those obtained for the C5 fraction on Si-STW, thus confirming the good performance of this zeolite for this separation, at least in what refers to the C5-C7 fractions.

Table 7.7: *Kinetic selectivities of relevant compound pairs on Si-STW at 15 (C6 fraction) and 5 (C7 fraction) kPa. Rows with light blue background contain information on the C7 fraction.*

Compounds	$\alpha^{kin,high}$
nC6/22DMB	586
2MP/22DMB	759
23DMB/22DMB	328
nC7/23DMPe	567
3MH/23DMPe	600
24DMPe/23DMPe	600

7.5 Conclusions on the use of zeolite Si-STW for the separation of linear, branched and dibranched paraffins

- Si-STW adsorbs linear and monobranched compounds in the C5 - C7 range preferentially and at a faster rate compared to dibranched ones.

- Additional selectivity among dibranched isomers is observed on Si-STW, with isomers presenting quaternary carbon atoms being practically excluded from the material and the rate of adsorption of dibranched isomers increasing with the distance between the branches.

- Zeolite Si-STW is superior to Si-MFI for carrying out the separation of dibranched paraffins from linear and monobranched ones in terms of equilibrium and kinetic selectivities and maximum adsorption capacity.

Chapter 8

Vapor phase separation of acetone, butanol and etanol using Si-STT

The separation of 1-butanol from vapors present in the overhead of ABE (acetone-butanol-ethanol) fermentation broth has been studied on a set of pure silica zeolites. Previously, Si-LTA in combination with Si-CHA or SAPO-34 (SAPO-CHA) proved useful in this separation [398]. Si-LTA (window size 4.1×4.1 Å) is selective towards butanol, the CHA-structured materials (window size 3.8×3.8 Å) are selective towards ethanol and none of them adsorb acetone in significant amounts. Water is also not adsorbed on the pure silica LTA and CHA materials. A high performance separation process was achieved thanks to these complementary selectivities. Both of the zeolite structures used in that work present 8-rings with similar window sizes and a tridirectional framework. The most remarkable structural difference affecting adsorption in this case is the tortuosity of the channel system, which is larger for CHA (4 openings/cavity) than for LTA (6 openings/cavity).

8.1 Materials description and characterization

In order to systematically study the effect of the opening size and the pore topology on the separation of butanol from ABE fermentation broth vapors and, if possible, to find promising adsorbents, a selection of unidirectional small pore pure silica zeolites was made. The selected materials present ITW, MTF, RTH and STT structures (see table 8.1) and all of them feature small pores and an essentially unidirectional channel system, i.e. 2 openings/cavity and thus, a larger tortuosity than CHA and LTA. As explained in chapter 6, ITW presents a channel-like topology with side pockets and a minimum window size of 3.9×4.2 Å. MTF presents a cavity-like topology, with cavities of ca. 6.25 Å in diameter which are interconnected by windows of 3.6×3.9 Å. RTH is also cavity-like, with cavities of ca. 8.18 Å in diameter interconnected by windows of 3.8×4.1 Å. STT is cavity-like, as well, with cavities of ca. 7.04 Å in diameter interconnected by windows of 3.7×5.3 Å.

The characterization results of the samples used are presented in table 8.2. XRD patterns and ^{29}Si MAS NMR spectra are included in appendix C Si-ITW and Si-MTF present no connectivity defects. Two different samples of Si-RTH, i.e. Si-RTH-a and Si-RTH-b, were used that present a tiny difference in the amount of connectivity defects (2% and 1%, respectively) and significative differences in their crystal size and shape, with Si-RTH-a particles being in the form of needle bundles of $10 \times 4 \times 4$ µm (i.e. 160 μm^3) and Si-RTH-b being composed of needles of $10 \times 0.5 \times 0.5$ µm (i.e. 2.5 μm^3). Si-STT presents a considerable amount of connectivity defects (5%).

Table 8.1: *Pore shape, opening size and framework topology of zeolites studied as CO_2 adsorbents in this chapter.*
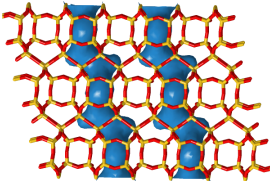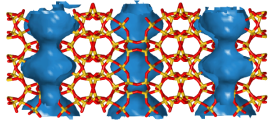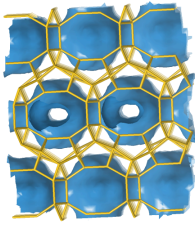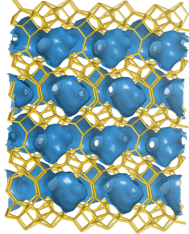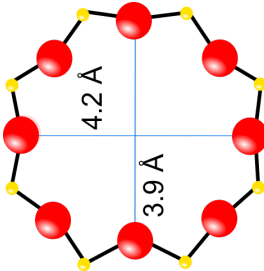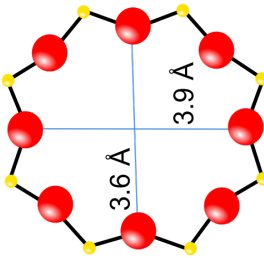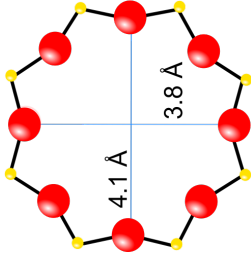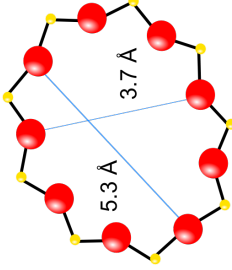
Descriptor	Si-ITW	Si-MTF	Si-RTH	Si-STT
Dimensionality	1D	1D	1D	1D
Topology	Channels	Cavities	Cavities	Cavities
View 1				
View 2				
Pore Opening Size (Å)	3.9 × 4.2	3.6 × 3.9	3.8 × 4.1	3.7 × 5.3

Table 8.2: *Characterization results of the samples after removal of occluded species.*

Sample	Si defects amount (% Q_3)	Crystal shape	Crystal dimensions (μm)	Pore diameter[a] (Å)	BET surface area (m^2/g)	DA surface area (m^2/g)	Micropore volume (cm^3/g)
Si–ITW	0	indefinite	2 - 30	4.8	356	-	0.18
Si–MTF	0	sheets	$5 \times 2 \times 0.1$	4.8	232	241	0.07
Si–RTH–a	2	needle bundles	$10 \times 4 \times 4$	-	598	-	0.24
Si–RTH–b	1	needles	$10 \times 0.5 \times 0.5$	-	606	-	0.23
Si–STT	5	smooth edged cuboid	$3a \times 2a \times a$ $2 < a < 10$	5.6	474	-	0.22

[a]Obtained by applying Horwatz-Kawazoe to the Ar adsorption isotherm at -186 °C.
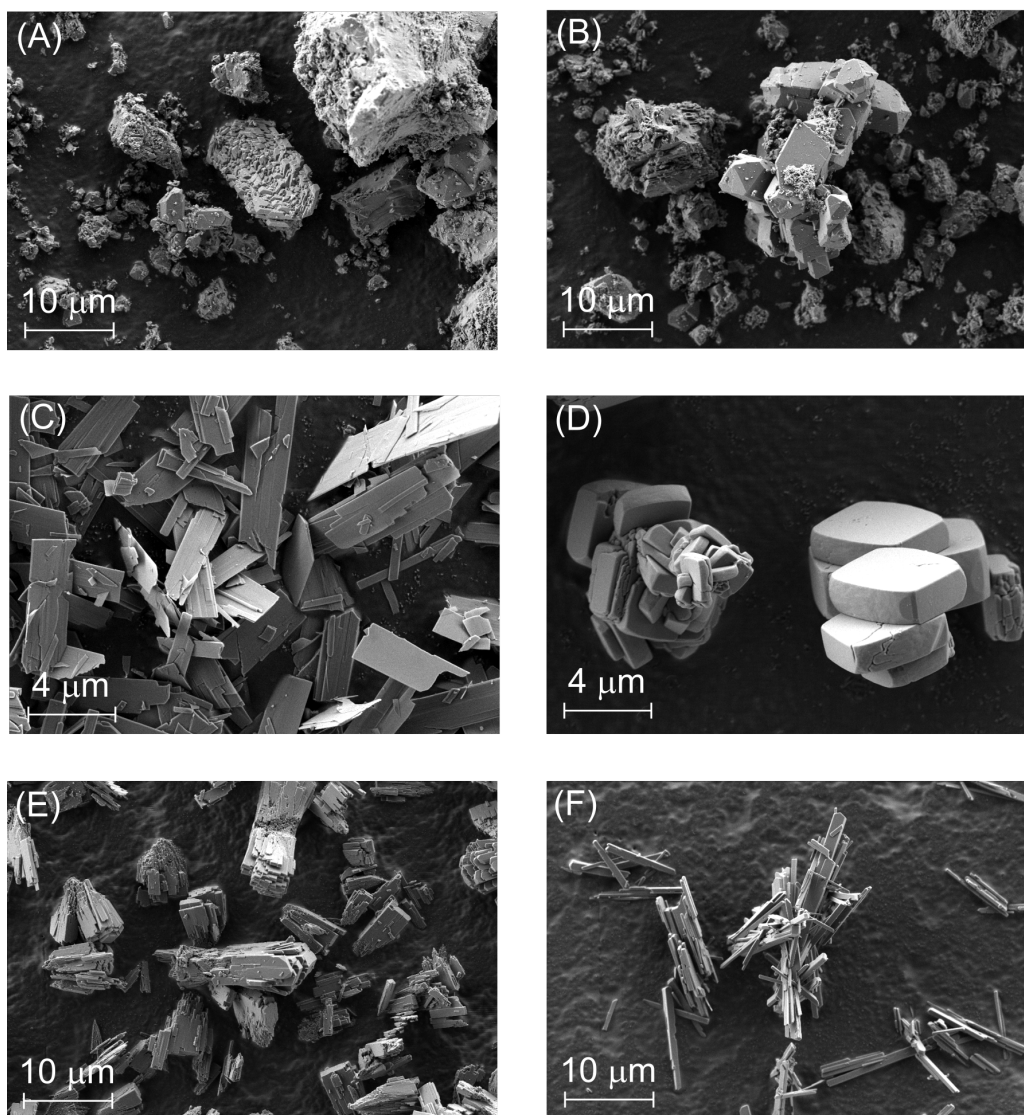
Figure 8.1: *SEM images of the samples used for this study. (A) and (B) are Si-ITW, and give an idea of the hetereogenity of the crystal size and shape of this sample. (C) is Si-MTF, (D) is Si-STT, (E) is Si-RTH-a and (B) is Si-RTH-b.*

8.2   Pure component vapor isotherms

Pure component isotherms of acetone, butanol, ethanol and water on different materials are presented in fig. 8.2. First, a screening of the adsorbents was made by measuring adsorption isotherms of 1-butanol and ethanol at 40 °C and up to a partial pressure of the vapor lower than their vapor pressure at that temperature. These were measured in a gravimetric VTI SGA 100H device and served to check whether the

materials could be used for preferentially adsorbing either 1-butanol or ethanol. 1-Butanol isotherms were not equilibrated, except for that on Si-STT, indicating important kinetic hindrance on RTH, ITW and MTF materials. Ethanol isotherms were equilibrated and reproducible for Si-STT, Si-RTH-a and Si-RTH-b, but not so on Si-MTF or Si-ITW. This meant that Si-ITW and Si-MTF could not be used for this application, as they do not adsorb significant amounts of neither butanol nor ethanol, which are the most relevant compounds involved in the separation. Si-STT was accordingly selected as a material capable of adsorbing both butanol and ethanol and Si-RTH-a and Si-RTH-b were selected as materials selective towards ethanol. Si-STT presents a larger adsorption capacity of ethanol than Si-RTH-a and Si-RTH-b, which present very similar isotherms, with that of Si-RTH-a being slightly above that of Si-RTH-b.

Later, isotherms of acetone, 1-butanol, ethanol and water on Si-STT were recorded on a Hiden IGA3 device available at the Vrije Universiteit Brussels (VUB), in order to have more accurate isotherms and more data at lower pressure. A good match was found between measurements recorded on Hiden IGA3 and on VTI SGA 100H. Unfortunately, during my stay at the VUB, there was not enough time to measure the RTH materials on the Hiden IGA3, too, but the goodness of the measurements is backed up by the fact that the kinetics of each point seem to be equilibrated. Water isotherms on the three materials were recorded on a BelSorp II Max device and the result for Si-STT is compatible with that obtained from the Hiden IGA3 at the Vrije Universiteit Brussels. Si-RTH-a presents a larger adsorption capacity of water at high pressure than Si-RTH-b, which may be related to the slightly larger amount of connectivity defects, i.e. hydrophilic silanol groups, on the first.
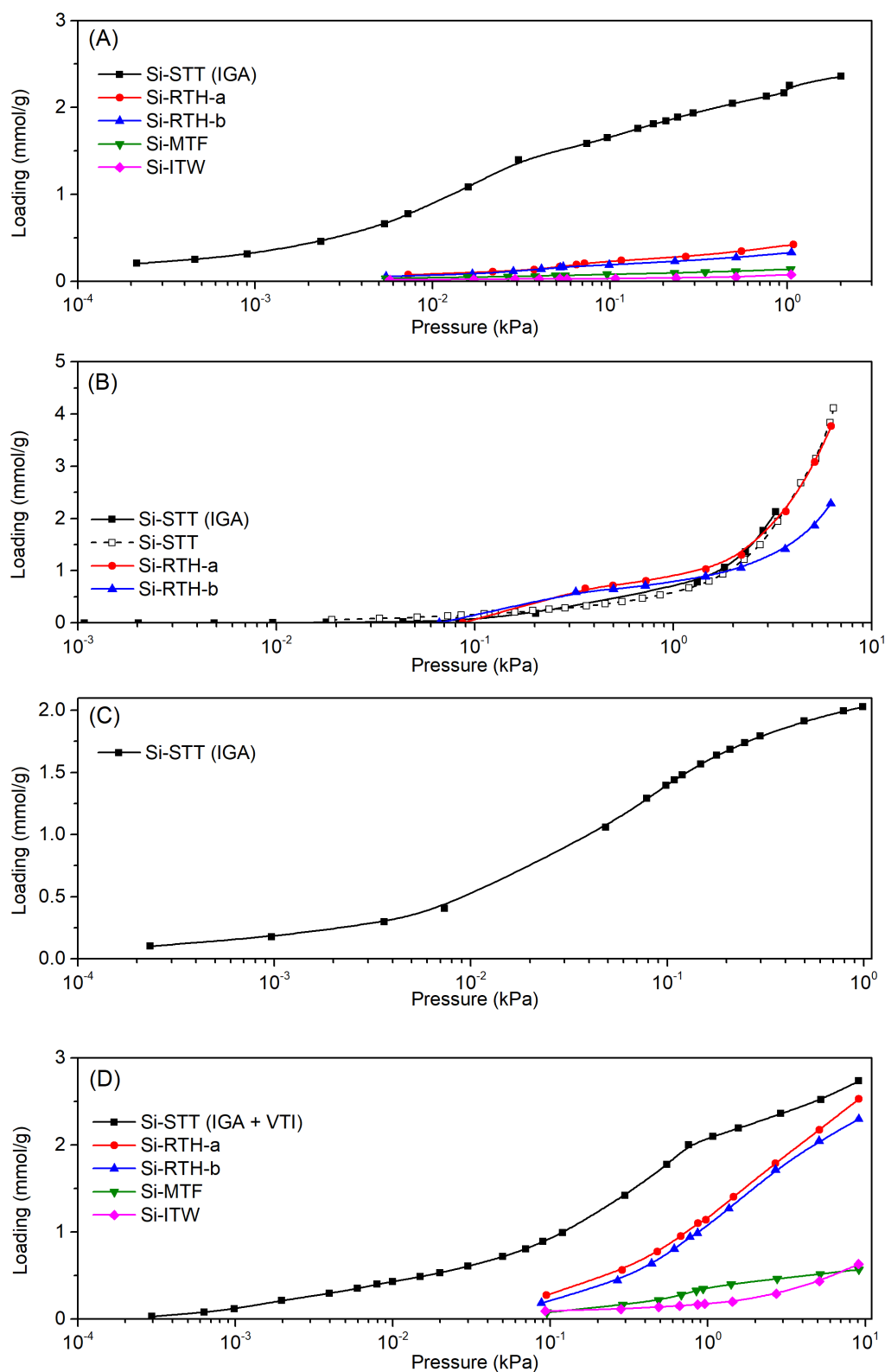
Figure 8.2: *Adsorption isotherms at 40 °C of (A) 1-butanol, (B) water, (C) acetone and (D) ethanol on Si-STT (black squares), Si-RTH-a (red circles), Si-RTH-b (blue up-triangles), Si-MTF (green down-triangles) and Si-ITW (magenta diamonds). 1-Butanol and ethanol isotherms were measured on VTI SGA 100H, and later for Si-STT remeasured on Hiden IGA3. Water isotherms were measured on BelSorp II Max, unless otherwise stated. Acetone on 8-ring zeolites is not shown here, as it is practically excluded (see fig. 8.4). Lines are guides to the eye. Note that the scales differ in the four graphs.*

229

8.3 Breakthrough adsorption experiments

8.3.1 Basic experiments analysis

Breakthrough adsorption experiments were carried out on the three selected materials, i.e. Si-STT, Si-RTH-a and Si-RTH-b, according to the method described in section 3.3.4.2, and representative profiles* for each material are presented in fig. 8.3.

The breakthrough of all the components of the vapour mixture are well distinguishable on Si-STT (see fig. 8.3A). Water breaks through in the first place and almost immediately (9 - 12 min), with no distinguishable roll-up (with a value of y/y_0 close to 1.03 until ethanol breaks through), confirming that it is not being adsorbed to a relevant extent. Ethanol breaks through in the second place (80 - 100 min), presenting an extremely high roll-up (reaching values of y/y_0 close to 7). Acetone breaks through after ca. 10 min, with a very steep increase in concentration to a roll-up value of 2. At this point the outcoming normalized concentration of ethanol is ca. 1.2. After 60 - 70 min butanol breaks through, with a more spread (70 - 90 min) increase.

The profiles on the RTH materials are very different from that on Si-STT, but similar to each other. Acetone and water both break through almost immediately (ca. 4 min), with acetone presenting a roll-up to 1.2 - 1.3 until butanol breaks through. This was surprising, as no adsorption of acetone is expected on the RTH materials at the experimental partial pressure (ca. 0.1 kPa) due to size exclusion (see fig. 8.4). One possible explanation of this phenomenon would be that in the presence of the other components of the ABE mixture, acetone is weakly adsorbed on the surface of the RTH crystals. The profile of water is also quite particular, as it reaches values above 0.9 in less than 10 min, but does not reach 1 until ca. 100 min, which is indicative of the existence of diffusion limitations.

---

*Each experiment was carried out 1 - 7 times. On Si-STT it was 7 times, to check the reproducibility of breakthrough times and adsorbed amounts. On Si-RTH-a, due to its poor performance, only a repetition was carried out. On Si-RTH-b 3 repetitions were done.
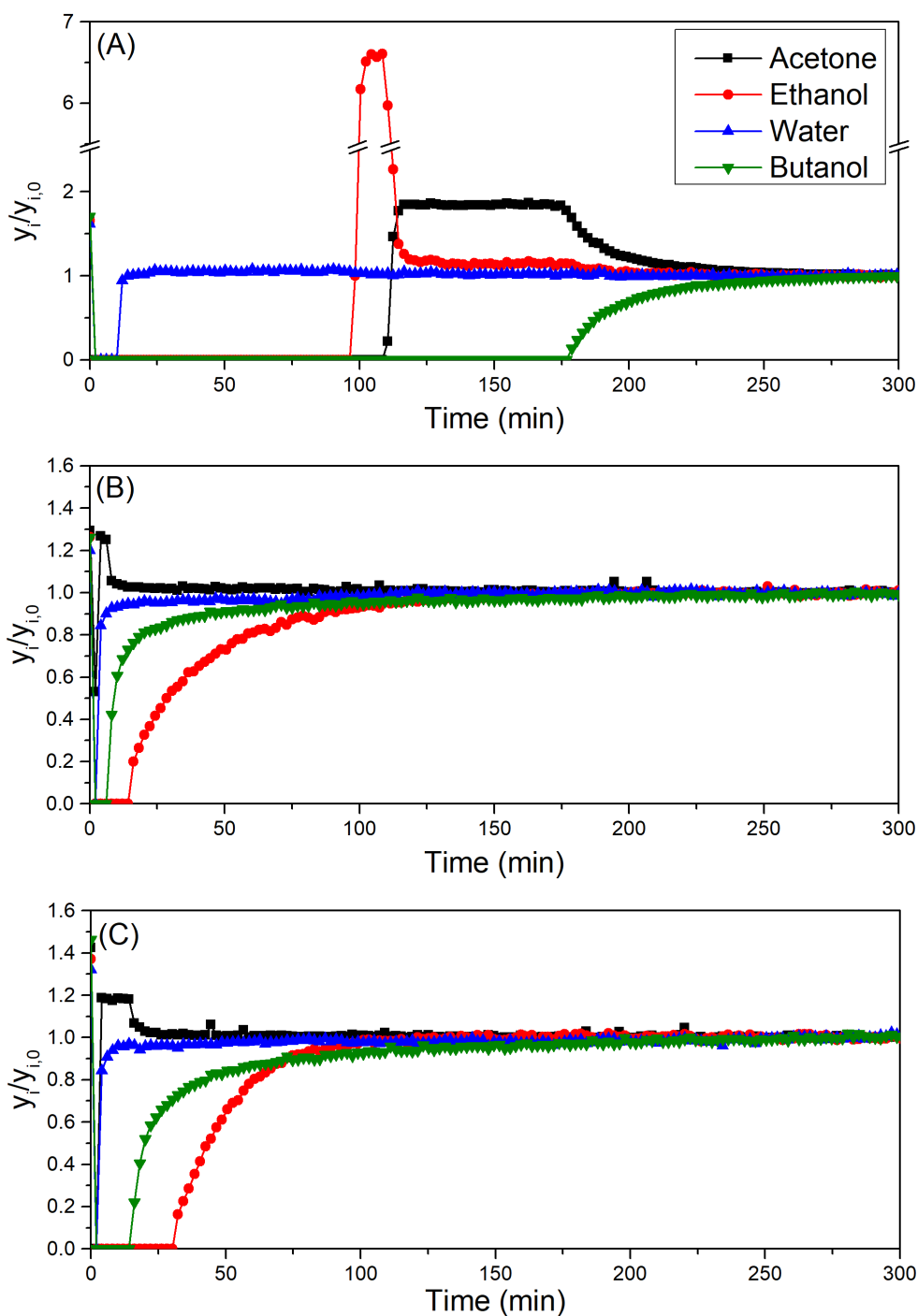
Figure 8.3: *Breakthrough profiles of the ABE vapor mixture described in table 3.2 at 40 °C and 15.1 cm³ STP/min of total He carrier gas flow on (A) Si-STT, (B) Si-RTH-a and (C) Si-RTH-b.*

Butanol breaks through next, at times < 10 min in Si-RTH-a and times between 10 and 20 min for Si-RTH-b. It is evident that the diffusion of butanol in RTH materials is hindered, as despite the initially steep breakthrough, equilibrium is approached very slowly and only reached

after ca. 250 min. Ethanol breaks through in the last place, at times of 10 - 20 min for Si-RTH-a and ca. 30 min for Si-RTH-b.
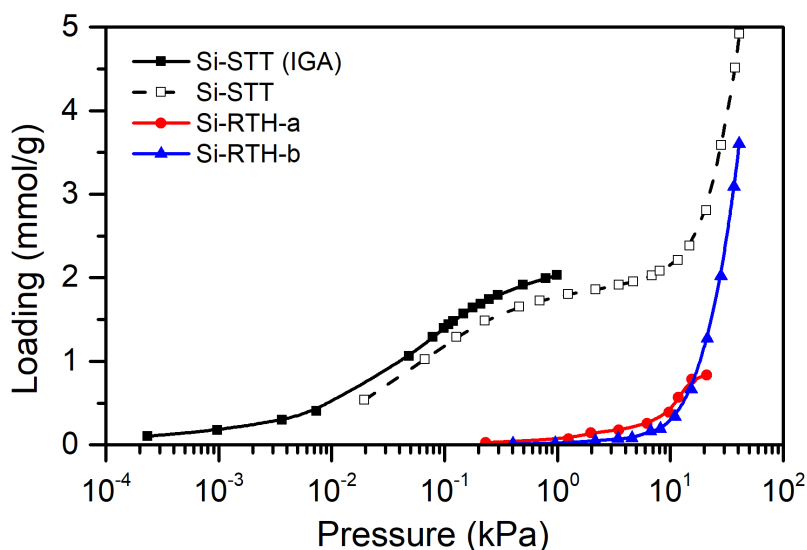
Figure 8.4: *Acetone adsorption isotherms on Si-STT, Si-RTH-a and Si-RTH-b recorded on the BelSorp II Max, unless otherwise specified. The isotherms on Si-STT differ in the two devices used (ca. 10% error at 0.1 kPa) but follow the same trend. The isotherms on the RTH materials are not equilibrated, only apparent.*

The adsorbed amounts calculated from the breakthrough profiles together with those obtained from interpolating the pure component adsorption isotherms are presented in table 8.3.

In general terms, the loadings calculated from the mixture breakthrough experiments are smaller than those obtained from the adsorption isotherms at the same pressure. The adsorbed amount of acetone on Si-STT calculated from breakthrough data is ca. 8 times lower than that obtained from the isotherm. The butanol loading on Si-STT is the one that presents the smallest variation when going from the pure component isotherm to the breakthrough experiment, decreasing only by a factor of 1.3. Due to the fast and large roll-up the ethanol loading on Si-STT varied between 0.013 to 0.037 for different breakthrough experiment repetitions and therefore it has a large relative error (ca. 50 %). It is ca. 30 times lower than the value given by the isotherm. The breakthrough of water on Si-STT was measured twice with the TCD and the first time there was a strange roll-up to 1.2 at times between 20 and 40 min,

Table 8.3: *Adsorbed amounts obtained from interpolation of the pure component adsorption isotherms and from analysis of the mixture breakthrough experiments. The values derived from the isotherms are calculated by linear interpolation of the partial pressure of the component (see table 3.2) between the closest experimental points.*

Material	Adsorbate	Q_{isot} (mmol/g)	Q_{BT} (mmol/g)
Si-STT	Acetone	1.421	0.166
	1-Butanol	1.810	1.378
	Ethanol	0.607	0.021
	Water	1.654	0.360
Si-RTH-a	Acetone	0.013	-0.018
	1-Butanol	0.258	0.220
	Ethanol	0.089	0.078
	Water	0.649	0.651
Si-RTH-b	Acetone	0.003	-0.013
	1-Butanol	0.214	0.241
	Ethanol	0.064	0.057
	Water	0.135	0.573

which was probably due to some instability in the vapor pressure. The loading calculated therefrom was of -0.445 mmol/g, which is indicative of the irregularities of this repetition. Therefore the water loading on Si-STT shown in the table (0.360 mmol/g) is the one calculated from the profile displayed in fig. 8.3A, which is still very low compared to the value obtained from the isotherm[*].

The acetone loadings on RTH materials are negligible[†], confirming that acetone is excluded from these materials. The butanol loadings on Si-RTH-a and Si-RTH-b are similar in breakthrough experiments and adsorption isotherms, and the same happens with the ethanol loadings. This indicates that the selectivity does not vary for these adsorbates when going from the pure components to the mixture. The water loadings

---

[*]Nonetheless, it will be seen below that it is not infrequent that the water profiles present problems related to its fast breakthrough and the low time resolution of these experiments (1 point every 2 min).

[†]The small negative values most probably have their origin in the low time resolution of these experiments again.

on RTH materials are relatively high, which may be due to adsorbate-adsorbate interactions with other components, probably ethanol. In fact, on Si-RTH-a the water loading calculated from the breakthrough curve is very similar to that measured in the adsorption isotherm, and for Si-RTH-b, the breakthrough loading is 4 times larger than that measured.

Overall, what is observed is that on Si-STT, the selectivity towards butanol increases in the mixture with respect to the pure components, while on Si-RTH there is no improvement in the selectivity towards any component, except for water in the case of Si-RTH-b. Thus, despite the differences in the breakthrough times of the ABE components, it does not seem that RTH materials will be able to carry out a convenient separation of ethanol.

8.3.2 Experiments carried out at different conditions

The effects of different experimental conditions on the breakthrough profiles and the calculated adsorbed amounts on Si-STT was studied by varying the temperature, flow rate, carrier gas composition and the presence or absence of water. On Si-RTH-b the effects of temperature and carrier gas composition were studied and on Si-RTH-a the effect of increasing the temperature. These results are presented in table 8.4.

As expected, increasing the temperature leads to an overall loss of adsorption capacity of any adsorbent. On Si-STT the amount adsorbed of butanol is comparatively larger at 80 °C, which means a larger selectivity despite the decrease in adsorption capacity. The breakthrough of butanol becomes steeper at higher temperature (see fig. 8.5). The adsorbed amount of water "becomes negative"* at this temperature, which is probably due to the low time resolution of these experiments (one experimental point every ca. 2 min). This, combined with an almost immediate breakthrough, a very light but prolonged roll-up, irregularities

---

*The first moment τ of water in this experiment is -6 s, the physical meaning of which is just that there is no substantial adsorption. However, when obtaining the adsorbed amount by applying eq. (3.31), this negative breakthrough time becomes a negative adsorbed amount.

Table 8.4: *Adsorbed amounts calculated from breakthrough experiments carried out at different conditions. The basic experiment is carried out at 40 °C, with He as carrier, a total flow of 15.1 mL STP/min and in the presence of water (see table 3.2).*

Material	Adsorbate	Q_{BT} (mmol/g)					
		Basic (40 °C)	60 °C	80 °C	No water	Total flow × 2	CO$_2$ as carrier gas
Si-STT	Acetone	0.166	0.098	0.047	0.218	0.160	0.186
	1-Butanol	1.378	1.135	0.976	1.337	1.410	1.397
	Ethanol	0.021	0.019	0.013	0.047	0.011	0.032
	Water	0.360	0.272	-0.574	-	-0.239	0.164
Si-RTH-a	Acetone	-0.018	-	-0.022	-	-	-
	1-Butanol	0.220	-	0.083	-	-	-
	Ethanol	0.078	-	0.012	-	-	-
	Water	0.651	-	0.293	-	-	-
Si-RTH-b	Acetone	-0.013	-	-0.006	-	-	-0.001
	1-Butanol	0.241	-	0.075	-	-	0.176
	Ethanol	0.057	-	0.012	-	-	0.049
	Water	0.573	-	0.293	-	-	0.430

in the water signal (see fig. 8.5) and the high concentration of water in the gas phase in comparison to the other vapors result in the anomalous value of the water loading on Si-STT (-0.574 mmol/g) under these conditions (80 °C). On Si-RTH-a and Si-RTH-b, the increase to 80 °C makes the material less selective towards ethanol, as well. Experimentally, this is observed as a simultaneous breakthrough of ethanol and butanol. Carrying out the ABE separation in the absence of water results in quite similar results compared to the original case, with acetone adsorption increasing slightly, ethanol adsorption increasing and butanol adsorption remaining practically unmodified. Doubling the total flow rate of the carrier gas modified the characteristic breakthrough times of the adsorbates by halving them, but did not affect the adsorbed amounts significantly. The use of CO$_2$ as a carrier gas has only a minor effect on the adsorbed amounts of the vapors on Si-STT, especially considering the large error inherent to the calculated water loadings, which are the only ones which

vary significantly. In Si-RTH-b, switching to CO_2 as the carrier gas lowers the amount adsorbed of butanol by 25 %, probably due to CO_2 being adsorbed on this material.
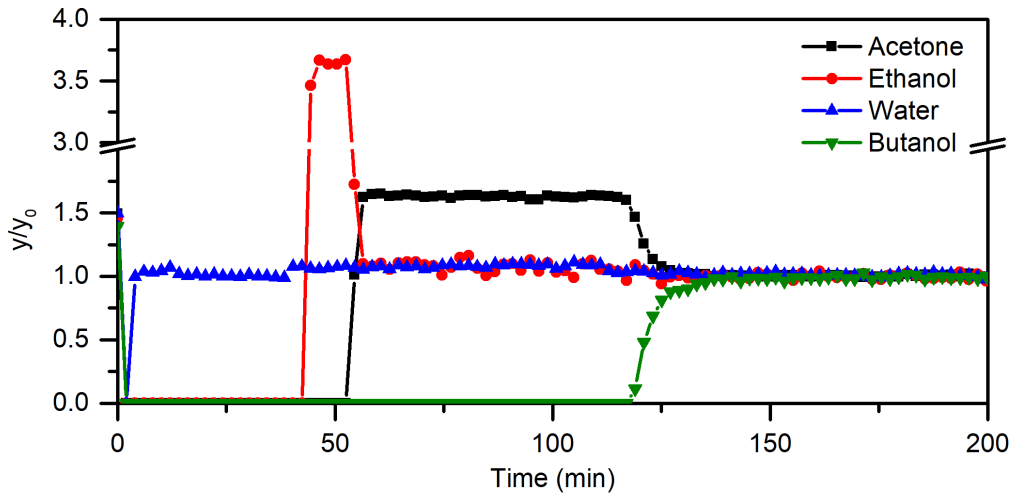
Figure 8.5: *Breakthrough experiment on Si-STT at 80 °C.*

8.3.3   Desorption data analysis

Desorption experiments were carried out after the basic breakthrough adsorption experiments, by switching the feed to pure carrier gas and, after 20 min, increasing the temperature to 120 °C at 1.4 °C/min, holding for 5 h and later increasing to 200 °C at 1 °C/min and holding for 2 h. The corresponding profiles for Si-STT and Si-RTH-b are depicted in fig. 8.6.

In fig. 8.6A, the desorption profile of zeolite Si-STT is presented. Water is desorbed almost immediately ($<$ 5 min). Up to 20 min there is a monotonic descent of the concentration of the three ABE components. After 20 min have passed, temperature starts increasing, upon which the desorption of the adsorbates becomes faster. Ethanol presents a small shoulder and then continues to decrease monotonically until it reaches values below 0.05 after 90 min and below the detection limit after 120 min. The normalized concentration of acetone increases up to a maximum of y/y_0 = 0.96 at 39 min, corresponding to a temperature of 57 °C and then decreases until it is $<$ 0.01 after 90 min and below the detection limit after ca. 110 min. Butanol presents three maxima, the first with a
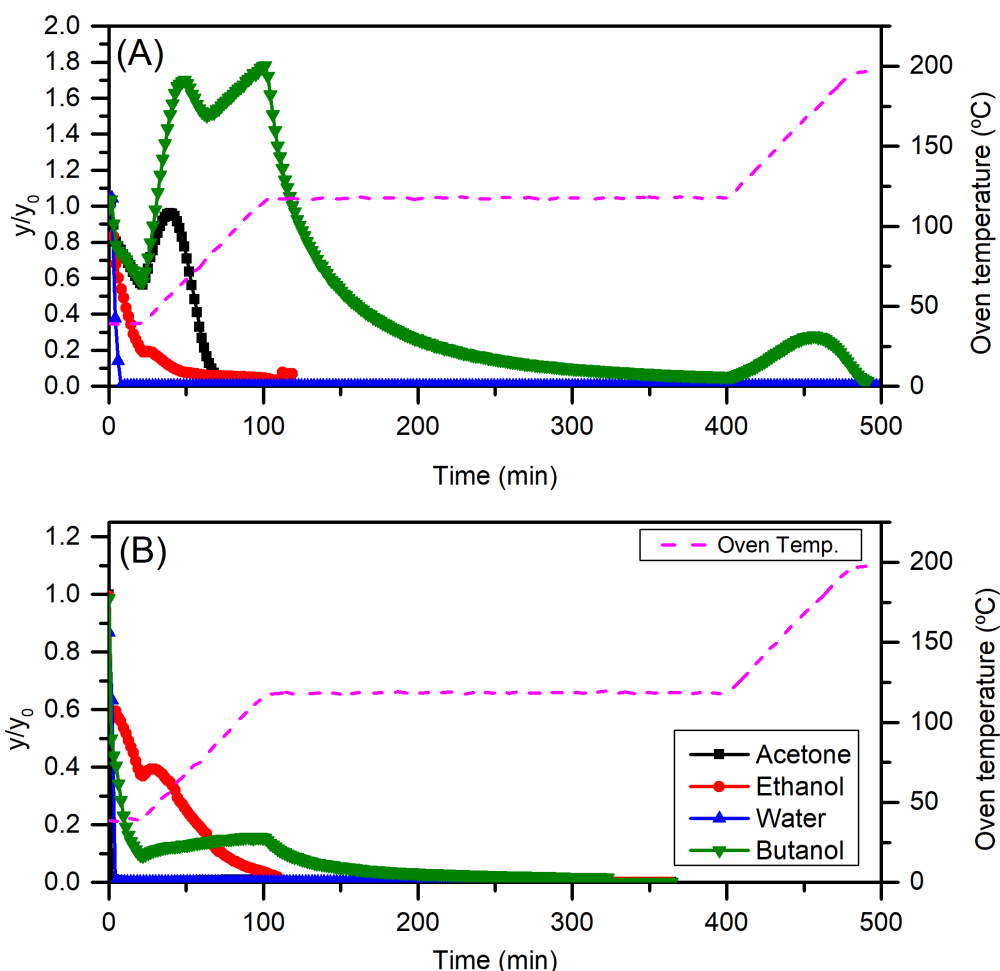
Figure 8.6: *Desorption profiles after basic brekathrough experiments on (A) Si-STT and (B) Si-RTH-b. The values for y_0 are defined according to the adsorption step feed.*

value of $y/y_0 = 1.70$ at 49 min and 67 °C, the second one with a value of $y/y_0 = 1.78$ at 110 min and 117 °C and the third one with a value of $y/y_0 = 0.28$ at 456 min and 171 °C*.

This last desorption peak points at a strong adsorbate-adsorbent interaction and corresponds to ca. 4.5% of the total 1-butanol desorbed. In an attempt to see if there is a relationship between this peak and the 5% of connectivity defects present in this material (see table 8.2), I determined the amount of silanols per unit cell and the amount of 1-butanol molecules per unit cell at saturation and that corresponding to the last peak. This is

---

*Curiously, the maximum of acetone and the second maximum of butanol match their respective boiling points. This is just a coincidence and does not require further explanation.

done simply by taking into account the chemical formula of the zeolite's unit cell ($Si_{64}O_{128}$) and its molar mass (3845.40 g/mol). I found that 5 molecules of butanol are present in a unit cell of the material at saturation and that the peak in question corresponds to 0.33 molecules per unit cell. The average number of defects per unit cell is of 3.2, which means that the stronger adsorbed 1-butanol molecules are not necessarily adsorbed on silanol groups.

In fig. 8.6B, the desorption profile of zeolite Si-RTH-b is presented. In this case, both acetone and water desorb immediately, reaching values below 0.01 before 4 min. The profiles of butanol and ethanol decrease monotonically until 20 min, with butanol decreasing notably faster. After 20 min, ethanol presents a maximum with a value of y/y_0 = 0.39 at 27 min and 45 °C and then decreases to values < 0.01 after 110 min. Butanol reaches a maximum with a value of y/y_0 = 0.16 at 98 min and 114 °C and then decreases slowly to values < 0.01 after 320 min.

As described in section 3.3.4.2, I calculated butanol recovery and purity depending on the time range selected for obtention of butanol during the desorption step on Si-STT[*]. A purity-recovery plot is presented in fig. 8.7. Butanol purities above 99% are achieved at recoveries below 70% and at complete recovery, a purity of 72% is obtained. A very good compromise can be achieved by selecting a purity of 90% at a recovery of 96% or a purity of 93% at a recovery of 90%. If the regeneration is stopped after dwelling for 2 h at 120 °C, the last peak in the regeneration is excluded from the product and, accordingly, the maximum recovery achievable decreases by 4.5%.

---

[*]Due to the close breakthrough times of butanol and ethanol on Si-RTH-b and the low adsorption capacities and selectivities, the calculation of recoveries and purities of butanol using this material was disregarded.
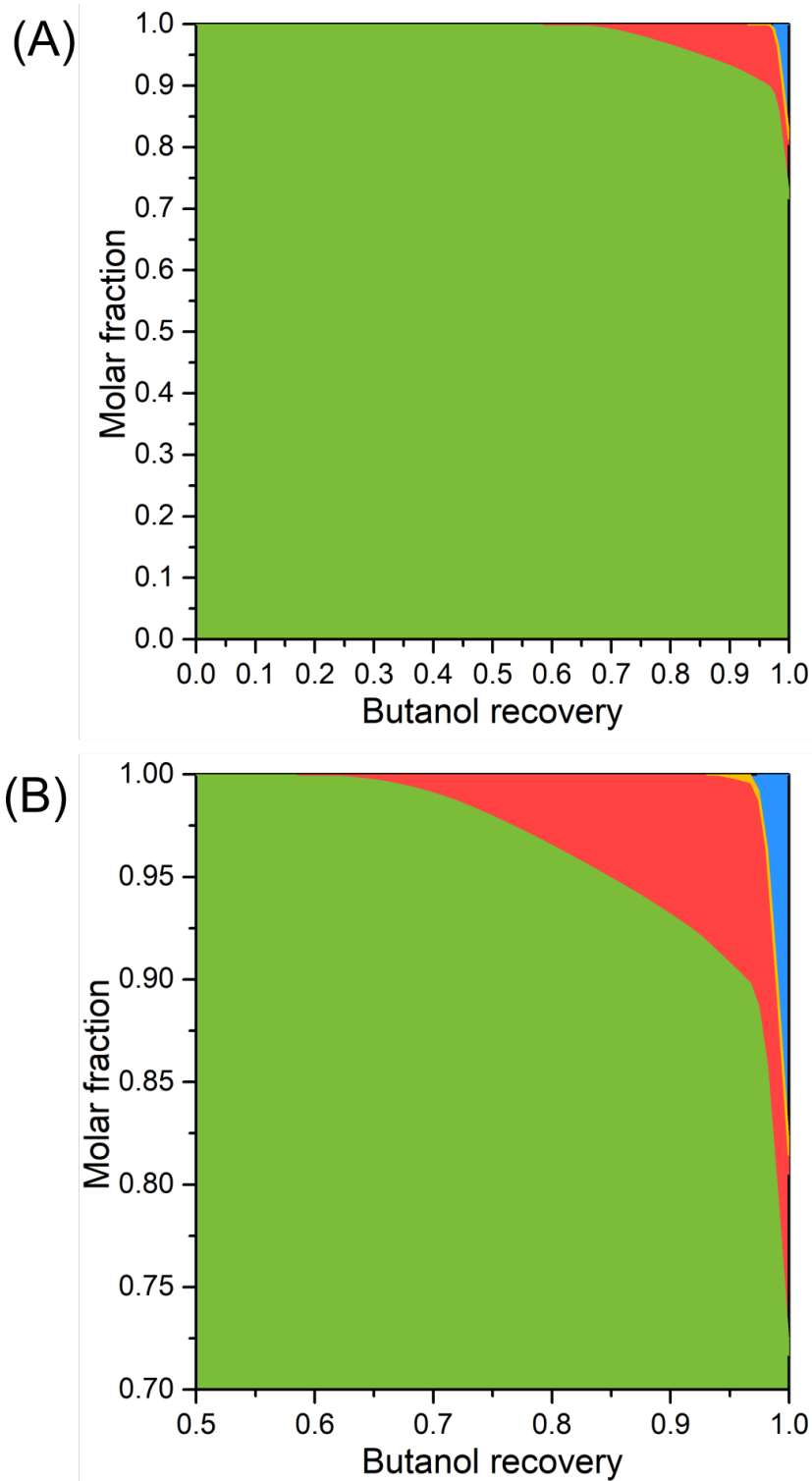
Figure 8.7: Purity-recovery plot of the ABE separation on Si-STT, (A) full-scale and (B) zoomed-in. The focus is put on butanol (green) but the molar fractions of the other components of the mixture, i.e. acetone (red), ethanol (yellow) and water (blue) are depicted, too.

8.4 Comparison of Si-STT with Si-LTA as adsorbents for the ABE separation from the vapor phase

One of the initial objectives of this work on the ABE separation was to find an adsorbent that could carry out the separation and to be able to compare it with previously reported Si-LTA and Si-CHA materials [398]. However, during my short stay in Brussels, and trying to solve some problems that kept coming up, I changed the feed composition by diluting it and lowering the partial pressure of water, as it caused oscillation of the signal. This makes it a bit difficult to directly compare my results with those previously reported, but I will try to give some key points.

First of all, prior to establishing this comparison, I will remind the reader of the experimental conditions used in both works. In table 8.5 the respective partial pressures of the vapors and ABE ratios are listed. Partial pressures in this work are lower by a factor of ca. 0.57. The temperature in both works was of 40 °C and the total flow through the column close to 15 cm^3 STP / min. The regeneration flow in this work was 15 cm^3 STP / min of He, but in the work by Van der Perre et al it was of 10 cm^3 STP / min.

Table 8.5: *Experimental partial pressures and ABE ratios of this thesis and a previous work by Van der Perre et al.*

Component	This thesis		Van der Perre et al. [398]	
	P_i (kPa)	Ratio to ethanol	P_i (kPa)	Ratio to ethanol
Acetone	0.105	3.4	0.192	3.8
1-Butanol	0.176	5.7	0.299	6.0
Ethanol	0.031	1	0.050	1
Water	2.377	77.4	4.220	84.4

Both Si-STT and Si-LTA are selective towards butanol over the other ABE components and can perform the separation on their own with relatively good performance. Thus, I have decided to let Si-CHA (and Si-RTH-b) out of this discussion. Out of Si-LTA and Si-STT, only the

latter adsorbs acetone significantly, which is a major drawback of this material. In table 8.6 I have compared the adsorbed amounts of acetone, 1-butanol, ethanol and water on Si-STT and Si-LTA at their respective experimental pressures. The loadings obtained from the pure component isotherms show that Si-STT adsorbs larger amounts of acetone, ethanol and water than Si-LTA. The amount adsorbed of butanol is slightly larger on Si-LTA. This may be partially due to the higher micropore volume of Si-LTA materials (0.32 cm^3/g) compared to the Si-STT materials (0.22 cm^3/g). When going to the loadings calculated from mixture breakthrough data analysis, it may be seen that the adsorbed amounts of acetone, ethanol and water drastically decrease on Si-STT, by 88%, 96% and 78%, respectively, respective to the pure component case. The amount adsorbed of acetone is still important, though. The decrease of butanol is much smaller, of 24%, which means that there is a clear preference towards butanol. In Si-LTA, going from pure component isotherms to the mixture breakthrough experiments leads to a decrease in the adsorption capacities of 84% (acetone), 23% (butanol), 65% (ethanol) and 19% (water). The decrease for butanol is very similar to Si-STT and the adsorbed amount, too, despite the lower pressure used in my experiment. Adsorption of acetone on Si-LTA is negligible. Considerable amounts of ethanol and water are adsorbed in the breakthrough experiment on Si -LTA. It would be interesting to compare these trends at similar experimental conditions, as possibly larger pressures would lead to larger adsorbed amounts of ethanol and water on Si-STT, too. By examining the shape of the isotherm and the corresponding adsorbed amounts of ethanol and water on Si-STT at the pressures of the experiments carried out in [398] the loading at those pressures can be calculated. Assuming that the loss in adsorption capacity on Si-STT when going from the isotherm to the breakthrough experiment remains constant at the higher pressure, an estimate of the adsorbed amounts of a hypothetical breakthrough experiment on Si-STT at the same conditions than Si-LTA can be obtained (see table 8.7). Apparently, increasing the partial

pressure of all the components to match those on Si-LTA would have a much larger effect on the adsorbed amount of water than on the adsorbed amount of the other components (ethanol included).

Table 8.6: *Adsorbed amounts on Si-STT and Si-LTA at their respective experimental pressures (those presented in table 8.5). The loss of adsorption capacity when going from pure component isotherms to mixture breakthrough experiments is also included. The isotherms on Si-LTA used for the calculation of pure component loadings were extracted from [398].*

Material	Adsorbate	Q_{isot} (mmol/g)	Q_{BT} (mmol/g)	Loss in adsorption capacity (%)
Si-STT	Acetone	1.421	0.166	88
	1-Butanol	1.810	1.378	24
	Ethanol	0.607	0.021	96
	Water	1.654	0.359	78
Si-LTA	Acetone	0.038[a]	0.006	84
	1-Butanol	1.895	1.458	23
	Ethanol	0.170	0.060	65
	Water	0.776	0.629	19

[a] The acetone isotherm on Si-LTA was not equilibrated, but it serves as orientative value.

Table 8.7: *Estimated adsorbed amounts of a mixture breakthrough experiment carried out on Si-STT at the conditions typical of the experiment on Si-LTA reported in [398].*

Compound	P_i (kPa)	Q_{isot} (mmol/g)	$Q_{BT,est}$ (mmol/g)
Acetone	0.192	1.813	0.212
1-Butanol	0.299	1.866	1.421
Ethanol	0.050	0.715	0.025
Water	4.22	3.167	0.687

Si-STT presents mixture selectivities of butanol over acetone and ethanol of 5 and 11, respectively, while Si-LTA presents a much larger selectivity over acetone ($>$ 150) but a smaller selectivity over ethanol, i.e. 4. According to the estimates presented in table 8.7, the selectivity of butanol over ethanol on Si-STT would decrease only slightly (ca. 9) if the partial pressures were set to similar values than for Si-LTA. Thus, it may be affirmed that Si-STT is a material that presents similar

butanol adsorption capacity to Si-LTA, larger butanol/ethanol selectivities and lower butanol/acetone selectivities at relevant conditions of the ABE separation.

The comparison of the purities and recoveries obtained from the analysis of the desorption profiles between the two materials may be done in qualitative terms. Despite the lower carrier gas flow (10 cm^3 STP / min) for Si-LTA, the initial part of the temperature ramp is the same as that of Si-STT. In the case of Si-STT, heating to 200 °C is necessary to completely regenerate the adsorbent, while on Si-LTA, heating to 120 °C was assumed to be sufficient. Si-STT presents a purity of 72% at full recovery, while for Si-LTA this purity is of 65%. However, for achieving purities above 99%, in Si-STT the recovery decreases to 70%, while in Si-LTA the recovery only decreases to 90%. This is due to the comparatively large amount adsorbed of acetone on Si-STT. Overall, it may be deduced that the compromise between recovery and purity is better accomplished on Si-LTA, unless full recovery is accounted for, in which case Si-STT provides a slightly better purity of the product.

8.5 Conclusions on the vapor phase ABE separation on Si-STT

- Materials with cavity-like topology are better suited for the adsorptive recovery of 1-butanol vapors. Furthermore, adsorbents need to possess pore openings with at least one dimension larger than 4.1 Å.

- Si-STT is an adsorbent that efficiently separates 1-butanol from vapor mixtures containing acetone, 1-butanol, ethanol and water at conditions close those of the overhead space of the ABE fermentor.

- A purity-recovery plot of 1-butanol shows that purities between 90 and 93% may be achieved at recoveries between 90 and 96% at these conditions. A purity of 72% is achieved at full recovery.

- Si-STT keeps a good 1-butanol selectivity in the presence of water and CO_2 and also at higher temperatures.

- Despite not excluding acetone, Si-STT presents an efficiency comparable to Si-LTA for carrying out this separation.

Chapter 9

Other work related to this thesis

9.1 Adsorption properties of ITQ-69

Andrés Sala synthesized a new silicogermanate material, ITQ-69 [502], and I took part in this work by carrying out part of the adsorption measurements and analyzing the adsorption data. ITQ-69 showed a high kinetic selectivity (ca. 5000) of propylene over propane and a moderate propylene adsorption capacity at 100 kPa and 25 °C. The material was found to be stable when kept in a dry atmosphere during and after calcination, with no loss of crystallinity after more than 40 adsorption-desorption cycles. This work was published in Angewandte Chemie International Edition in 2021 [502].

9.2 Roads to nowhere

9.2.1 Quasi-elastic Neutron Scattering for the study of propane and propene diffusion in zeolite Si-LTA

Prior to this thesis (2012-2014), my group recorded QENS spectra of a system containing Si-LTA and mixtures of propane and propene (one of them being fully deuterated). These experiments were performed at ISIS Neutron Source, more specifically at an instrument called LET. The purpose of these experiments was to study the microscopic diffusion of

propane and propane in mutual presence when adsorbed on zeolite Si-LTA (Si-ITQ-29).

In my Master's degre thesis, under the supervision of Pablo Bereciartua, I performed a first treatment and analysis of the recorded data. During the first two years of my thesis I dedicated a considerable amount of time attempting to obtain more information out of these data, by improving the analysis procedure and carrying out MD simulations and comparing simulated QENS spectra with the experiments. However, despite fruitful discussions with Victoria García-Sakai and Alexander O'Malley, the lack of an expert in the matter directly involved in this work made it very difficult for me to progress. This required too much of my time for a 4-year thesis and I, with the approval of my directors, decided to put it aside for the moment.

Another reasons which may be related to the difficulty in the data analysis and obtention of results are related to imperfect experiment design, as the studied temperatures were too low, and the selected instrument was not established for this kind of measurements.

9.2.2 Development of the VOLGRAV method

Some years ago, before I was a part of the A-Team of the ITQ, my fellow team members decided to develop a method to be able to measure 2-component isotherms by combining gravimetric and volumetric measurements. A set of binary CO_2 and CH_4 isotherms at different compositions of the gas phase on a set of high silica materials (Si-LTA, Si-BEA and a B containing DDR material) were measured on both a gravimetric (Hiden IGA) and a volumetric (Quantachrome iSorbHP) devices. Considering that for the volumetric device the total amount adsorbed n_{tot} is known:

$$n_{tot} = n_{CO_2} + n_{CH_4} \tag{9.1}$$

And for the gravimetric device the total mass adsorbed m_{tot} is known:

$$m_{tot} = n_{CO_2} \cdot M_{r,CO_2} + n_{CH_4} \cdot M_{r,CH_4} \qquad (9.2)$$

Where M_r is the molar mass of the adsorbate. From eqns. 9.1 and 9.2 it follows that:

$$n_{CH_4} = \frac{m_{tot} + n_{tot} \cdot M_{r,CO_2}}{M_{r,CH_4} - M_{r,CO_2}} \qquad (9.3)$$

Which theoretically allows to obtain the amount adsorbed of each of the two components.

However, after some months dedicated to analyzing the data on this matter, I came to the conclusion that we were missing something. The first suspicious fact I noticed was that I was getting negative adsorbed amounts for CH_4 at low pressures on DDR. After long discussion and evaluation, I came to the conclusion that the composition of the gas phase had been wrongfully and implicitly assumed to remain constant during the measurement. If the material adsorbs preferentially one of the two gases, which is the case, and the adsorption volume is finite, the composition of the gas phase will vary while adsorption is taking place. The effect will be especially important for small adsorption volumes, and low partial pressures of the strongest adsorbed component. The adsorption volume in Hiden IGA (ca. 3000 cm^3) was enough for considering the binary isotherms measured on it accurate. On the contrary, the volume in iSorbHP is much smaller, of ca. 15 cm^3, and the error in the gas phase composition at low pressures was estimated to be of ca. 50% for a 20:80 CO_2/CH_4 mixture on DDR and $> 15\%$ for Si-LTA and Si-BEA.

Therefore, it is evident that for carrying out such a study, either a large adsorption volume is needed or the composition of the gas phase needs to be monitored. Large adsorption volumes are detrimental for the obtention of precise volumetric isotherms, as the pressure variations from which the adsorbed amounts are calculated will be smaller in a larger volume and thus, subject to larger error. Monitoring the composition of the gas phase and correcting it in real time is only possible on a device especially

designed for measuring binary isotherms, which we did not have (and still do not have) at our disposal.

Chapter 10

Conclusions

- Zeolite Si-RWR is an interesting adsorbent with molecular sieving properties, the adsorption properties of which depend strongly on the synthesis procedure and characteristics of the lamellar precursor RUB-18. It is a relatively cheap pure silica zeolite that completely excludes methane at temperatures ranging from -196 to 25 °C and that poses kinetic restrictions to other small molecules, such as CO_2, CO or N_2 that become more important at low temperatures.

- AlPO and SAPO materials of LTA, CHA and AFI structure present lower isosteric heats of adsorption of CO_2 than their zeolitic counterparts, but the CO_2/CH_4 selectivity is maintained or even increased when going from a zeolite to its isostructural AlPO/SAPO material. This makes AlPOs and SAPOs promising adsorbents in CO_2 separation processes, which could lower the energy needed for regeneration

- Small pore channel-like zeolites present higher CO_2/CH_4 selectivities than cavity-like zeolites with the same composition and similar pore size.

- Zeolite Si-ITW is a very promising adsorbent for separating CO_2 from CH_4, being capable of separating bulk mixtures of these gases at relevant conditions with a performance comparable to that of LTA-6 and easier regeneration.

- Breakthrough experiments are a very powerful tool to study adsorbents for their use in industrial separations, giving a closer approximate of how an adsorbent performs under relevant conditions.

- Zeolite Si-STW preferentially adsorbs linear and monobranched compounds in the C5 - C7 range preferentially and at a faster rate compared to dibranched ones, practically excluding isomers presenting quaternary carbon atoms. The diffusion rate decreases with the distance between the branches of dibranched isomers.

- Zeolite Si-STW is superior to Si-MFI for carrying out the separation of dibranched paraffins from linear and monobranched ones in terms of equilibrium and kinetic selectivities and especially because of its larger adsorption capacity.

- Zeolite Si-STT is an adsorbent that efficiently separates 1-butanol from vapor mixtures containing acetone, 1-butanol, ethanol and water at conditions close those of the overhead space of the ABE fermentor. A good 1-butanol selectivity is maintained in the presence of CO_2 and also at higher temperatures.

- A purity-recovery plot of 1-butanol shows that purities between 90 and 93% may be achieved at recoveries between 90 and 96% at these conditions. A purity of 72% is achieved at full recovery. Despite not excluding acetone, Si-STT presents an efficiency comparable to Si-LTA for carrying out this separation.

Appendix A

Appendix to chapter 6

A.1   XRD patterns and ^{29}Si MAS NMR spectra

The XRD patterns and ^{29}Si MAS NMR spectra of the samples used in chapter 6 are presented in this appendix. The XRD patterns confirm the structural identity of the samples. The ^{29}Si MAS NMR spectra of the spectra allowed us to establish that the amount of Si defects (Q_3) is very low in all pure silica zeolites, save for Si-CHA, that possesses 8 % of Q_3 environments.
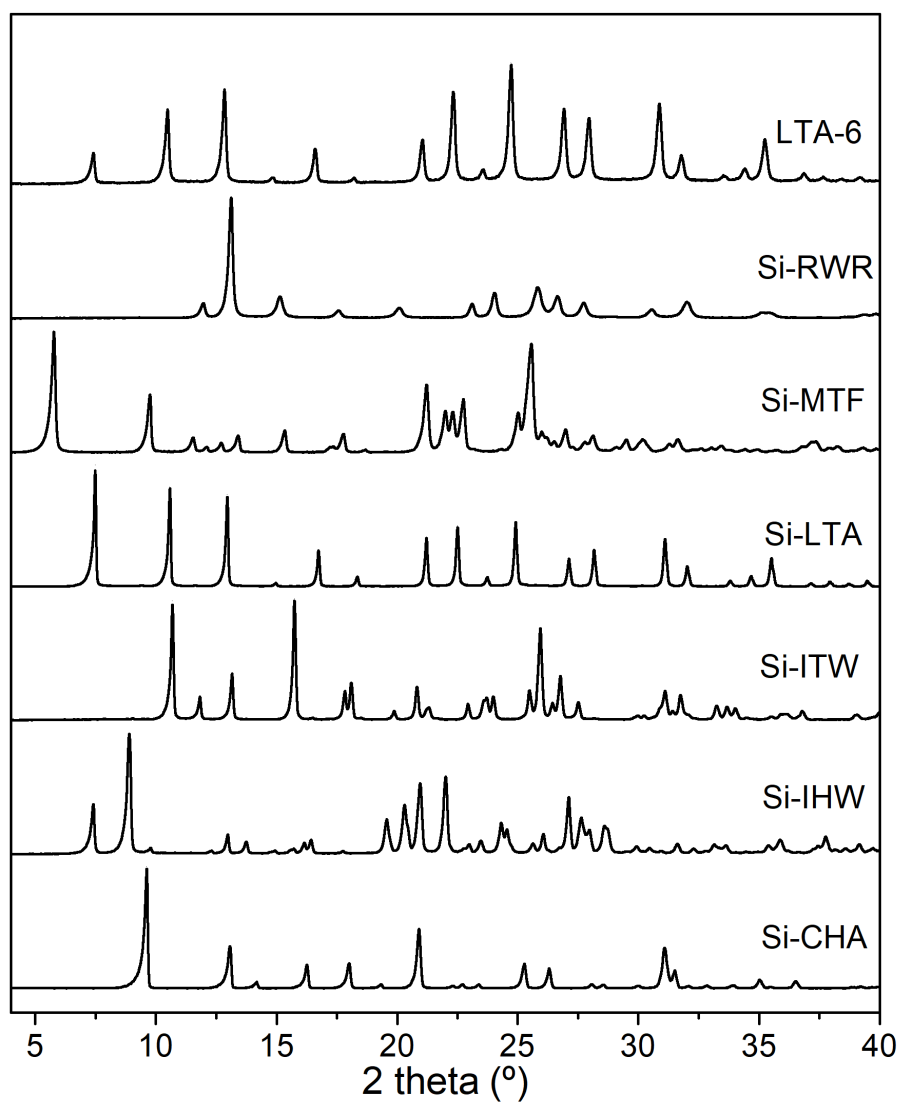
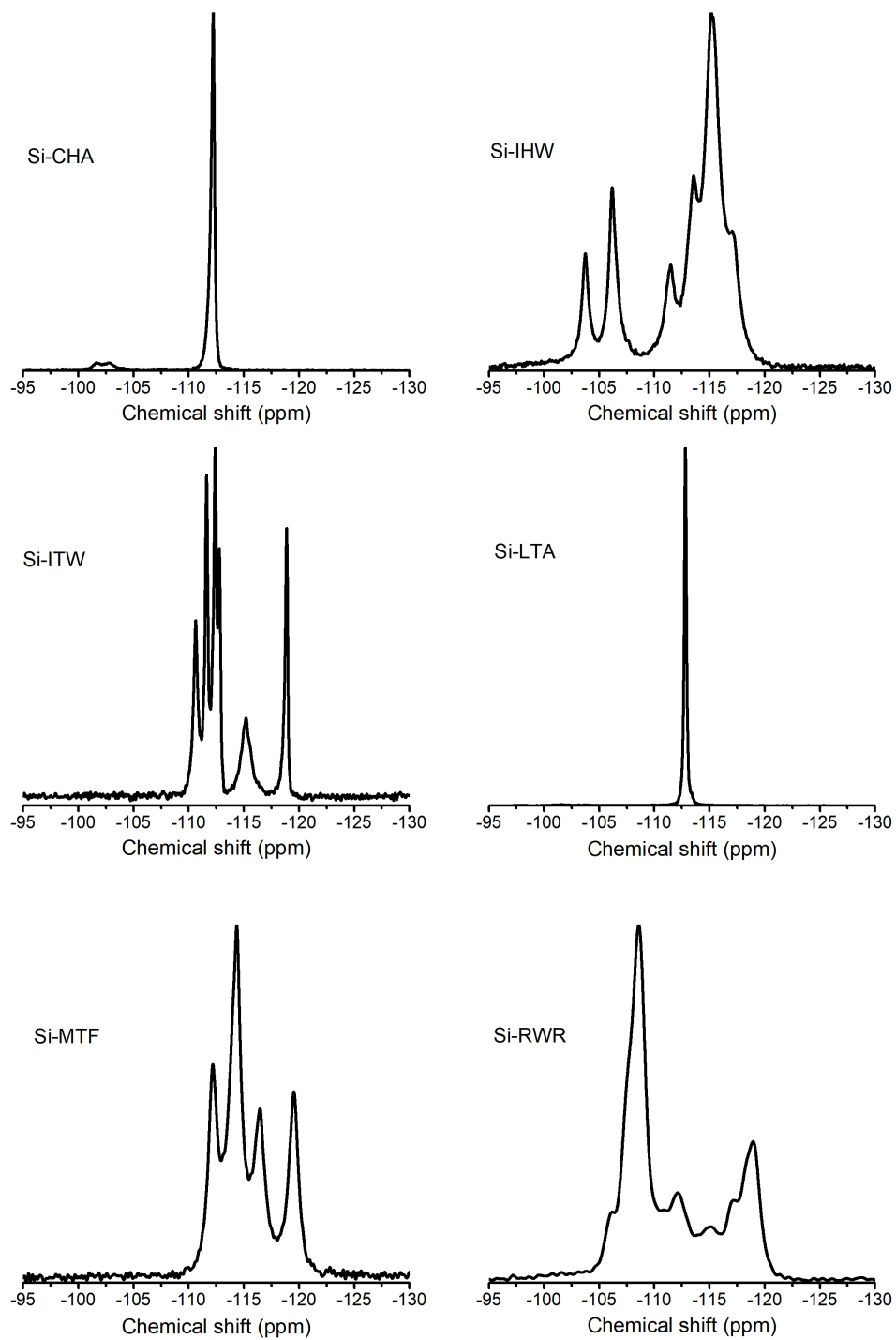**Figure A.1:** *XRD patterns of the samples used in this chapter.*

Figure A.2: ^{29}Si MAS NMR spectra of the pure silica zeolites used in this chapter.
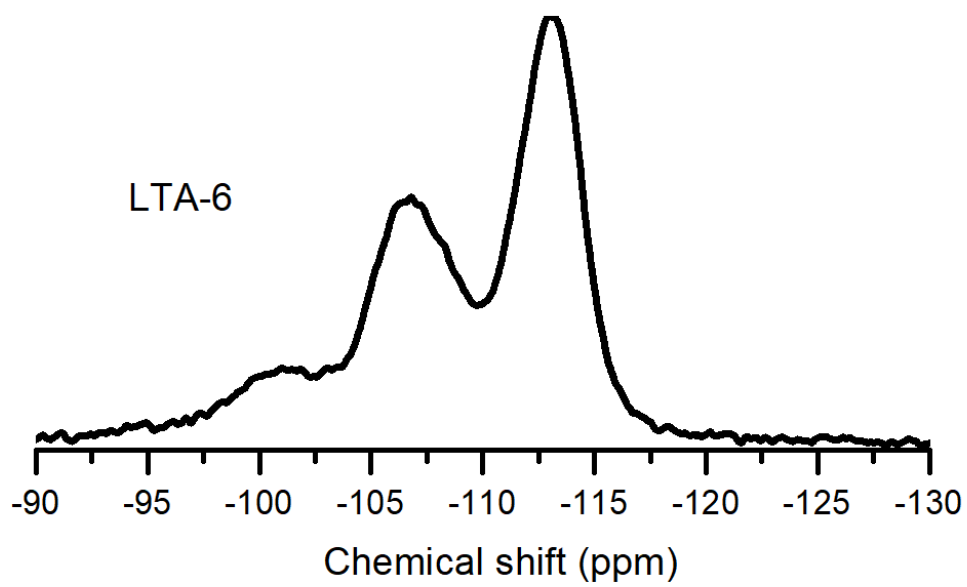
Figure A.3: ^{29} *Si MAS NMR spectrum of LTA-6.*

A.2 Estimation of isotherms at 25 °C on Si-ITW

The adsorption isotherms of CO_2 and CH_4 at 25 °C on Si-ITW shown in fig. 6.6 were estimated departing from the experimental isotherms at 10, 20, 30, 45 and 60 °C. These were fitted to the Langmuir model (see eq. (3.6); fit shown in fig. A.4A and B, fit parameters presented in table A.1).
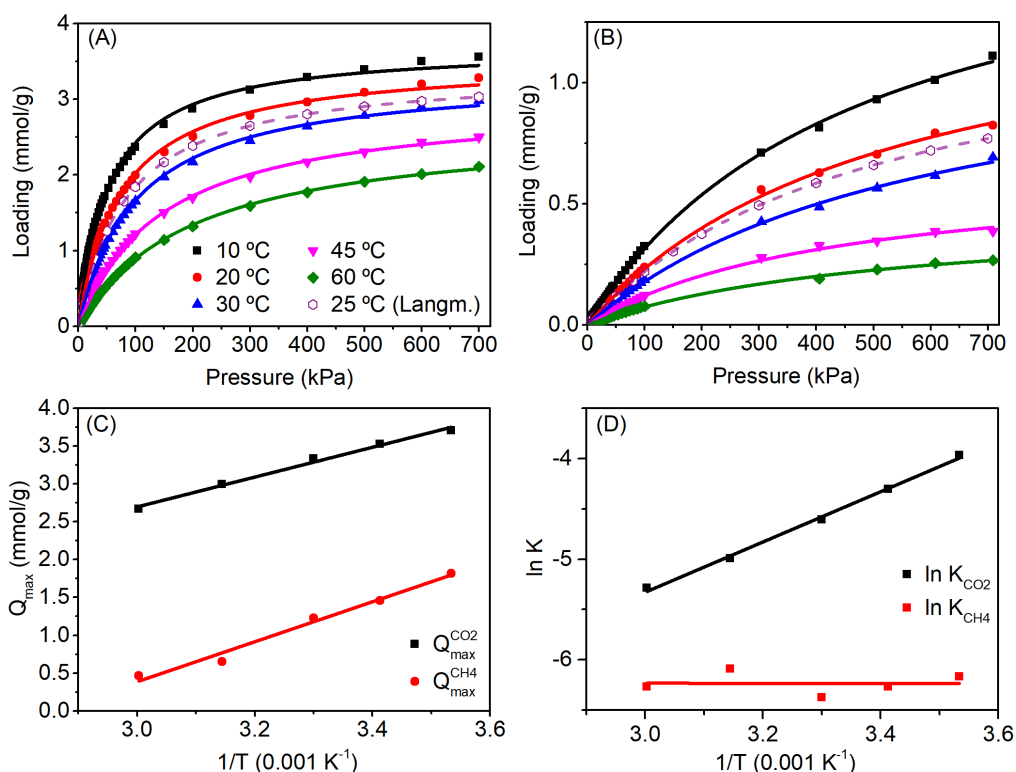
Figure A.4: *Experimental and estimated adsorption isotherms of (A) CO_2 and (B) CH_4 on Si-ITW and linear fits of the (C) Q_{max} and (D) $\ln K$ parameters of the Langmuir fits of the experimental isotherms. The lines in (A) and (B) are the Langmuir fits of the isotherms.*

The goodness of the fits (> 0.99) allowed me to obtain the corresponding Langmuir parameters for a hypothetical isotherm at 25 °C by plotting the Q_{max} and $\ln K$ values against $1/T$ (fig. A.4C and D). In the case of methane, the K parameter did not present a good linear correlation with $1/T$, but seemed to oscillate around a value of ca. 0.02 instead (see fig. A.4D) and thus, the average of K at the experimental temperatures was taken as the estimate for K at 25 °C.

Table A.1: *Langmuir fit parameters for CO_2 and CH_4 adsorption isotherms on Si-ITW at temperatures ranging from 10 to 60 ºC.*

T (K)	$1/T$ (K^{-1})	$Q_{max}^{CO_2}$ (mmol/g)	K_{CO_2} (kPa^{-1})	ln K_{CO_2}	$Q_{max}^{CH_4}$ (mmol/g)	K_{CH_4} (kPa^{-1})	ln K_{CH_4}
283	$3.53 \cdot 10^{-3}$	3.71	$1.89 \cdot 10^{-2}$	-3.97	1.82	$2.10 \cdot 10^{-3}$	-6.17
293	$3.41 \cdot 10^{-3}$	3.53	$1.35 \cdot 10^{-2}$	-4.31	1.46	$1.90 \cdot 10^{-3}$	-6.27
303	$3.30 \cdot 10^{-3}$	3.33	$1.00 \cdot 10^{-2}$	-4.61	1.23	$1.71 \cdot 10^{-3}$	-6.37
318	$3.14 \cdot 10^{-3}$	2.99	$6.79 \cdot 10^{-3}$	-4.99	0.65	$2.27 \cdot 10^{-3}$	-6.09
333	$3.00 \cdot 10^{-3}$	2.67	$5.05 \cdot 10^{-3}$	-5.29	0.46	$1.90 \cdot 10^{-3}$	-6.27

A.3   Breakthrough and regeneration profiles

This section includes all the breakthrough and regeneration profiles of CO_2/CH_4 mixtures used in chapter 6.

Figure A.5: *Breakthrough curves at 25 °C and 200 kPa of a 20:80 CO₂/CH₄ mixture on (A) Si-LTA, (B) LTA-6, (C) Si-ITW and (D) Si-RWR-a.*

Figure A.6: *Breakthrough curves at 25 °C and 700 kPa of a 20:80 CO₂/CH₄ mixture on (A) Si-LTA, (B) LTA-6, (C) Si-ITW and (D) Si-RWR-a.*
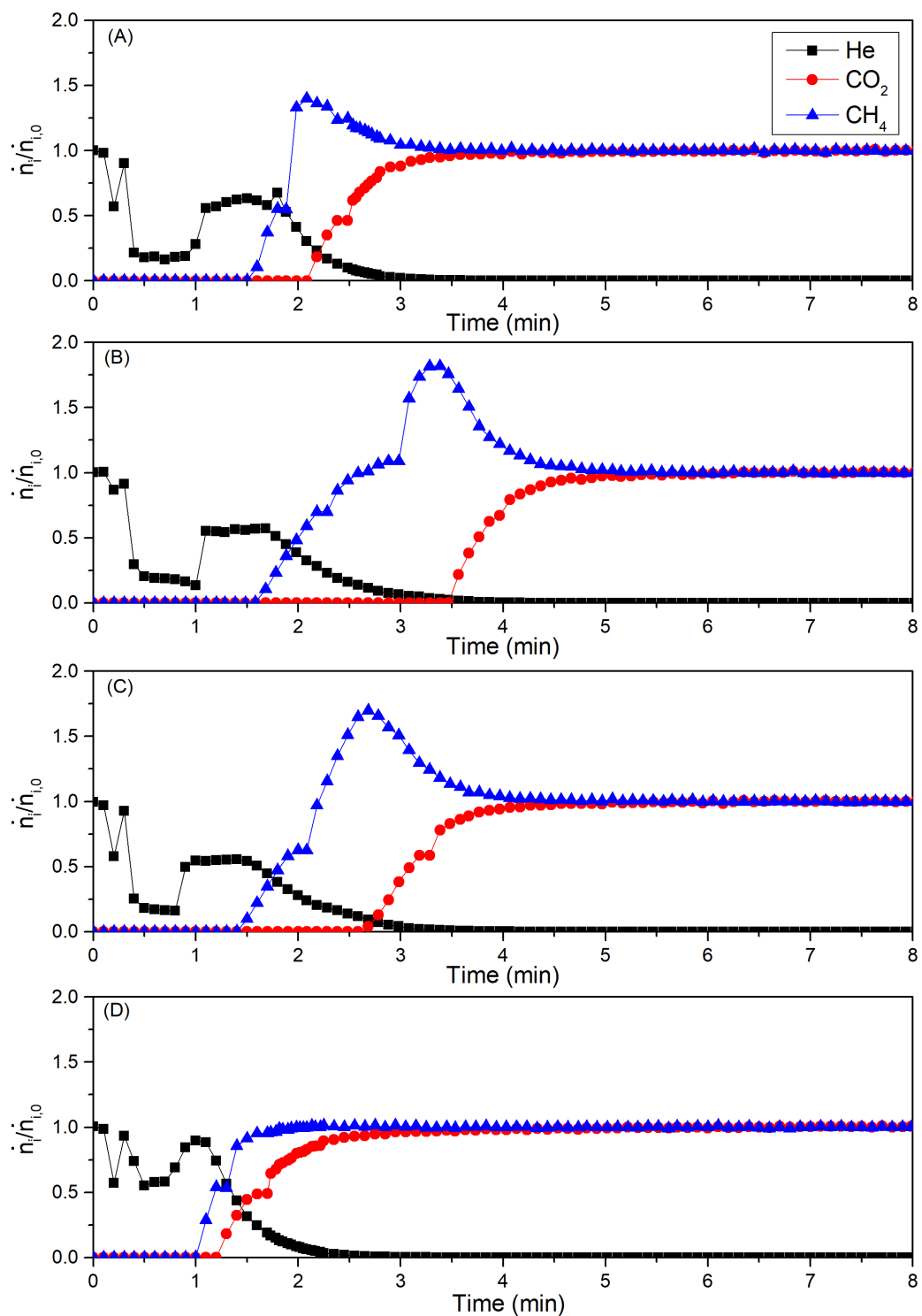
Figure A.7: *Breakthrough curves at 25 °C and 200 kPa of a 50:50 CO₂/CH₄ mixture on (A) Si-LTA, (B) LTA-6, (C) Si-ITW and (D) Si-RWR-a.*
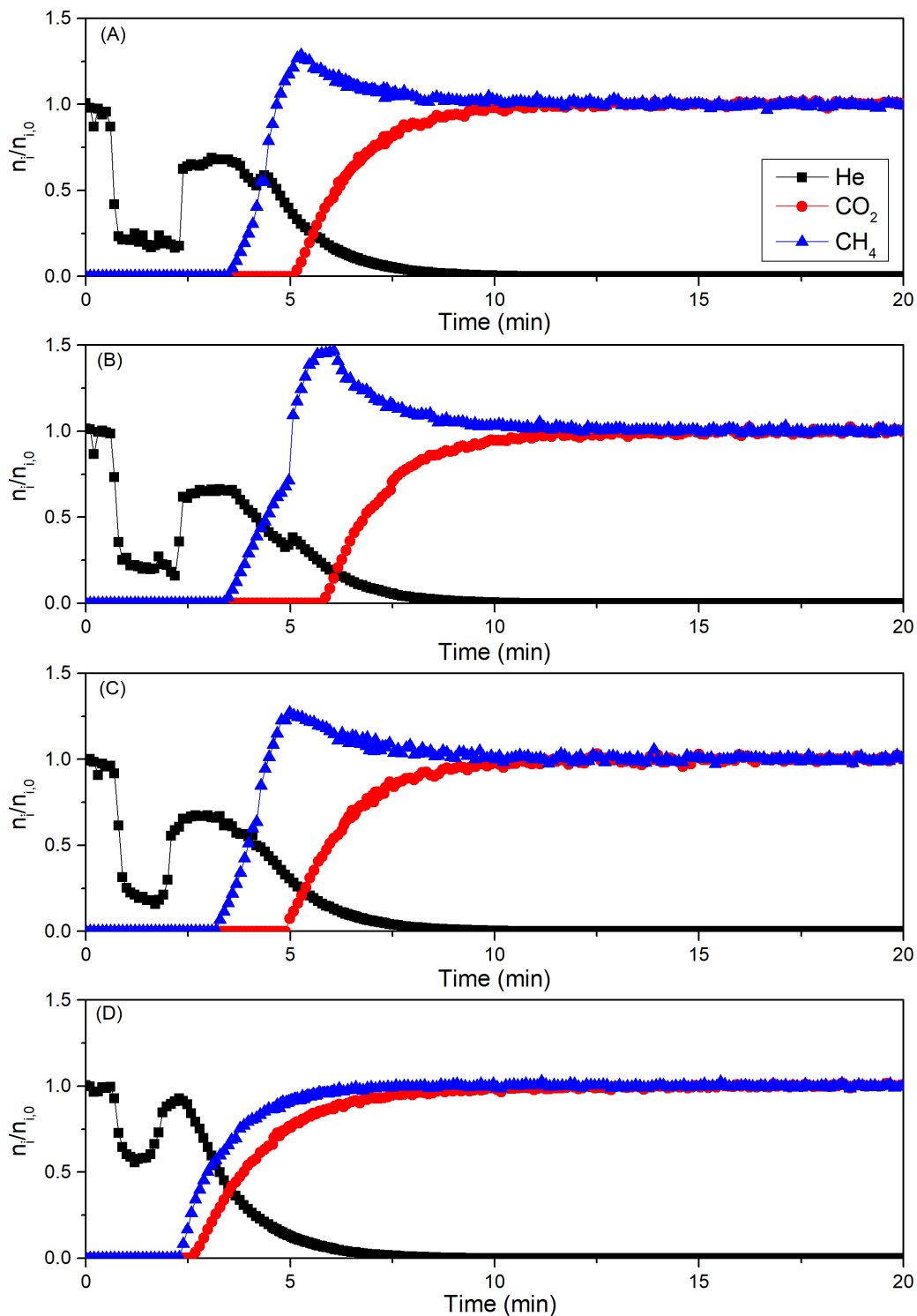
Figure A.8: *Breakthrough curves at 25 °C and 700 kPa of a 50:50 CO₂/CH₄ mixture on (A) Si-LTA, (B) LTA-6, (C) Si-ITW and (D) Si-RWR-a.*
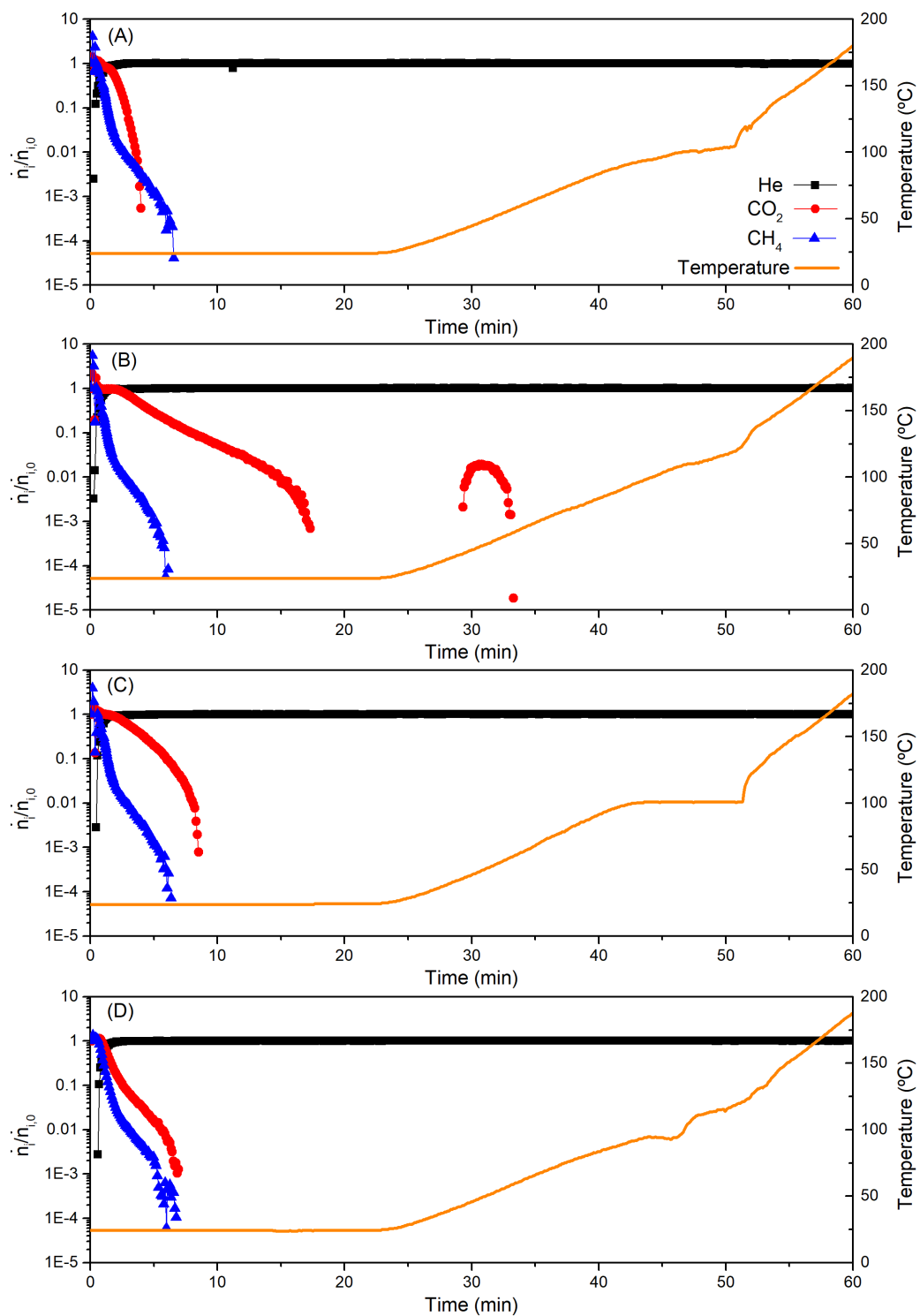
Figure A.9: *Regeneration experiment at 25 °C and 200 kPa of a 20:80 CO₂/CH₄ mixture on (A) Si-LTA, (B) LTA-6, (C) Si-ITW and (D) Si-RWR-a.*
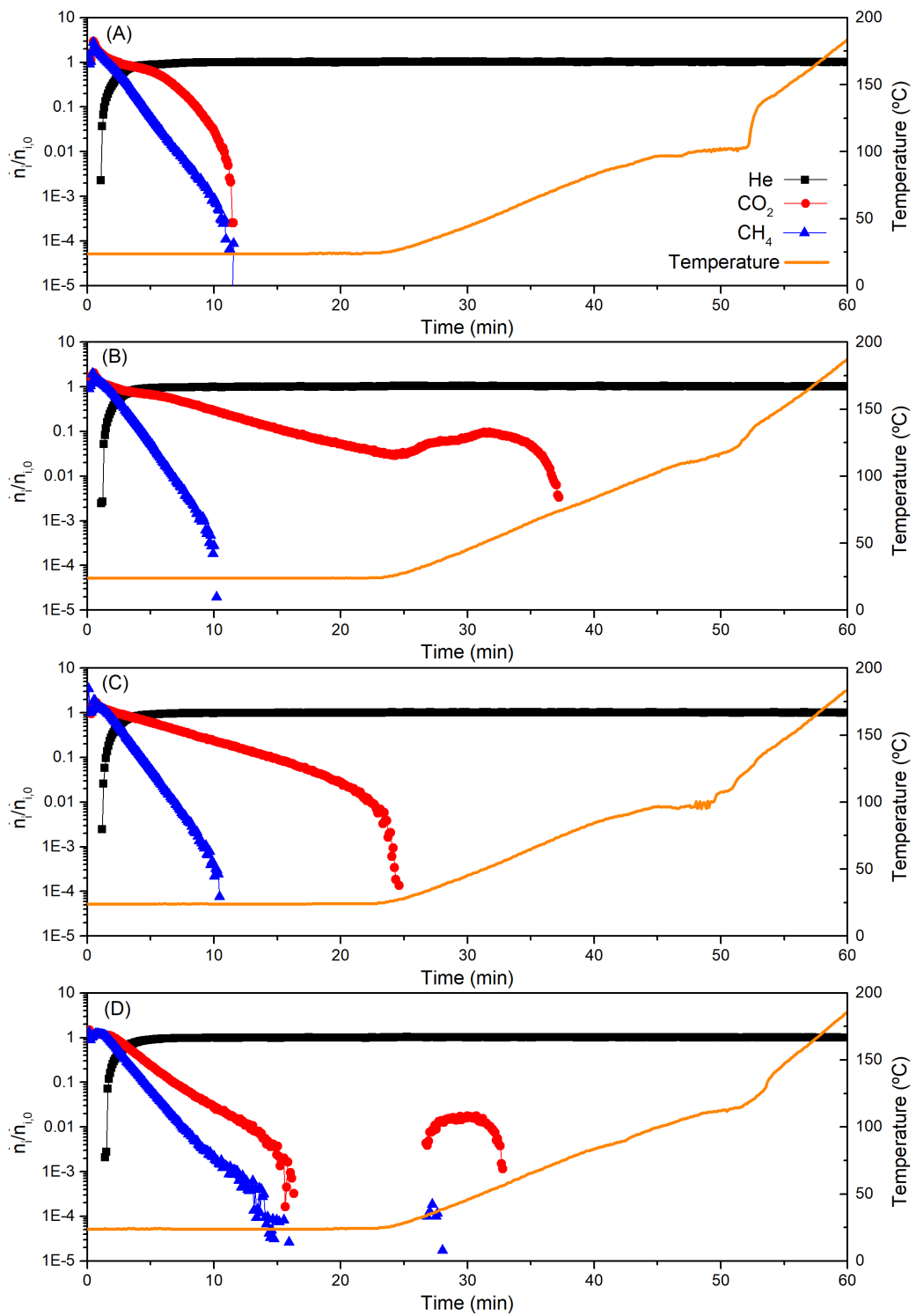
Figure A.10: *Regeneration curves at 25 °C and 700 kPa of a 20:80 CO$_2$/CH$_4$ mixture on (A) Si-LTA, (B) LTA-6, (C) Si-ITW and (D) Si-RWR-a.*
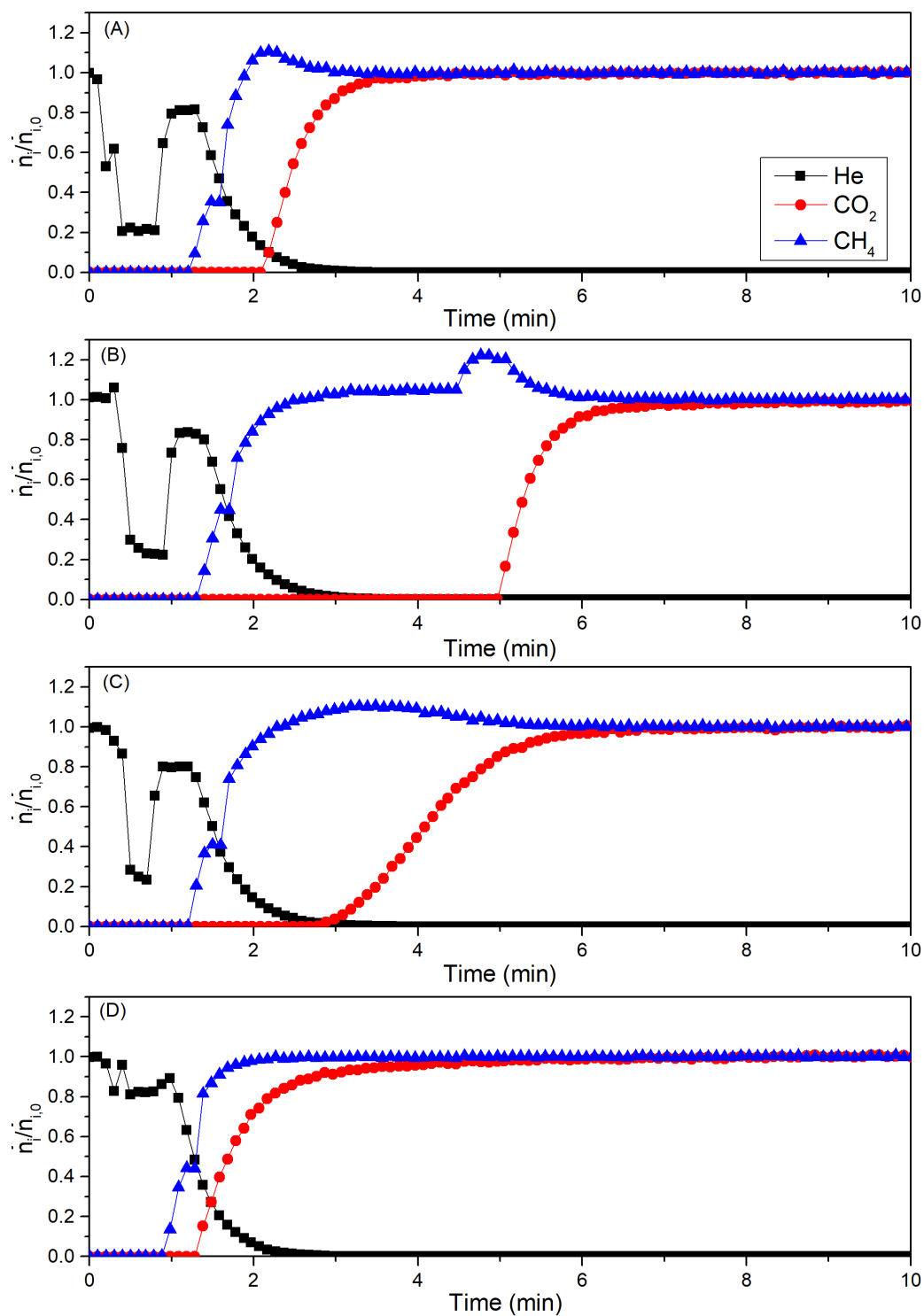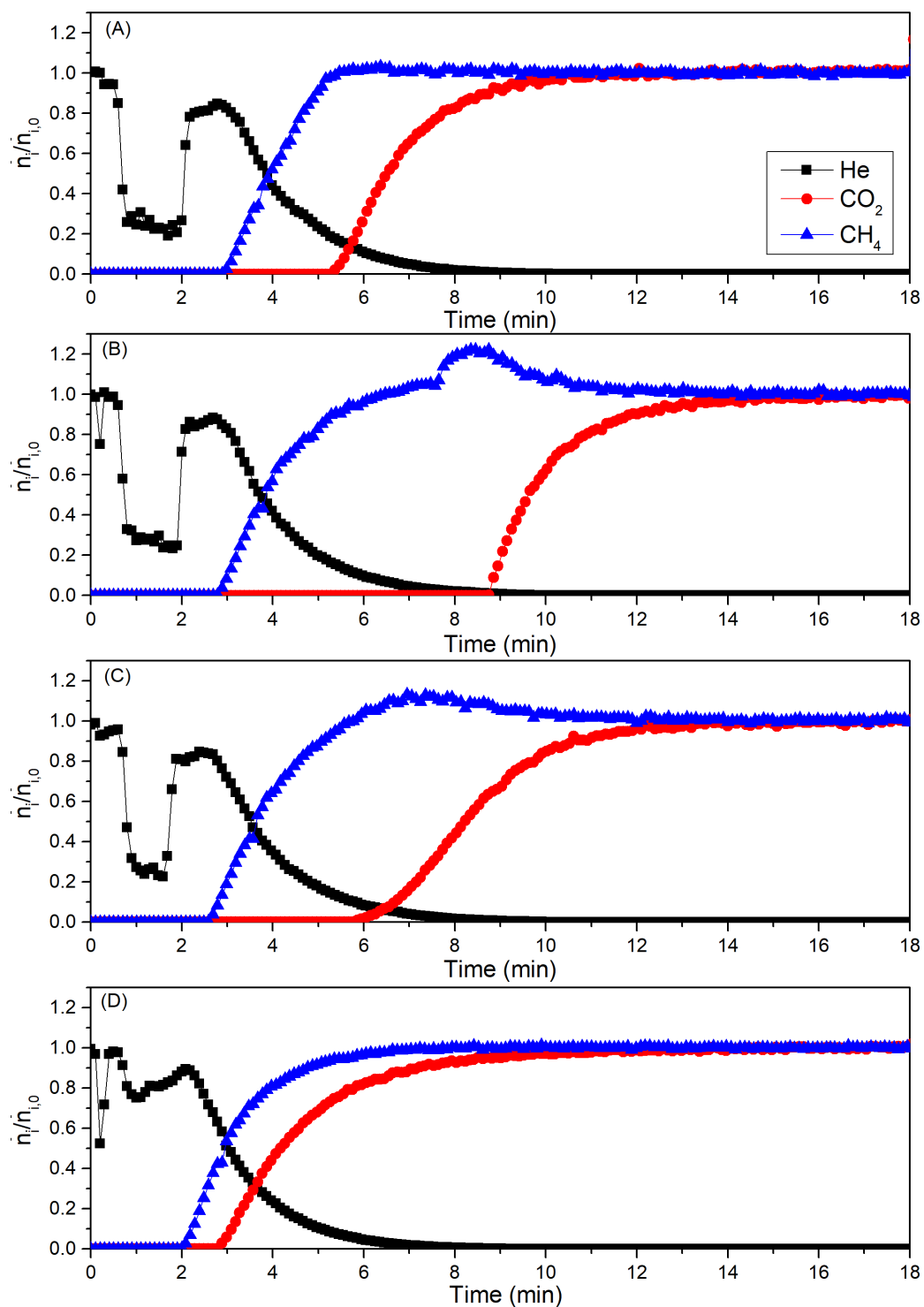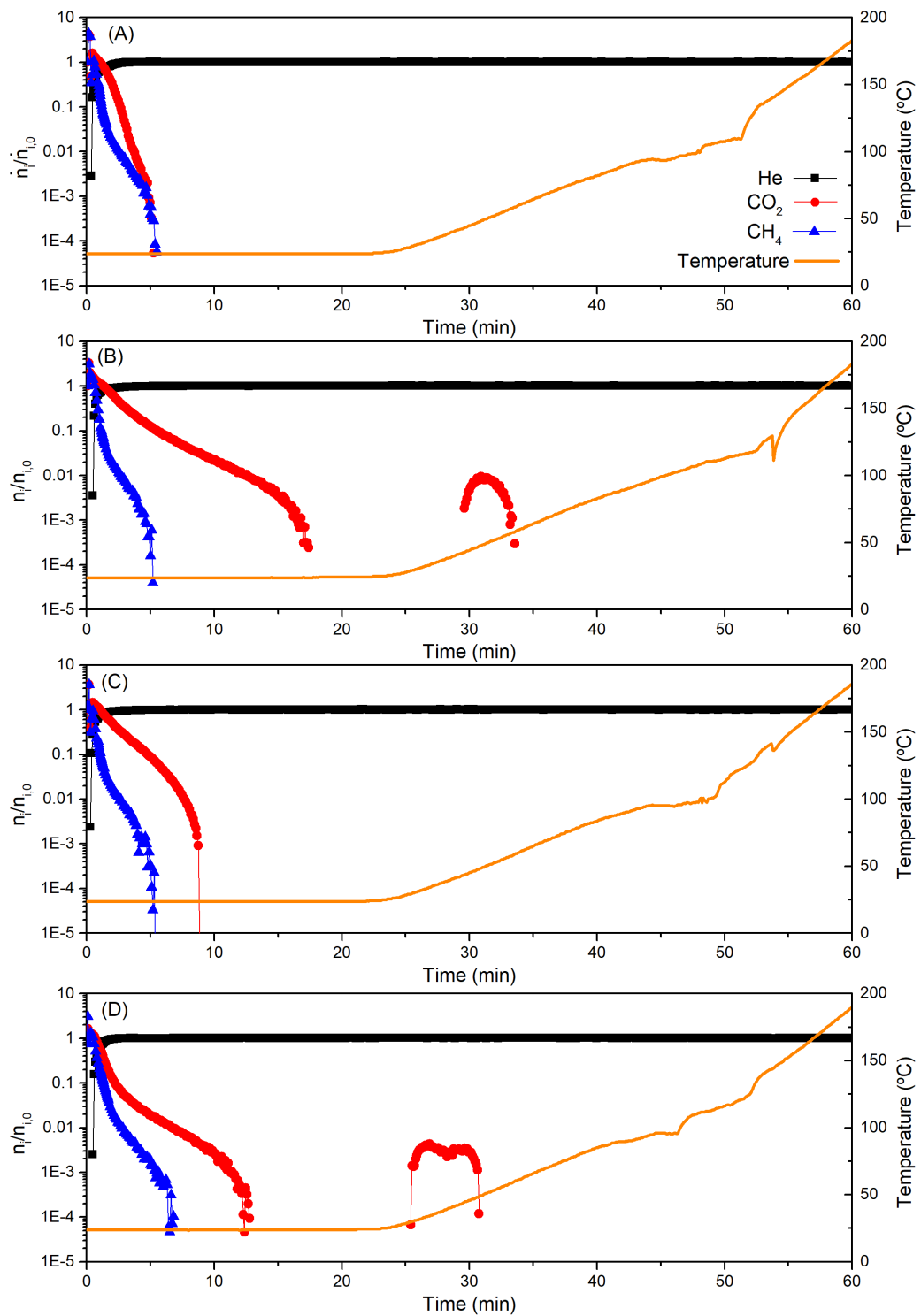
Figure A.11: *Regeneration curves at 25 °C and 200 kPa of a 50:50 CO₂/CH₄ mixture on (A) Si-LTA, (B) LTA-6, (C) Si-ITW and (D) Si-RWR-a.*
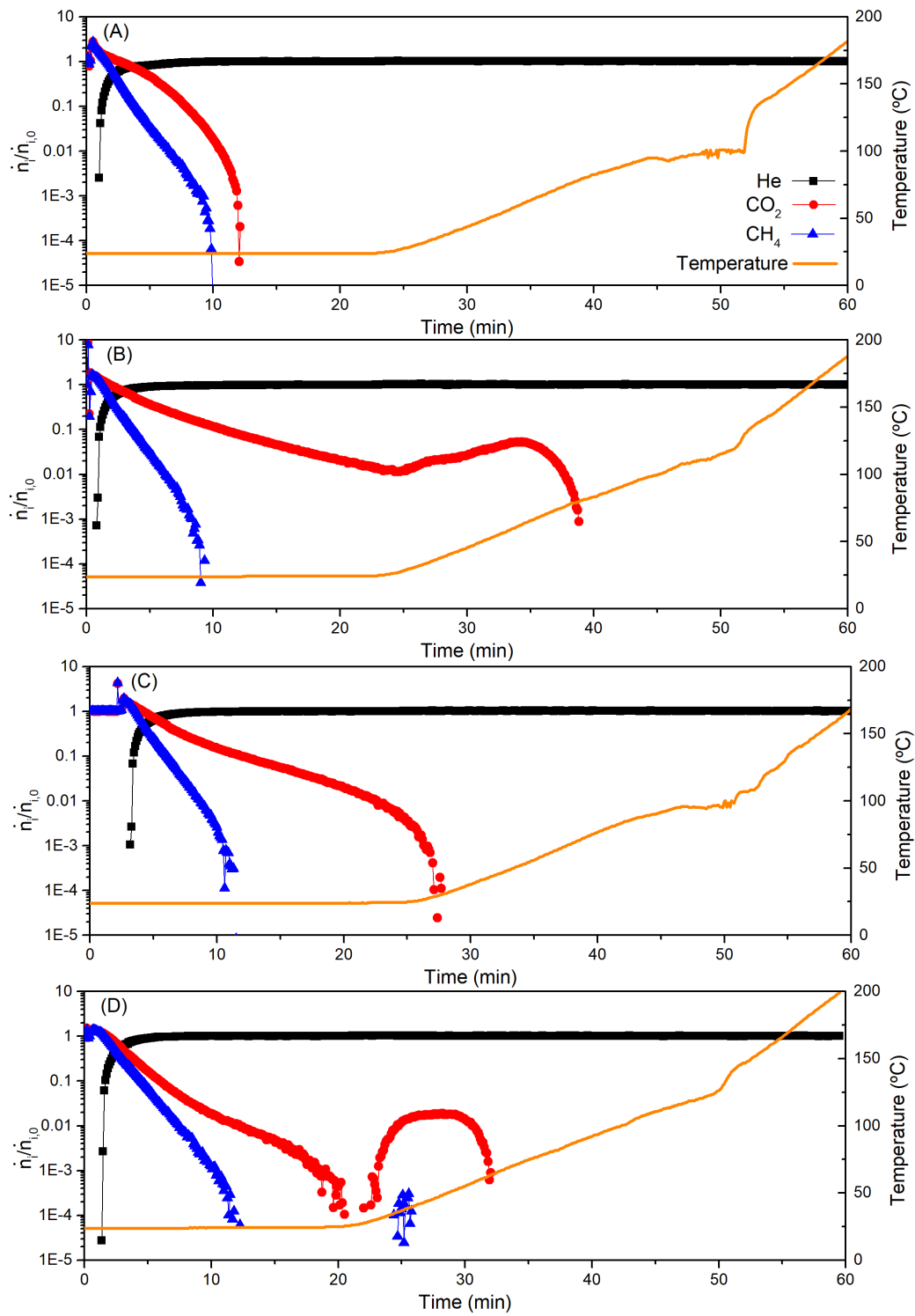
Figure A.12: *Regeneration curves at 25 °C and 700 kPa of a 50:50 CO₂/CH₄ mixture on (A) Si-LTA, (B) LTA-6, (C) Si-ITW and (D) Si-RWR-a.*

Appendix B

Appendix to chapter 7

B.1   XRD patterns and ^{29}Si MAS NMR spectra

The XRD patterns confirm the structural identity of the samples. The ^{29}Si MAS NMR spectra indicate that only Si-MFI-b presents a significant amount of connectivity defects (ca. 10 %).
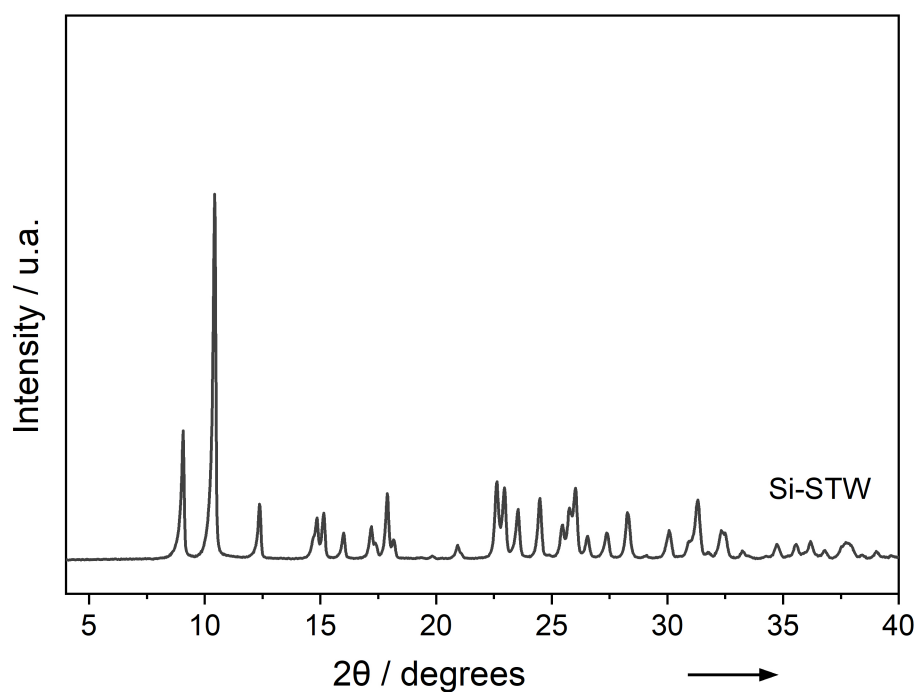
Figure B.1: *XRD pattern of Si-STW.*
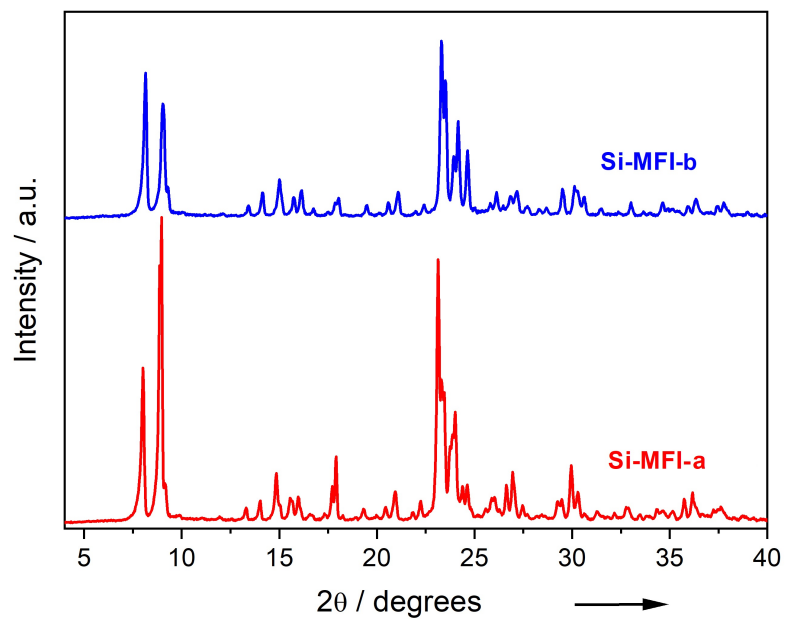
Figure B.2: *XRD pattern of Si-MFI-a and Si-MFI-b.*
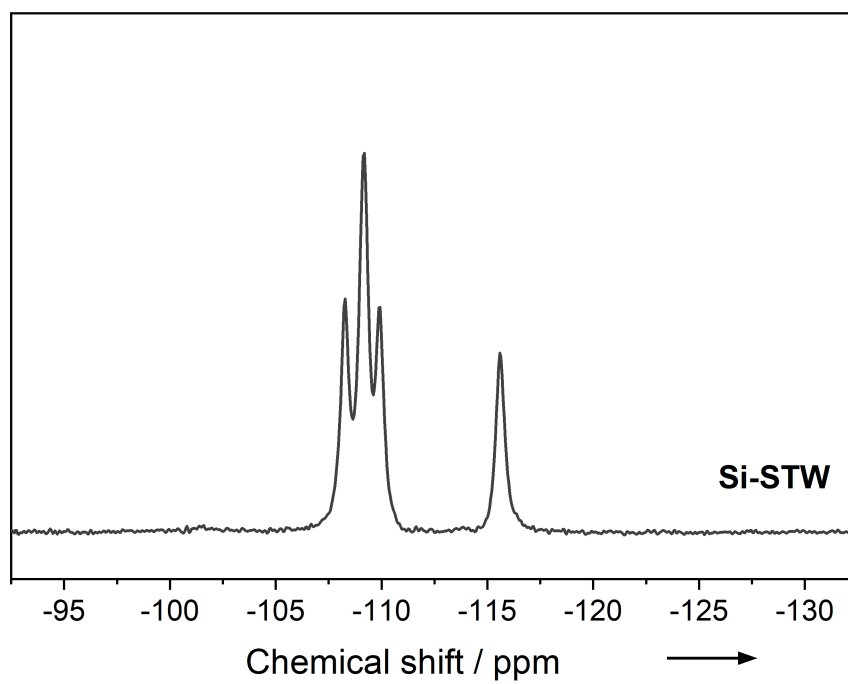
Figure B.3: *^{29}Si MAS NMR spectrum of Si-STW.*
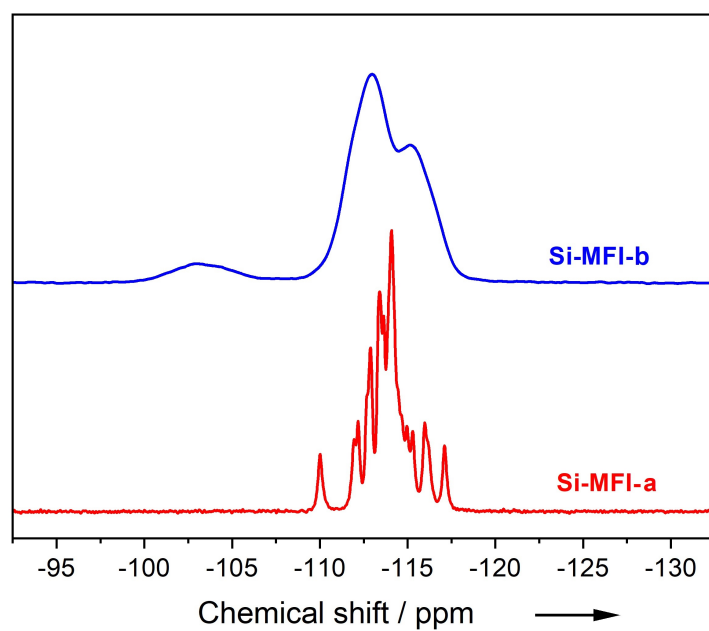
Figure B.4: ^{29}Si MAS NMR spectra of Si-MFI-a and Si-MFI-b.

Appendix C

Appendix to chapter 8

C.1   XRD patterns and ^{29}Si MAS NMR spectra

The XRD patterns and ^{29}Si MAS NMR spectra of the samples used in chapter 8 are presented in this appendix. The XRD patterns confirm the structural identity of the samples. The ^{29}Si MAS NMR spectra of the spectra allowed us to establish that the amount of Si defects (Q_3). Si-RTH-a and Si-RTH-b, possess 2 % and 1 % of Q_3 environments, respectively, and Si-STT possesses 5 %.
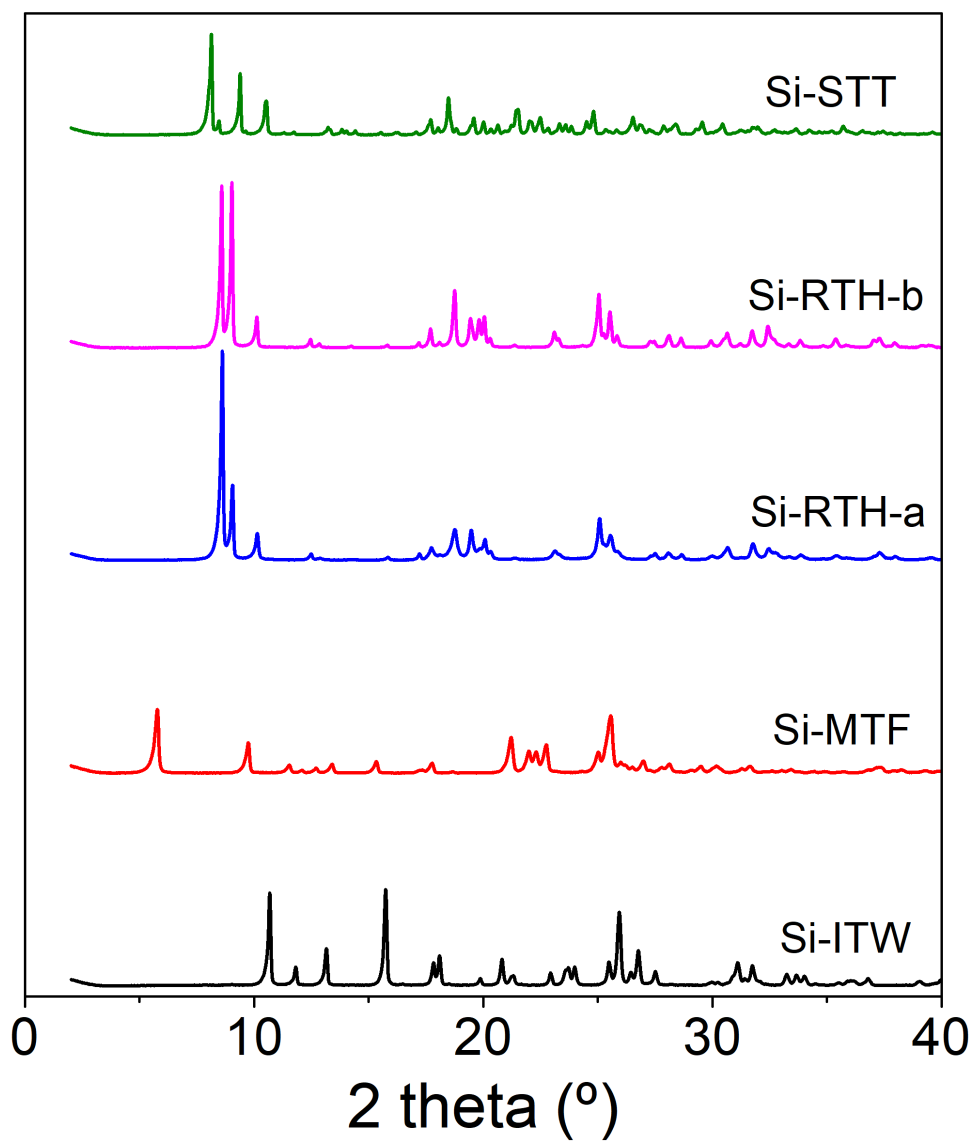
Figure C.1: *XRD patterns of the samples used in this chapter.*
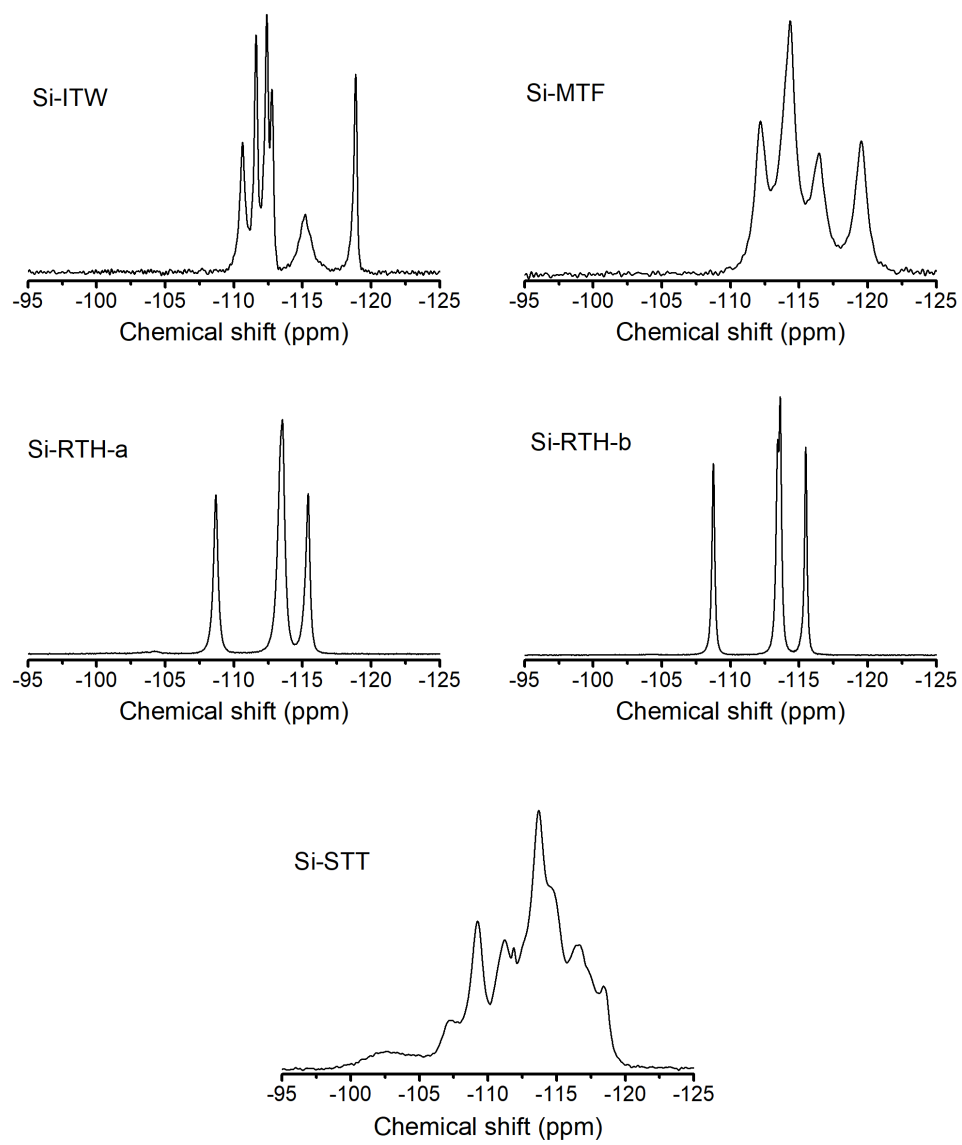
Figure C.2: ^{29}Si MAS NMR spectra of the samples used in this chapter.

Bibliography

(1) Flanigen, E. M.; Rabo, J. A. *Microporous and Mesoporous Materials* **2001**, *47*, 119–123.

(2) Flanigen, E. M. *Pure and Applied Chemistry* **1980**, *52*, 2191–2211.

(3) Milton, R. M. Molecular sieve adsorbents. US 2882243, 1959.

(4) Milton, R. M. Molecular sieve adsorbents. US 2882244, 1959.

(5) Cronstedt, A. F. *Kongl. Vetenskaps Acad. Handl.* **1756**, *17*, 120–123.

(6) Colella, C.; Gualtieri, A. F. *Microporous and Mesoporous Materials* **2007**, *105*, 213–221.

(7) Damour, M. A. *Annales des mines* **1840**, *3*, 202.

(8) Eichhorn, H. *Annalen der Physik und Chemie* **1858**, *181*, 126–133.

(9) Sainte-Claire-Deville, M. H. *Comptes rendus hebdomadaires des séances de l'Académie des sciences* **1862**, *54*, 324–327.

(10) Gans, R. *Jahrbuch der Königlich Preussischen Geologischen Landesanstalt* **1905**, *26*, 179–211.

(11) Gans, R. *Jahrbuch der Königlich Preussischen Geologischen Landesanstalt* **1906**, *27*, 63–94.

(12) Gans, R. Alumino-silicate or artificial zeolite. US 943535, 1909.

(13) Friedel, G. *Bulletin de la Société Française de Minéralogie* **1896**, *19*, 94–118.

(14) Grandjean, M. F. *Comptes rendus hebdomadaires des séances de l'Académie des sciences* **1909**, *149*, 866–868.

(15) Weigel, O.; Steinhoff, E. *Zeitschrift für Kristallographie - Crystalline Materials* **1924**, *61*, DOI: `10.1524/zkri.1924.61.1.125`.

(16) Pauling, L. *Zeitschrift für Kristallographie - Crystalline Materials* **1930**, *74*, 213–225.

(17) Pauling, L. *Proceedings of the National Academy of Sciences* **1930**, *16*, 453–459.

(18) Taylor, W. H. *Zeitschrift für Kristallographie - Crystalline Materials* **1930**, *74*, 1–19.

(19) McBain, J. W. In *The Sorption of Gases and Vapors by Solids*; G. Routledge & sons: London, 1932; Chapter 5.

(20) Rees, L. V. C. *Biographical Memoirs of Fellows of the Royal Society* **1998**, *44*, 37–49.

(21) Barrer, R. M. *Proceedings of the Royal Society A: Mathematical, Physical and Engineering Sciences* **1938**, *167*, 392–420.

(22) Barrer, R. M. *Transactions of the Faraday Society* **1941**, *37*, 590.

(23) Barrer, R. M.; White, E. A. D. *Journal of the Chemical Society* **1952**, 1561–1571.

(24) Barrer, R. M.; Riley, D. W. *Journal of the Chemical Society* **1948**, 133.

(25) Barrer, R. M. *Journal of the Chemical Society* **1948**, 127.

(26) Barrer, R. M.; Robinson, D. J. *Zeitschrift für Kristallographie* **1972**, *135*, 374–390.

(27) Barrer, R. M. *Nature* **1949**, *164*, 112–113.

(28) Barrer, R. M.; Denny, P. J. *Journal of the Chemical Society* **1961**, 971–982.

(29) Barrer, R. M.; Denny, P. J.; Flanigen, E. M. Molecular sieve adsorbents. US 3306922, 1967.

(30) Barrer, R. M.; Villiger, H. *Journal of the Chemical Society D: Chemical Communications* **1969**, 659.

(31) Wright, P. A.; Lozinska, M. In *ZEOLITES AND ORDERED POROUS SOLIDS: FUNDAMENTALS AND APPLICATIONS*, Martinez Sanchez, C., Perez Pariente, J., Eds.; Editorial Universitat Politecnica de Valencia: Valencia, 2011; Chapter 1.

(32) Moliner, M. In *Zeolites and ordered porous solids: Fundamentals and applications*, Martínez, C., Pérez-Pariente, J., Eds., 1st ed.; Universitat Politècnica de València: Valencia, 2011; Chapter 2, pp 37–66.

(33) Gómez-Hortigüela, L.; Camblor, M. In *Insights into the Chemistry of Organic Structure-Directing Agents in the Synthesis of Zeolitic Materials*, Gómez-Hortigüela, L., Ed., 1st ed.; Springer International Publishing AG: Cham, 2017; Chapter 1, pp 1–41.

(34) Zones, S. I. *Microporous and Mesoporous Materials* **2011**, *144*, 1–8.

(35) Milton, R. M. In *Zeolite Synthesis*, Occelli, M. L., Robson, H. E., Eds.; ACS Symposium Series, Vol. 398; American Chemical Society: Washington, DC, 1989; Chapter 1, pp 1–10.

(36) Breck, D. W.; Eversole, W. G.; Milton, R. M. *Journal of the American Chemical Society* **1956**, *78*, 2338–2339.

(37) Breck, D. W.; Eversole, W. G.; Milton, R. M.; Reed, T. B.; Thomas, T. L. *Journal of the American Chemical Society* **1956**, *78*, 5963–5972.

(38) Reed, T. B.; Breck, D. W. *Journal of the American Chemical Society* **1956**, *78*, 5972–5977.

(39) Loewenstein, W. *American Mineralogist* **1954**, *39*, 92–96.

(40) Breck, D. W., *Zeolite Molecular Sieves: Structure, Chemistry and Use*; John Wiley & Sons, Inc.: 1974.

(41) Piccione, P. M.; Laberty, C.; Yang, S.; Camblor, M. A.; Navrotsky, A.; Davis, M. E. *The Journal of Physical Chemistry B* **2002**, *104*, 10001–10011.

(42) Burton, A. *Catalysis Reviews - Science and Engineering* **2017**, *00*, 1–44.

(43) Pérez-Botella, E.; Palomino, M.; Valencia, S.; Rey, F. In *Nanoporous Materials for Gas Storage*, Kaneko, K., Rodríguez-Reinoso, F., Eds.; Green Energy and Technology; Springer Singapore: Singapore, 2019; Chapter 7, pp 173–208.

(44) Ch. Baerlocher; McCusker, L. Database of Zeolite Structures, http://www.iza-structure.org/databases/, (accessed Aug 23 2021).

(45) Jiang, J.; Yu, J.; Corma, A. *Angewandte Chemie - International Edition* **2010**, *49*, 3120–3145.

(46) Wright, P. A.; Connor, J. A. In *Microporous Framework Solids*; RSC Materials Monographs; Royal Society of Chemistry: Cambridge, 2008; Chapter 2, pp 8–78.

(47) Davis, M. E. *Nature* **2002**, *417*, 813–821.

(48) Flanigen, E. M.; Lok, B. M.; Patton, R. L.; Wilson, S. T. *Pure and Applied Chemistry* **1986**, *58*, 1351–1358.

(49) Hartmann, M.; Kevan, L. *Chemical Reviews* **1999**, *99*, 635–663.

(50) Man, P. P.; Briend, M.; Peltre, M. J.; Lamy, A.; Beaunier, P.; Barthomeuf, D. *Zeolites* **1991**, *11*, 563–572.

(51) Martínez-Franco, R.; Li, Z.; Martínez-Triguero, J.; Moliner, M.; Corma, A. *Catalysis Science and Technology* **2016**, *6*, 2796–2806.

(52) Martínez-Franco, R.; Cantín, Vidal-Moya, A.; Moliner, M.; Corma, A. *Chemistry of Materials* **2015**, *27*, 2981–2989.

(53) Martens, J. A.; Grobet, P. J.; Jacobs, P. A. *Journal of Catalysis* **1990**, *126*, 299–305.

(54) Davis, M. E. *Industrial and Engineering Chemistry Research* **1991**, *30*, 1675–1683.

(55) Notari, B. *Catalysis Today* **1993**, *18*, 163–172.

(56) Flanigen, E. M.; Broach, R. W.; Wilson, S. T. In *Zeolites in Industrial Separation and Catalysis*, Kulprathipanja, S., Ed.; Wiley-VCH Verlag GmbH & Co. KGaA: Weinheim, Germany, 2010; Chapter 1, pp 1–26.

(57) Townsend, R. P.; Coker, E. N. *Studies in Surface Science and Catalysis* **2001**, *137*, 467–524.

(58) Foster, M. D.; Treacy, M. M. A Database of Hypothetical Zeolite Structures, http://www.hypotheticalzeolites.net/, (accessed Aug 23 2020).

(59) McCusker, L. B.; Liebau, F.; Engelhardt, G. *Pure Appl. Chem.* **2001**, *73*, 381–394.

(60) Barrer, R. M., *Zeolites and clay minerals as sorbents and molecular sieves*; London: Academic Press: 1978.

(61) Barrer, R. M. *Discussions of the Faraday Society* **1949**, *5*, 326.

(62) Colella, C. In *Studies in Surface Science and Catalysis*, Čejka, J., Van Bekkum, H., Eds.; Elsevier B.V.: 2005; Vol. 157, pp 13–40.

(63) IZA International Zeolite Association Synthesis Commission, http://www.iza-online.org/synthesis/default.htm, (accessed Aug 23 2021).

(64) *Insights into the Chemistry of Organic Structure-Directing Agents in the Synthesis of Zeolitic Materials*, 1st ed.; Gómez-Hortigüela, L., Ed.; Structure and Bonding, Vol. 175; Springer International Publishing: Cham, 2018.

(65) Lok, B. M.; Cannan, T. R.; Messina, C. A. *Zeolites* **1983**, *3*, 282–291.

(66)   Rey, F.; Simancas, J. In *Insights into the Chemistry of Organic Structure-Directing Agents in the Synthesis of Zeolitic Materials*, Gómez-Hortigüela, L., Ed., 1st ed.; Springer International Publishing: Cham, 2017; Chapter 4, pp 103–138.

(67)   Corma, A.; Davis, M. E. *ChemPhysChem* **2004**, *5*, 304–313.

(68)   Cundy, C. S.; Cox, P. A. *Microporous and Mesoporous Materials* **2005**, *82*, 1–78.

(69)   Moliner, M.; Rey, F.; Corma, A. *Angewandte Chemie - International Edition* **2013**, *52*, 13880–13889.

(70)   Gallego, E. M.; Portilla, M. T.; Paris, C.; León-Escamilla, A.; Boronat, M.; Moliner, M.; Corma, A. *Science* **2017**, *355*, 1051–1054.

(71)   Sastre, G.; Leiva, S.; Sabater, M. J.; Gimenez, I.; Rey, F.; Valencia, S.; Corma, A. *Journal of Physical Chemistry B* **2003**, *107*, 5432–5440.

(72)   Burton, A. W.; Zones, S. I. *Studies in Surface Science and Catalysis* **2007**, *168*, 137–179.

(73)   Koller, H.; Wölker, A.; Villaescusa, L. A.; Díaz-Cabañas, M. J.; Valencia, S.; Camblor, M. A. *Journal of the American Chemical Society* **1999**, *121*, 3368–3376.

(74)   Camblor, M. A.; Barrett, P. A.; Díaz-Cabaas, M. J.; Villaescusa, L. A.; Puche, M.; Boix, T.; Pérez, E.; Koller, H. *Microporous and Mesoporous Materials* **2001**, *48*, 11–22.

(75)   Camblor, M. A.; Villaescusa, L. A.; Díaz-Cabañas, M. J. *Topics in Catalysis* **1999**, *9*, 59–76.

(76)   Zones, S. I.; Hwang, S. J.; Elomari, S.; Ogino, I.; Davis, M. E.; Burton, A. W. *Comptes Rendus Chimie* **2005**, *8*, 267–282.

(77)   Zones, S. I.; Darton, R. J.; Morris, R.; Hwang, S. J. *Journal of Physical Chemistry B* **2005**, *109*, 652–661.

(78) Kühl, G. H. In *Catalysis and Zeolites*; Springer Berlin Heidelberg: Berlin, Heidelberg, 1999, pp 81–197.

(79) Guth, J.-L.; Kessler, H. In *Catalysis and Zeolites*; Springer Berlin Heidelberg: Berlin, Heidelberg, 1999; Chapter 1, pp 1–52.

(80) Szostak, R. *Studies in Surface Science and Catalysis* **2001**, *137*, 261–297.

(81) Goepper, M.; Guth, F.; Delmotte, L.; Guth, J. L.; Kessler, H. *Studies in Surface Science and Catalysis* **1989**, *49*, 857–866.

(82) Peeters, M. P.; Van De Ven, L. J.; De Haan, J. W.; Van Hooff, J. H. *Journal of Physical Chemistry* **1993**, *97*, 8254–8260.

(83) Vomscheid, R.; Briend, M.; Peltre, M. J.; Massiani, P.; Man, P. P.; Barthomeuf, D. *Journal of the Chemical Society, Chemical Communications* **1993**, 544–546.

(84) Buzimov, A. Y.; Kulkov, S. N.; Eckl, W; Pappert, S; Gömze, L. A.; Kurovics, E; Kocserha, I.; Géber, R. *Journal of Physics: Conference Series* **2017**, *790*, 012004.

(85) Nikashina, V. A.; Streletskii, A. N.; Kolbanev, I. V.; Meshkova, I. N.; Grinev, V. G.; Serova, I. B.; Yusupov, T. S.; Shumskaya, L. G. *Inorganic Materials* **2011**, *47*, 1341–1346.

(86) Ruthven, D. M. *Chemie-Ingenieur-Technik* **2011**, *83*, 44–52.

(87) Martínez, C.; Corma, A. *Coordination Chemistry Reviews* **2011**, *255*, 1558–1580.

(88) Barrer, R. M.; Sammon, D. C. *Journal of the Chemical Society (Resumed)* **1955**, 2838.

(89) Barrer, R. *Proc. Chem. Soc.* **1958**, 99–112.

(90) Breck, D. W. *Journal of Chemical Education* **1964**, *41*, 678–689.

(91) Dyer, A. In *Introduction to Zeolite Science and Practice*, Čejka, J., Van Bekkum, H., Corma, A., Schüth, F., Eds., 3rd; Elsevier B.V.: Amsterdam, 2007; Chapter 16, pp 525–553.

(92) Harjula, R.; Dyer, A.; Pearson, S. D.; Townsend, R. P. *J. Chem. Soc., Faraday Trans.* **1992**, *88*, 1591–1597.

(93) Drummond, D.; De Jonge, A.; Rees, L. V. C. *The Journal of Physical Chemistry* **1983**, *87*, 1967–1971.

(94) Delkash, M.; Ebrazi Bakhshayesh, B.; Kazemian, H. *Microporous and Mesoporous Materials* **2015**, *214*, 224–241.

(95) Zaidi, S. In *Ion Exchange Technology II*, Inamuddin, Luqman, M., Eds.; Springer Netherlands: Dordrecht, 2012, pp 183–215.

(96) Kallo, D. *Reviews in Mineralogy and Geochemistry* **2001**, *45*, 519–550.

(97) Schwuger, M.; Liphard, M. In *Zeolites as Catalysts, Sorbents and Detergent Builders*, Karge, H. G., Weitkamp, J., Eds.; 46; Elsevier Science B.V.: Amsterdam, 1989, pp 673–690.

(98) Allen, S.; Carr, S.; Chapple, A.; Dyer, A.; Heywood, B. *Physical Chemistry Chemical Physics* **2002**, *4*, 2409–2415.

(99) Adams, C. J.; Araya, A.; Carr, S. W.; Chapple, A. P.; Graham, P.; Minihan, A. R.; Osinga, T. J. In *Zeolite Science 1994: Recent Progress and Discussions*, Karge, H., Weitkamp, J., Eds.; Elsevier Science B.V.: Amsterdam, 1995; Vol. 98, pp 206–207.

(100) Ames, L. L. *The American Mineralogist* **1962**, *47*, 1317–1326.

(101) Dyer, A. In *Environmental Mineralogy Microbial Interactions, Anthropogenic Influences, Contaminated Land and Waste Management*, Cotter-Howells, J. D., Campbell; L. S., Valsami-Jones; E., Batchelder, M., Eds., 9th; Mineralogical Society of Great Britain and Ireland: London, 2000; Chapter 17, pp 319 –353.

(102) Marrocchelli, A.; Pietrelli, L. *Solvent Extraction and Ion Exchange* **1989**, *7*, 159–172.

(103) Inglezakis, V. J. *Journal of Colloid and Interface Science* **2005**, *281*, 68–79.

(104) Gómez-Hortigüela, L.; Pérez-Pariente, J.; García, R.; Chebude, Y.; Díaz, I. *Separation and Purification Technology* **2013**, *120*, 224–229.

(105) Breck, D. W.; Milton, R. M. Cadmium-loaded molecular sieve. US 3013983, 1961.

(106) Breck, D. W.; Milton, R. M. Metal loading of molecular sieves. US 3013982, 1961.

(107) Breck, D. W.; Milton, R. M. Group IB metal catalyst.s, US 3013985, 1961.

(108) Milton, R. M. Hydrocarbon upgrading process. US 3236903, 1966.

(109) Milton, R. M. Zeolitic molecular sieves containing a platinum group metal in the inner adsorption region. US 3200083, 1965.

(110) Rabo, J. A.; Pickert, P. E.; Boyle, J. E. Hydrocarbon conversion catalysts. US 3367885, 1968.

(111) Rabo, J. A.; Pickert, P. E.; Boyle, J. E. Hydrocarbon conversion process with the use of a Y type crystalline zeolite. US 3236762, 1966.

(112) Rabo, J. A.; Pickert, P. E.; Boyle, J. E. Decationized molecular sieve compositions. US 3130006, 1964.

(113) Weisz, P. B.; Frilette, V. J. *The Journal of Physical Chemistry* **1960**, *64*, 382–382.

(114) Plank, C. J.; Rosinski, E. J.; Hawthorne, W. P. *Industrial & Engineering Chemistry Product Research and Development* **1964**, *3*, 165–169.

(115) Vermeiren, W.; Gilson, J. P. *Topics in Catalysis* **2009**, *52*, 1131–1161.

(116) Perego, C; Carati, A In *Zeolites: From Model Materials to Industrial Catalysts*, Cejka, J., Perez-Pariente, J., Roth, W., Eds.; 2; Transworld Research Network: Kerala, India, 2008; Vol. 661; Chapter 14, pp 357–389.

(117) Corma, A. In *Zeolite Microporous Solids: Synthesis, Structure, and Reactivity*, Derouane, E. G., Lemos, F., Naccache, C., Ribeiro, F. R., Eds.; 1; Springer Netherlands: Dordrecht, 1992; Vol. 100; Chapter 18, pp 373–436.

(118) Jones, D. S. J. S.; Pujado, P. R., *Handbook of Petroleum Processing*; Springer: 2006, p 1417.

(119) Degnan, T. F. *Topics in Catalysis* **2000**, *13*, 349–356.

(120) Meyers, R. A., *Handbook of Petroleum Refining Processes*; McGraw-Hill: New York, 2004, p 894.

(121) Vogt, E. T.; Weckhuysen, B. M. *Chemical Society Reviews* **2015**, *44*, 7342–7370.

(122) Speight, J. G. In *The Refinery of the Future*, Speight, J. G., Ed., 2nd; Elsevier: Cambridge, MA, US; Oxford, UK, 2020; Chapter 9, pp 303–342.

(123) Lawrence, P. A.; Aitken, R. W.; Harris, R. J. K. Improvements relating to the production of lubricating oils. GB 1134015, 1968.

(124) Chen, N. Y.; Lucki, S. J.; Garwood, W. E. Dewaxing of oils by shape selective cracking and hydrocracking over zeolites ZSM-5 and ZSM-8. US 3700585, 1972.

(125) Miller, S. J. *Microporous Materials* **1994**, *2*, 439–449.

(126) Miller, S. J. *Studies in Surface Science and Catalysis* **1994**, *84*, 2319–2326.

(127) Chen, N. Y. *ACS Symposium Series* **1999**, *738*, 39–63.

(128) LaPierre, R. B.; Partridge, R. D.; Chen, N. Y.; Wong, S. S. Catalytic dewaxing process. US 4419220, 1983.

(129) Chen, N. Y.; Garwood, W. E.; Quang, N. L.; Wong, S. S. Lubricant production process. US 4919788, 1990.

(130) Chen, N. Y.; Garwood, W. E. Selective catalytic conversion with a crystalline aluminosilicate. US 3379640, 1968.

(131) Bonacci, J. C.; Patterson, J. R. Noble metal reforming of naphta. US 4292167, 1981.

(132) Corma, A. *Catalysis Letters* **1993**, *22*, 33–52.

(133) Rossini, S. *Catalysis Today* **2003**, *77*, 467–484.

(134) Kuhlmann, E. J.; Pascoe, J. R.; Thom, C. J. Skeletal isomerization of n-pentenes to isopetene on pretreated zeolites. US 5463160, 1995.

(135) Pellet, R. J.; O'Young, C.-L.; Hadowanetz, J.; Browne, J. E. Treated bound ferrierite zeolites for skeletal isomerization of n-olefins to iso-olefins. US 5523510, 1996.

(136) O'Young, C.-L.; Pellet, R. J.; Hadowanetz, A. E.; Hazen, J.; Browne, J. E. Skeletal isomerization of n-olefins to iso-olefins on binded ferrierite zeolites. US 5510560, 1996.

(137) Diáz Velázquez, H.; Likhanova, N.; Aljammal, N.; Verpoort, F.; Martínez-Palou, R. *Energy and Fuels* **2020**, DOI: 10.1021/acs.energyfuels.0c02962.

(138) Van Broekhoven, E. H.; Mas Cabre, F. R.; Bogaard, P.; Klaver, G.; Vonhof, M. Process for alkylating hydrocarbons. US 5986158, 1999.

(139) Marcilly, C. *Journal of Catalysis* **2003**, *216*, 47–62.

(140) Maxwell, I.; Stork, W. In, 1991, pp 571–630.

(141) Garwood, W. E.; Lee, W. Process for the treatment of olefinic gasoline. US 4211640, 1980.

(142) Miller, S. J. Oligomerization of liquid olefins. GB 2106131 B, 1981.

(143) Tabak, S. A.; Krambeck, F. J.; Garwood, W. E. *AIChE Journal* **1986**, *32*, 1526–1531.

(144) Chen, J. Q.; Bozzano, A.; Glover, B.; Fuglerud, T.; Kvisle, S. *Catalysis Today* **2005**, *106*, 103–107.

(145) Air   Liquide
       Lurgi MTP™ - Methanol-to-Propylene, https://www.engineering-
       airliquide.com/lurgi-mtp-methanol-propylene, (accessed Aug 23
       2021).

(146) Bjørgen, M.; Svelle, S.; Joensen, F.; Nerlov, J.; Kolboe, S.; Bonino,
       F.; Palumbo, L.; Bordiga, S.; Olsbye, U. *Journal of Catalysis* **2007**,
       249, 195–207.

(147) Zhou, L. In *Handbook of Petroleum Refining Processes*, Meyers,
       R. A., Ed.; McGraw-Hill: New York, 2004; Chapter 2.4, pp 29–2.

(148) Doolan, P. C.; Pujado, P. R. *Hydrocarbon Processing; (USA)* **1989**,
       68.

(149) Chevron   Philips
       Chemical Aromatics Technology, https://www.cpchem.com/what-
       we-do/licensing/aromatics-technology, (accessed Aug. 24 2021).

(150) Kaeding, W. W.; Barile, G. C.; Wu, M. M. *Catalysis Reviews* **1984**,
       26, 597–612.

(151) Olson, D. H.; Haag, W. O. In *ACS Symposium Series*, Whyte,
       T. E., Betta, R. A. D., Derouane, E. G., Baker, R. T. K., Eds.;
       American Chemical Society: Washington, DC, 1984; Chapter 14,
       pp 275–307.

(152) Zeolyst   International
       Transalkylation Catalyst. 20102013, https://www.zeolyst.com/our-
       products/specialty-catalysts/aromatics-hydrocarbons-
       processing.html (accessed Aug. 24 2021).

(153) Zeolyst International ATA-21 : A new standard for transalkylation
       catalysis. 2013, https://www.zeolyst.com/our-products/specialty-
       catalysts/aromatics-hydrocarbons-processing.html   (accessed
       Aug. 24 2021).

(154) Beck, J. S.; Dandekar, A. B.; Degnan, T. In *Zeolites for Cleaner
       Technologies*, Guisnet, M., Gilson, J. P., Eds.; Imperial College
       Press: London, 2002; Chapter 11, pp 223–238.

(155) Bellussi, G.; Perego, C. *Cattech* **2000**, *4*, 4–16.

(156) Barrer, R. M. Fractionation of mixtures of hydrocarbons. US 2306610, 1942.

(157) Barrett, P. a.; Stephenson, N. A. In *ZEOLITES AND ORDERED POROUS SOLIDS: FUNDAMENTALS AND APPLICATIONS*, Martínez Sánchez, C., Pérez Pariente, J., Eds.; Editorial Universitat Politecnica de Valencia: Valencia, 2011; Chapter 6, pp 149–180.

(158) Thommes, M.; Kaneko, K.; Neimark, A. V.; Olivier, J. P.; Rodriguez-Reinoso, F.; Rouquerol, J.; Sing, K. S. W. *Pure and Applied Chemistry* **2015**, *87*, 1051–1069.

(159) Wright, P. A. In *Microporous Framework Solids*; Royal Society of Chemistry: Cambridge, 2008; Chapter 7, pp 257–311.

(160) Sircar, S.; Myers, A. In *Handbook of Zeolite Science and Technology*, 2003.

(161) Breck, D. W.; Smith., J. V. *Scientific American* **1959**, *200*, 85–96.

(162) Kärger, J.; Ruthven, D. M.; Theodorou, D. N., *Diffusion in Nanoporous Materials*; Wiley-VCH Verlag & Co. KGaA: 2012.

(163) Yang, R. T., *Adsorbents: fundamentals and applications*; Yang, R., Ed.; Wiley-Interscience: 2003.

(164) Lively, R. P.; Realff, M. J. *AIChE Journal* **2016**, *62*, 3699–3705.

(165) Sircar, S; Myers, A. L. *Adsorption Science & Technology* **1985**, *2*, 69–87.

(166) Skarstrom, C. W. Method and apparatus for fractionating gaseous mixtures by adsorption. US 2944627, 1960.

(167) Guerin de Montgareuil, P.; Domine, D. Process for separating a binary gaseous mixture by adsorption. US 3155468, 1964.

(168) Yang, R. T., *Gas Separation by Adsorption Processes*, 1987, pp 347–352.

(169) Grande, C. A. *ISRN Chemical Engineering* **2012**, *2012*, 1–13.

(170) Ribeiro, R. P.; Grande, C. A.; Rodrigues, A. E. *Separation Science and Technology (Philadelphia)* **2014**, *49*, 1985–2002.

(171) Sircar, S. In *Particle Technology and Applications*, Lee, S., Henthorn, K. H., Eds.; CRC Press Taylor & Francis Group: Boca Raton, 2012; Chapter 7, pp 87–110.

(172) Seader, J. D.; Henley, E. J.; Roper, D. K., *Separation Process Principles: chemical and biochemical separations*, Third Edit; John Wiley & Sons, Inc.: 2011.

(173) Sholl, D. S.; Lively, R. P. *Nature* **2016**, *532*, 435–437.

(174) Kulprathipanja, S.; Johnson, J. A. In *Handbook of Porous Solids*; Wiley-VCH Verlag GmbH: Weinheim, Germany, 2002; Vol. 4, pp 2568–2622.

(175) IUPAC, *IUPAC Compendium of Chemical Terminology*; International Union of Pure and Applied Chemistry: Research Triangle Park, NC, 2014.

(176) Galizia, M.; Chi, W. S.; Smith, Z. P.; Merkel, T. C.; Baker, R. W.; Freeman, B. D. *Macromolecules* **2017**, *50*, 7809–7843.

(177) Li, J. R.; Kuppler, R. J.; Zhou, H. C. *Chemical Society Reviews* **2009**, *38*, 1477–1504.

(178) Sircar, S. *Industrial & Engineering Chemistry Research* **2006**, *45*, 5435–5448.

(179) Smyth, C. P., *Dielectric Behavior and Structure: Dielectric Constant and Loss, Dipole Moment and Molecular Structure*; McGraw-Hill: 1955.

(180) U.S. Secretary of Commerce Chemistry Webbook of NIST, http://webbook.nist.gov/chemistry/, (accessed Aug 23 2021).

(181) Song, Z.; Huang, Y.; Xu, W. L.; Wang, L.; Bao, Y.; Li, S.; Yu, M. *Scientific Reports* **2015**, *5*, 1–7.

(182) Sommer, S.; Melin, T.; Falconer, J. L.; Noble, R. D. *Journal of Membrane Science* **2003**, *224*, 51–67.

(183) Jiménez-Cruz, F.; Laredo, G. C. *Fuel* **2004**, *83*, 2183–2188.

(184) Sircar, S.; Golden, T. C. In *Hydrogen and Syngas Production and Purification Technologies*; John Wiley & Sons, Inc.: Hoboken, NJ, USA, 2009, pp 414–450.

(185) Sircar, S.; Golden, T. C. *Separation Science and Technology* **2000**, *35*, 667–687.

(186) Fuderer, A. Selective adsorption process for production of ammonia synthesis gas mixtures. US 4375363, 1983.

(187) Sircar, S. Recovery of nitrogen, hydrogen and carbon dioxide from hydrocarbon reformate. US 4813980, 1989.

(188) Sircar, S.; Golden, T. C. In *Hydrogen and Syngas Production and Purification Technologies*, Liu, K., Song, C., Subramani, V., Eds.; John Wiley & Sons, Inc.: Hoboken, 2010; Chapter 10, pp 414–450.

(189) Ogden, J. M. *Annual Review of Energy and the Environment* **1999**, *24*, 227–279.

(190) Ackley, M. W.; Barrett, P. A. Silver-exchanged zeolites and methods of manufacture therefor. US 7455718 B2, 2008.

(191) Edlund, D. In *Hydrogen and Syngas Production and Purification Technologies*, Liu, K., Song, C., Subramani, V., Eds.; John Wiley & Sons, Inc.: Hoboken, 2010; Chapter 8, pp 357–384.

(192) Bryk, V.; Guglya, A.; Kalchenko, A.; Marchenko, I.; Marchenko, Y.; Melnikova, E. S.; Vlasov, V.; Zubarev, E. *OALib* **2015**, *02*, 1–11.

(193) Goncharov, A.; Guglya, A.; Melnikova, E. *International Journal of Hydrogen Energy* **2012**, *37*, 18061–18073.

(194) Fuderer, A.; Rudelstorfer, E. Selective adsorption process.S, US 3986849, 1976.

(195) Russell, B. P.; Patel, K. M.; Rastelli, H. Pressure swing adsorption process and apparatus for purifying a hydrogen-containing gas stream. US 2018/0036671 A1, 2018.

(196) Yamaguchi, T.; Kobayashi, Y. Gas separation process. US 5250088, 1993.

(197) Sircar, S.; Kratz, W. C. *Separation Science and Technology* **1988**, *23*, 2397–2415.

(198) Reddy, S. Hydrogen and carbon dioxide coproduction. US 6500241 B2, 2002.

(199) Perez-Carbajo, J.; Parra, J. B.; Ania, C. O.; Merkling, P. J.; Calero, S. *ACS Applied Materials & Interfaces* **2019**, *11*, 18833–18840.

(200) Liu, M. et al. *Science* **2019**, *366*, 613–620.

(201) Cai, J.; Xing, Y.; Zhao, X. *RSC Advances* **2012**, *2*, 8579–8586.

(202) Kirk, A **2015**.

(203) Demange, D.; Antunes, R.; Borisevich, O.; Frances, L.; Rapisarda, D.; Santucci, A.; Utili, M. *Fusion Engineering and Design* **2016**, *109-111*, 912–916.

(204) Kessel, C. et al. *Fusion Engineering and Design* **2018**, *135*, 236–270.

(205) Pautrot, P.; Damiani, M. In *Separation of Hydrogen Isotopes*, Rae, H. K., Ed.; American Chemical Society: Washington D.C., 1978; Chapter 12, pp 163–170.

(206) Kowalczyk, P.; Gauden, P. A.; Terzyk, A. P. *Journal of Physical Chemistry B* **2008**, *112*, 8275–8284.

(207) Rae, H. K. In *Separation of Hydrogen Isotopes*, Rae, H. K., Ed.; American Chemical Society: Washington, D.C., 1978; Chapter 1, pp 1–26.

(208) KEYSER, G. M.; McCONNELL, D. B.; ANYAS-WEISS, N.; KIRKBY, P. In *Separation of Hydrogen Isotopes*, Rae, H. K., Ed.; American Chemical Society: Washington D.C., 1978; Chapter 9, pp 126–133.

(209) Vasaru, G., *Tritium Isotope Separation*; CRC Press Taylor & Francis Group: Boca Raton, 1993.

(210) Smith, R.; Whittaker, D. A.; Butler, B.; Hollingsworth, A.; Lawless, R. E.; Lefebvre, X.; Medley, S. A.; Parracho, A. I.; Wakeling, B. *Journal of Alloys and Compounds* **2015**, *645*, S51–S55.

(211) Hammerli, M.; Stevens, W. H.; Butler, J. P. In *Separation of Hydrogen Isotopes*, Rae, H. K., Ed.; American Chemical Society: Washington, D.C., 1978; Chapter 8, pp 110–125.

(212) Alekseev, I. A.; Bondarenko, S. D.; Fedorchenko, O. A.; Vasyanina, T. V.; Konoplev, K. A.; Arkhipov, E. A.; Voronina, T. V.; Grushko, A. I.; Tchijov, A. S.; Uborsky, V. V. *Fusion Engineering and Design* **2003**, *69*, 33–37.

(213) Sugiyama, T.; Asakura, Y.; Uda, T.; Shiozaki, T.; Enokida, Y.; Yamamoto, I. *Fusion Engineering and Design* **2006**, *81 A*, 833–838.

(214) Beenakker, J.; Borman, V.; Krylov, S. *Chemical Physics Letters* **1995**, *232*, 379–382.

(215) Gould, A. J.; Bleakney, W.; Taylor, H. S. *The Journal of Chemical Physics* **1934**, *2*, 362–373.

(216) Van Dingenen, W.; van Itterbeek, A. *Physica* **1939**, *6*, 49–58.

(217) Harteck, P.; Melkonian, G. A. *Die Naturwissenschaften* **1950**, *37*, 450–450.

(218) White, D.; Haubach, W. J. *The Journal of Chemical Physics* **1959**, *30*, 1368–1369.

(219) Basmadjian, D. *Canadian Journal of Chemistry* **1960**, *38*.

(220) Jones, P. M. S.; Hutcheson, C. G. *Nature* **1967**, *213*, 490–491.

(221) Edse, R.; Harteck, P. *Angewandte Chemie* **1940**, *53*, 210–213.

(222) Oh, H.; Savchenko, I.; Mavrandonakis, A.; Heine, T.; Hirscher, M. *ACS Nano* **2014**, *8*, 761–770.

(223) Savchenko, I.; Mavrandonakis, A.; Heine, T.; Oh, H.; Teufel, J.; Hirscher, M. *Microporous and Mesoporous Materials* **2014**, *216*, 133–137.

(224) Niimura, S.; Fujimori, T.; Minami, D.; Hattori, Y.; Abrams, L.; Corbin, D.; Hata, K.; Kaneko, K. *Journal of the American Chemical Society* **2012**, *134*, 18483–18486.

(225) Chu, X. Z.; Cheng, Z. P.; Xiang, X. X.; Xu, J. M.; Zhao, Y. J.; Zhang, W. G.; Lv, J. S.; Zhou, Y. P.; Zhou, L.; Moon, D. K.; Lee, C. H. *International Journal of Hydrogen Energy* **2014**, *39*, 4437–4446.

(226) Salazar, J.; Lectez, S.; Gauvin, C.; Macaud, M.; Bellat, J.; Weber, G.; Bezverkhyy, I.; Simon, J. *International Journal of Hydrogen Energy* **2017**, *42*, 13099–13110.

(227) Giraudet, M.; Bezverkhyy, I.; Weber, G.; Dirand, C.; Macaud, M.; Bellat, J. P. *Microporous and Mesoporous Materials* **2018**, *270*, 211–219.

(228) Xiong, R.; Balderas Xicohténcatl, R.; Zhang, L.; Li, P.; Yao, Y.; Sang, G.; Chen, C.; Tang, T.; Luo, D.; Hirscher, M. *Microporous and Mesoporous Materials* **2018**, *264*, 22–27.

(229) Physick, A. J. W.; Wales, D. J.; Owens, S. H. R.; Shang, J.; Webley, P. A.; Mays, T. J.; Ting, V. P. *Chemical Engineering Journal* **2016**, *288*, 161–168.

(230) Wang, Q.; Challa, S.; Sholl, D.; Johnson, J. *Physical Review Letters* **1999**, *82*, 956–959.

(231) Kowalczyk, P.; Gauden, P. a.; Terzyk, A. P.; Furmaniak, S. *Journal of physics. Condensed matter : an Institute of Physics journal* **2009**, *21*, 144210.

(232)   Gotzias, a.; Charalambopoulou, G.; Ampoumogli, a.; Krkljus, I.; Hirscher, M.; Steriotis, T. *Adsorption* **2013**, *19*, 373–379.

(233)   Garberoglio, G.; DeKlavon, M. M.; Johnson, J. K. *Journal of Physical Chemistry B* **2006**, *110*, 1733–1741.

(234)   Kagita, H.; Ohba, T.; Fujimori, T.; Tanaka, H.; Hata, K.; Taira, S. I.; Kanoh, H.; Minami, D.; Hattori, Y.; Itoh, T.; Masu, H.; Endo, M.; Kaneko, K. *Journal of Physical Chemistry C* **2012**, *116*, 20918–20922.

(235)   Lozada-Hidalgo, M.; Hu, S.; Marshall, O.; Mishchenko, A.; Grigorenko, A. N.; Dryfe, R. A.; Radha, B.; Grigorieva, I. V.; Geim, A. K. *Science* **2016**, *351*, 68–70.

(236)   Oh, H.; Park, K. S.; Kalidindi, S. B.; Fischer, R. a.; Hirscher, M. *Journal of Materials Chemistry A* **2013**, *1*, 3244.

(237)   Teufel, J.; Oh, H.; Hirscher, M.; Wahiduzzaman, M.; Zhechkov, L.; Kuc, A.; Heine, T.; Denysenko, D.; Volkmer, D. *Advanced Materials* **2013**, *25*, 635–639.

(238)   Noguchi, D.; Tanaka, H.; Kondo, A.; Kajiro, H.; Noguchi, H.; Ohba, T.; Kanoh, H.; Kaneko, K. *Journal of the American Chemical Society* **2008**, *130*, 6367–6372.

(239)   Chen, B.; Zhao, X.; Putkham, A.; Hong, K.; Lobkovsky, E. B.; Hurtado, E. J.; Fletcher, A. J.; Thomas, K. M. *Journal of the American Chemical Society* **2008**, *130*, 6411–6423.

(240)   Kumar, a. V. A.; Jobic, H.; Bhatia, S. K. *Adsorption* **2007**, *13*, 501–508.

(241)   Kumar, A. V. A.; Bhatia, S. K. *The Journal of Physical Chemistry C* **2008**, *112*, 11421–11426.

(242)   Tagliabue, M.; Farrusseng, D.; Valencia, S.; Aguado, S.; Ravon, U.; Rizzo, C.; Corma, A.; Mirodatos, C. *Chemical Engineering Journal* **2009**, *155*, 553–566.

(243)   Boot-Handford, M. E. et al. *Energy Environ. Sci.* **2014**, *7*, 130–189.

(244) Global CCS Institute *Global Status Report of CCS*; tech. rep.; Global CCS Institute, 2019.

(245) Sapag, K.; Vallone, A.; Garcia, A.; Solar, C. In *Natural Gas*, Potocnik, P., Ed.; Sciyo: paris, 2010; Chapter 10, pp 205–245.

(246) Saha, D.; Grappe, H. A.; Chakraborty, A.; Orkoulas, G. *Chemical Reviews* **2016**, DOI: `10.1021/acs.chemrev.5b00745`.

(247) Kidnay, A. J.; Parrish, W. R., *Fundamentals of natural gas processing*; Taylor & Francis Group: 2006, p 418.

(248) Bakar, W. A. W. A.; Ali, R. In *Natural Gas*, Potocnik, P., Ed.; Sciyo: Paris, 2010; Chapter 1.

(249) Flores, R. M. *International Journal of Coal Geology* **1998**, *35*, 3–26.

(250) Kim, A. G. *The Composition of Coalbed Gas (Report of Investigations 7762)*; tech. rep.; U.S. Bureau of Mines, 1973.

(251) Ripepi, N.; Louk, K.; Amante, J.; Schlosser, C.; Tang, X.; Gilliland, E. *Energies* **2017**, *10*, 1533.

(252) Li, Q.; Ju, Y.; Bao, Y.; Yan, Z.; Li, X.; Sun, Y. *Energy and Fuels* **2015**, *29*, 546–555.

(253) Sun, Q.; Li, H.; Yan, J.; Liu, L.; Yu, Z.; Yu, X. *Renewable and Sustainable Energy Reviews* **2015**, *51*, 521–532.

(254) Energy Information Administration *Renewable energy annual 1996*; tech. rep.; Washington, DC: Energy Information Administration, 1997.

(255) Leung, D. Y.; Caramanna, G.; Maroto-Valer, M. M. *Renewable and Sustainable Energy Reviews* **2014**, *39*, 426–443.

(256) Rufford, T. E.; Smart, S.; Watson, G. C.; Graham, B. F.; Boxall, J.; Diniz da Costa, J. C.; May, E. F. *Journal of Petroleum Science and Engineering* **2012**, *94-95*, 123–154.

(257) International Energy Agency *Global Energy & CO2 Status Report 2019*; tech. rep.; Paris: International Energy Agency, 2019.

(258) World Energy Council *Full report: The Role of Natural Gas (Perspective from the 2016 World Energy Scenarios)*; tech. rep.; London, UK: World Energy Council, 2017.

(259) Van Hook, J. P. *Catalysis Reviews - Science and Engineering* **1980**, *21*, 1–51.

(260) Levalley, T. L.; Richard, A. R.; Fan, M. *International Journal of Hydrogen Energy* **2014**, *39*, 16983–17000.

(261) Neiva, L. S.; Gama, L. In *Natural Gas*, Potocnik, P., Ed.; Sciyo: Paris, 2010; Chapter 3, pp 71–85.

(262) Ozekmekci, M.; Salkic, G.; Fellah, M. F. *Fuel Processing Technology* **2015**, *139*, 49–60.

(263) Yang, Y.; Burke, N.; Ali, S.; Huang, S.; Lim, S.; Zhu, Y. *RSC Adv.* **2017**, *7*, 12629–12638.

(264) Kohl, A. L.; Nielsen, R. B., *Gas Purification*, Fifth; Gulf Publishing Company: Houston, Texas, 1997.

(265) García, E. J.; Pérez-Pellitero, J.; Pirngruber, G. D.; Jallut, C.; Palomino, M.; Rey, F.; Valencia, S. *Industrial & Engineering Chemistry Research* **2014**, *53*, 9860–9874.

(266) Abdulsalam, J.; Mulopo, J.; Amosa, M. K.; Bada, S.; Falcon, R.; Oboirien, B. O. *Separation Science and Technology (Philadelphia)* **2019**, *54*, 2461–2497.

(267) Collins, J. J. Bulk separation of carbon dioxide from natural gas. US 3751878, 1973.

(268) Kumar, R. Adsorptive process for producing two gas streams from a gas mixture. US 5026406, 1991.

(269) Sircar, S.; Kumar, R.; Koch, W. R.; VanSloun, J. Recovery of methane from land fill gas. US 4770676, 1988.

(270) Seery, M. W. Bulk separation of carbon dioxide from methane using natural clinoptilolite. US 5938819, 1999.

(271) Molecular Gate® Adsorption Technology, https://www.guildassociates.com/gas-processing-systems/mgtech/, (accessed Aug 23 2021).

(272) Montanari, T.; Finocchio, E.; Salvatore, E.; Garuti, G.; Giordano, A.; Pistarino, C.; Busca, G. *Energy* **2011**, *36*, 314–319.

(273) Bonenfant, D.; Kharoune, M.; Niquette, P.; Mimeault, M.; Hausler, R. *Science and Technology of Advanced Materials* **2008**, *9*, DOI: 10.1088/1468-6996/9/1/013007.

(274) Milton, R. M. Sweetening and drying of natural gas. US 3078634, 1963.

(275) Aitani, A. M. *Hydrocarbon processing* **1993**, 67–73.

(276) Wang, Y.; LeVan, M. D. *Journal of Chemical & Engineering Data* **2010**, *55*, 3189–3195.

(277) Brandani, F.; Ruthven, D. M. *Industrial & Engineering Chemistry Research* **2004**, *43*, 8339–8344.

(278) Grajciar, L.; Čejka, J.; Zukal, A.; Otero Areán, C.; Turnes Palomino, G.; Nachtigall, P. *ChemSusChem* **2012**, *5*, 2011–2022.

(279) Palomino, M.; Corma, A.; Rey, F.; Valencia, S. *Langmuir* **2010**, *26*, 1910–1917.

(280) Palomino, M.; Corma, A.; Jordá, J. L.; Rey, F.; Valencia, S. *Chemical communications (Cambridge, England)* **2012**, *48*, 215–7.

(281) Min, J. G.; Kemp, K. C.; Hong, S. B. *Journal of Physical Chemistry C* **2017**, *121*, 3404–3409.

(282) Lee, H.; Shin, J.; Choi, W.; Choi, H. J.; Yang, T.; Zou, X.; Hong, S. B. *Chemistry of Materials* **2018**, acs.chemmater.8b03311.

(283) Pourmahdi, Z.; Maghsoudi, H. *Adsorption* **2017**, *23*, 799–807.

(284) Pham, T. D.; Lobo, R. F. *Microporous and Mesoporous Materials* **2016**, *236*, 100–108.

(285) Su, X.; Tian, P.; Fan, D.; Xia, Q.; Yang, Y.; Xu, S.; Zhang, L.; Zhang, Y.; Wang, D.; Liu, Z. *ChemSusChem* **2013**, *6*, 911–918.

(286) Bacsik, Z.; Cheung, O.; Vasiliev, P.; Hedin, N. *Applied Energy* **2016**, *162*, 613–621.

(287) Cheung, O.; Liu, Q.; Bacsik, Z.; Hedin, N. *Microporous and Mesoporous Materials* **2012**, *156*, 90–96.

(288) Liu, X.; Vlugt, T. J. H.; Bardow, A. *Fluid Phase Equilibria* **2011**, *301*, 110–117.

(289) Pérez-Botella, E.; Martínez-Franco, R.; González-Camuñas, N.; Cantín, Palomino, M.; Moliner, M.; Valencia, S.; Rey, F. *Frontiers in Chemistry* **2020**, *8*, 1–10.

(290) Xie, D.; Zones, S. I.; Huang, H.-m.; Thompson, J. A.; Lacheen, H. S.; Mathieux, C. Separation of gases using zeolite SSZ-45. US 8926735 B1, 2015.

(291) Corma Canos, A.; Palomino Roca, M.; Rey Garcia, F.; Valencia Valencia, S. Use of a microporous crystalline material of zeolitic nature with RHO structure in natural gas processing. EP 2420551 A1, 2012.

(292) Corcoran, E. W. J.; Corma Canos, A.; Rey Garcia, F.; Valencia Valencia, S.; Cantin Sanz, A.; Palomino Roca, M. Separation, storage and catalytic conversion of fluids using ITQ-55. WO 2015/196023 A1, 2015.

(293) Lincoln, S. F. *Ambio* **2005**, *34*, 621–627.

(294) IPCC *IPCC 2014: Climate Change 2014: Synthesis Report*; tech. rep.; Geneva, Switzerland: Intergovernmental Panel on Climate Change, 2014.

(295) Olajire, A. A. *Energy* **2010**, *35*, 2610–2628.

(296) Sifat, N. S.; Haseli, Y. *Energies* **2019**, *12*, DOI: `10.3390/en12214143`.

(297) MacDowell, N.; Florin, N.; Buchard, A.; Hallett, J.; Galindo, A.; Jackson, G.; Adjiman, C. S.; Williams, C. K.; Shah, N.; Fennell, P. *Energy and Environmental Science* **2010**, *3*, 1645–1669.

(298) Air Products *2020 Sustainability Report*; tech. rep.; Allentown, PA: Air Products Inc., 2020.

(299) Spath, P. L.; Dayton, D. C. *Preliminary Screening – Technical and Economic Assessment of Synthesis Gas to Fuels and Chemicals with Emphasis on the Potential for Biomass-Derived Syngas*; tech. rep. December; 2003, pp 1 –160.

(300) Jones, C. W. *Annual Review of Chemical and Biomolecular Engineering* **2011**, *2*, 31–52.

(301) Li, B.; Duan, Y.; Luebke, D.; Morreale, B. *Applied Energy* **2013**, *102*, 1439–1447.

(302) Riboldi, L.; Bolland, O. *Energy Procedia* **2017**, *114*, 2390–2400.

(303) Lee, S. Y.; Park, S. J. *Journal of Industrial and Engineering Chemistry* **2015**, *23*, 1–11.

(304) Hedin, N.; Chen, L.; Laaksonen, A. *Nanoscale* **2010**, *2*, 1819.

(305) Wang, Q.; Luo, J.; Zhong, Z.; Borgna, A. *Energy Environ. Sci.* **2011**, *4*, 42–55.

(306) Abanades, J. C.; Arias, B.; Lyngfelt, A.; Mattisson, T.; Wiley, D. E.; Li, H.; Ho, M. T.; Mangano, E.; Brandani, S. *International Journal of Greenhouse Gas Control* **2015**, *40*, 126–166.

(307) Chang, F.; Zhou, J.; Chen, P.; Chen, Y.; Jia, H.; Saad, S. M. I.; Gao, Y.; Cao, X.; Zheng, T. *Asia-Pacific Journal of Chemical Engineering* **2013**, *8*, 618–626.

(308) Kumar, R. Removal of water and carbon dioxide from atmospheric air. US 4711645, 1987.

(309) Cheung, O.; Hedin, N. *RSC Adv.* **2014**, *4*, 14480–14494.

(310) Gómez-Álvarez, P.; Calero, S. *Chemistry - A European Journal* **2016**, *22*, 18705–18708.

(311) Pham, T. D.; Xiong, R.; Sandler, S. I.; Lobo, R. F. *Microporous and Mesoporous Materials* **2014**, *185*, 157–166.

(312) Pham, T. D.; Hudson, M. R.; Brown, C. M.; Lobo, R. F. *ChemSusChem* **2014**, *7*, 3031–3038.

(313) Pham, T. D.; Liu, Q.; Lobo, R. F. *Langmuir* **2013**, *29*, 832–839.

(314) Miyamoto, M.; Fujioka, Y.; Yogo, K. *Journal of Materials Chemistry* **2012**, *22*, 20186.

(315) Himeno, S.; Tomita, T.; Suzuki, K.; Nakayama, K.; Yajima, K.; Yoshida, S. *Industrial and Engineering Chemistry Research* **2007**, *46*, 6989–6997.

(316) Couck, S.; Lefevere, J.; Mullens, S.; Protasova, L.; Meynen, V.; Desmet, G.; Baron, G. V.; Denayer, J. F. M. *Chemical Engineering Journal* **2017**, *308*, 719–726.

(317) Fischer, M. *Phys. Chem. Chem. Phys.* **2017**, *19*, 22801–22812.

(318) Market Research Future Global Light Olefins Market Information: By Type (Ethylene, Propylene), Derivatives (Polypropylene, Propylene Oxide, Acrylonitrile, Cumene, Acrylic Acid, Oxo Alcohols, Polyethylene), Application (Chemical Commodities, Refinery), And By Region – Forecast Till 2027, https://www.marketresearchfuture.com/reports/light-olefin-market-1037, 2021 (accessed Aug 23 2021).

(319) Amghizar, I.; Vandewalle, L. A.; Van Geem, K. M.; Marin, G. B. *Engineering* **2017**, *3*, 171–178.

(320) Chauvel, A.; Lefebvre, G., *Petrochemical processes : technical and economic characteristics*; Technip: Paris, 1989.

(321) Eldridge, R. B. *Ind. Eng. Chem. Res.* **1993**, *32*, 2208–2212.

(322) Wang, Y.; Peh, S. B.; Zhao, D. *Small* **2019**, *1900058*, 1–38.

(323) Yang, R. T.; Kikkinides, E. S. *AIChE Journal* **1995**, *41*, 509–517.

(324) Chen, J. P.; Yang, R. T. *Langmuir* **1995**, *11*, 3450–3456.

(325) Jayaraman, A.; Yang, R. T.; Munson, C. L.; Chinn, D. *Industrial and Engineering Chemistry Research* **2001**, *40*, 4370–4376.

(326) Liang, W.; Xu, F.; Zhou, X.; Xiao, J.; Xia, Q.; Li, Y.; Li, Z. *Chemical Engineering Science* **2016**, *148*, 275–281.

(327) Wang, X.; Wu, Y.; Zhou, X.; Xiao, J.; Xia, Q.; Wang, H.; Li, Z. *Chemical Engineering Science* **2016**, *155*, 338–347.

(328) Pintor Labandeira, A. *Empleo de materiales porosos como adsorbentes selectivos en la separación de olefinas / parafinas .* Tech. rep.; Universitat Politècnica de València - Consejo Superior de Investigaciones Científicas, 2020.

(329) Olson, D. H. Light Hydrocarbon Separation Using 8-Member Ring Zeolites. US 6488741 B2, 2002.

(330) Olson, D. H.; Yang, X.; Camblor, M. A. *Journal of Physical Chemistry B* **2004**, *108*, 11044–11048.

(331) Olson, D. H.; Camblor, M. A.; Villaescusa, L. A.; Kuehl, G. H. *Microporous and Mesoporous Materials* **2004**, *67*, 27–33.

(332) Gutiérrez-Sevillano, J. J.; Dubbeldam, D.; Rey, F.; Valencia, S.; Palomino, M.; Martín-Calvo, A.; Calero, S. *J. Phys. Chem. C* **2010**, *114*, 14907–14914.

(333) Palomino, M.; Cantín, A.; Corma, A.; Leiva, S.; Rey, F.; Valencia, S. *Chemical Communications* **2007**, 1233–1235.

(334) Gutiérrez-Sevillano, J. J.; Calero, S.; Hamad, S.; Grau-Crespo, R.; Rey, F.; Valencia, S.; Palomino, M.; Balestra, S. R. G.; Ruiz-Salvador, A. R. *Chemistry - A European Journal* **2016**, *22*, 10036–10043.

(335) Bereciartua, P. J. et al. *Science* **2017**, *358*, 1068–1071.

(336) Lin, R.-B.; Li, L.; Zhou, H.-L.; Wu, H.; He, C.; Li, S.; Krishna, R.; Li, J.; Zhou, W.; Chen, B. *Nature Materials* **2018**, DOI: 10.1038/s41563-018-0206-2.

(337) Casty, G. L.; Hall, R. B.; Reyes, S. C.; Reynolds JR., R. P.; Strohmaier, K. G. Separation of 1-butene from C4 feed streams. US 2004/0260138 A1, 2004.

(338) Demirbas, A.; Balubaid, M. A.; Basahel, A. M.; Ahmad, W.; Sheikh, M. H. *Petroleum Science and Technology* **2015**, *33*, 1190–1197.

(339) Valavarasu, G.; Sairam, B. *Petroleum Science and Technology* **2013**, *31*, 580–595.

(340) Aitani, A.; Akhtar, M. N.; Al-Khattaf, S.; Jin, Y.; Koseoglo, O.; Klein, M. T. *Energy & Fuels* **2019**, *33*, 3828–3843.

(341) Graeme, S.; Ross, J. *Advanced Solutions for Paraffins Isomerization*; tech. rep.; Washington, DC: National Petrochemical & Refiners Association, 2004, pp 1–26.

(342) Denayer, J. F. M.; Ocakoglu, R. A.; De Meyer, K.; Baron, G. V. *Adsorption* **2005**, *11*, 49–53.

(343) Asher, W. J.; Epperly, W. R. Hydrocarbon separation process. US 3070542, 1962.

(344) IsoSiv *Chemical & Engineering News* **1962**, *40*, 59–63.

(345) Asher, W. J.; Campbell, M. L.; Epperly, W. R.; Robertson, J. L. *Hydrocarbon processing* **1969**, *48*, 134–138.

(346) Anderson, R. A. In *Molecular Sieves - II*, Katzer, J. R., Ed.; American Chemical Society: Washington, DC, 1977; Chapter 53, pp 637–649.

(347) Águeda, V. I.; Uguina, M. A.; Delgado, J. A.; Holik, M. T.; Aranda, D.; López, I. D.; Lázaro, J. J.; Peláez, J. *Adsorption* **2017**, *23*, 257–269.

(348) Barrer, R. M.; Belchetz, L. *Journal of the Society of Chemical Industry* **1945**, *64*, 130–135.

(349) Kulprathipanja, S.; Neuzil, R. W. Process for separating normal paraffins using silicalite adsorbent. US 4367364, 1983.

(350) Kulprathipanja, S.; Neuzil, R. W. Low temperature process for separating hydrocarbons. US 4455444, 1984.

(351) Neuzil, R. W. Selectively adsorbing multibranched paraffins. US 3706813, 1972.

(352) Owaysi, F. A.; Al-Ameeri, R. S. Purfication of liquid paraffins. EP 0164905 A1, 1985.

(353) Dandekar, H. W.; Funk, G. A.; Zinnen, H. A. Process for separating and recovering multimethyl-branched alkanes. US 6069289 A, 2000.

(354) Calero, S.; Smit, B.; Krishna, R. *Physical Chemistry Chemical Physics* **2001**, *3*, 4390–4398.

(355) Dubbeldam, D.; Krishna, R.; Calero, S.; Yazaydin, A. *Angewandte Chemie - International Edition* **2012**, *51*, 11867–11871.

(356) Bayati, B.; Belbasi, Z.; Ejtemaei, M.; Charchi Aghdam, N.; Babaluo, A. A.; Haghighi, M.; Drioli, E. *Separation and Purification Technology* **2013**, *106*, 56–62.

(357) Funke, H. H.; Argo, A. M.; Falconer, J. L.; Noble, R. D. *Industrial and Engineering Chemistry Research* **1997**, *36*, 137–143.

(358) Ragil, K.; Prevost, I.; Clause, O.; Larue, J.; Millot, B. Process for separating a C5-C8 feed or an intermediate feed into three effluents, respectively rich in straight chain, non-branched and multi-branched paraffins. US 6156950, 2000.

(359) Baudot, A.; Bournay, L. *Oil & Gas Science and Technology - Revue de l'IFP* **2009**, *64*, 759–771.

(360) Ducreux, O; Jolimaitre, E Process Combining Hydroisomerization and Separation Using a Zeolitic Adsorbent with a Mixed Structure for the Production of High Octane Number Gasolines. US 6809228 B2, 2004.

(361) Ragil, K.; Jullian, S.; Durand, J.-P.; Hotier, G.; Clause, O. High octane number gasolines and their production using a process associating hydro-isomerization and separation. US 6338791 B1, 2002.

(362) Jolimaitre, E.; Ragil, K.; Tayakout-Fayolle, M.; Jallut, C. *AIChE Journal* **2002**, *48*, 1927–1937.

(363) McCulloch, B.; Lansbarkis, J. R.; Raghuram, S.; Haizmann, R. S. Extraction of Dimethyl Paraffins from Isomerates. US 5107052, 1992.

(364) Maesen, T.; Harris, T. Process for producing high RON gasoline using ATS zeolite. US 7029572 B2, 2006.

(365) Maesen, T.; Harris, T. Process for producing high RON gasoline using CFI zeolite. US 7037422 B2, 2006.

(366) Jolimaitre, E.; Ducreux, O. Process for separating multibranched paraffins using a zeolitic adsorbent with a mixed structure. US 6784334 B2, 2004.

(367) Denayer, J.; Ocakoglu, R.; Baron, G. Method for separating hydrocarbons and use of a zeolite therefor. US 7435865 B2, 2008.

(368) Laredo, G. C.; Trejo-Zarraga, F.; Jimenez-Cruz, F.; Garcia-Gutierrez, J. L. *Recent Patents on Chemical Engineering* **2012**, *5*, 153–173.

(369) Luque, R.; Herrero-Davila, L.; Campelo, J. M.; Clark, J. H.; Hidalgo, J. M.; Luna, D.; Marinas, J. M.; Romero, A. A. *Energy and Environmental Science* **2008**, *1*, 542–564.

(370) Ezeji, T. C.; Qureshi, N.; Blaschek, H. P. *A Chemical Record* **2004**, *4*, 305–314.

(371) Weizmann, C. Perfectionnements apportés à la production de l'acétone et de l'alcool butylique par procédés bactériologiques. FR 498703, 1916.

(372) Weizmann, C. Perfectionnements apportés aux procédés de production par fermentation de l'acétone et de l'alcool butylique. FR 499582, 1918.

(373) Weizmann, C. Fermentation process for the production of acetone and butyl alcohol. US 1437697, 1922.

(374) Dürre, P. *Biotechnology Journal* **2007**, *2*, 1525–1534.

(375) Ndaba, B.; Adeleke, R.; Makofane, R.; Daramola, M. O.; Moshokoa, M. In *Valorization of Biomass to Value-Added Commodities Current Trends, Challenges, and Future Prospects.* Daramola, M. O., Ayeni, A. O., Eds.; Green Energy and Technology; Springer International Publishing: Cham, 2020; Chapter 18, pp 371–398.

(376) Huang, H. J.; Ramaswamy, S.; Liu, Y. *Separation and Purification Technology* **2014**, *132*, 513–540.

(377) Oudshoorn, A.; Van Der Wielen, L. A.; Straathof, A. J. *Industrial and Engineering Chemistry Research* **2009**, *48*, 7325–7336.

(378) Abdehagh, N.; Tezel, F. H.; Thibault, J. *Biomass and Bioenergy* **2014**, *60*, 222–246.

(379) Abdehagh, N.; Tezel, F. H.; Thibault, J. *Adsorption* **2013**, *19*, 1263–1272.

(380) Abdehagh, N.; Gurnani, P.; Tezel, F. H.; Thibault, J. *Adsorption* **2015**, *21*, 185–194.

(381) Groot, W. J.; Luyben, K. C. A. *Applied Microbiology and Biotechnology* **1986**, *25*, 29–31.

(382) Cousinsaintremi, J.; Rémy, T.; Vanhunskerken, V.; Vandeperre, S.; Duerinck, T.; Maes, M.; Devos, D.; Gobechiya, E.; Kirschhock, C. E.; Baron, G. V.; Denayer, J. F. *ChemSusChem* **2011**, *4*, 1074–1077.

(383) Qureshi, N.; Hughes, S.; Maddox, I. S.; Cotta, M. A. *Bioprocess and Biosystems Engineering* **2005**, *27*, 215–222.

(384) Cousin Saint Remi, J.; Baron, G.; Denayer, J. F. M. *Adsorption* **2012**, *18*, 367–373.

(385) Nielsen, D. R.; Prather, K. J. *Biotechnology and Bioengineering* **2009**, *102*, 811–821.

(386) Nielsen, L.; Larsson, M.; Holst, O.; Mattiasson, B. *Applied Microbiology and Biotechnology* **1988**, *28*, 335–339.

(387) Ennis, B. M.; Qureshi, N.; Maddox, I. S. *Enzyme and Microbial Technology* **1987**, *9*, 672–675.

(388) Raganati, F.; Procentese, A.; Olivieri, G.; Russo, M. E.; Salatino, P.; Marzocchella, A. *Separation and Purification Technology* **2020**, *235*, 116145.

(389) Faisal, A.; Zarebska, A.; Saremi, P.; Korelskiy, D.; Ohlin, L.; Rova, U.; Hedlund, J.; Grahn, M. *Adsorption* **2014**, *20*, 465–470.

(390) Oudshoorn, A.; van der Wielen, L. A.; Straathof, A. J. *Biochemical Engineering Journal* **2009**, *48*, 99–103.

(391) Long, Y.-c.; Jiang, H.-w.; Zeng, H. *Langmuir* **1997**, *13*, 4094–4101.

(392) Maddox, I. S. *Biotechnology Letters* **1982**, *4*, 759–760.

(393) Gómez-Álvarez, P.; Noya, E. G.; Lomba, E.; Valencia, S.; Pires, J. *Langmuir* **2018**, *34*, 12739–12750.

(394) Faisal, A.; Zhou, M.; Hedlund, J.; Grahn, M. *Biomass Conversion and Biorefinery* **2018**, *8*, 679–687.

(395) Cao, Y.; Wang, K.; Wang, X.; Gu, Z.; Gibbons, W.; Vu, H. *Applied Surface Science* **2015**, *349*, 1–7.

(396) Cao, Y.; Wang, K.; Wang, X.; Gu, Z.; Gibbons, W.; Vu, H. *Bioresource Technology* **2015**, *196*, 525–532.

(397) Abdehagh, N.; Dai, B.; Thibault, J.; Handan Tezel, F. *Journal of Chemical Technology and Biotechnology* **2017**, *92*, 245–251.

(398)   Van der Perre, S.; Gelin, P.; Claessens, B.; Martin-Calvo, A.; Cousin Saint Remi, J.; Duerinck, T.; Baron, G. V.; Palomino, M.; Sánchez, L. Y.; Valencia, S.; Shang, J.; Singh, R.; Webley, P. A.; Rey, F.; Denayer, J. F. M. *ChemSusChem* **2017**, *10*, 2968–2977.

(399)   Farzaneh, A.; Zhou, M.; Potapova, E.; Bacsik, Z.; Ohlin, L.; Holmgren, A.; Hedlund, J.; Grahn, M. *Langmuir* **2015**, *31*, 4887–4894.

(400)   Farzaneh, A.; Zhou, M.; Antzutkin, O. N.; Bacsik, Z.; Hedlund, J.; Holmgren, A.; Grahn, M. *Langmuir* **2016**, *32*, 11789–11798.

(401)   Martin-Calvo, A.; Van Der Perre, S.; Claessens, B.; Calero, S.; Denayer, J. F. *Physical Chemistry Chemical Physics* **2018**, *20*, 9957–9964.

(402)   Claessens, B.; Dubois, N.; Lefevere, J.; Mullens, S.; Cousin-Saint-Remi, J.; Denayer, J. F. *Industrial and Engineering Chemistry Research* **2020**, *59*, 8813–8824.

(403)   Bhattacharyya, S.; Jayachandrababu, K. C.; Chiang, Y.; Sholl, D. S.; Nair, S. *ACS Sustainable Chemistry and Engineering* **2017**, *5*, 9467–9476.

(404)   Flanigen, E. M.; Bennett, J. M.; Grose, R. W.; Cohen, J. P.; Patton, R. L.; Kirchner, R. M.; Smith, J. V. *Nature* **1978**, *271*, 512–516.

(405)   Claessens, B.; Cousin-Saint-Remi, J.; Denayer, J. F. M. In; September, 2020, pp 85–119.

(406)   Sircar, S. In *Handbook of Porous Solids*; Wiley-VCH Verlag GmbH: Weinheim, Germany, 2002; Vol. 4, pp 2533–2567.

(407)   Milton, R. M. Water separation from a vapor mixture. US 3078635, 1963.

(408)   Milton, R. M. Drying of natural gas by adsorption. US 3024867, 1962.

(409)   Milton, R. M. Drying cracked gas. US 3130021, 1964.

(410) Milton, R. M. Water removal from gas mixtures. US 3164453, 1965.

(411) Ausikaitis, J. P.; Garg, D. R. Adsorption separation cycl.e, US 4373935, 1983.

(412) Teo, W. K.; Ruthven, D. M. *Industrial & Engineering Chemistry Process Design and Development* **1986**, *25*, 17–21.

(413) Sowerby, B.; Crittenden, B. D. *Gas Separation and Purification* **1988**, *2*, 77–83.

(414) Wang, Y.; Deckman, H. W.; Wittrig, A. M.; Strohmaier, K. G.; Leta, D. P.; Ravikovitch, P. I. Swing adsorption processes using zeolite structures. US 2018/0056235 A1, 2018.

(415) Wang, Y.; Deckmann, H. W.; Wittrig, A. M.; Strohmaier, K. G.; Leta, D. P.; Ravikovitch, P. I. Swing adsorption processes using zeolite structures. US 2020/0179870 A1, 2020.

(416) Burfield, D. R.; Lee, K. H.; Smithers, R. H. *Journal of Organic Chemistry* **1977**, *42*, 3060–3065.

(417) McKee, D. W. Separation of an oxygen-nitrogen mixture. US 3140932, 1964.

(418) Chao, C. C. Process for separating nitrogen from mixtures thereof with less polar substances. US 4859217, 1989.

(419) McRobbie, H. Separation of an oxygen-nitrogen mixture. US 3140931, 1964.

(420) McKee, D. W. Separation of an oxygen-nitrogen mixture. US 3140933, 1964.

(421) Berlin, N. H. Vacuum cycle adsorption. US 3313091, 1967.

(422) Coe, C. G.; Kuznicki, S. M. Polyvalent ion exchanged adsorbent for air separation. US 4481018, 1984.

(423) Sircar, S.; Conrad, R. R.; William J. Am Binary ion exchanged type X zeolite adsorbent. US 4557736, 1985.

(424) Kirner, J. F. Nitrogen adsorption with highly Li exchanged X-zeolites with low Si/Al ratio. US 5268023, 1993.

(425) Sircar, S; Rao, M. B.; Golden, T. C. In *Adsorption and Its Applications in Industry and Environmental Protection, Vol I: Applications in Industry*, Dabrowski, A., Ed.; Elsevier Science B.V.: 1999; Vol. 120, pp 395–423.

(426) Wu, C.-W.; Kothare, M. V.; Sircar, S. *Industrial & Engineering Chemistry Research* **2014**, *53*, 7195–7201.

(427) Kuznicki, S. M.; Bell, V. A.; Petrovic, I.; Desai, B. T. Small-pored crystalline titanium molecular sieve zeolites and their use in gas separation processes. US 6068682, 2000.

(428) Kuznicki, S. M.; Bell, V. A.; Nair, S.; Hillhouse, H. W.; Jacubinas, R. M.; Braunbarth, C. M.; Toby, B. H.; Tsapatsis, M. *Nature* **2001**, *412*, 720–724.

(429) Dolan, W. B.; Butwell, K. F. Selective removal of nitrogen from natural gas by pressure swing adsorption. US 6444012 B1, 2002.

(430) Habgood, H. W. Removal of nitrogen from natural gas. US 2843219, 1958.

(431) Habgood, H. W. *Canadian Journal of Chemistry* **1958**, *36*, 1384–1397.

(432) Frankiewicz, T. C.; Donnelly, R. G. In *Industrial Gas Separations*, 1983; Vol. 223; Chapter 11, pp 213–233.

(433) Chao, C. C. Selective adsorption on magnesium-containing clinoptilolites. US 4964889, 1990.

(434) Bhadra, S. J.; Farooq, S. *Industrial and Engineering Chemistry Research* **2011**, *50*, 14030–14045.

(435) Mitariten, M. *Oil & Gas Journal* **2001**, *99*, 42–44.

(436) Mafra, L.; Vidal-Moya, J. A.; Blasco, T., *Structural Characterization of Zeolites by Advanced Solid State NMR Spectroscopic Methods*, 2012; Vol. 77, pp 259–351.

(437) Mackenzie, K. J. D.; Smith, M. E., *Multinuclear Solid-State NMR of Inorganic Materials Multinuclear Solid-State NMR of Inorganic Materials*; Cahn, R. W., Ed.; Pergamon: Amsterdam, 2002; Vol. 6.

(438) Blackwell, C. S.; Patton, R. L. *Journal of Physical Chemistry* **1988**, *92*, 3965–3970.

(439) Appleyard, I. P.; Harris, R. K.; Fitch, F. R. *Chemistry Letters* **1985**, 1747–1750.

(440) Zibrowius, B.; Löffler, E.; Hunger, M. *Zeolites* **1992**, *12*, 167–174.

(441) Brunauer, S.; Emmett, P. H.; Teller, E. *Journal of the American Chemical Society* **1938**, *60*, 309–319.

(442) De Boer, J. H.; Lippens, B. C.; Linsen, B. G.; Broekhoff, J. C.; van den Heuvel, A.; Osinga, T. J. *Journal of Colloid And Interface Science* **1966**, *21*, 405–414.

(443) Kawazoe, K.; Horváth, G. *Journal of Chemical Engineering of Japan* **1983**, *16*, 470–475.

(444) Dubinin, M. In *Progress in Surface and Membrane Science*, Cadenhead, D., Danielli, J., Rosenberg, M., Eds.; Elsevier: 1975; Vol. 9, pp 1–70.

(445) Nordstrand, R. A. V.; Santilli, D. S.; Zones, S. I. In *Perspectives in Molecular Sieve Science*, Flank, W. H., Whyte, T. E., Eds., Washington DC, 1988; Chapter 15, pp 236–245.

(446) Girnus, I.; Jancke, K.; Vetter, R.; Richter-Mendau, J.; Caro, J. *Zeolites* **1995**, *15*, 33–39.

(447) Young, D.; Davis, M. E. *Zeolites* **1991**, *11*, 277–281.

(448) Díaz-Cabañas, M.-J.; Barrett, P. A. *Chemical Communications* **1998**, *29*, 1881–1882.

(449) Zones, S. I.; Van Nordstrand, R. A. *Zeolites* **1988**, *8*, 166–174.

(450) Zones, S. I. *Journal of the Chemical Society, Faraday Transactions* **1991**, *87*, 3709.

(451)   Bourgogne, M.; Guth, J.-L.; Wey, R. Process for the preparation of synthetic zeolites, and zeolites obtained by said process. US 4503024, 1985.

(452)   Prakash, A. M.; Unnikrishnan, S. *Journal of the Chemical Society, Faraday Transactions* **1994**, *90*, 2291.

(453)   Cantín, A.; Corma, A.; Leiva, S.; Rey, F.; Rius, J.; Valencia, S. *Journal of the American Chemical Society* **2005**, *127*, 11560–11561.

(454)   Boix, T.; Puche, M.; Camblor, M. A.; Corma, A. Synthetic porous crystalline material ITQ-12, its synthesis and use. US 6471939 B1, 2002.

(455)   Barrett, P.; Boix, T.; Puche, M. *Chemical Communications* **2003**, 2114–2115.

(456)   Corma, A.; Rey, F.; Rius, J.; Sabater, M. J.; Valencia, S. *Nature* **2004**, *431*, 287–290.

(457)   Lemishko, T.; Valencia, S.; Rey, F.; Jiménez-Ruiz, M.; Sastre, G. *Journal of Physical Chemistry C* **2016**, *120*, 24904–24909.

(458)   Moscoso, J. G.; Lewis, G. J.; Gisselquist, J. L.; Miller, M. A.; Rohde, L. M. Crystalline aluminosilicate zeolitic composition: UZM-9. WO 03068679 A1, 2003.

(459)   Küehl, G. H. Preparation of shape selective zeolite alpha as catalyst. US 4191663 A, 1980.

(460)   Schreyeck, L.; Stumbe, J.; Caullet, P.; Mougenel, J.-C.; Marler, B. *Microporous and Mesoporous Materials* **1998**, *22*, 87–106.

(461)   Guth, J. L.; Kessler, H.; Wey, R. In *Studies in Surface Science and Catalysis*, Murakami, Y., Iijima, A., Ward, J., Eds.; C; Elsevier: 1986; Vol. 28, pp 121–128.

(462)   Kitamura, M.; Ichihashi, H.; Tojima, H. Process for producing epsilon-caprolactam and activating solid catalysts therefor. EP 0494535 B1, 1991.

(463) Barrett, P. a.; Diaz-Cabañas, M.-J.; Camblor, M. a. *Chemistry of Materials* **1999**, *11*, 2919–2927.

(464) Lemishko, T.; Simancas, J.; Hernández-Rodríguez, M.; Jiménez-Ruiz, M.; Sastre, G.; Rey, F. *Physical Chemistry Chemical Physics* **2016**, *18*, 17244–17252.

(465) Ramos, F. S.; Munsignatti, E. C.; Pastore, H. O. *Microporous and Mesoporous Materials* **2013**, *177*, 143–150.

(466) Ramos, F. S.; Pastore, H. O. *Dalton Transactions* **2017**, *46*, 11728–11737.

(467) Asakura, Y.; Osada, S.; Hosaka, N.; Terasawa, T.; Kuroda, K. *Dalton Trans.* **2014**, *43*, 10392–10395.

(468) Camblor, M. A.; Díaz-Cabañas, M. J.; Cox, P. A.; Shannon, I. J.; Wright, P. A.; Morris, R. E. *Chemistry of Materials* **1999**, *11*, 2878–2885.

(469) Lu, P.; Gómez-Hortigüela, L.; Xu, L.; Camblor, M. A. *Journal of Materials Chemistry A* **2018**, *6*, 1485–1495.

(470) Leachman, J. W.; Jacobsen, R. T.; Penoncello, S. G.; Lemmon, E. W. *Journal of Physical and Chemical Reference Data* **2009**, *38*, 721–748.

(471) Richardson, I. A.; Leachman, J. W.; Lemmon, E. W. *Journal of Physical and Chemical Reference Data* **2014**, *43*, DOI: `10.1063/1.4864752`.

(472) Span, R.; Wagner, W. *Journal of Physical and Chemical Reference Data* **1996**, *25*, 1509–1596.

(473) Span, R.; Lemmon, E. W.; Jacobsen, R. T.; Wagner, W.; Yokozeki, A. *Journal of Physical and Chemical Reference Data* **2000**, *29*, 1361–1401.

(474) Setzmann, U.; Wagner, W. *Journal of Physical and Chemical Reference Data* **1991**, *20*, 1061–1155.

(475) McCarty, R. Correlations for the Thermophysical Properties of Carbon Monoxide, Boulder, CO, 1989.

(476) McCarty, R.; Arp, V. D. In *Advances in Cryogenic Engineering*, R.W., F., Ed.; Springer: Boston, MA, 1990, pp 1465–1475.

(477) Langmuir, I. *Journal of the American Chemical Society* **1918**, *40*, 1361–1403.

(478) Freundlich, H., *Kapillarchemie; eine Darstellung der Chemie der Kolloide und verwandter Gebiete*; Akademische Verlagsgesellschaft m.b.H.: Leipzig, 1909.

(479) Toth, *Adsorption Theory Modeling and Analysis*, 1st; Marcel Dekker, Inc.: New York, Basel, 2002.

(480) Pierotti, R. *Chemical Physics Letters* **1968**, *2*, 385–388.

(481) Crank, J, *The Mathematics of Diffusion*; Oxford University Press: Oxford, 1975.

(482) Malek, A.; Farooq, S. *Journal of Chemical & Engineering Data* **1996**, *41*, 25–32.

(483) Silva, J. A. C.; Cunha, A. F.; Schumann, K.; Rodrigues, A. E. *Microporous and Mesoporous Materials* **2014**, *187*, 100–107.

(484) Benyahia, F.; O'Neill, K. E. *Particulate Science and Technology* **2005**, *23*, 169–177.

(485) Foss, M. M. *Interstate Natural Gas — Quality Specifications & Interchangeability*; tech. rep. December; Sugar Land, TX: Center for Energy Economics, 2004.

(486) Wagner, W. *Cryogenics* **1973**, *13*, 470–482.

(487) Poling, B. E.; Prausnitz, J. M.; O'Connell, J. P., *The Properties of Gases and Liquids*, 5th Editio; McGraw-Hill: 2000.

(488) Sastre, G.; Corma, A. *Journal of Molecular Catalysis A: Chemical* **2009**, *305*, 3–7.

(489) Shang, J.; Li, G.; Singh, R.; Gu, Q.; Nairn, K. M.; Bastow, T. J.; Medhekar, N.; Doherty, C. M.; Hill, A. J.; Liu, J. Z.; Webley, P. A. *Journal of the American Chemical Society* **2012**, *134*, 19246–19253.

(490) U.S. Secretary of Commerce NIST Chemistry WebBook, SRD 69 - Carbon Dioxide, https://webbook.nist.gov/cgi/cbook.cgi?ID=C124389, (accessed Aug 23 2021).

(491) Takeguchi, T.; Tanakulrungsank, W.; Inui, T. *Gas Separation and Purification* **1993**, *7*, 3–9.

(492) Poshusta, J. C.; Tuan, V. A.; Falconer, J. L.; Noble, R. D. *Industrial and Engineering Chemistry Research* **1998**, *37*, 3924–3929.

(493) Li, S.; Falconer, J. L.; Noble, R. D. *Advanced Materials* **2006**, *18*, 2601–2603.

(494) Palomino, M. ESTUDIO DE PROCESOS DE SEPARACIÓN DE HIDROCARBUROS LIGEROS MEDIANTE EL EMPLEO DE TAMICES MOLECULARES, Ph.D. Thesis, UNIVERSITAT POLITÈCNICA DE VALÈNCIA, 2016.

(495) Remy, T.; Gobechiya, E.; Danaci, D.; Peter, S. A.; Xiao, P.; Van Tendeloo, L.; Couck, S.; Shang, J.; Kirschhock, C. E. A.; Singh, R. K.; Martens, J. A.; Baron, G. V.; Webley, P. A.; Denayer, J. F. M. *RSC Advances* **2014**, *4*, 62511–62524.

(496) Pérez-Botella, E.; Misturini, A.; Sala, A.; Palomino, M.; Corma, A.; Sastre, G.; Valencia, S.; Rey, F. *The Journal of Physical Chemistry C* **2020**, *124*, 26821–26829.

(497) Denayer, J. F. M.; Baron, G. V.; Martens, J. A.; Jacobs, P. A. *The Journal of Physical Chemistry B* **1998**, *102*, 3077–3081.

(498) Ferreira, A. F.; Mittelmeijer-Hazeleger, M. C.; Bliek, A. *Adsorption* **2007**, *13*, 105–114.

(499) Dubbeldam, D.; Calero, S.; Vlugt, T. J.; Krishna, R.; Maesen, T. L.; Smit, B. *Journal of Physical Chemistry B* **2004**, *108*, 12301–12313.

(500) Denayer, J. F.; Souverijns, W.; Jacobs, P. A.; Martens, J. A.; Baron, G. V. *The Journal of Physical Chemistry B* **1998**, *102*, 4588–4597.

(501) Min, J. G.; Luna-Triguero, A.; Byun, Y.; Balestra, S. R. G.; Vicent-Luna, J. M.; Calero, S.; Hong, S. B.; Camblor, M. A. *Langmuir* **2018**, *34*, 4774–4779.

(502) Sala, A.; Pérez-Botella, E.; Jordá, J. L.; Cantín, A.; Rey, F.; Valencia, S. *Angewandte Chemie International Edition* **2021**, *60*, 11745–11750.